

UNIVERSIDAD DE SEVILLA

Sistemas de Conversión de Energía y Producción de Potencia

Terrestrial Demonstrator for the Hydrogen Extraction of Oxygen from Lunar Regolith with Concentrated Solar Energy



UNIVERSIDAD DE SEVILLA

Dissertation

Presented by: Thorsten Denk, January 2022

Director: Carlos Gómez Camacho



Thorsten Denk

Terrestrial Demonstrator for the Hydrogen Extraction of Oxygen from Lunar Regolith with Concentrated Solar Energy

Thorsten Denk

Ciemat - Plataforma Solar de Almería

Tabernas, Almería, Spain

tdenk@psa.es

oresol@tdenk.eu

For my parents,
my brothers,
Isabel,
Flory, Pablo, and Félix.

Thorsten Denk

Terrestrial Demonstrator for the Hydrogen Extraction of Oxygen from Lunar Regolith with Concentrated Solar Energy

Abstract

An experimental plant for the reduction of granular ilmenite (FeTiO_3) with hydrogen (H_2) powered by concentrated solar radiation was designed, built, and tested to demonstrate extraction of oxygen from lunar soil at the Plataforma Solar de Almería (PSA). This is done by a two-step process with water (H_2O) as the intermediate product. The center-piece of the system is a fluidized bed reactor with a capacity of 22 kg of ilmenite, capable of operating in fully continuous mode. The reactor has a large quartz window that allows the concentrated solar radiation to heat the particles directly without the need for any heat exchanger surfaces. The system includes most of the peripheral components required to demonstrate its functioning as close as possible to what can be expected on the Moon. This includes in particular the cleaning system for the off-gas from the reactor, the extraction of the product water, and the gas recovery. The system was operated in the 60 kW Solar Furnace at PSA with solar power during 150 hours in four test campaigns. All initial test goals were successfully achieved. The maximum operation temperature in the reactor was 977°C , and during a total of 21 hours of operation with hydrogen, the chemical reaction produced more than 1300 ml of water. To this date, this is the only large scale terrestrial demonstrator in Europe that has successfully produced water from minerals present in lunar regolith solely with concentrated solar power as heat source, showing a path for future chemical production on the lunar surface.

Resumen

En la Plataforma Solar de Almería (PSA) se ha diseñado, construido y probado una planta experimental para la reducción de ilmenita granular (FeTiO_3) con hidrógeno (H_2), alimentada por radiación solar concentrada con el objetivo de demostrar la extracción de oxígeno de la roca lunar. Esto se hace mediante un proceso de dos pasos con agua (H_2O) como producto intermedio. La pieza central del sistema es un reactor tipo lecho fluidizado con una capacidad de 22 kg de ilmenita, capaz de funcionar completamente en modo continuo. El reactor tiene una gran ventana de cuarzo que permite que el rayo solar concentrado caliente directamente las partículas sin necesidad de ninguna superficie de intercambio de calor. El sistema incluye la mayoría de los componentes periféricos necesarios para demostrar su funcionamiento lo más parecido posible a lo que se puede esperar en la Luna. Esto incluye, en particular, el sistema de limpieza del gas de salida del reactor, la extracción del agua producto, y la recirculación del gas. El sistema fue operado en el Horno Solar de 60 kW en la PSA con energía solar durante 150 horas en cuatro campañas de ensayo. Todos los objetivos iniciales se alcanzaron con éxito. La temperatura máxima en el reactor fue de 977°C , y durante un total de 21 horas de operación con hidrógeno, la reacción química produjo más de 1300 ml de agua. Hasta la fecha, este es el único demostrador terrestre a gran escala en Europa que ha producido con éxito agua a partir de minerales presentes en el regolito lunar únicamente con energía solar concentrada como fuente de calor, mostrando un camino para una futura producción química en la superficie lunar.

Kurzfassung

Auf der Plataforma Solar de Almería (PSA) wurde eine mit konzentrierter Solarstrahlung betriebene Versuchsanlage zur Reduktion von granuletem Ilmenit (FeTiO_3) mit Wasserstoff (H_2) entworfen, gebaut und getestet, um die Gewinnung von Sauerstoff aus Mondgestein zu demonstrieren. Dies geschieht in einem zweistufigen Prozess mit Wasser (H_2O) als Zwischenprodukt. Das Herzstück des Systems ist ein Wirbelschichtreaktor mit einem Fassungsvermögen von 22 kg Ilmenit, der vollständig im kontinuierlichen Modus betrieben werden kann. Der Reaktor verfügt über ein großes Quarzfenster, durch das die konzentrierte Solarstrahlung die Partikel direkt erwärmen kann, ohne dass irgendwelche Wärmetauscherflächen erforderlich wären. Das System umfasst die meisten peripheren Komponenten, die notwendig sind, um seine Funktionsweise so nah wie möglich an dem zu demonstrieren, was auf dem Mond zu erwarten ist. Dazu gehören insbesondere das Reinigungssystem für das Gas aus dem Reaktor, die Extraktion des Produktwassers sowie die Gasrückführung. Das System wurde im 60 kW-Sonnenofen der PSA in vier Testkampagnen für 150 Stunden mit Solarenergie betrieben. Alle anfänglichen Testziele wurden erfolgreich erreicht. Die maximale Betriebstemperatur im Reaktor betrug $977\text{ }^\circ\text{C}$, und während des insgesamt 21-stündigen Betriebs mit Wasserstoff wurden durch die chemische Reaktion mehr als 1300 ml Wasser erzeugt. Bis heute ist dies der einzige in größerem Maßstab gebaute terrestrische Demonstrator in Europa, der erfolgreich Wasser aus den im Mondregolith vorhandenen Mineralen ausschließlich mit konzentrierter Solarenergie als Wärmequelle hergestellt hat, was einen Weg für zukünftige chemische Produktion auf der Mondoberfläche aufzeigt.

Résumé

Une installation expérimentale pour la réduction de l'ilménite granulaire (FeTiO_3) avec de l'hydrogène (H_2), alimentée par le rayonnement solaire concentré, a été conçue, construite et testée à la Plataforma Solar de Almería (PSA) pour démontrer l'extraction de l'oxygène du sable lunaire. Ce processus se déroule en deux étapes, l'eau (H_2O) étant un produit intermédiaire. La pièce centrale du système est un réacteur à lit fluidisé d'une capacité de 22 kg d'ilménite, capable de fonctionner entièrement en continu. Le réacteur est doté d'une grande fenêtre en quartz qui permet au rayon solaire concentré de chauffer directement les particules sans qu'aucune surface d'échange thermique ne soit nécessaire. Le système comprend la plupart des composants périphériques nécessaires à une démonstration de son fonctionnement le plus proche possible de ce qui peut être envisagé sur la Lune. Il s'agit notamment du système d'épuration du gaz d'échappement du réacteur, de l'extraction de l'eau du produit et de la recirculation du gaz. Le système a fonctionné dans le four solaire de 60 kW de la PSA avec de l'énergie solaire pendant 150 heures au cours de quatre campagnes d'essai. Tous les objectifs initiaux ont été atteints avec succès. La température maximale de fonctionnement dans le réacteur était de $977\text{ }^\circ\text{C}$, et pendant un total de 21 heures de fonctionnement avec de l'hydrogène, la réaction chimique a produit plus de 1300 ml d'eau. À ce jour, il s'agit du seul démonstrateur terrestre à grande échelle en Europe qui a réussi à produire de l'eau à partir de minéraux présents dans le régolithe lunaire en utilisant uniquement l'énergie solaire concentrée comme source de chaleur, montrant ainsi une voie à suivre pour la production chimique future sur la surface lunaire.

🇨🇳 摘要 ¹

在阿尔梅里亚太阳能平台 (PSA) 设计、建造和测试了一个用氢气 (H₂) 还原粒状钛铁矿 (FeTiO₃) 的实验工厂，以证明从月岩中提取氧气。这是以水 (H₂O) 为中间产品的两步流程完成的。该系统的核心是一个流化床反应器，容量为22公斤的钛铁矿，能够完全连续运行。该反应器有一个大的石英窗，允许集中的太阳光束直接加热粒子，而不需要任何热交换表面。该系统包括大部分必要的外围部件，以证明其操作尽可能接近月球上的预期。这尤其包括反应器废气净化系统、产品水提取和气体再循环。该系统在PSA的60千瓦太阳能炉中用太阳能运行了150小时，进行了四次测试活动。所有最初的目标都已成功实现。反应器中的最高工作温度为977°C，在总共21小时的氢气操作中，化学反应产生了超过1300毫升的水。迄今为止，这是欧洲唯一的大规模陆地示范装置，它只用集中的太阳能作为热源，就成功地从月球岩石中存在的矿物中生产出了水，为未来在月球表面进行化学生产指明了方向。

🇪🇬 خلاصة 1

في منصة ألميريا الشمسية (PSA)، تم تصميم وبناء واختبار محطة تجريبية لتقليل الإلمنيت الحبيبي (FeTiO₃) مع الهيدروجين (H₂)، الذي يعمل بالإشعاع الشمسي المركز بهدف إظهار استخراج الأكسجين من القمر صخر. يتم ذلك من خلال عملية من خطوتين مع الماء (H₂O) كمنتج وسيط. محور النظام عبارة عن مفاعل من نوع الطبقة المميعة بسعة 22 كجم من الإلمنيت، وهو قادر على التشغيل المستمر بشكل كامل. يحتوي المفاعل على نافذة كوارتز كبيرة تسمح للأشعة الشمسية المركزة بتسخين الجسيمات مباشرة دون الحاجة إلى أي سطح للتبادل الحراري. يشتمل النظام على معظم المكونات الطرفية اللازمة لإثبات تشغيله في أقرب وقت ممكن مما يمكن توقعه على القمر. وهذا يشمل، على وجه الخصوص، نظام تنظيف غاز مخرج المفاعل، وإزالة الماء المنتج، وإعادة تدوير الغاز. تم تشغيل النظام في فرن شمسي بقدرة 60 كيلو واط في PSA باستخدام الطاقة الشمسية لمدة 150 ساعة في أربع حملات اختبارية. تم تحقيق جميع الأهداف الأولية بنجاح. كانت أقصى درجة حرارة في المفاعل 977 درجة مئوية، وخلال 21 ساعة من التشغيل بالهيدروجين، أنتج التفاعل الكيميائي أكثر من 1300 مل من الماء. حتى الآن، هذا هو المتظاهر الأرضي الوحيد على نطاق واسع في أوروبا الذي نجح في إنتاج المياه من المعادن الموجودة في الثرى القمري فقط باستخدام الطاقة الشمسية المركزة كمصدر للحرارة، مما يوضح مسارًا للإنتاج الكيميائي المستقبلي على سطح الأرض.

¹ Automatic translation, no warranty for accuracy.

自动翻译 <https://www.deepl.com/translator>

الترجمة الآلية <https://translate.google.com/?sl=es&tl=ar&op=translate>

Keywords

lunar oxygen production, concentrated solar power, solar reactor, lunar resources, ilmenite reduction, fluidized bed, In-Situ Resource Utilization (ISRU)

Preface

In the night from July 20 to 21, 1969, with Neil Armstrong and Buzz Aldrin, humans set foot on the Moon for the first time. Two boys, twins, three and a half years old, in a small village in southwestern Germany, were not interested at all². This changed in spring 1976, when they received the astronomy book "*Bürgels Himmelskunde*" (Bürgel, 1975) as an Easter present. From then on, a steadily growing knowledge of astronomy developed, which eventually paved the way for the decision to study aerospace engineering. While my twin brother remained in spaceflight after graduation, I decided to go into solar energy research, inspired among many other things by my knowledge of the greenhouse atmosphere of the planet Venus. My first project was a particle receiver in which concentrated solar radiation was absorbed by a free-falling particle curtain. For the tests, I had the opportunity to spend several months in southern Spain at the Plataforma Solar de Almería for the first time.

In the meantime, public interest in flights to the Moon had reached zero. Scientists were limited to analyzing lunar samples. On the 20th anniversary of the lunar landing in 1989, there was a first attempt by then U.S. President George Bush to revive human spaceflight beyond low Earth orbit. Due to poor political coordination (especially with the Congress) as well as the high expected costs, the Initiative rapidly vanished after only a few years (Whittington, 2015). Sixteen years later, a new attempt, the *Constellation program*, was launched by his son, George W. Bush, in 2005. The goals were, still under the impression of the Space Shuttle Columbia disaster, the "completion of the International Space Station" and a "return to the Moon no later than 2020". For both programs, it was important not just to conduct another "flags and footprints" mission, but to go to the Moon, "this time to stay". NASA also asked the question "Why return to the Moon?"³. Instead of long lists, I most like the answer given by Paul Spudis⁴ (Spudis, 2016):

"Using the Moon to learn how to live and work productively in space"

By this time, I was already working permanently at the PSA, including on projects involving a solar-powered gas turbine and a solar reactor for the production of syngas. On Christmas 2006, I received a call from my colleague Inma Cañadas informing me that the PSA could collaborate on a project to extract oxygen from lunar rocks. This resonated with me because it was a unique opportunity to combine all three of my areas of expertise within one project: solar energy, particle technology, and spaceflight. The seed for the *Oresol* project was laid.

After the administrative preparations were completed, the project officially began on January 01, 2008. Not long after, the political priorities in space travel changed again with the election of Barack Obama as US president. The Moon was once more out of fashion, instead it was planned to fly to an asteroid, or simply just "somewhere". Many voices still advocated going directly to Mars. But to me, entirely in the spirit of Paul Spudis, it was very clear at any moment that, if at all, the Moon would definitely be the first place where to go. It is simply so close to Earth compared to other destinations that it would be very unwise not to at least test future interplanetary space systems on the Moon first. Therefore, I continued undeterred with my work, in the confidence that one day the Moon would return to the focus of attention.

² Source: My mother, personal communication.

³ https://www.nasa.gov/exploration/home/why_moon.html

⁴ <https://www.spudislunarresources.com/>

And so it happened. After Donald Trump became president in 2017, the Moon landing was again declared the next goal of human spaceflight. For this purpose, the *Artemis program* was launched. Around this time, many results from Oresol (Fig. 1) were already available and the decision was made to publish this work in the form of a PhD thesis. This text is the result. Despite the recent, yet again change of government in the USA, it now looks as if the Moon landing will not be cancelled this time. So there is a reasonable chance that from about 2025 on, humans will set foot on the Moon again. This time to... learn how to produce oxygen?

Thorsten Denk

Almería, Spain

January 2022

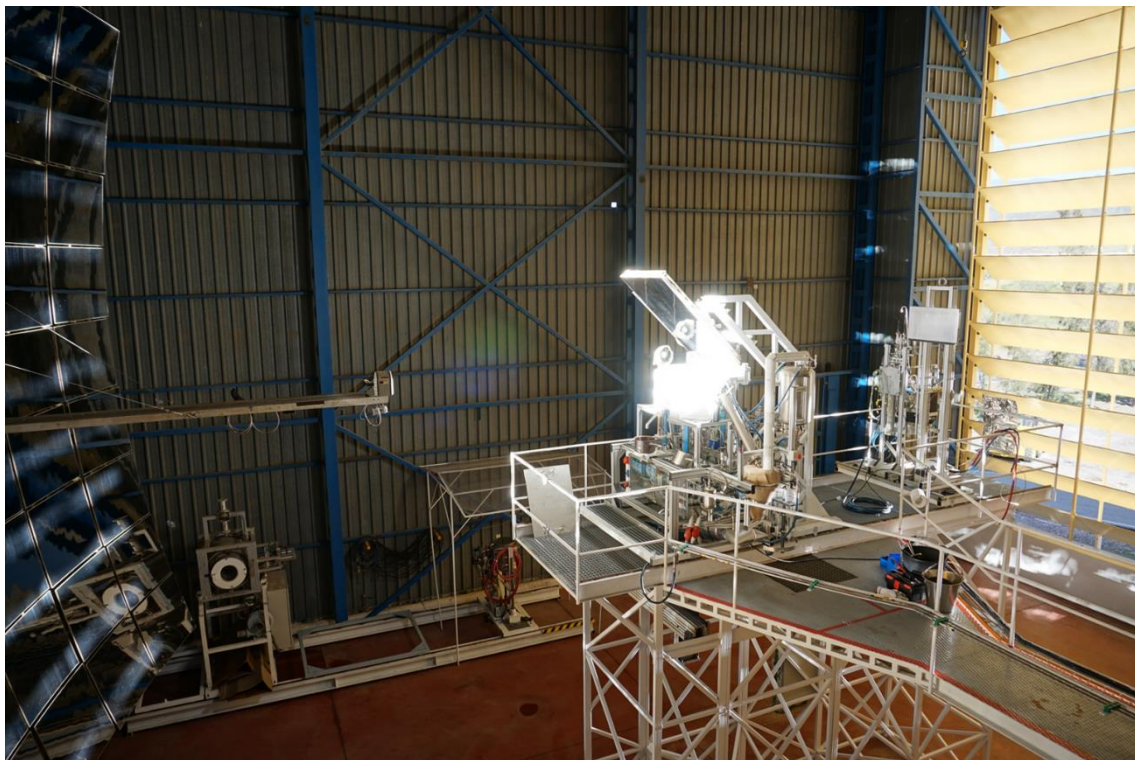


Fig. 1: Solar operation of the Oresol plant in the SF-60 Solar Furnace of the PSA.

Acknowledgements

I would like to thank all colleagues of the Plataforma Solar de Almería who directly or indirectly contributed to the success of this work. First and foremost, José Galindo, the technician of the Solar Furnace, who solves problems even before they are formulated, and who works for three people at the same time without you noticing (you think he works exclusively for you). My thanks also goes to the manager of the Solar Furnace, José "Pepe" Rodríguez, and the other technical staff, Fabi and Andrés, for their always reliable help whenever it was needed (Fig. 120 on page 145).

My special thanks go to Alfonso Vidal, my boss, who made it possible for me to work more or less continuously on this project despite many other obligations, and who always saved me from tough administrative tasks.

Further thanks go to my colleagues Diego Martínez and Inmaculada Cañadas. Diego for having managed well the initial funding of the project, and Inma for having me supported not only practically but also morally, especially in the initial phase of the project. When I had doubts, she cheered me up: "We will make lunar water, and if we have to, we'll make lunar wine too!"

Many thanks go also to the Instrumentation group of Ginés García, to José Liria and JuanRa López, who designed and assembled the complete electrical system according to my (somewhat demanding) requirements; as well as to Jesús Valero for the very helpful support with the data acquisition software. Further thanks go to Eli Ramos from the chemistry lab for the analysis of the water samples, and to Guillermo De Velasco, the safety responsible, for the prompt management and approval of the operation of the plant with hydrogen. Further thanks go to the staff of the Maintenance and Operation Group, without whom the installation and operation of the plant would not have been possible; and finally to all other employees of the PSA who have somehow directly or indirectly contributed to the success. This includes in particular my office mate Aurelio as well as María Elena and Marina, who always ensured a pleasant atmosphere with their joyful nature.

A very special thanks goes to my old friend Olaf Goebel from the Hochschule Hamm-Lippstadt in Germany, who sent me two of his students for internships; Miriam, who among other things did the conversion of the scale for the consumed particles from 10kg to 80kg, and Andre, who assisted me with many small things and especially during the tests in fall/winter 2018/19. Many thanks to both of you! Furthermore, I would like to mention at this point my niece Tanja Denk, who, among other things, designed and illustrated the beautiful Oresol project logo during her three weeks of internship at PSA (see Fig. 35 on page 63). Awesome work, thank you, Tanja!

The first year of this work has been funded by the Spanish Ministerio de Ciencia e Innovación, ref. ESP2007-29981-E. I thank the Plataforma Solar de Almería for facilitating access to the Solar Furnace within the "Infraestructuras Científicas y Técnicas Singulares" (ICTS) access program. Moreover, I thank the Tioxide Company for ceding the ilmenite particles used for this work (chapter 3.3.2).

Special thanks go to Paco Gimeno of the supplier company Imecal, where a large part of the hardware used in this work was built. Without your prompt and professional help, this project would not have been possible this way, Paco!

Moreover, special thanks belong to the *Internet*, which is not only an inexhaustible source of knowledge to countless major and minor questions, but which in particular also provides very useful sites such as *LEO*⁵ and especially *deepl*⁶, without which the efficient preparation of this document in a language that is not my mother tongue would have been possible only in considerably lower quality.







A triple thanks goes out to the director of this thesis, Carlos Gómez Camacho. First, for pulling the strings on the ERA-STAR Regions program, which made this entire activity possible in the first place. Second for accepting to take over the tutoring even though the work was already far advanced. And third for the numerous online meetings during which he not only gave me many useful tips and asked follow-up questions that led to many explanatory footnotes, but also that he repeatedly gave me the famous gentle "kick in the butt" that is unavoidably needed when you want to finish a work in a timely manner.

Finally, a big thank you deserves my family. Isabel, my dear wife, for always having comprehension for my time at the computer until late at night. Pablo, for having given me the best of all possible reasons to live 2000 km away from home. And Félix, for his practical support in this work, like having "forced" me to learn LabVIEW ("Papá, ¡hoy toca capítulo 3!") (Georgi & Metin, 2012), as well as his support in measuring the reflectance of the particles (Fig. 114 on page 141) and distilling the product water in his "*Felab*" (sample 025a5, see ch. 5.5.3). Particularly "important" was also the contribution of my sister-in-law Pepa, who gifted me the mascot of the project, the plastic kitten "Oregato" (see Fig. 96 on page 124 and Fig. 136 on page 165). And last but by no means least, a huge *Danke* goes to my parents for the moral support from so far away. My mother always had the desire that one of her sons would obtain a doctorate, and after all I really couldn't deny her that wish.

⁵ <https://dict.leo.org/englisch-deutsch/>

⁶ <https://www.deepl.com/translator>

Table of Contents

 ABSTRACT	5
 RESUMEN	5
 KURZFASSUNG	6
 RÉSUMÉ	6
 摘要	7
 خلاصة	7
KEYWORDS	8
PREFACE	9
ACKNOWLEDGEMENTS	11
TABLE OF CONTENTS	13
SYMBOLS	17
ORGANIZATION OF THE DOCUMENT	20
1 FUNDAMENTALS	21
1.1 The Moon	21
1.1.1 Spaceflight	21
1.1.2 Surface	23
1.2 Lunar Oxygen Production	25
1.2.1 Ilmenite Reduction with Hydrogen	26
1.2.2 Glass Reduction with Hydrogen	31
1.2.3 Ilmenite Reduction with Carbon Monoxide	32
1.2.4 Ilmenite Reduction with Methane	32
1.2.5 Carbothermal Reduction	32
1.2.6 Molten and Fluxed Molten Silicate Electrolysis	33
1.2.7 Vapor Phase Reduction	34
1.2.8 Solid Regolith Electrolysis in Molten Salt	35
1.2.9 Polar Ice	37
1.3 Concentrated Solar Power	38
1.3.1 Thermal Radiation	38
1.3.2 Solar Radiation	40

1.3.3	Concentration	41
1.3.4	Absorption, Reflection, Transmission	42
1.3.5	Losses	43
1.3.6	CSP on Earth	45
1.3.7	CSP on the Moon	48
1.4	Particle Technology	48
1.4.1	Fluidized Beds	50
1.4.2	Minimum Fluidization	53
1.4.3	Geldart Groups	56
1.4.4	Gas-Solid Reactions	57
2	THE PROJECT	61
2.1	Plataforma Solar de Almería	61
2.2	Oresol Background	62
2.3	Process Selection	64
2.4	Goals	66
3	THE SOLAR FLUIDIZED BED CHEMICAL PLANT	67
3.1	General Considerations	67
3.1.1	Overall Facility Concept	67
3.1.2	Material Accumulation and Recovery	69
3.2	Process	70
3.2.1	Summarized Description	70
3.2.2	Piping and Instrumentation	71
3.2.3	Temperature Measurement	76
3.2.4	Basic Design Parameters	79
3.2.5	Operation Parameters	79
3.3	Feedstock	82
3.3.1	Gas	82
3.3.2	Particles	83
3.4	Solar Concentrator	84
3.5	Reactor	86
3.5.1	Window	87
3.5.2	Aperture Cone	89
3.5.3	Base Plate	89
3.5.4	Gas Distributor	90
3.5.5	Reaction Volume	91
3.5.6	Solids In- and Outlet	91
3.5.7	Gas Outlet	92
3.5.8	Thermal Insulation	93
3.5.9	Radiation Shield	94
3.5.10	Further Details	95

3.6	Gas Supply ("Upstream")	96
3.7	Particle Supply	97
3.8	Particle Removal	99
3.9	Off-Gas Treatment ("Downstream")	100
3.9.1	Pre-Cooling	102
3.9.2	Solids Separation	103
3.9.3	Water Condensation	106
3.9.4	Water Separation	107
3.9.5	Gas Analysis, Pressure Control, and Venting	110
3.10	Gas Recirculation	112
3.11	Electrolyzer	115
3.12	Support Structure	116
3.13	Instrumentation	118
3.13.1	Temperature	118
3.13.2	Gas Flow	119
3.13.3	Solids Flow	120
3.13.4	Pressure	121
3.13.5	H ₂ O and H ₂	121
3.13.6	A/D-Converters	122
3.14	Control Software	123
3.14.1	Front Panel	124
3.14.2	Block Diagram	129
3.14.3	Sub-VIs	136
3.14.4	Simulation Mode	136
4	SOLAR CHEMICAL REACTOR OPERATION	137
4.1	Test Campaigns	137
4.1.1	Installation and Non-Solar Pre-Tests	138
4.1.2	Ilmenite with Air	145
4.1.3	Ilmenite with Argon	149
4.1.4	Ilmenite with Ar + <8% H ₂	152
4.1.5	Ilmenite with Ar + >8% H ₂	155
4.2	Example of a Test Day	158
4.2.1	Protocol and Check-List	158
4.2.2	Preparation	159
4.2.3	Fluidized Bed Operation	162
4.2.4	Solar Operation	162
4.2.5	Particle Inflow	162
4.2.6	Water of Crystallization	163
4.2.7	Chemical Operation	164
4.2.8	Filter Cleaning	165
4.2.9	Water Production	165
4.2.10	Minimum Fluidization	166

4.2.11	Wrap-Up	167
5	DATA EVALUATION AND DISCUSSION	169
5.1	Gas Demand	169
5.2	Particle Feed	171
5.3	Temperature and Power	172
5.4	Pressure	180
5.5	Product Water	183
5.5.1	Water Quantity	183
5.5.2	Water Separation	188
5.5.3	Water Chemistry	190
5.6	Miscellaneous	192
6	SUMMARY AND CONCLUSIONS	197
7	OUTLOOK	201
7.1	Further Tests on Earth	201
7.2	Oxygen Production on the Moon	202
	APPENDIX	205
A.1	Chemical Elements and Substance Properties	205
A.2	Units and Conversions	206
A.3	Brief Historical Review	208
A.4	Technical Drawings	209
A.5	Instrumentation	211
A.6	Solar Operation	213
	REFERENCES	215

Symbols

Abbreviations

ALCHEMIST	A Lunar CHEMical In-Situ resource utilization Test plant
ALPHA	ALchemist PHase A
CIEMAT	Centro de Investigaciones Energéticas, Medioambientales y Tecnológicas
CSP	Concentrated Solar Power
DNI	Direct Normal Irradiance (in W/m^2)
ESA	European Space Agency
ESRIC	European Space Resources Innovation Centre
HTF	Heat Transfer Fluid
ISRU	In-Situ Resource Utilization
LEO	Low Earth Orbit
LRO	Lunar Reconnaissance Orbiter
NASA	National Aeronautics and Space Administration
Oresol	obtención de Oxígeno a partir de Regolita lunar con Energía SOLar concentrada (obtaining Oxygen from lunar Regolith with concentrated SOLar Energy)
PSA	Plataforma Solar de Almería
PV	Photovoltaics
TEC	Thermo Electric Cooler

Symbols Chapter 1.3.1

c	m/s (km/s)	Speed of light in vacuum $c = 299792458 \text{ m/s}$
E	W/m^2	Radiation (total power radiated from a body per unit surface area)
E_b	W/m^2	Black body radiation (total power radiated from a black body per unit surface area)
$E_{b\lambda}$	$\text{W}/\text{m}^2 \cdot \text{m}$ ($\text{W}/\text{m}^2 \cdot \text{nm}$)	Black body spectral radiation (energy density of the radiation emitted at a given wavelength λ by a black body)
h	Js	Planck constant $h = 6.62607015 \cdot 10^{-34} \text{ Js}$
k	J/K	Boltzmann constant $k = 1.380649 \cdot 10^{-23} \text{ J/K}$

n	[-]	Refractive index
T	K (°C)	Temperature
α	[-] (%)	Absorptance
ε	[-] (%)	Emissivity
η	[-] (%)	Efficiency
θ	rad (°)	Incidence angle (of a ray)
λ	m (nm)	Wavelength
λ_{max}	m (nm)	Wavelength of the maximum radiation
ρ	[-] (%)	Reflectance
σ	W/m ² K ⁴	Stefan–Boltzmann constant $\sigma = 5.670367 \cdot 10^{-8}$ W/m ² K ⁴
τ	[-] (%)	Transmittance
ω	rad (°)	Angular aperture

Symbols Chapter 1.4.2

A_{FB}	m ²	Fluidized bed cross section
Ar	[-]	Archimedes number, eq. (22)
d_P	m (μm)	Particle diameter
g	m/s ²	Acceleration of gravity
h_{FB}	m (mm)	Fluidized bed height
K_1, K_2	[-]	Constants, eq. (20)
Δp	Pa (mbar, bar)	Pressure drop
Re_{mf}	[-]	Reynolds number at minimum fluidizing conditions, eq. (21)
u_G	m/s (cm/s)	Superficial gas velocity
u_{mf}	m/s (cm/s)	Superficial gas velocity at minimum fluidizing conditions
ε_{mf}	[-] (%)	Void fraction in a bed at minimum fluidization
μ	kg/m·s	Dynamic viscosity of gas
ϕ_s	[-]	Sphericity of a particle
ρ_g	kg/m ³	Gas density
ρ_s	kg/m ³ (kg/dm ³)	Density of solids

Symbols Chapter 1.4.4 and 5.5.1

O	(index)	Norm conditions
G	(index)	Gas (reactant)
P	(index)	Product (gas)
R	(index)	Residuals (solid)
S	(index)	Solid (reactant)
A_{FB}	m^2	Fluidized bed cross section
C_G	[-] (%)	Fraction (by volume) of reacting gas in the feed gas
C_S	[-] (%)	Fraction (by mass) of usable feedstock in the regolith
d_{FB}	m (mm)	Fluidized bed diameter
h_{FB}	m (mm)	Fluidized bed height
m_{FB}	kg	Solids mass in the fluidized bed
M	(k)g/mol	Molar Mass $M=m/n$
\dot{m}	kg/s	Mass flow rate
\dot{n}	mol/s	Molar flow rate
p	Pa (mbar,bar)	Absolute pressure
p_0	Pa (mbar,bar)	Norm-pressure (absolute) $p_0 = 101325$ Pa
T	K (°C)	Temperature
T_0	K (°C)	Norm-Temperature $T_0 = 273.15$ K
\bar{t}	s (min, h)	Mean residence time of the solids in the reactor
u_G	m/s	Gas velocity (empty reactor)
V_m	m^3/mol	Molar volume of an ideal gas at ambient conditions: $V_m = 22.414$ dm ³ /mol
\dot{V}	m^3/s	Volume flow rate
Y_{PG}	[-] (%)	Yield of product P from reactant G
Y_{PS}	[-] (%)	Yield of product P from reactant S
ε_{FB}	[-]	Void fraction in a fluidized bed above minimum fluidization
ν	[-]	Stoichiometric coefficient
ρ_s	kg/m ³ (kg/dm ³)	Density of solids

Organization of the Document

Chapter 1 is about the basics. First, a few aspects of lunar spaceflight are highlighted to show the usefulness of lunar oxygen production, and the corresponding important properties of the lunar surface for this purpose are presented (1.1). Then a selection of different proposed processes is presented in detail (1.2). The following subchapter explains the theory and practice of concentrated solar power (1.3). Finally, the fundamentals of particle technology and, in particular, fluidized bed technology are presented (1.4).

Chapter 2 treats the framework of the project (named Oresol). First, the location of the work, the Plataforma Solar de Almería, is presented (2.1). Then the origins of the project are explained (2.2). Thereafter, the selection of the process used, the ilmenite reduction with hydrogen, is justified (2.3). Finally, the objectives of the experimental work are defined (2.4).

Chapter 3 goes into detail about all the hardware. After some general considerations (3.1), the process with the piping diagram is presented, as well as the measuring points for the temperature and design and operating parameters (3.2). A subchapter is dedicated to the gaseous and solid feedstock (3.3). This is followed by a detailed description of all components, starting with the solar concentrator (3.4) and the reactor itself (3.5). Then follows the gas supply (3.6), and particle feed (3.7) and removal (3.8). The complex off-gas treatment (3.9) consisting of several components including the gas recirculation (3.10) is explained in detail. The additional components, the electrolysis (3.11) and support structure (3.12), complete the hardware part. Finally, the last two subchapters are dedicated to the measurement technique, one for the sensors (3.13) and the other for the control software (3.14).

Chapter 4 describes the operation of the system. The various test campaigns are explained in chapter 4.1. Then, an example day is used to show how the tests generally proceeded, how the goals were achieved, but also which problems occurred and how these were solved, if possible (4.2).

Chapter 5 presents some results of the experimental runs. These are, at first, basic engineering parameters such as gas demand at high temperatures (5.1) and the control of the solids mass flow rate (5.2). Then, the temperatures in the reactor are examined and the various heat sinks are quantified using an energy balance (5.3). The next subchapter is dedicated to the pressure profile across the gas loop (5.4). Then the ultimate goal of the system, the production of water from lunar rocks, is analyzed in detail (5.5). The quantities produced, the separation from the gas stream, and finally the impurities found in the water are discussed. The last subchapter goes into additional details (5.6).

Chapter 6 summarizes the work.

Chapter 7 finally provides an outlook on future tasks. A distinction is made between near term work on the PSA (7.1) and longer term questions including research that can ultimately be done only on the Moon itself (7.2).

1 Fundamentals

1.1 The Moon

1.1.1 Spaceflight

With an average distance of 384400 km, the Moon is the nearest natural celestial body, and therefore a primary destination for robotic and human spaceflight beyond Low Earth Orbit (LEO). Barely two years after the launch of the first artificial Earth satellite in 1957, *Sputnik-1*, the first human-made object, *Lunik-2*, hit the lunar surface. During the so-called Space Race of the 1960s, a total of 7 successful robotic soft landings occurred. The first was done by the Soviet probe *Luna-9* on February 3, 1966, followed by *Luna-13* and five (out of seven) US *Surveyor* probes. The culmination was the manned⁷ landing of *Apollo 11* on July 20, 1969, followed by five more human landings with increasingly longer stays on the lunar surface. The astronauts brought back a total of 384 kg of rock samples from the Moon. Meanwhile, the Soviet Union continued its program with automatic space probes. Two *Lunokhod* rovers traveled 10.5 and 37 km on the lunar surface, and three sample return probes brought a total of 300 g of lunar material back to Earth. On August 19, 1976, the final one of these spacecraft, *Luna-24*, launched from the Moon to return to Earth, marking the end of the first phase of lunar exploration with space probes.

This rather intense era was followed by a decades-long break. Only in the 90s and 00s, this changed again with new orbiters. A remarkable contrast to the 60s and 70s was that the probes now came from many different countries, including *Japan*, *Europe*, *India* and *China*. One of the most important results came from the US impact probe *LCROSS*. On October 9, 2009, it was able to directly detect the already previously suspected ice at the lunar south pole (Colaprete et al., 2010). But since *Luna-24*, it took more than 37 years until December 14, 2013, when with the Chinese lander 嫦娥三號 (*Cháng'é-3*) and rover 玉兔 (*Yùtù*), another terrestrial spacecraft successfully soft-landed on the Moon. Followed by 嫦娥四號 (*Cháng'é-4*) landing on the lunar far side and the sample return mission of 嫦娥五號 (*Cháng'é-5*), the Chinese Moon program in the 2010s proved to be very successful. In the meantime, a landing attempt by the Indian *Vikram* lander had failed.

In addition to the international aspect, the 2010s also saw a sharp rise in *private and commercial space* activities. In particular, the *Google Lunar X-Prize* stimulated a large amount of private lunar activity. The deadline to win the prize expired in March 2018 without a winner, as no team was able to attempt a lunar landing by that date. Nevertheless, some teams came very close to the goal, and in fact, one of them, *SpaceIL* from Israel, made an (unsuccessful) landing attempt with their בְּרֶאשִׁית (*Beresheet*) probe in April 2019. Several of the teams are now participating in NASA's *CLPS* (Commercial Lunar Payload Services) program.

At the time of the writing of these lines end of 2021⁸, a total of 21 spacecraft, including six with astronauts and four with remote controlled rovers on board, have successfully landed on the Moon. All were governmental, none was private so far. Ten of them then launched again from the Lunar surface (Fig. 2) for the return of samples (and astronauts) to Earth.

⁷ Due to the historical context, the word "manned", commonly used at that time, is adopted here. The appropriate term today would be "crewed" landing.

⁸ Alone for 2022, at least 6(!) robotic probes are scheduled to land on the Moon: Nova-C (2x) and Peregrine (USA), SLIM and Hakuto-R (Japan) with UAE's راشد (*Rashid*) rover, and Luna-25 (Russia). Most landers have rovers on board, but none will return to Earth. Will at least one of them succeed?

In spite of the discovery of ice, no soft landing has yet been attempted close to any of the lunar poles, but there are many plans for the coming years. By far the most outstanding project is certainly the human “return” to the Moon as part of the U.S. *Artemis* program at the earliest in 2025. While the *SLS launch vehicle* and the *Orion crew capsule* are in development for a long time, construction of the actual *human lunar lander* was only recently awarded. As a surprise to many, the winner was SpaceX's *Lunar Starship* (Fig. 3)⁹.

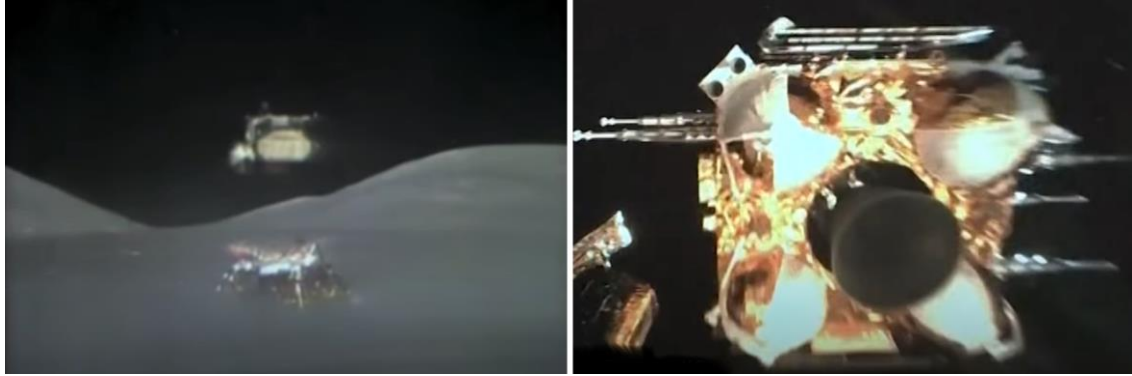


Fig. 2: Launches from the lunar surface. Left: *Apollo 17*. Right: 嫦娥五號 (*Cháng'é-5*).



Fig. 3: *Starship* on the lunar Surface (artist's view)⁹.

The goal of the *Starship* project is the development of a 100% reusable spacecraft fleet capable of transporting huge quantities of material to the Moon and Mars at unprecedented low cost. Besides mass production, 100% reusability, and rapid turnaround, the key feature of *Starship* is that it can be refueled both in space and on the surface of the Moon or Mars. Therefore, its payload capacity is always the one from Earth surface to LEO (>100 tons) regardless of the destination in the solar system (SpaceX, 2020). With an expected empty mass of about 120 t, it can be loaded with up to 300 t of liquid methane (CH₄) as fuel and 900 t of liquid oxygen (LOX) as oxidizer¹⁰. Nevertheless, for a direct return trajectory from the lunar surface to Earth, only about one fourth of the fuel tank capacity is needed (exact numbers¹¹ depend on payload

⁹ <https://www.spacex.com/updates/starship-moon-announcement/index.html>

¹⁰ Data from end of 2021, subject to change.

¹¹ Numbers used here (own calculation): Dry mass: 120 t, payload: 150 t, fuel: 80 t (CH₄) + 240 t (O₂), specific impulse (I_{sp}) = 380 s (3.7 km/s) → Δv =2.9 km/s (min. required: 2.54 km/s)

mass¹², trajectory, and margins requirements). This means that 80 tons of methane still need to be brought from Earth, but 240 tons of oxygen¹³ could be refueled on the lunar surface (and therefore be freed up for other purposes on the inbound flight¹⁴) if an oxygen production facility were available on the Moon.

The overarching goal of the *Artemis* Project is not just to "return" to the Moon, but to establish a base with permanent human presence. But to become sustainable, future lunar flights cannot be limited to science. Instead, they must also open up commercially viable fields. Examples include space tourism, or the use of extra-terrestrial natural resources, generally referred to as *In-Situ Resource Utilization*, or *ISRU*.

To survive, an average person needs about 0.84 kg of oxygen per Earth-day (Tchobanoglous & Schroeder, 1987), or 25 kg per lunar day (including night). Hence, even a crew of let's say 40 astronauts (and supposing no recycling) consumes barely more than about 12 tons per year, a one-digit percentage compared to the need of one *Starship* of several hundred tons per flight. Therefore, by far the most needed consumable in space flight in terms of mass is the rocket fuel. The lunar landers of the Apollo project used Aerozin-50 as the fuel and dinitrogen tetroxide as the oxidizer. These substances are storable at room temperature, but have only a moderate specific impulse and are also very toxic. For future Moon landers, liquid hydrogen or methane as the fuel and liquid oxygen as the oxidizer are likely to be used. In these cryogenic fuel combinations, at least three-quarters of the mass account for the oxygen. Considering that the fuel is more than half of the mass of a lunar lander, it becomes clear that oxygen is an extremely attractive lunar resource.

1.1.2 Surface

Almost the entire lunar surface is covered with a thick layer of fine-grained dust, called *regolith* and also sometimes *lunar soil* (especially when referred to the sub-centimeter fraction of the lunar regolith in an engineering geology sense). It is the result of 4.6 billion years of impacts of large and small meteoroids breaking down surface rocks. The regolith is generally from 4 to 5 m thick in Mare areas and from 10 to 15 m in Highland regions. Moon rocks and regolith consist mostly of silicate and oxide minerals (and a minor fraction of glass), composed mainly of *metal* atoms as cations and *oxygen* atoms as anions ("Lunar Sourcebook - A User's Guide to the Moon," 1991). The main metallic constituents are silicon, aluminum, iron, magnesium, calcium and titanium, with certain differences between Mare and Highland areas (Fig. 4). While oxygen and silicon dominate everywhere, the differences are mainly in the higher aluminum content of the *anorthositic Highlands* (with the main constituent Anorthite¹⁵ $\text{CaAl}_2\text{Si}_2\text{O}_8$), and the higher iron and titanium content of the *basaltic Mare* areas (mainly olivine $(\text{Mg,Fe})_2\text{SiO}_4$, pyroxene $(\text{Ca,Fe,Mg})_2\text{Si}_2\text{O}_6$, and ilmenite FeTiO_3), giving them the dark aspect of the "Face of the Moon". Depending on the titanium oxide (TiO_2) content, the Mare (Latin plural: Maria) area are further subdivided into "low-Ti" ($\text{TiO}_2 < 6\%$) and "high-Ti" ($\text{TiO}_2 > 6\%$)

¹² A fully fueled Starship on the lunar surface in theory should be able to launch up to 900 t of payload towards Earth. Reentry and landing wouldn't be possible there of course, but bringing that much lunar material to other destinations in the Earth-Moon system for the construction of massive structures might make sense in a more distant future.

¹³ A rough rule of thumb is: 40% of the mass leaving the Moon for Earth (or any other, only slightly hyperbolic escape trajectory) is oxygen.

¹⁴ E.g., the elimination of complex-to-choreograph tanker flights in highly elliptical transfer orbits.

¹⁵ Anorthite is the mineral, Anorthosite is the rock (made mostly of Anorthite).

(Neal & Taylor, 1992). Among the oxygen-free substances, the sulfur¹⁶ compounds stand out. In particular, the iron sulfide mineral Troilite (FeS) is one of the most abundant on the lunar surface with a share of about 0.2% (Highland) to 0.5% (Mare) by weight (“Lunar Sourcebook - A User’s Guide to the Moon,” 1991).

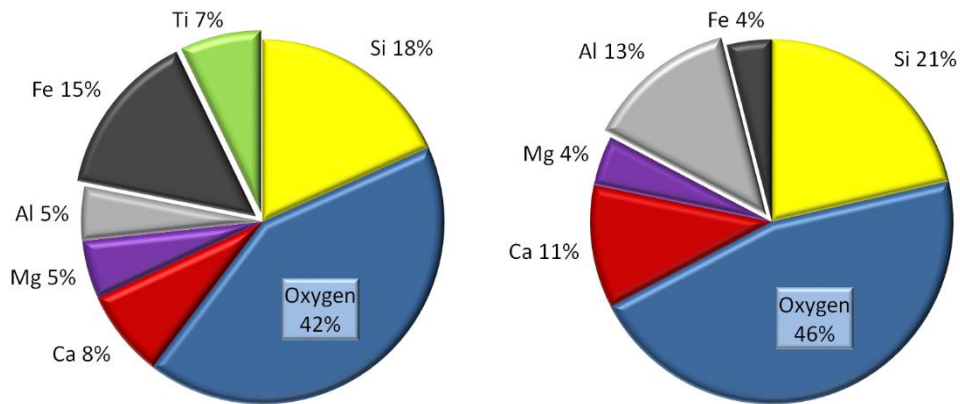


Fig. 4: Elemental composition of the lunar regolith, calculated from data given in (“Lunar Sourcebook - A User’s Guide to the Moon,” 1991). Left: Apollo 17 mare basalts as an example for High-Ti Mare regions. Right: Apollo 16 polymict breccias (mixtures of rocks) as an example for Highland regions.

Many of the possible processes for oxygen extraction from lunar rocks are based on the reduction of iron oxide FeO (see chapter 1.2). Therefore, sites with pyroclastic deposits or a high concentration of the mineral ilmenite are particularly interesting. A possibility to identify them remotely is the *Diviner* instrument on the *Lunar Reconnaissance Orbiter (LRO)*, a near- and thermal-infrared mapping radiometer with three channels centered near 8 μm that are

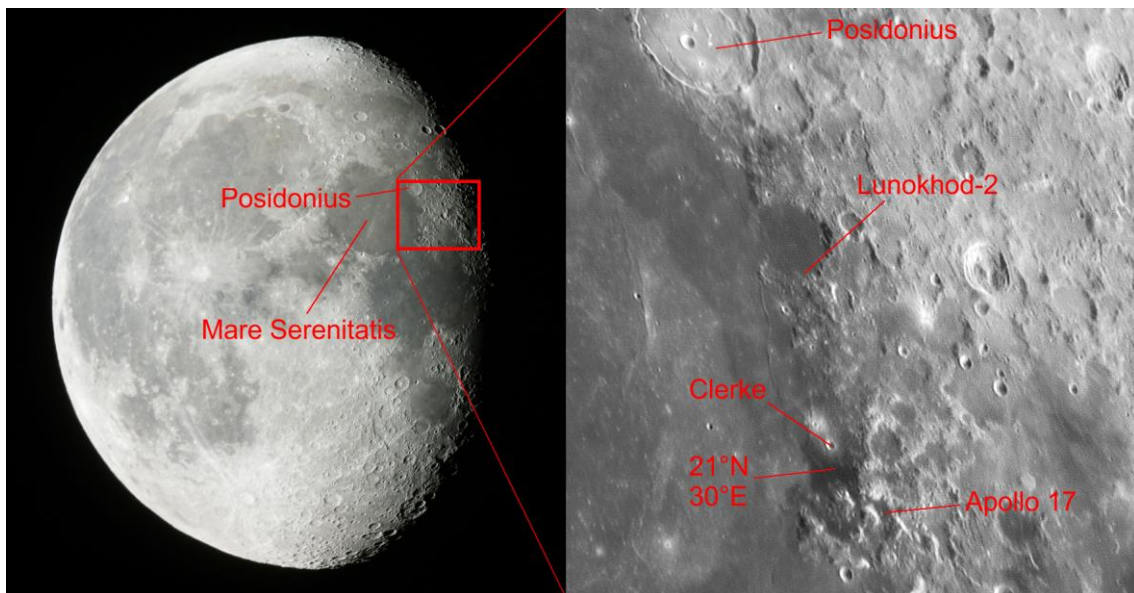


Fig. 5: Eastern rim of the Mare Serenitatis with a FeO-rich area south of the crater Clerke. (For scale: The crater Posidonius has a diameter of 100 km. North is up.)¹⁷

¹⁶ Besides sulfur, the spelling Sulphur also exists. There is no binding rule, but the tendency is that sulfur is used for the element and Sulphur for the mineral.

¹⁷ Photo on the right courtesy of Leonor Ana Hernández, AstroHita, Toledo (Spain).

used to calculate the emissivity maximum known as the “Christiansen feature” (CF). CF values are closely correlated to major element oxide abundances, particularly FeO¹⁸. One of the locations with the highest CF value on the Moon is located at 21°N, 30°E, on the eastern rim of the Mare Serenitatis, south of the crater Clerke and not far from the landing sites of Apollo 17 and the rover Lunokhod-2 (Fig. 5). The FeO abundance of this place is about 21.5 wt. % (Allen, 2015). The site also stands out to visual observers with a telescope for its darkness.

Observations of the Moon at 6 μm with the NASA/DLR Stratospheric Observatory for Infrared Astronomy (SOFIA) (Honniball et al., 2021) suggest that *molecular water is trapped* in the glass fraction of the lunar regolith even at mid-latitudes. Abundances in the Clavius region range from about 100 to 400 $\mu\text{g/g}$ H₂O with a mean of about 200 $\mu\text{g/g}$ or 0.02% by mass. This is in good agreement with latest findings of 120-180 ppm by the Cháng'é-5 lander near the Mons Rümker volcanic complex (Lin et al., 2022), and might help processes for oxygen extraction from lunar rocks working with hydrogen to minimize or even eliminate the need of replenishment from Earth of this reagent due to inevitable small losses.

1.2 Lunar Oxygen Production

Oxygen is available everywhere on the Moon, but bound to metal atoms, not in free form. Since these chemical bonds are very strong, high temperatures are needed to release the oxygen (Ellingham, 1944). Fig. 6 shows that bivalent iron oxide in the form of FeO¹⁹ is by far the easiest oxide to be thermochemically split, and the only one for which this is possible below the sintering point of lunar soil (around 1050 °C). Furthermore, Fig. 6 shows that it's probable that the sulfide Troilite (FeS) is reduced first when present, and that carbon has only a marginal advantage over hydrogen as a reducing agent at this temperature level.

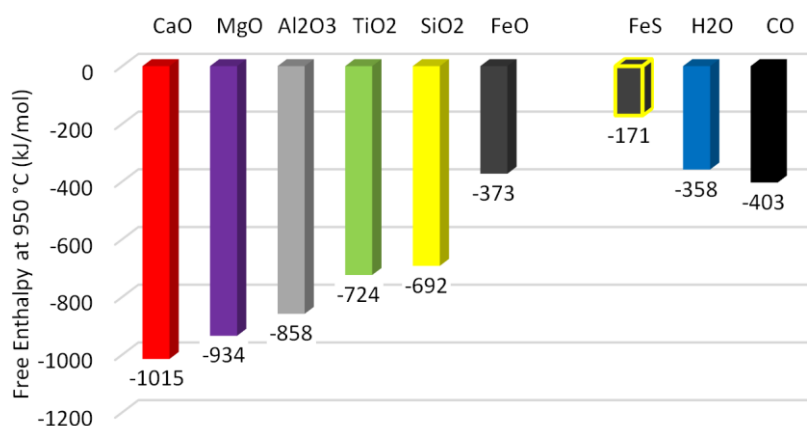


Fig. 6: Free Enthalpy (Gibbs energy) for the most important oxides in the lunar regolith. On the right, for comparison, values for Troilite (FeS) and the products of the two reducing agents H₂ and C are included. Calculated with the online-tool (University of Cambridge, 2021).

One of the very first publications concerning lunar resources utilization is (Carr, 1963), where several processes for the recovery of oxygen by reduction of lunar rock, and even the extraction of water from hydrated rocks, are proposed. 30 years and 9 sample return missions later, Taylor and Carrier (Taylor & Carrier, 1993) compiled a list of 20 possible processes for

¹⁸ Since the Spanish word "feo" means "ugly" in English, the motto for the site selection should be (pun intended!): "*FeO is beautiful!*"

¹⁹ As the lunar formation occurred under reducing conditions, trivalent iron oxide in the form of Fe₂O₃ ($\Delta G = -338$ kJ/mol at 950 °C) doesn't exist on the Moon.

oxygen production on the Moon. They classified the processes into the five sub-groups Solid/Gas Interaction, Silicate/Oxide Melt, Pyrolysis, Aqueous Solutions, and Co-Product Recovery. Then, they made a ranking based on the four criteria Technology Readiness, Number of Major Steps, Process Conditions, and Feedstock Requirements, giving every process between 1 and 10 points in each category. The authors recognize explicitly that “there is considerable subjectivity in these rankings, and even that the four different factors themselves are not really of identical importance”. It is therefore up to the reader to adapt the ranking to his or her own priorities. Since this ranking has received widespread attention in the ISRU community, it will serve here as a basis for an overview of the most important processes. Eight of them were picked and are listed in Table 1.

A recent review of techniques for In-Situ oxygen extraction on the Moon can be found in (Schlüter & Cowley, 2020). From the processes mentioned above, they included Hydrogen Reduction, Solid State and Partially Molten Reduction with Methane, Fluorination, Electrolysis of Molten Regolith, and Vapor Phase Pyrolysis. Furthermore, they included two more recent developments, Electrolysis in Molten Salt and Polar Ice, which are also listed in Table 1. All processes were examined under the aspects of general principle, thermodynamic fundamentals, reactor and kinetics, state of the art, and inputs and outputs.

Rank (Points)	Process	Sub-Group	Chapter
1 (30)	Vapor Phase Reduction	Pyrolysis	1.2.7
2 (29)	Glass Reduction with Hydrogen	Solid/Gas Reactions	1.2.2
2 (29)	Molten Silicate Electrolysis	Silicate / Oxide Melt	1.2.6
4 (27)	Ilmenite Reduction with Hydrogen	Solid/Gas Reactions	1.2.1
4 (27)	Fluxed Molten Silicate Electrolysis	Silicate / Oxide Melt	1.2.6
7 (25)	Ilmenite Reduction with Carbon Monoxide	Solid/Gas Reactions	1.2.3
7 (25)	Ilmenite Reduction with methane	Solid/Gas Reactions	1.2.4
12 (22)	Carbothermal Reduction	Silicate / Oxide Melt	1.2.5
n/a	Solid Regolith Electrolysis in Molten Salt		1.2.8
n/a	Polar Ice		1.2.9

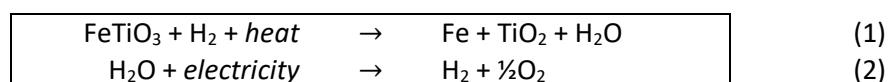
Table 1: List of eight processes including ranking²⁰, total points achieved, and sub-group assigned in (Taylor & Carrier, 1993); and two “new” processes taken from (Schlüter & Cowley, 2020). These 10 processes are presented in the following chapters.

From all these options, the *Ilmenite Reduction with Hydrogen* (chapter 1.2.1) was chosen for this work. The reasons for this selection will be outlined in detail in chapter 2.3.

1.2.1 Ilmenite Reduction with Hydrogen

Chemistry

As the name already suggests, in this process, ilmenite (FeTiO_3) is reduced with hydrogen at 800-1000 °C (1), followed by water electrolysis (2):



²⁰ In the original table in (Taylor & Carrier, 1993), the ranks were given consecutively (1, 2, 3, ...) even when the total points achieved were equal. This is corrected here.

In the first reaction, the ilmenite contained in the lunar rocks releases one of its oxygen atoms at high temperature to the hydrogen. Water²¹ is formed as the intermediate product. This reaction requires high temperature heat as energy source. In the second step, the water is decomposed by means of electrical energy into its components hydrogen and oxygen. The hydrogen is needed again for the first reaction, and the oxygen is the end product.

Previous Work

This process was already proposed as early as 1963 in the mentioned paper (Carr, 1963), where even a schematic diagram not very far from modern ideas was given (Fig. 7).

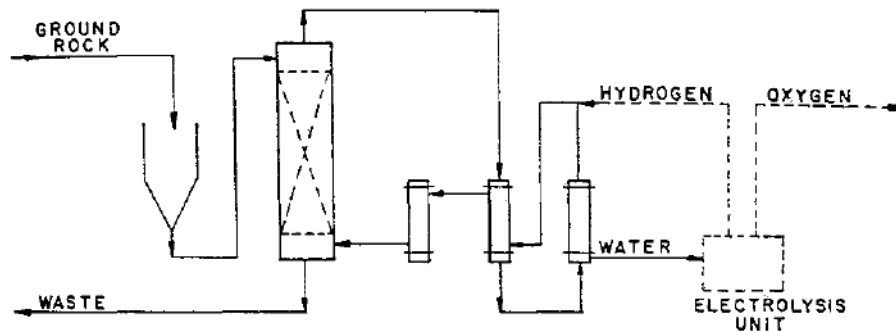


Fig. 7: Schematic diagram proposed by (Carr, 1963) “for the production of water by rock dehydration²² [solid lines] or production of oxygen by reduction of [iron and other] heavy metal oxides [solid and dashed lines]”.

With respect to hardware and experimental testing, more than 35 years ago, (Ouaida, Badie, & Flamant, 1985) showed the feasibility of the ilmenite reduction with a solar concentrator at Odeillo in the French Pyrenees. They used a fluidized bed that was operated alternatively with methane or with a 60%-Ar/40%-H₂ gas mixture, and heated by direct concentrated solar radiation with up to 6.5 kW. Although their goal was the recovery of TiO₂ for titanium production, the experimental arrangement could also have been used for oxygen extraction from ilmenite.

(Gibson & Knudsen, 1985) proposed a three-staged fluidized bed stacked vertically with the gas flowing upwards and the particles downwards (Fig. 8). The idea was to recover this way a large part of the sensible heat stored in the spent particles. For the same reason they also proposed a vapor phase electrolysis operating at reactor temperature (900 °C) for the water splitting step. The process works in continuous mode and the spent regolith is discharged through two alternating locks with a vacuum pump to minimize loss of interstitial hydrogen to the lunar vacuum. They recognized the importance of gas cleaning to protect the blower and the electrolysis device. Numbers were given for a plant scaled to an oxygen production capacity of 1000 tons per year.

With the release of the Vision for Space Exploration (VSE) in 2004 with the goal of harnessing the Moon’s resources, the United States National Aeronautics and Space Administration (NASA) initiated the ISRU project in the Exploration Technology Development Program (ETDP) to develop the technologies and systems needed to meet this goal. Among many other ISRU related activities (Gerald B. Sanders & Larson, 2015), two reactors for hydrogen reduction

²¹ Since water is extremely scarce on the Moon, we occasionally refer to it as the "lunar gold."

²² A yield of about 1% was expected. In 1963, it was not yet known that the lunar regolith is almost completely dehydrated.

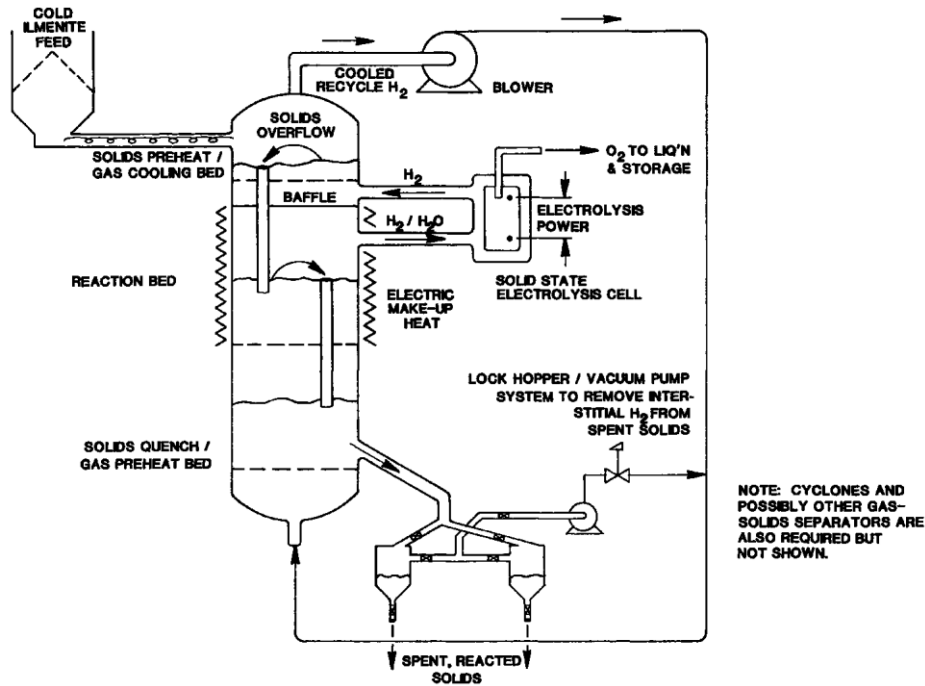


Fig. 8: Conceptual flow plan proposed by (Gibson & Knudsen, 1985) with a three staged countercurrent fluidized bed and vapor phase electrolysis.

were built and tested in autumn 2008 in so called “analog” tests. This means the testing was done in a location that simulates several aspects of the future destination. In this case, the site was on the slope of the Mauna Kea Mountain in Hawaii near a cinder cone that provided terrain features and volcanic tephra similar to what can be expected on the Moon. The first reactor was NASA’s Regolith-Oxygen (ROxygen) system (G.B. Sanders, Simon, & Larson, 2009) (Mueller & Townsend, 2009), a pair of vertical fluidized bed reactors with an auger to improve the contact between the hydrogen gas and the regolith (Fig. 9a). Working in one-hour batches, each reactor was able to produce about 40 g of water²³. The water needed to be cleaned before electrolyzing. An improved version (Fig. 9b) was designed but not tested because of the cancellation of ETDP. The second reactor, named “Precursor ISRU Lunar Oxygen Testbed” or PILOT (Fig. 9c), was built by Lockheed Martin (Clark, Keller, & Kirkland, 2009). It was a kind of

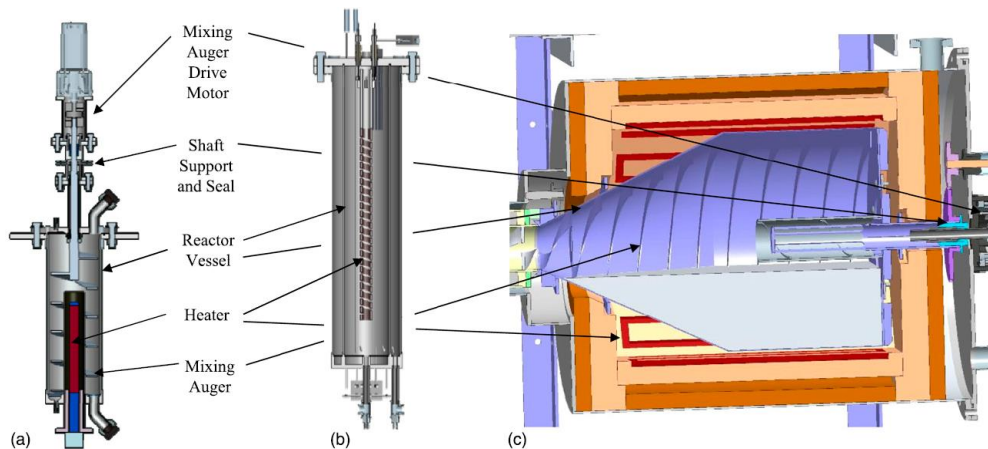


Fig. 9: NASA VSE/ETDP hydrogen reduction reactors: (a) ROxygen Gen I reactor, (b) ROxygen Gen II reactor, (c) PILOT rotating reactor. From (Gerald B. Sanders & Larson, 2013).

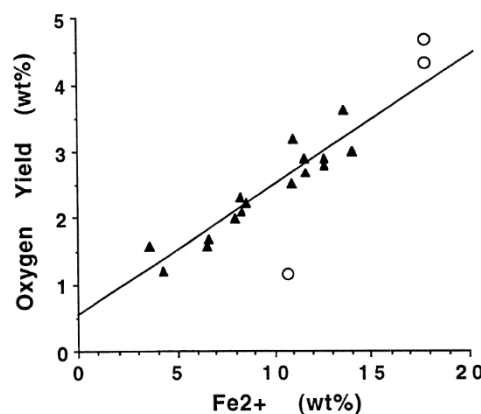
²³ Own estimation derived from data provided in (Gerald B. Sanders & Larson, 2015).

rotary kiln (“cement mixer”) with a tumbling reactor to turn over the solids for good contact with the gas. Each batch of about 10 kg regolith took about four hours producing 200 g of water²³. Just like with ROxygen, the product water had to be purified first. Taking into account the prototype character of the development, both reactors fulfilled the expectations. At temperatures above 1000 °C, issues with sintering were observed. Furthermore, unwanted by-products like hydrogen fluoride, hydrogen chloride, and hydrogen sulfide were also created in parts per million concentrations from constituents in the lunar regolith simulant (Gerald B. Sanders & Larson, 2013).

Experiments with Lunar Samples

Since real lunar material is not available in large quantities, all experiments with ISRU-prototypes are carried out with so-called lunar simulants. Nevertheless, small laboratory tests have also been run *with real lunar samples* on a gram scale.

Allen et al. (Allen, Morris, & McKay, 1996) tested the hydrogen reduction on 16 lunar soil and 3 lunar pyroclastic glass samples. They exposed the samples to flowing hydrogen at 1050 °C for 3 hours each in a thermogravimetric analyser. Oxygen extraction was strongly correlated with the initial Fe²⁺ abundance. The most efficient extraction was from ilmenite, followed by glass and olivine, and almost nothing from pyroxene. In particular, even the largest ilmenite grains (80 µm) appeared to be completely reduced with no evidence of unreacted cores. The low reaction rate of pyroxene is attributed to the very slow diffusion of water through this mineral. After the tests, the samples were somewhat darker than before the reaction. They also were slightly sintered, but it was easy to disaggregate them by gentle pressure. The oxygen yield was determined by measuring the weight loss of the sample. The smallest amounts were produced by iron-poor highland samples, while the highest yield was achieved by iron-rich pyroclastic glasses, among them sample 74220, the famous Apollo 17 “orange soil”. The results show a strong, linear dependence on the initial FeO content (Fig. 10). Mößbauer spectroscopy of the reduced samples indicated that the offset from direct proportionality in Fig. 10 is caused by the reduction of other elements than Fe. Additional experiments undertaken by the authors suggest the reduction of TiO₂ to Ti₄O₇ and the reduction of a small amount of SiO₂ to SiO and H₂O. As a conclusion with respect to lunar oxygen production, the authors claim that the oxygen yield can be predicted with nearly 90% confidence based solely on the iron abundance. As feedstock they propose (in this order) pyroclastic glass, lunar soil, and (crushed) basalt. Processing times of 1 to 3 hours should be employed.



The Russian spacecraft *Luna-27*, presently scheduled for launch in August 2025, is planned to land on a high-latitude region of the Moon. Among others, it will carry a European payload named PROSPECT for sampling of the polar lunar regolith. Part of this payload is the analytical module ProSPA that heats samples of about 40 milligrams to up to 1000 °C to measure the liberation of volatiles. It offers the option to perform this heating in a hydrogen atmosphere and can therefore trigger the ilmenite reaction. Sargeant (Sargeant, 2020) developed and optimized a breadboard to demonstrate experimentally the feasibility. It was used for the reduction of lunar-like and real lunar materials, including a lunar highland simulant, crushed lunar meteorite, and two Apollo soil samples. Water was successfully produced from all samples in a four-hour reaction. The highest yields were produced from the high-ilmenite-bearing Apollo-11 soil sample 10084, resulting in an average yield of 0.94 wt % O₂. The low-ilmenite-bearing Apollo-16 highland sample 60500, arguably more representative for high latitude sampling sites, produced still 0.18 wt % O₂. If *Luna-27* is successful and on time, it could be one of the first in-situ resource utilization (ISRU) demonstrations to be performed on the Moon.

ESA / ALCHEMIST

The European Space Agency (ESA) is preparing an ISRU Demonstration Mission to test technologies that enable In-Situ Resource Utilization (ISRU) on the Moon. Therefore, the Belgian company Space Applications Services has performed the conceptual design of a lunar demonstrator that can make water from regolith on the Moon²⁴. The goal of the project, called



Fig. 11: 3D-printed cold model for demonstration purposes of the ALCHEMIST reactor. Left: Empty “reactor”. Right: Filled with particles. Top: Look into the viewport; the two filter candles, the shaft of the stirrer, and the surface of the fluidized bed are visible. Bottom: Close-up view of the gas distributor (orange) and the stirrer (blue). The stirrer is designed to efficiently scrape the walls of the reactor, the location that is most prone for sintering.

²⁴ An ALCHEMIST on the Moon, 2018/Oct/26

<https://www.spaceapplications.com/news/an-alcchemist-on-the-moon>

ALCHEMIST (A Lunar CHEMical In-Situ resource utilization Test plant), which ran from March to November 2018, was to design a system able to produce and store 100 g of water from regolith on the Moon within one lunar day (Fereres et al., 2021). Due to our experience with the topic, Ciemat-PSA (see chapter 2.1) was invited to participate in the consortium. The centerpiece of the hardware for the hydrogen reduction is a small, electrically heated fluidized bed with a capacity for the solids of 0.79 dm³. Among my tasks was the conceptual design of that reactor. Fig. 11 shows a 3D-printed cold model. Except for the heater, this is a fully functional fluidized bed including a sparger-type gas distributor and two filter candles made of porous sintered metal at the gas outlets. The use of two filters instead of just one, and the installation directly within the reactor, enables the filters to be cleaned by reverse flushing without the need to interrupt regular reactor operation. Beyond the requirements of *ALCHEMIST*, this model has a viewport and a stirrer with torque sensors. The follow-up project was named ALPHA (“ALchemist PHase A”) and lasted from November 2018 to January 2021. Another model based on these plans (but without the stirrer and viewport) was 3D printed from metal by Space Applications Services. It will have a possible use in the future at ESRI²⁵ in Luxembourg for end-to-end testing.

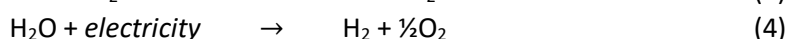
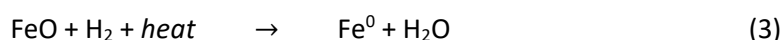
Assessment

In the ranking established in (Taylor & Carrier, 1993), the ilmenite reduction process with hydrogen reached the 4th place. It was best in all categories except “feedstock” with only 3 out of 10 points, because it depends on ilmenite-rich locations. Furthermore, as only FeO is reduced, it has a rather low yield. Even from 100% pure ilmenite not more than 10.5% (by mass) of oxygen can be extracted²⁶.

For electricity generation, photovoltaics (PV) is usually used in space today. But since the reaction (1) requires a significant amount of heat, it might be interesting to use concentrated solar radiation for it (Denk, González-Pardo, Cañadas, & Vidal, 2017).

1.2.2 Glass Reduction with Hydrogen

Lunar glass from pyroclastic deposits (also termed dark mantled deposits) can contain a significant amount of FeO. The resulting reaction is very similar to the hydrogen reduction of ilmenite:



With Rank 2, this process is on the top of the list in (Taylor & Carrier, 1993). The better ranking compared to the hydrogen reduction of ilmenite is due to the supposed better feedstock availability. Over 100 regions covered with volcanic glass as pyroclastic deposits with a depth of 1 to 4 m were identified on the Moon, with at least 20 of them extending more than 1000 km² (Gaddis, Staid, Tyburczy, Hawke, & Petro, 2003). From a technical standpoint, the narrow grain size distribution of the glass beads around 40 µm (Pieters, Mccord, Charette, & Adams, 1974) and the possibly high amount of bound water (Hauri, Weinreich, Saal, Rutherford, & Van Orman, 2011) might be an additional advantage. The amorphous state of glass results in a rapid kinetics (Taylor & Carrier, 1993). However, sintering might become a problem, as well as devitrification to pyroxene.

²⁵ European Space Resources Innovation Centre <https://www.esric.lu/facilities>

²⁶ Ilmenite FeTiO₃ molar mass: 55.8u+47.9u+3·16.0u = 151.7u. O/FeTiO₃: 16.0u/151.7u = 10.5%

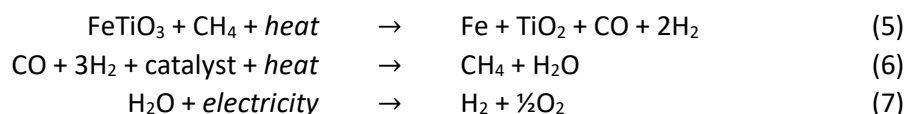
Experimental work on this subject seems to be rather scarce to date, possibly because of the difficulty of producing a suitable simulant for lunar glass or because of the close similarity from an engineering standpoint to the reduction of ilmenite. Experiments with such a simulated lunar glass were made by McKay et al. (McKay, Morris, & Jurewicz, 1991) using elemental carbon, carbon monoxide and hydrogen as reducing agents. The glass simulant corresponded quite well in composition to Apollo 11 sample 10084, in particular it contained only FeO and no Fe₂O₃. Mößbauer spectroscopy was used to determine the amount of reduced iron. While no significant reduction occurred with CO, elemental C produced primarily cementite (Fe₃C) instead of pure iron. Reduction with hydrogen worked best by far, with 53% of the iron being converted at 1000°C in 24 hours. In contrast, Allen (Allen et al., 1996) achieved a 90% yield with real lunar pyroclastic material with a reaction time of only 1 to 3 hours. Ultimately, the yield should be comparable to the ilmenite reduction, but prior screening and enrichment of the solid reactant might not be required. During heating, the formation of crystalline ilmenite and pyroxene was observed.

1.2.3 Ilmenite Reduction with Carbon Monoxide

Instead of hydrogen, carbon monoxide (CO) can be used as reducing agent. The chemical reactions are very similar to the ones with hydrogen, only that CO₂ is formed instead of water. In the ranking in (Taylor & Carrier, 1993) it was seventh, mainly because of the slower kinetics compared to the hydrogen reduction. A further important obstacle when working with CO is its toxicity.

1.2.4 Ilmenite Reduction with Methane

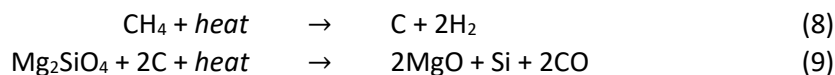
This reaction needs 3 steps to be carried out:



This process also ranked seventh in (Taylor & Carrier, 1993), because of the need of a third reaction step compared to the hydrogen reduction. Furthermore, the catalyst in reaction (6) is very sensitive to the presence of sulfur that must be removed from the feedstock in a previous step.

1.2.5 Carbothermal Reduction

When performed with molten regolith at significantly increased temperatures around 1600 to 1800 °C, the reduction with methane (or other carbon involving reactants) is referred to as “carbothermal” (Taylor & Carrier, 1993) and is able to reduce oxides beyond ilmenite, therefore no longer being limited to high-Ti Mare sites. The methane cokes by the heat to carbon and hydrogen (8), and the elemental carbon then reduces the (molten) silicate mineral, for example olivine (9):



Other feedstock minerals are possible as well. The recuperation of the methane and the production of the oxygen are made according to reactions (6) and (7) described in the previous chapter. Carbon, if trapped in the tailings in the form of FeC_x, can be recuperated by controlled addition of (product) oxygen to form CO. The process has a certain similarity to the terrestrial blast furnace process for iron production.

Within the NASA VSE/ETDP project, the company Orbitec developed a carbothermal reactor (Gerald B. Sanders & Larson, 2015). It used solar radiation concentrated by a Cassegrain design and coupled into the reactor through a fiber optic (Gerald B. Sanders & Larson, 2013) (Nakamura, Van Pelt, Smith, & Clark, 2008) (Fig. 12). It worked in batch mode and used the regolith itself as insulation material to protect the reactor walls from the heat. After termination of the reaction, the regolith had to freeze first before a rake system removed it from the reactor and prepared the next batch.

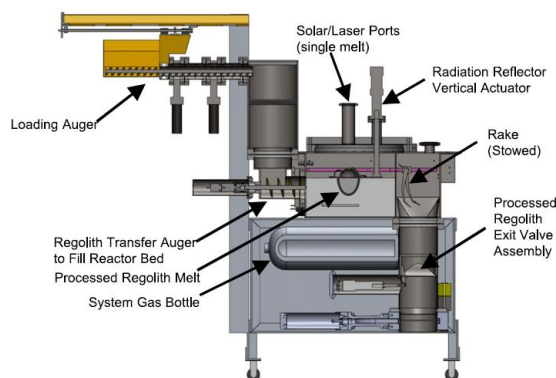


Fig. 12: NASA VSE/ETDP carbothermal reduction reactor. From (Gerald B. Sanders & Larson, 2013).

(Lavagna & Lunghi, 2018) built a laboratory breadboard including a pipe-shaped fixed bed carbothermal reactor, a methanation reactor and a water condenser. Although the reactor is operated below 1000°C, the authors claim that “it reduces any oxide present onto the lunar soil, differently from the hydrogen reduction which asks for ilmenite presence”. In their experiments, the regolith simulant was reduced in 4 cycles lasting 2.5 h each. To avoid methane losses due to C formation, an additional “washing” step was included in the cycle, which in principle uses water vapor to convert elemental carbon trapped in the regolith into CO and H₂. This step took another 4.5 h, so that a complete cycle lasted 7 h and the entire batch 28 h. Conversion of 4.45% of the regolith simulant resulted in a net water production of 45.3g. Despite the “washing” step, methane losses due to C formation were still 8% of the mass of oxygen produced.

This process only ranked 12th in (Taylor & Carrier, 1993) because it is considered “complex” and “needing many steps” (only 3 points out of 10), and considerable carbon loss (“5 to 20%”) is expected.

1.2.6 Molten and Fluxed Molten Silicate Electrolysis

Molten lunar regolith or rock (magma) is conductive enough to sustain direct electrolysis, producing oxygen at the anode and metals at the cathode. In (Taylor & Carrier, 1993) this process reached rank 2 due to the low number of required steps and its “omnivore” ability, meaning that it is not very demanding with the feedstock.

Sibille (Sibille et al., 2009) built an electrolytic cell able to reduce 500 g of regolith per batch. Critical design components include inert anodes capable of passing continuous currents of several Amperes, container materials, and direct gas analysis capability to determine the gas components co-evolving with oxygen. The presence of iron in the regolith increases the conduction, but it lowers the overall current efficiency at the anode. This translates into less oxygen produced for a given current value in melts containing iron oxides. To allow a

continuous process, a system working with vacuum has been designed to enable the withdrawal of reduced molten metals and spent molten oxide electrolyte. Electrode stability at the high temperature near 1600 °C is a major problem (Wang, Gmitter, & Sadoway, 2011).

With respect to commercial activities, the Israeli space tech startup Helios aims to “mine oxygen on the Moon using molten oxide electrolysis to split the metal atoms from the oxygen” (Ovadia, 2021).

Adding a flux such as a fluorite melt can reduce the temperature and increase the conductivity of the electrolyte. Nevertheless, in (Taylor & Carrier, 1993) this process (“fluxed molten silicate electrolysis”) reached with rank 4 a lower evaluation than the “simple” molten silicate electrolysis because more process steps are needed. Especially the full recovery of the fluxing reagent is expected to be a major problem.

1.2.7 Vapor Phase Reduction

In this process, the feedstock is vaporized at very high temperatures of 2200 to 2700 °C. At these temperatures, most of the oxygen compounds dissociate. Then, the gas must be rapidly cooled to condense everything back to liquid or solid except the oxygen. This step must be executed extremely fast (quenching) to avoid re-oxidation of the substances.

This process was the winner of the ranking in (Taylor & Carrier, 1993). In a certain way, it uses all available lunar resources like regolith, solar radiation, and hard vacuum (Fig. 13). In principle it can be fed by unbeneficiated feedstock and requires no consumables.

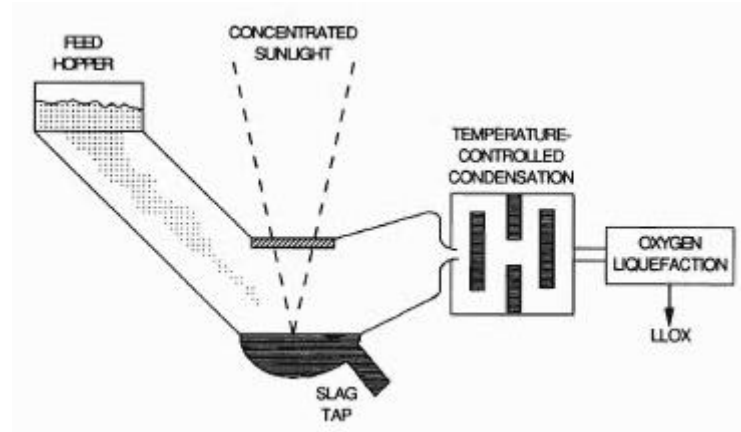


Fig. 13: Vapor phase reduction of lunar regolith with concentrated solar power. From (Taylor & Carrier, 1993).

Extensive experimental study of this process was done by (Sauerborn, 2005), but at "only" just under 1600 °C. At this temperature, the regolith is still liquid and not vaporized. In his work, silicate mineral samples and various oxides were irradiated with concentrated solar radiation in the Solar Furnace of the German Aerospace Center (DLR) in Cologne (Germany) with a power of a few kilowatts in order to separate metals or suboxides and oxygen from each other under high vacuum by means of high temperature pyrolysis. The vacuum chamber with a diameter of 300 mm was covered at the top by a dome made of borosilicate glass, which, however, was damaged in 5 of the 24 experiments. Nevertheless, this solution was less expensive than a dome made of quartz glass. The sample material used for the pyrolysis experiments was the JSC-1 lunar dust simulant (more about this in chapter 3.3.2). The sample size was about one gram for most of the experiments, and the high-temperature phase of the

experiments usually lasted less than one minute²⁷. In order to observe the gas chemistry in the system and to directly detect the production of oxygen, a quadrupole mass spectrometer (QMS) was integrated into the setup. A water-cooled cold trap was used to collect metallic vapors and suboxide vapors from the sample for later analysis.

With a clear saddle point in the temperature rise during the high temperature phase, the temperature measurements showed that the lunar dust simulant melts at values between about 1200 and 1300 °C. During the high temperature phase, the QMS detected a significant increase in the oxygen partial pressure starting at about 1425 °C. A comparison with experiments with different reference samples showed that this oxygen must have originated from the irradiated basaltic lunar dust simulant.

The samples from the experiments were subjected to extensive mineralogical analyses. It was found that the oxygen content in all heated samples decreased by 1.4 to 6.6% compared to the unirradiated sample. However, it could not be proven with certainty that this oxygen had also escaped as a free gas.

Under the given experimental conditions, it was also not possible to make a well-founded statement on the quantity of oxygen extraction. Furthermore, due to the small number of experiments, the ideal temperature range for pyrolysis with maximum oxygen yield could not be determined in more detail.

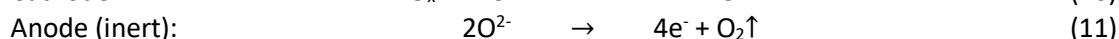
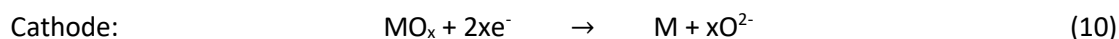
Examination of the irradiated sample carriers showed that some of the materials used (tantalum, molybdenum, aluminum oxide) were severely attacked by the hot melt. In the case of continuous operation on the Moon, difficulties resulting from such material problems must be generally avoided.

Nevertheless, according to the author's opinion, the results of the gas analyses and the mineralogical investigations of the samples from the solar furnace experiments demonstrated that solar thermal vacuum pyrolysis is a possible process technology that can be used for oxygen production on the Moon.

However, the required high temperature and the need for rapid quenching remain a major engineering challenge.

1.2.8 Solid Regolith Electrolysis in Molten Salt

In this more recent process, the lunar regolith is submerged in a molten salt, usually calcium chloride (CaCl₂) at around 900 °C (Schwandt, Hamilton, Fray, & Crawford, 2012). The *regolith acts as the cathode* where the metal oxides (MO_x) are reduced (10). The oxygen ions move to the anode where they are oxidized (11) and released. The chemical reactions are:



This process is derived from the FFC-Cambridge (Fray, Farthing, Chen – University of Cambridge/UK) process for the electro-deoxidation of metals and metal oxides (Fray, 2001). While the original FFC process works with a carbon anode that produces CO₂ and therefore is consumed during the batch, the modified process needed for oxygen production on the Moon requires an inert anode that liberates pure oxygen (Fig. 14). Possible materials for this anode are tin oxide (SnO₂) doped with 2% of Sb₂O₃ and 1% of CuO to improve conductivity and

²⁷ In the final test, 7.9 g of the simulant were heated during 174 s to up to 1580 °C.

reduce brittleness, or a solid solution of calcium titanate and calcium ruthenate ($\text{CaTi}_x\text{Ru}_{1-x}\text{O}_3$). During experiments, the latter one showed better stability (Schwandt et al., 2012).

(Lomax et al., 2020) performed the first successful demonstration of solid-state powder-to-powder regolith simulant processing that yields metal alloys as products. They processed 30 g of JSC-2A lunar regolith simulant in 1600 g CaCl_2 salt at 950 °C for 50 hours with a constant electric current of 4 A. The simulant was sieved to a grain size $>53 \mu\text{m}$ to avoid particle loss through the $50 \mu\text{m}$ mesh of the cathode basket. Anode material was doped tin oxide (SnO_2 with 1% Sb_2O_3 and 0.45% CuO). The Faradaic efficiency is reported having started with 49% and then dropped to 23% towards the end of the test. Analysis of the reduced simulant gave an average of only 3.1 wt% oxygen remaining. This corresponds to an oxygen recovery²⁸ of 96% or a yield²⁹ of 42%. However, the quantity of liberated oxygen (recovery) detected by the mass spectrometer corresponded with 4.48 g only to around 34% of the oxygen available in the sample. The authors suspect that the remaining oxygen went into the corrosion of the reactor vessel, not really a surprise because the design was originally made for a carbon anode and not for hot, highly corrosive oxygen. The metallic product was dominated by an Al/Fe alloy (ratio approx. 3:1), and notably depleted of Si and Mg. As these elements couldn't be found in the salt, it is hypothesized that they floated out of the cathode basket in form of the liquid metal, opening the intriguing possibility to separate the different metals from each other already during the processing. Furthermore, it seemed that a significant proportion of the Ca remained in the regolith simulant. This is important because accumulation of CaO in the salt would complicate its reusability. Na and K seemed to have dissolved into the electrolyte as oxides or chlorides, but this is seen as of minor importance because these elements are rare on the Moon. Also, there was some evidence of anode-derived Sn in the metallic product, and the anode even broke once near the end of the test. Finally, the mass spectrometer was able to detect if other gases than O_2 , such as HCl or Cl_2 , also have evolved from the anode, but the paper says nothing about whether that actually happened. Nevertheless, the authors don't see any fundamental reason as to why this process should not operate effectively with lunar regolith, therefore offering "an exciting alternative to other technologies for oxygen production on the lunar surface." The most recent research (Meurisse et al., 2021) attempts to lower the operation temperature to 660 °C by using eutectic mixtures of the CaCl_2 salt with KCl, NaCl or LiCl.

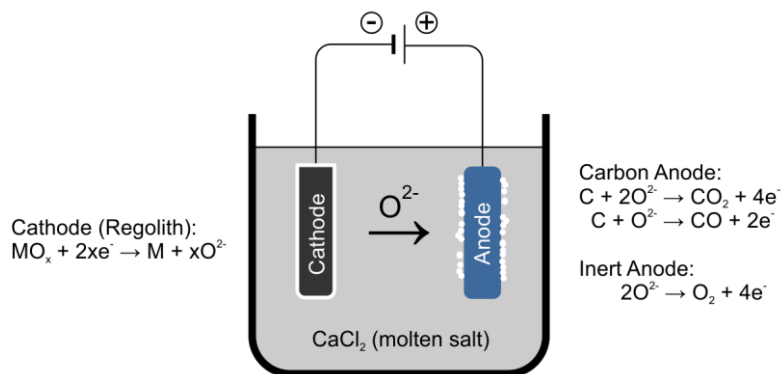


Fig. 14: The FFC process. For terrestrial applications, the carbon anode is consumed. On the Moon, it must be inert. Drawing adapted from (Lomax et al., 2020).

²⁸ Recovery = extracted oxygen / oxygen available in the feedstock

²⁹ Yield = mass of extracted oxygen / total mass of the feedstock

Airbus Defence and Space is developing a demonstrator able to produce 100 g of oxygen and extract a similar amount of metal on the Moon in less than one lunar day (Seidel et al., 2021). High-purity oxygen is produced by the anode within a tube made of yttrium-stabilized zirconia. The metal cathode cup that's holding the regolith is porous with pore sizes in the range from μm up to several mm. The reactor works in vacuum and the salt is recovered from the regolith on the cathode by evaporation.

The FFC and related processes promise to reduce almost all of the metal oxides at comparatively low temperatures. Possible challenges are the stability of the anode, the slow reduction rate, and the complete recycling of the consumables, especially salt and carrier gas (Fereres et al., 2021). Furthermore, the ratio of regolith to salt of up to 1:50 is still very unfavorable.

In recent years, this process became quite popular among lunar ISRU scientists. One interesting reason for this is that it plays a lead role in the novel "Artemis" by Andy Weir (Weir, 2017), widely known as the author of "The Martian".

1.2.9 Polar Ice

Due to the very low tilt of the Moon's rotational axis of only 1.5° with respect to the poles of the ecliptic, the Moon has practically no seasons (as opposed to Earth with a tilt of 23.5°). Therefore, the (center of the) Sun never rises more than 1.5° above the (mathematical) horizon at the lunar poles. As a consequence, on the one hand, there are mountains that are almost continuously illuminated by the Sun ("peaks of eternal light"), while on the other hand, some crater floors haven't seen the Sun for billions of years. The resulting, extremely low temperatures act as a cold trap for all kind of volatile materials, among them water (H_2O). This was hypothesized for a long time, and definitely confirmed by the impact of the LCROSS mission in 2009 (Colaprete et al., 2010).



Fig. 15: Lunar polar ice mining with direct solar power supply from large heliostats located on the rim of the crater. From (Sowers, 2020).

The water (and other volatiles) in principle can be easily extracted by simply applying heat. Some concepts (Sowers, 2020) propose the use of large mirrors (heliostats) positioned on the

crater rim, reflecting sunlight into the darkness of the crater floor onto mobile capture tents (ø30 m), equipped with cold fingers installed on rovers (“ice haulers”) which collect the sublimating ice (Fig. 15). The water must be purified and can then be electrolyzed into hydrogen and oxygen. The processing in principle should be straight forward, but the extracted material generally has to be transported several km out of the permanently shaded crater requiring roads in a very mountainous environment, and the working conditions at the extremely low temperatures are harsh. Furthermore, compared to all other lunar oxygen extraction techniques, only very few locations exist for lunar polar ice extraction.

1.3 Concentrated Solar Power

Generating energy from solar radiation has great advantages in space. On the one hand, the offer is independent of the weather and thus precisely predictable. On the other hand, the solar radiation is inexhaustible, i.e., it does not have to be refueled. As downside it has to be mentioned that a direct line of sight to the sun is always necessary, which is not given especially on the night side of planetary bodies. The overwhelming majority of all spacecraft power systems uses solar cell generators, at least partially (Messerschmid & Fasoulas, 2011). It is a simple and robust technique, and does not necessarily require moving parts. In addition, it generates electricity, which is desirable for the vast majority of applications. When heat is needed, it is usually generated by the intermediate step of electricity. The very high design flexibility and usually relatively low power demand makes up for the lower efficiency.

This changes, however, when large quantities of lunar material are to be heated to high temperatures. Then the question arises whether a higher efficiency can be achieved by the direct coupling of solar radiation.

1.3.1 Thermal Radiation

All bodies with a temperature $T > 0$ K (i.e.: all) emit *thermal radiation*. The thermal movement causes an excitation of the states of atoms, molecules and electrons. When they then return to lower states, electromagnetic radiation is emitted. The irradiance or energy density $E_{b\lambda}$ of the radiation emitted at a given wavelength λ by a “perfect” radiator, usually called a *black body*, only depends on the temperature T (in Kelvin) and is given by *Planck's law* (Goswami, 2015):

$$E_{b\lambda}(\lambda, T, n) = \frac{2\pi hc^2}{(e^{hc/\lambda kT} - 1)\lambda^5 n^2} \quad (12)$$

with the Planck constant $h = 6.62607015 \cdot 10^{-34}$ Js, the speed of light in vacuum $c = 299792458$ m/s, and the Boltzmann constant $k = 1.380649 \cdot 10^{-23}$ J/K. If the radiator is in a vacuum, the refractive index is $n = 1$; in air it's with $n = 1.0003$ only slightly larger. The resulting spectra (black body radiation) rise steeply in the short wavelength range, quickly reach a maximum, and then slowly fall off again at longer wavelengths to asymptotically drop towards zero. Fig. 16 shows some examples. The vertical axis is plotted logarithmically, because otherwise it would not be possible to cover the extremely large range of radiation powers within a single diagram.

Deriving of Planck's law (12) and equaling to zero leads to *Wien's displacement law*, which describes the wavelength with the maximum radiation in the form of a simple reciprocal law:

$$\lambda_{\max} = \frac{2897.8 \mu m K}{T} \quad (13)$$

In Fig. 16 it is drawn as the black, dashed line.

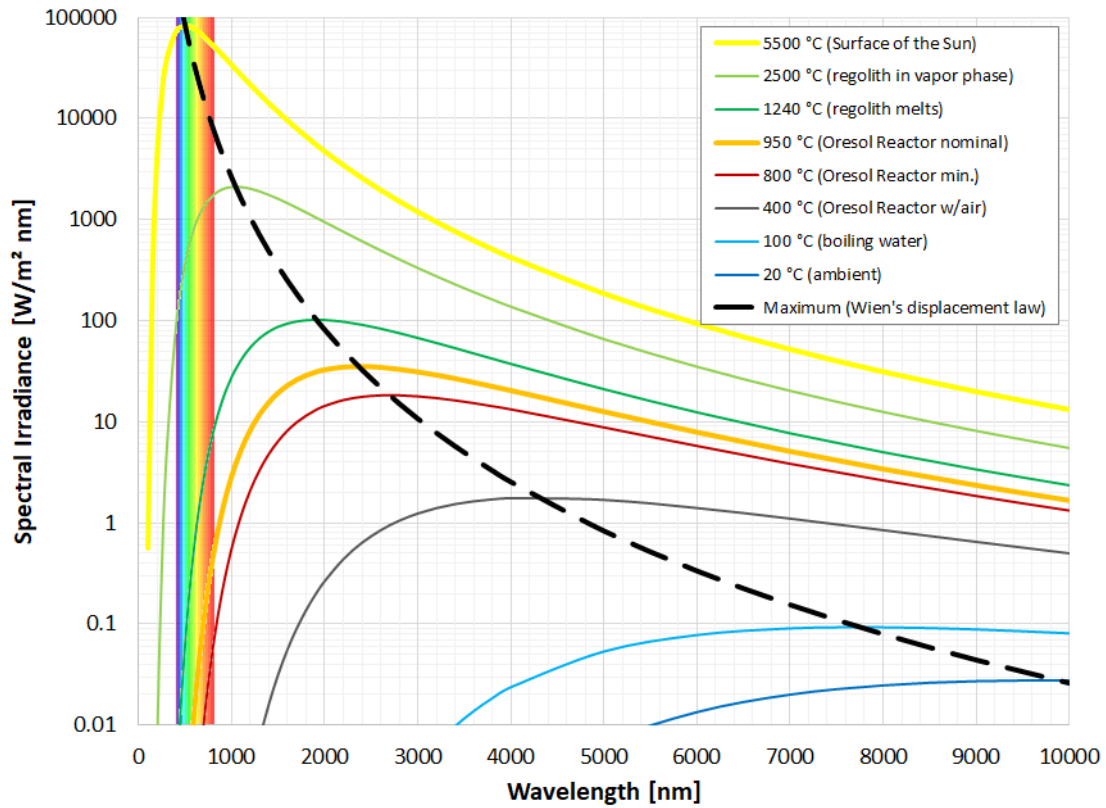


Fig. 16: Black body spectral irradiance examples, calculated with Planck's law (eq. (12)). The black, dashed curve shows the maxima calculated with Wien's displacement law (eq. (13)). The temperatures of the phase changes of the regolith are approximate. The different operating conditions of the Oresol Reactor are shown in Fig. 17.



Fig. 17: Photographs of the Oresol reactor at 400 °C (left), 800 °C (center), and 950 °C (right). The color and brightness difference of the emitted radiation due to the different temperatures is clearly visible.

The integration of Planck's law (12) over all wavelengths ($\lambda = 0 \dots \infty$) gives the *Stefan-Boltzmann law*, which describes the total power radiated from a black body per unit surface area as a function of its temperature:

$$E_b = \sigma T^4 \quad (14)$$

with the Stefan–Boltzmann constant $\sigma = 2\pi^5 k^4 / 15c^2 h^3 = 5.670367 \cdot 10^{-8} \text{ W/m}^2 \text{K}^4$ (Mamajek et al., 2015). The dependence on the temperature in the fourth power means that the emitted radiation increases very strongly with the temperature. It's plotted in Fig. 18, together with the three examples from the Oresol reactor operation. From the figure it becomes clear that the increase of the temperature from 400 to 800 °C means a huge increase (factor 6.5) of the

thermal radiation, and also that apparently small changes at high temperatures affect the radiation considerably (e.g.: 800 °C → 950 °C: +70%, 800 °C → 1000 °C: +100%).

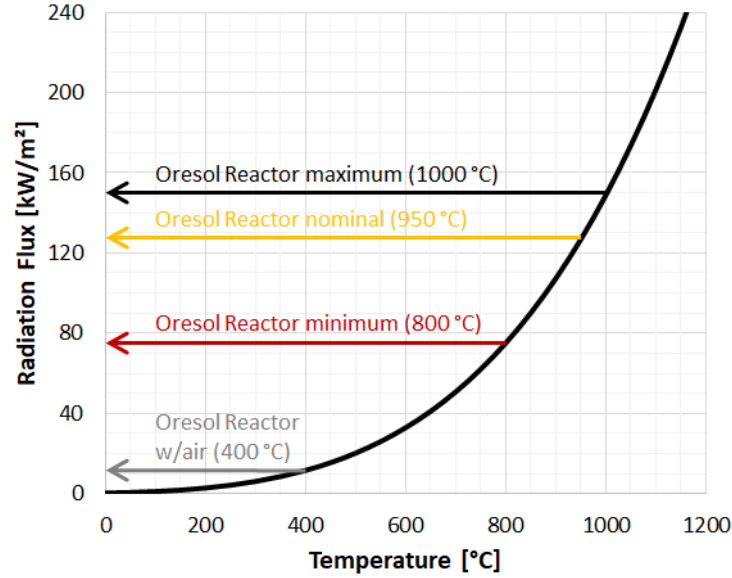


Fig. 18: Area-specific radiative power of a black body according to the Stefan-Boltzmann law (eq. (14)).

Non-ideal surfaces generally emit less radiation than the ideal black body. This is taken into account by the emissivity ε . For exact calculations, ε must be considered wavelength-dependent, but for practical purposes it is often sufficient to calculate with an average value. In this case, the radiated power becomes:

$$E = \varepsilon \sigma T^4 \quad (0 \leq \varepsilon \leq 1) \quad (15)$$

Black body radiation is always diffuse radiation, which means that it has no preferred direction, but is emitted uniformly into the entire half-space lying above the surface element.

1.3.2 Solar Radiation

The radiation coming from the Sun can be approximated by the radiation of a black body with the effective temperature of 5772 (± 0.8) K (Mamajek et al., 2015). With eq. (14) this translates into a radiation flux of 62.9 MW/m² on the surface of the Sun, with 99% of it between 200 and 3000 nm. With increasing distance, this value decreases according to the inverse square law.

The direct (i.e., without diffuse components) solar radiation available at a given location is called *Direct Normal Irradiance (DNI)*. The value of DNI in the vicinity of the Earth, called the extraterrestrial solar “constant”, is 1361 (± 1) W/m² according to the latest definition³⁰ of the International Astronomical Union (IAU) (Mamajek et al., 2015). It describes the radiative power falling perpendicularly on a given surface, measured over the entire solar spectrum at a distance of exactly one astronomical unit (au) from the Sun. Thereby 1 au is the mean geometric³¹ distance of the Earth from the Sun, its value corresponds to 149.6 million km. Since the Earth's orbit deviates slightly from the circular shape (numerical eccentricity 0.0167), the Earth is slightly closer to the Sun at the beginning of January (perihelion distance 0.983 au

³⁰ Before 2015, the official value was 1367 W/m².

³¹ In the time average, the distance between the Earth and the Sun is slightly larger than 1 au (namely 1.00014 au). The reason is that the Earth moves slower in the orbital section around the aphelion.

or 147.1 million km) and slightly further away at the beginning of July (aphelion distance 1.017 au or 152.1 million km), corresponding to a difference of 3.4%. Since the intensity of solar radiation decreases with the square of the distance, its value is 1408 W/m^2 at perihelion and 1316 W/m^2 at aphelion, a noticeable difference of almost 7%. The extension of the lunar orbit (semi-major axis $384400 \text{ km} = 0.0026 \text{ au}$) increases these values slightly, they are then in the extreme cases 1416 W/m^2 in the perihelion³² and 1309 W/m^2 in the aphelion, a difference of almost 8%.

The power of the solar radiation reaching the Earth's surface is noticeably lower because of absorption and scattering in the atmosphere. On very clear days in (northern) winter (perihelion!), 1000 W/m^2 can be reached around solar noon (in high mountain areas even more), but a DNI around 800 W/m^2 or 60% of the extraterrestrial value is more the rule. On cloudy days, the DNI can even drop to zero, with the remaining illumination then coming exclusively from diffuse radiation, which cannot be concentrated, but still be used e.g., by PV systems. On the atmosphere-free Moon, however, the full solar radiation is available from immediately after sunrise until immediately before sunset, assuming that a collector system is used that can be oriented perpendicular to the Sun and free of shading at any time of the day (for an example see chapter 1.3.7). This means that a solar powered facility on the Moon can operate on average for 354 hours³³ without interruption and with precisely predictable output.

Equation (14) can also be used to calculate the maximum temperature a black body³⁴ can reach in near-Earth space. With the solar “constant” of 1361 W/m^2 , the result is 120°C .

1.3.3 Concentration

In order to achieve higher temperatures, the solar radiation flux must be increased (i.e., *concentrated*) far beyond the value of the thermal emission at the desired temperature. For example, to achieve a temperature of 1000°C , at least the radiation power of 149 kW/m^2 must be compensated (Fig. 18). In near Earth space (with a mean DNI of 1361 W/m^2), this corresponds to a concentration ratio of 110x, on the surface of the Earth rather 150x to 180x. In practice, significantly more is necessary because not only all sorts of other losses must be compensated, but also useful power for heating of the lunar material and possibly for a chemical reaction must remain available.

Fig. 19 shows schematically the basic configuration of most concentrated solar power (CSP) systems. The radiation from the sun (1) hits mostly parallel (the angle is $32' = 9.3 \text{ mrad}$) the concentrator (2). As the sun moves across the sky during the day and only direct radiation can be concentrated, a sun-tracking system (3) is needed. Since the full available solar power is usually not needed all the time, a power control (4) is helpful. The concentrated radiation hits the receiver (5), and there in particular a black surface, referred to as the absorber. This is the place where the radiative energy is converted into heat, and, in most cases when a solar reactor is involved, the chemical reaction occurs. This heat has to be carried away (6) from the receiver, usually by a heat transfer fluid (HTF) like molten salt, thermal oil, water/steam, supercritical CO_2 , ambient or pressurized air, products from a chemical reaction (mostly gases), or solid particles. The heat is then finally transferred to a device (7) where the desired product

³² Since this case can only occur around the new moon phase, it is only relevant for a facility on the far side of the Moon.

³³ A mean synodic month lasts $29 \text{ d } 12 \text{ h } 44 \text{ min } 2.9 \text{ s} = 708.734 \text{ h} = 2 \times 354.367 \text{ h}$.

³⁴ Under certain circumstances, the temperature can become higher for a non-black body, see chapter 1.3.4.

(electricity, hydrogen, lunar water...) is extracted. This can be a thermodynamic cycle (steam or gas turbine process) with generator in the case that the purpose of the CSP plant is to produce electricity. If the goal is to make solar chemistry, then the product separation and post-processing happens here.

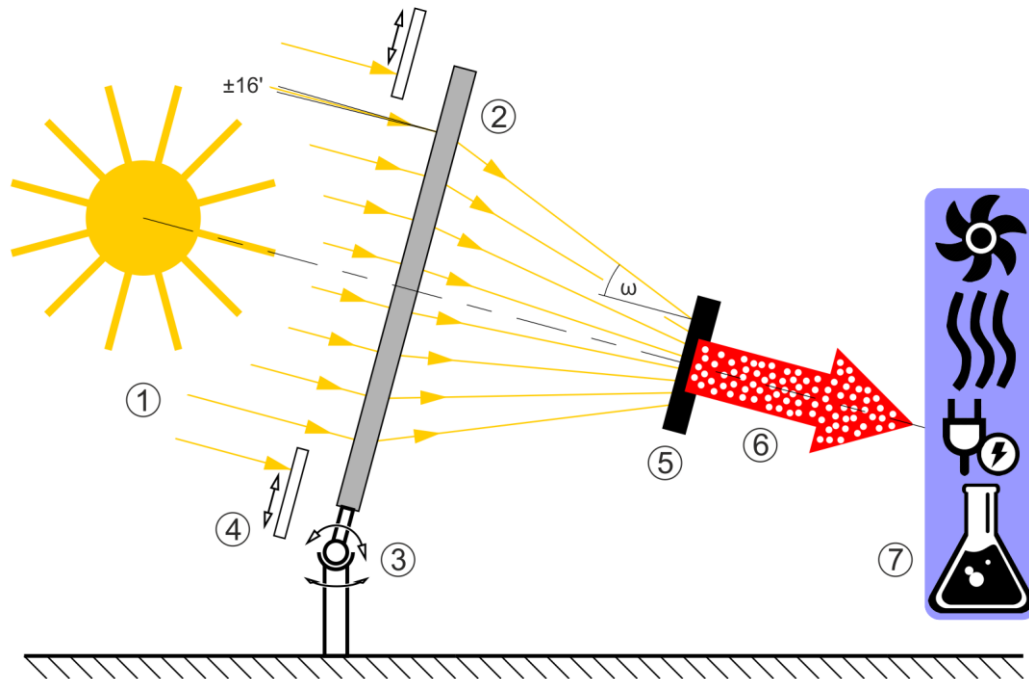


Fig. 19: Schematic illustration of a concentrator system for solar radiation. For the numbers see text.

The ratio of the areas of the concentrator and the receiver is the geometric concentration ratio and easy to determine. The optical (real) concentration ratio, the ratio of the solar flux on the receiver and the concentrator, is always lower due to losses in the system and non-uniform flux distribution. In the overwhelming majority of all cases, the concentrator is made of mirrors, which means that the optical path is folded, unlike the scheme in Fig. 19. It is important to note that the angular aperture of the concentrated radiation on the receiver (angle ω in Fig. 19) is always considerably larger than the apparent diameter of the solar disk ($\pm 16'$). This has a major impact on the design of a solar receiver, especially the aperture area.

1.3.4 Absorption, Reflection, Transmission

When radiation hits the surface of a solid, liquid, or gaseous body, basically³⁵ three things can happen (Fig. 20 left):

- **Reflection.** There exist two extreme subcases. On the one hand, the reflection can be ideally specular. This means that the reflected ray leaves the surface under the same angle as the incoming ray, but on the opposed side with respect to the normal vector on the intersection point; without leaving the plane that's defined by the normal vector and the vector of the incoming ray (Fig. 20a). The other extreme is the ideally diffuse reflection. Here, the reflected radiation goes uniformly into the half-space over the surface element (Fig. 20b). An example for the first case is a mirror, while a matt finished white painted wall represents the second case. In practice, most surfaces show a mix between the two extremes (Fig. 20c).

³⁵ Further effects like scattering, refraction, diffraction, polarization, etc. shall not be considered here.

- Absorption. The energy of the radiation is transferred to the surface or the volume of the body, usually resulting in an increase of the temperature.
- Transmission. The radiation leaves the body on the other side, in the same or in a different direction. It depends on material properties and the thickness of the body. Opaque bodies don't have transmission.

If the power of the ray is normalized to 1, this can be expressed by

$$\alpha + \rho + \tau = 1 \quad (16)$$

with α ...absorptance, ρ ...reflectance, and τ ...transmittance. These values, just like the emissivity ε , are material and wavelength dependent. According to Kirchhoff's law of thermal radiation, the absorptance is equal to the emissivity for any given wavelength. In particular, for an ideal black body, $\alpha = \varepsilon = 1$ is valid over the whole electromagnetic spectrum (Duffie & Beckman, 1980). In the rare case that the emissivity at long wavelengths is lower than the absorptance in visible light, a body can heat up beyond the temperature calculated for a black body.

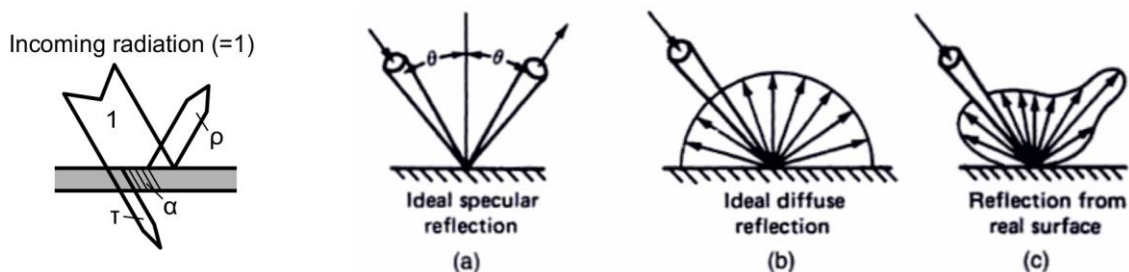


Fig. 20: Left: Interaction of radiation with a surface. Right: Different forms of reflection. From (Goswami, 2015).

In practice, calculation of wavelength dependence is often reduced to two cases, solar radiation (visible light) and thermal radiation (infrared).

1.3.5 Losses

Like all energy conversion systems, CSP plants have losses. They are presented in the following, generalized list. The order is based on the path of the solar radiation and separated by concentrator and receiver. Not all points exist for all CSP technologies.

Concentrator:

- Shading.
This is caused by objects in the ray path before the concentrator, such as other mirrors, support structures, the tower, or the receiver itself. The contribution to the losses is usually minor, but can become significant when the sun is just barely above the horizon. This has to be taken into account e.g. for locations near the lunar poles.
- Cosine.
This is a geometrical effect. As long as the sun, the concentrator and the receiver are not on a straight line, the concentrator has to be rotated or tilted, thus reducing its apparent surface from the sun's point of view. This is calculated with the cosine of the corresponding angle, therefore the name. Cosine losses can reach double-digit percentages, depending on the CSP system, time of day, and season. Often they are the largest contribution to the losses of the concentrator system.

- Reflectance.
Mirrors reflect most of the incident light, but not all of it. With clean silver mirrors, the values range between 92 and 96% (Goswami, 2015). When dirty, it can be considerably less.
- Blocking.
This is caused by objects in the ray path after the concentrator, such as other mirrors. The contribution to the losses is usually minor.
- Atmospheric Attenuation.
If the distance between concentrator and receiver is very long (many 100 m), then it is possible that a non-negligible part of the energy is absorbed or scattered by the air in between. This phenomenon mainly affects large tower installations on Earth.

Interface Concentrator/Receiver:

- Spillage or Intercept.
Usually not the whole concentrated solar radiation hits the aperture of the receiver, a (small) part misses. This can be caused by deviations of the concentrator from the ideal shape and/or tracking. But spillage can also be an intentional feature of the design, see below at bullet point “Thermal Radiation”.

Receiver:

- Reflection.
If the absorber surface is not perfectly black, some of the light is reflected back and lost. Therefore, if possible, deep black materials (and/or a cavity shape) are used so that the absorption coefficient is usually well above 90%.
- Thermal Radiation.
For CSP systems operating at high temperatures, this is by far the most important loss mechanism of the receiver. Its working principle is explained in chapter 1.3.1. To keep it low, the aperture area of the receiver must be kept as small as possible, which in turn increases spillage losses. For an optimal design, a compromise must be found between the two loss mechanisms. When operating at high temperatures, the use of a secondary concentrator can be helpful. At low temperatures, selective surface coatings are often utilized to minimize radiative losses.
- Convection and Conduction.
These losses can be almost completely avoided by suitable thermal insulation of the receiver and the piping of the heat transfer fluid. The exception is the aperture, where, e.g. due to wind, a noticeable loss by convection is possible. Convection can be ignored when operating in a vacuum.

Optics for astronomical telescopes require extraordinarily high precision. For good imaging quality, they must be polished to an accuracy of $\frac{1}{4}$ wavelength, that is about 100 nm. For solar concentrators however, this is not possible both for cost reasons and because of the size of the mirrors. Therefore, they usually do not provide a perfect image of the sun but a more or less Gaussian distributed radiation spot in the focal plane. These *mirror errors* can be subdivided according to the scale of the cause into micro errors (roughness of the mirror surface, non-specular reflection), macro, shape, or slope errors (waviness of the mirror panel), and canting errors (entire panels are not perfectly aligned). If the entire concentrator is misaligned, then it is called tracking error. These errors are usually smaller or of the same order of magnitude as the apparent diameter of the Sun (a few mrad).

1.3.6 CSP on Earth

The concentration of the solar radiation is usually achieved by curved mirrors that track the Sun. On Earth, both, uniaxial (line-concentrating) and biaxial (point-concentrating) curved systems are used commercially. While the former allow only lower concentrations ($< 70\times$) and temperatures ($< 400\text{ }^{\circ}\text{C}$), with the latter, very high concentrations of several thousand times and temperatures above $1000\text{ }^{\circ}\text{C}$ can be achieved (Winter, Sizmann, & Vant-Hull, 1991).

Commercial Systems

The majority of all commercial CSP plants is working with the line-concentrating *Parabolic Trough* technology. This technology works with long rows of north-south oriented, parabolic curved mirrors that concentrate the solar radiation onto a long tube (Fig. 21). The HTF within this tube is mostly a synthetic oil that is heated up to nearly $400\text{ }^{\circ}\text{C}$. Many of these plants have an electrical unit power of 50 MW. Their advantage is the long operational experience of over 30 years, the disadvantage is the relatively low efficiency due to the low HTF temperature and the cosine losses during winter at mid-latitude sites.



Fig. 21: Parabolic trough (line concentrating) systems. Left: Operational principle (SolarPACES, 2018). Right: Aerial view of the Andasol plant in southern Spain³⁶.

Point-concentrating *Solar Tower* or Central Receiver Systems (CRS) utilize sun-tracking mirrors called heliostats to focus sunlight onto a receiver at the top of a tower (Fig. 22). The most



Fig. 22: Solar tower (point concentrating) systems. Left: Operational principle (SolarPACES, 2018). Right: Aerial view of the Gemasolar plant in southern Spain³⁷.

³⁶ By BSMPS-Own work, CC BY-SA 4.0, <https://commons.wikimedia.org/w/index.php?curid=8801773>

³⁷ By kallerna-Own work, CC BY-SA 4.0, <https://commons.wikimedia.org/w/index.php?curid=104866886>

commonly used HTF is liquid salt between 265 °C and 565 °C because it can be stored cheaply for many hours, thus largely decoupling electricity production from solar radiation supply. When water/steam is directly heated in the receiver, the storage capacity is generally quite low. The largest plants have an electrical power output above 100 MW. Problems are the durability of the receiver and the danger of salt freezing in the pipes. In order to achieve higher temperatures and therefore better efficiencies in the thermodynamic cycle, research is being done on particle receivers (Ho, 2016) (Ebert et al., 2019).

Small Systems

Several smaller systems have been developed and are used for small commercial sites or research purposes. A *Parabolic Dish* system consists of a parabolic-shaped point focus concentrator in the form of a dish that tracks the sun and reflects solar radiation onto a receiver mounted at the focal point (Fig. 23 left). Parabolic dishes have the highest efficiency of all CSP systems, because they avoid cosine losses, need only one reflection, and can reach very high concentrations (2500x). The engine in the focus is often a Stirling³⁸ engine because it works with external heat supply. The disadvantage is that dishes can only be scaled by number, but hardly by size, and that the receiver has to be moved and tilted with the concentrator high above the ground, and therefore only small and gravity-independent devices can be used. Closely related to the parabolic dish concentrator is the *Cassegrain* system. In this design, a hyperbolic secondary mirror is located close to the focal plane which reflects the radiation back to a bore in the primary mirror. Fig. 23 right shows a concept where an optical fiber then guides the light towards the reactor.

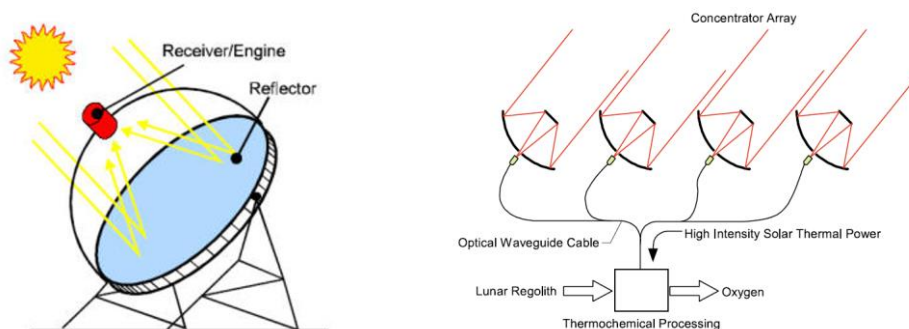


Fig. 23: Left: Solar dish (point concentrating) system, operational principle (SolarPACES, 2018). Right: Cassegrain concentrator with optical fiber (Gerald B. Sanders & Larson, 2013).

A *Solar Furnace* uses one (or several) flat heliostat(s) and a fixed concentrator. It's usually built with a horizontal optical axes, but vertical designs are also possible. Like dishes, the furnace can reach very high concentrations. A big advantage is that the focus hardly changes position, shape, and power during the day, the disadvantage is that two instead of one large mirrors are needed. A more detailed description can be found in the next chapter (1.3.7) and in chapter 3.4.

For very small systems with a power in the order of 1 kW, a *Fresnel Lens* can be used. For example, 3D-printing by sintering of lunar soil simulant was tested with a Fresnel lens in the EU-H2020-project RegoLight (Urbina et al., 2017). In Fig. 24 it becomes obvious that the advantage of solar thermal heating over "conventional" photovoltaic heating is the very high efficiency and the non-necessity of additional heating hardware. A PV system with the same

³⁸ Developed in 1816 by Robert Stirling and frequently misspelled as "Sterling".

output would have to be at least a factor of 4 larger than the solar concentrator³⁹. The problem of the Fresnel lens is that the whole concentrator has to be moved above the experiment, and that the geometry is very disadvantageous when the sun is low over the horizon. Furthermore, scaling is very difficult, because a lens can be supported only on its edge, in contrast to concentrators made of mirrors that can be supported everywhere on their back surface⁴⁰.

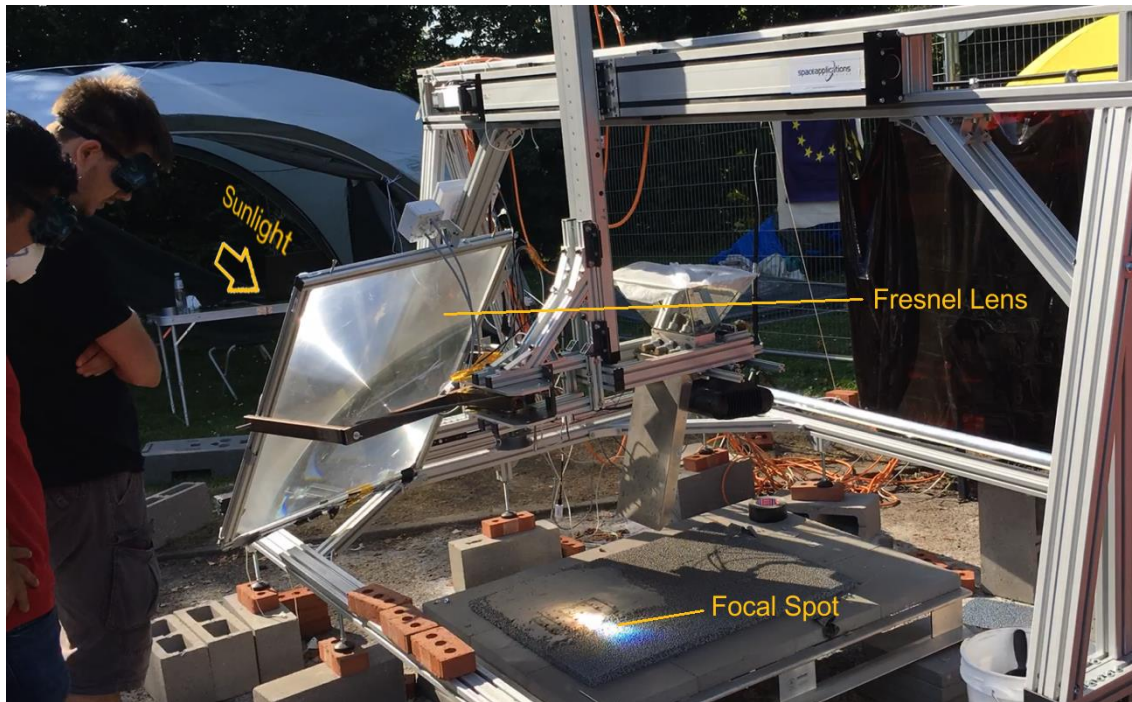


Fig. 24: Solar sintering with a Fresnel Lens.⁴¹

The most important properties of the presented CSP technologies are summarized in Table 2.

Technology	Conc.	Unit Power	Comment
Parabolic Trough	Medium	50 MW	For liquids < 400 °C. Only tube receivers.
Solar Tower	High	>100 MW	For solids or gases ≥ 1000 °C, liquids < 600 °C.
Parabolic Dish	Very high	<100 kW	High efficiency. Receiver moving and rotating.
Solar Furnace	Very high	2-1000 kW	Fixed and constant focus. Two reflections.
Fresnel Lens	Very high	1 kW	Sun tracking unduly cumbersome.

Table 2: Comparison of different Concentrated Solar Power (CSP) technologies.

In principle it's possible to reach very high temperatures (>2000 °C) with concentrated solar power. But in practice this is only possible at the expense of a very low efficiency due to high thermal radiation losses. Therefore, to get a meaningful efficiency, the temperature required in the receiver or reactor rarely exceeds 1000 °C.

³⁹ For $\eta_{PV} = 25\%$, $\eta_{Heater} = 100\%$, and $\alpha_{Regolith} = 1$. If heating were done with microwave or laser ($\eta_{Heater} = 50\%$), the required size of the PV would be even 8x the size of a solar concentrator.

⁴⁰ For the same reason, large astronomical telescopes today are built exclusively as reflectors. The largest usable refracting telescope ever built is the Yerkes telescope with a diameter of 1.02 m (40 inch). It dates back to the year 1897.

⁴¹ Photo courtesy of Diego Urbina, Space Applications Services, Zaventem (Belgium).

1.3.7 CSP on the Moon

The best concentrator concept for the Moon is probably the *Solar Furnace*. It is ideal for thermal applications between 5 and 100+ kW as can be expected to be needed near or mid-term on the Moon. If properly designed, it has a high quality and in particular an unchanging focal spot throughout the day. A common terrestrial Solar Furnace consists of (Fig. 25 left):

- (1) A flat heliostat for the tracking of the Sun.
- (2) An attenuator (shutter) for power control.
- (3) A fixed, biaxial curved, concave mirror.
- (4) The receiver or reactor.
- (5) If a vertical beam is needed, this can be achieved by having a 45° inclined, cooled "diagonal" mirror near the focal plane.

Improved concepts have been proposed for the Moon. In (González-Pardo & Denk, 2016), the concentrator and the diagonal mirror are combined into a single, off-axis concentrator (Fig. 25 right). This eliminates the (considerable) cooling requirement of the diagonal mirror as well as the third reflection. If the heliostat is oversized by a factor of $\sqrt{2}$ in comparison to the diameter of the concentrator, cosine losses are avoided for a solar azimuth and elevation of up to $\pm 90^\circ$ with respect to the optical axis. Furthermore, the location of the reactor on the ground is an important advantage. This applies not only to oxygen production in a reactor, but in general to any process that requires a large solar heat input. This configuration should be very well suited for example for sintering of regolith with the purpose of stabilization of landing pads (Hintze, Curran, & Back, 2009) or the construction of lunar roads. Since there is no wind on the Moon, both mirrors can be made of very lightweight foil material. However, it is important to make sure that the mirror errors (and in particular the shape errors) remain within an acceptable range. It must also be taken into account that the focus is no longer circular but somewhat elliptical. The shutter can be omitted if the power adjustment can be accomplished by other means, for example slight deformation of the heliostat. With this concept, it should be possible to provide high solar thermal power through a collector system with extremely low mass.

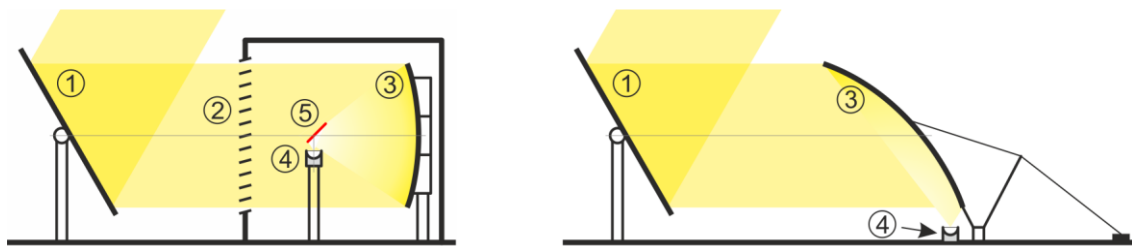


Fig. 25: Solar Furnace concepts. Left: Common configuration for a vertical beam. Right: Proposed modification for application on the Moon (González-Pardo & Denk, 2016). For the meaning of the numbers see the list in the text.

1.4 Particle Technology

The behavior of particles is notoriously difficult to predict⁴² (Fig. 26). One reason is that the intergranular forces depend widely on their shapes. While “perfect” spherical particles are

⁴² During the work on my first project with particles in 1995, we “formulated” (not so very seriously) the two “particle laws”: 1) “The Particles are Always and Everywhere.” 2) “The Particles do What They Want (and NOT necessarily what the experimenter wants).” While the conclusion from 1) is that a vacuum cleaner is among the most important tools, 2) dictates that the prototypes need wide operational margins and from time to time a gentle stroke with a hammer.

more or less easy to handle, more irregular shapes can cause a behavior not only far away from theoretical predictions but also often difficult to reproduce. Therefore, all devices working with granular material need thorough experimental testing.

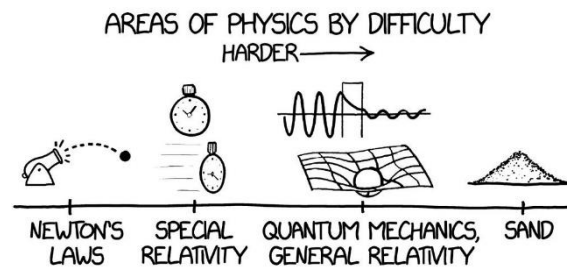


Fig. 26: The physics of sand is extremely complex and hence many theoretical predictions must be checked by experiments.⁴³

By far the easiest way to access raw material on the Moon is simple scooping (Just, Smith, Joy, & Roy, 2020). Therefore, the feedstock will be present in granular form and hence all subsequent equipment must be able to handle and process *particles*.

The different possibilities that exist for *contacting of gas and solids* are summarized in the following list, including a short description and the most important corresponding advantages or disadvantages (Kunii & Levenspiel, 1991):

- *Fixed Bed:* Gas is flowing from the bottom through a contained pile of particles at a velocity low enough so that the particles don't move. No continuous operation, large temperature gradients, poor heat exchange. Suitable for very large particles (pellets...).
- *Moving Bed:* Like fixed bed, but with vertical, horizontal, or inclined, slow movement of the particles. Fairly large and uniform particles required. Inefficient heat exchange.
- *Bubbling and Turbulent Fluidized Bed:* Gas flows from the bottom, fast enough to levitate the particles. Wide range of particle size distribution possible. Efficient heat transport and transfer, uniform temperature. Deep beds have high pressure drop. Wide range of residence time for the solids.
- *Fast Fluidized Bed and Concurrent Pneumatic Transport:* Gas velocity so high that the particles are carried away by the gas. Difficult temperature control, good for rapid reactions.
- *Rotary Cylinder (Kiln):* Slightly inclined, long rotating tube, the gas flows over the particles. Difficult temperature control, poor heat exchange, therefore often very long cylinders needed. Good for any size of particles, also those which may sinter or agglomerate.
- *Flat Hearth:* Mechanical horizontal particles transport, gas flows above. Difficult temperature control, poor heat exchange. Good for any size of particles, also those which may sinter or agglomerate or melt.

A *solar thermal reactor for lunar soil processing* should satisfy the following requirements:

- It should be operated in continuous mode to maximize the use of solar radiation.
- It must be able to process large quantities of granular solids.
- It must ensure good mixing (contacting) of gas and solids.

⁴³ by Randall Munroe, xkcd. <https://xkcd.com>

- For a good conversion, the temperature distribution in the reactor should be as homogeneous as possible.
- It should allow a mean residence time of tens of minutes up to one hour or even more for the solids.
- It should offer a well-defined surface where the solar radiation can be absorbed.

A comparison of solar gas heating between a packed bed and a fluidized bed was done by (Flamant & Olalde, 1983). While the efficiency of the packed bed receiver reached only 20-40%, the fluidized bed showed with 40-70% a far superior performance. Taking into account all the properties in the lists above, it turns out that the low-expansion, dense phase, or bubbling fluidized bed is the best way to fulfill these requirements.

1.4.1 Fluidized Beds

According to (Kunii & Levenspiel, 1991), “fluidization is the operation by which solid particles are transformed into a fluid-like state through suspension in a gas or liquid.” The most basic configuration of a fluidized bed consists of a container filled with particles (the “bed”). At the bottom there is a base (*gas distributor*) which allows the gas to flow upwards and at the same time prevents that the particles fall down. The most important parameter of a fluidized bed is the *gas velocity*. If very low, the fluid percolates through the voids in the bed without causing any movement of the particles. This is called a fixed bed (Fig. 27a). When the gas flow increases, the particles start to levitate. When the gas flow is high enough that the vertical mechanical forces between the particles disappear, or with other words, when the aerodynamic force is in equilibrium with the weight force of the particles, then the point of *minimum fluidization* is reached (Fig. 27b). With further increase of the gas flow, bubbles appear (Fig. 27c). An important characteristic in this state is that the fluidized bed has still a well-defined surface. As the mass of the solids is much larger than the mass of the gas in a given volume, these systems are also called dense-phase systems. If the gas speed is increased (a lot) further, the bed becomes quite turbulent. The surface is more and more agitated until it finally disappears altogether and a significant portion of the particles is entrained from the bed (Fig. 27d). In the extreme case of very high gas velocity, all particles are carried out of the bed. This is called pneumatic transport or lean phase fluidization (Fig. 27e).

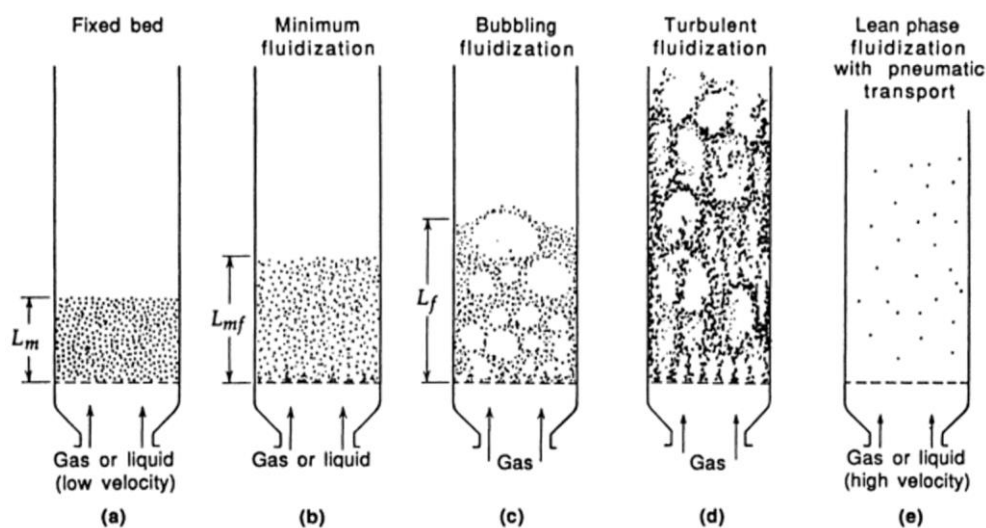


Fig. 27: Various forms of contacting of a batch of solids by a fluid (adapted from (Kunii & Levenspiel, 1991)).

Properties

Maybe the most important property of fluidized beds is that they do not only look like but they really behave in many ways like a (boiling) liquid. They form a horizontal surface even when the vessel is tilted, light objects submerged in the bed float like a boat while heavy objects sink, solids spill out when there is a hole in the vessel, two interconnected fluidized beds equalize the level of their surfaces, and particles can flow between them like if it were a liquid. Furthermore, the static pressure difference between two points in the bed is determined by the density of the particles (incl. voids) between the two points, just as with a column of liquid.

The following lists (Kunii & Levenspiel, 1991) (Werther, 2007) point out the advantages and disadvantages of fluidized beds.

Advantages:

- Continuous operation with easy handling.
- Close to isothermal conditions throughout the reactor.
- Large thermal mass helps to avoid abrupt temperature changes.
- Easy movement of particles from one bed to another allows large heat flows.
- Suitable for large scale operation.
- High heat and mass transfer rates between gas and particles.
- High heat transfer rates with immersed objects like heat exchangers, heaters...

Disadvantages:

- Gas flow deviates widely from plug flow and therefore high conversion of the gas can be difficult.
- Rapid mixing of solids leads to non-uniform residence time and therefore incomplete conversion.
- Fine dust from friable solids might be entrained with the gas and needs to be separated.
- Erosion or abrasion of vessels and pipes.
- Sintering of fine particles might require operation at lower than optimum temperature.

Solids Mixing

The excellent thermal behavior of fluidized beds is mainly due to *rapid solids mixing* (Kunii & Levenspiel, 1991). Complete mixing of freshly introduced particles within the bed can occur in less than one minute (see e.g. Fig. 117 on page 143). Mixing of particles in fluidized beds is primarily caused by the behavior of the bubbles that are rising in the bed. Especially for large, shallow beds, horizontal mixing is also of importance. Horizontal dispersion is roughly one order of magnitude smaller than vertical dispersion (Bellgardt & Werther, 1984). This means that concentrated solar radiation hitting the upper surface of a fluidized bed should be transferred quite well deep into the bed by vertical mixing. Coefficients of heat transfer with surfaces (wall or submerged) are in the order of 200 - 400 W/m²K. At high temperatures (like 800 °C), this value can increase another 100 - 200 W/m²K due to the increase of thermal conductivity of the gas and of radiant heat transfer.

Gas Distributor

The *gas distributor* is located at the bottom of the bed. Its task is to provide a homogeneous distribution of the feed gas and at the same time to prevent particles from falling down into the volume below. To achieve a uniform gas flow over the whole cross section of the bed, the pressure drop in the gas distributor should be about 15% of the static pressure of the bed above (Kunii & Levenspiel, 1991). Especially with highly variable operating conditions, this rule is not easy to meet. Best for small scale applications are porous plate distributors like sintered metals. They have a relatively high pressure drop and therefore can guarantee a uniform gas flow distribution. But especially when operated at high temperature, they have some drawbacks, like limited mechanical stability, and the danger of gradual clogging by fine particles due to repeated thermal expansion and contraction. Alternatives are perforated plates, tuyeres/caps designs, or pipe grids and spargers. A tuyere (from French: tuyère) is a tube, nozzle or pipe through which air is blown into a furnace or hearth. In fluidized beds, tuyeres often have the shape of a mushroom with the nozzles arranged at the side or the bottom of the cap. Fig. 28 left shows an example where a screw is used. Note that the shaft of the screws extends to the bottom of the gas distributor to ensure mechanical stability. A sparger is a (horizontal) pipe with 45° downwards oriented bores (Fig. 28 right). They are quite simple to fabricate. Another important advantage of spargers is that there remain gaps between the pipes where the particles can flow through when the bed has to be drained.

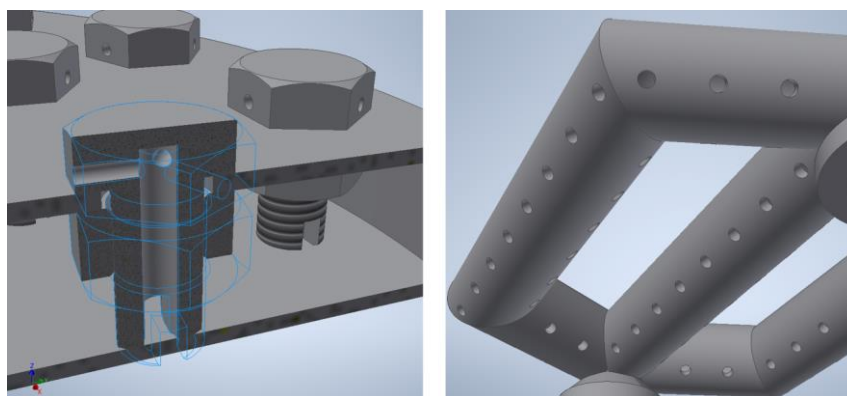


Fig. 28: Examples for gas distributors. Left: tuyeres. Right: sparger.

Modeling

No generally accepted model of the fluidized bed reactor exists; instead, many models have been proposed on the basis of more-or-less extensive experimental findings for various applications (Werther, 2007). According to (Kunii & Levenspiel, 1991), *“some process designers feel that fluidization is an interesting operation but is not for them because it is still too much of an art requiring practical experience and know-how, and because too much uncertainty is involved, particularly in scale-up, at which stage the cost failure is serious. [However], fluidization is not such a black art, and if we keep careful tab of our uncertainties and get the needed information for scale-up, we should be able to design fluidized beds successfully.”*⁴⁴

⁴⁴ One of the best websites for *intuitive* understanding of fluidized beds that I have found so far in the web is this 10 minute video made by Mark Rober: <https://www.youtube.com/watch?v=My4RA5I0FKs>

1.4.2 Minimum Fluidization

Minimum Fluidizing Velocity

One of the most important parameters for designing a fluidized bed is the *minimum fluidizing velocity*. According to (Kunii & Levenspiel, 1991), minimum fluidization is the point where all the particles are just suspended by the upward streaming fluid. It is described by the superficial gas velocity at minimum fluidizing conditions, u_{mf} . It can be derived by the condition that the drag force by upward moving gas is in equilibrium with the weight force of the particles (Werther, 2007):

$$\Delta p A_{FB} = A_{FB} h_{FB} (1 - \varepsilon_{mf}) (\rho_s - \rho_g) g \quad (17)$$

With the Ergun equation (Ergun, 1952)

$$\frac{\Delta p}{h_{FB}} = 150 \frac{(1 - \varepsilon_{mf})^2}{\varepsilon_{mf}^3} \frac{\mu u_{mf}}{(\phi_s d_p)^2} + 1.75 \frac{1 - \varepsilon_{mf}}{\varepsilon_{mf}^3} \frac{\rho_g u_{mf}^2}{\phi_s d_p} \quad (18)$$

which originally describes the friction of a gas flow in a packed bed but can reasonably be extrapolated to minimum fluidizing conditions, equating (17) and (18) results in an expression of the form:

$$K_1 \text{Re}_{mf}^2 + K_2 \text{Re}_{mf} = Ar \quad (19)$$

with the two constants

$$K_1 = \frac{1.75}{\varepsilon_{mf}^3 \phi_s} \quad \text{and} \quad K_2 = \frac{150(1 - \varepsilon_{mf})}{\varepsilon_{mf}^3 \phi_s^2}, \quad (20)$$

the Reynolds number at minimum fluidizing conditions

$$\text{Re}_{mf} = \frac{d_p u_{mf} \rho_g}{\mu}, \quad (21)$$

and the Archimedes number

$$Ar = \frac{d_p^3 \rho_g (\rho_s - \rho_g) g}{\mu^2}. \quad (22)$$

Equation (19) is quadratic for the Reynolds number Re_{mf} and therefore the minimum fluidization gas velocity u_{mf} . For small particles, it becomes linear in Re and can be easily resolved to u_{mf} :

$$u_{mf} = \frac{d_p^2 (\rho_s - \rho_g) g}{150 \mu} \frac{\varepsilon_{mf}^3 \phi_s^2}{1 - \varepsilon_{mf}} \quad (\text{Re}_{mf} < 20) \quad (23)$$

Particles Properties

Eq. (23) contains parameters for both particle and gas properties. For the particles, the following data is needed:

- d_p ... Particle grain size (diameter), unit [m], measured by screening. For particles with $d_p > 30 \mu\text{m}$, this value can be measured by screening of the particles, or simply be found in the data sheet if available.

- ρ_s ... Density of the solids (not the bulk!), unit $[\text{kg}/\text{m}^3]$. This value can be found in the data sheet of the used particles.
- ϕ_s ... Sphericity. It's defined as the ratio of the surface of a sphere and the surface of a particle with both of the same volume. For perfect spheres is $\phi_s = 1$, for all other particles applies $0 < \phi_s < 1$. Values for typical granular solids range from 0.6 to 0.8. The Ergun equation (18) can be used for determination by experiment.
- ε_{mf} ... Void fraction, or porosity, at minimum fluidizing conditions. It can be determined by careful measurement of the bulk density of the bed and the grain density of the solid. The relation $\varepsilon_{mf} = 1/(14\phi_s)^{1/3}$ between the sphericity ϕ_s and the void fraction ε_{mf} was proposed by (Wen & Yu, 1966)⁴⁵.

Gas Properties

The required gas properties are:

- ρ_g ... Density of the gas, unit $[\text{kg}/\text{m}^3]$. For the gases used here it can be calculated by the ideal gas law.
- μ ... Dynamic viscosity of the gas, unit $[\text{kg}/\text{m}\cdot\text{s}]$. It can be calculated by the coefficients given in (Rohsenow, Hartnett, & Cho, 1998).

Temperature

The minimum fluidizing velocity u_{mf} depends not only on the solids and the chosen gas, but also on the temperature T , because the gas properties do so. With the values $d_p = 150 \mu\text{m}$, $\rho_s = 4450 \text{ kg}/\text{m}^3$, $\phi_s = 0.66$ and $\varepsilon_{mf} = 0.48$ for the solids ("Ilmenite-150", see chapter 3.3.2), Fig. 29 shows the calculated values of the minimum fluidizing velocity, the gas density, and the viscosity for the three gases air, argon, and hydrogen. It turns out that u_{mf} can be expressed with sufficient accuracy by a proportionality law with $1/T^{0.7}$ (T in Kelvin); this is drawn as the thick lines in Fig. 29. As the gas density is proportional to $1/T$, the actual gas velocity would

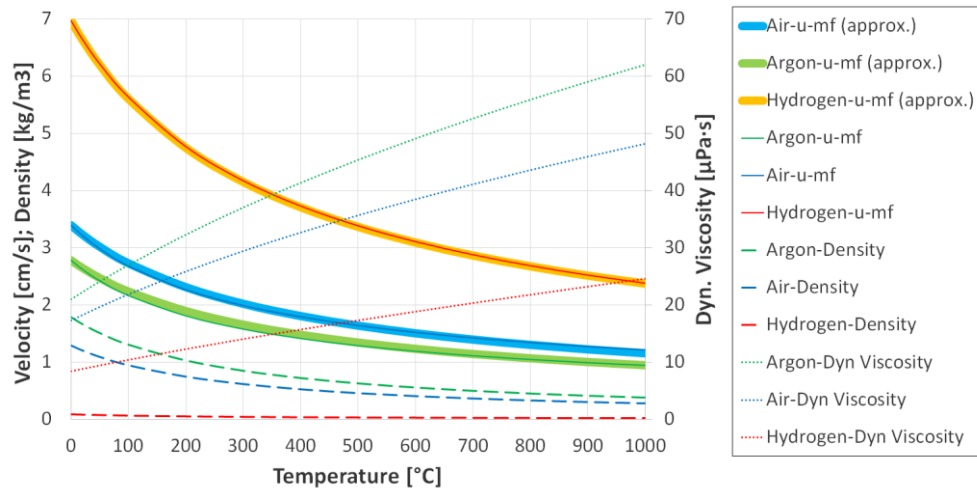


Fig. 29: Minimum fluidizing velocity “u-mf”, density (dashed), and viscosity (dotted) for air (blue), argon (green), and hydrogen (red) as a function of the temperature. Also drawn the approximation with the $1/T^{0.7}$ -law for u-mf (thick lines).

⁴⁵ Wen&Yu also noted that the factors K_1 and K_2 in eq. (19) remain mostly constant for different kinds of particles over a wide range of conditions. When ε_{mf} and ϕ_s are not known, they propose to use $K_1 = 24.5$ and $K_2 = 1650$.

increase linearly with T if the feed gas flow were to remain constant. Therefore, if the goal is to maintain minimum fluidizing conditions, the gas norm-volume (or mass) flow rate, which is ultimately the variable that has to be set in the flow controllers, has to be proportional to $1/T^{1.7}$. An interesting observation is that the ratio for the minimum fluidizing velocity between hydrogen and argon is 2.5 for the whole temperature range. This is useful when working with mixtures of the two gases.

Gravity

Examining closely equation (23) for the minimum fluidizing velocity, there is still another parameter which only very rarely receives attention, the *gravitational acceleration* g . The reason is obvious, until today, practically all fluidized beds ever built were operated on the surface of Earth. Therefore, always the value $g = 9.81 \text{ m/s}^2$ has to be applied. If one day a fluidized bed is operated on the Moon, then the lunar value $g = 1.62 \text{ m/s}^2$ must be used. Since this is about six times smaller than on Earth, and g is linear in eq. (23), it is to be expected that the minimum fluidizing velocity for systems on the Moon will be six times smaller than for identical systems on Earth.

Measurement

The minimum fluidizing velocity u_{mf} can be *measured* relatively quickly, easily and accurately (Fig. 30). For this purpose, the flow rate of the gas is slowly increased starting from zero, and simultaneously, the pressure difference over the fluidized bed is measured. First, the pressure increases mostly linearly with the gas flow until a point is reached where the pressure suddenly drops again somewhat. It is at this moment that the first bubbles in the fluidized bed can be observed. As the gas flow continues to rise, the pressure increases further only slightly, but fluctuates more and more around an average value as the gas flow increases. If the experiment is reversed and the gas flow slows down, it can be observed that the oscillations become weaker and finally stop altogether. At this point, the bubbles also disappear from the fluidized bed, and the pressure now again decreases linearly with the gas flow to zero. The point of minimum fluidization can be determined relatively well as the intersection between the linearly increasing and the almost horizontal part of the pressure curve (red line in Fig. 30).

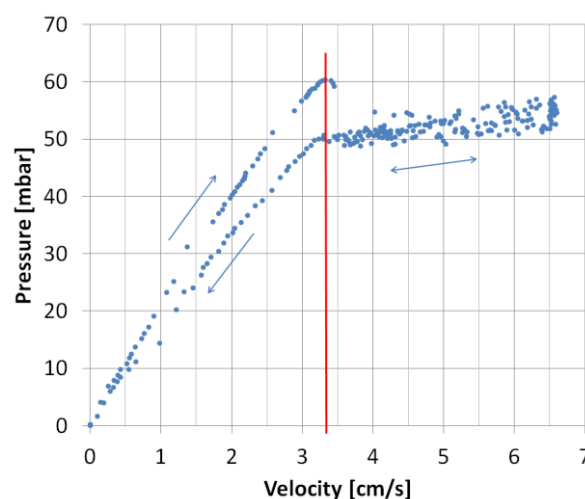


Fig. 30: Pressure drop vs. gas flow diagram (Ilmenite-150/air at 20°C, own measurement from Dec. 16, 2013). The red line marks the measured minimum fluidizing velocity falling between 3.3 and 3.4 cm/s. The theoretical value calculated with eq. (23) is 3.21 cm/s.

In order not to interrupt the operation of the fluidized bed for an unnecessarily long time, the procedure can also be reversed in practice: first reduction of the flow to a value close to zero, and then again increase up to the previous operating point. This procedure is particularly useful at high temperatures, because it minimizes the time required for the measurement to less than three minutes. Since the solar energy supply must be interrupted during the measurement, this keeps the unavoidable temperature drop in the reactor as small as possible. An example for the practical application of this measuring method during hot operation can be found in chapter 4.2.10.

Gas Demand beyond Minimum Fluidization

For achieving good mixing of the fluidized bed, in real operation the superficial gas velocity u_G must be increased above the minimum fluidizing velocity u_{mf} . For this purpose, it is helpful to work with the dimensionless ratio u_G/u_{mf} . The bed is fluidized when $u_G/u_{mf} > 1$. How this turned out in practice can be found in chapter 5.1.

1.4.3 Geldart Groups

Not all solids fluidize the same way. Derek Geldart (Geldart, 1973) recognized that there are four different kinds of particle behaviors which he classified in groups, giving them letters from A to D. The following list summarizes them from smallest particles to largest. The properties put in quotes and parenthesis for every group are an informal way to help for memorizing their basic characteristics. They are (Kunii & Levenspiel, 1991):

- Group C (“Cohesive”):
Cohesive or very fine powders. Difficult to fluidize because interparticle forces are greater than forces from the gas. In small beds, they tend to form slugs or plugs. In larger beds, channeling occurs, this means that the gas shortcuts the bed through one or several vertical, mostly particle free channels, and no fluidization and hence no gas-solids mixing occurs. Geldart C particles are the “worst case”. Possible, but not easy solutions are mechanical aids like a stirrer, or well distributed gas nozzles that stir the bed by the action of their jets.
- Group A (“Aeratable”):
Quite small particles, but larger than C-type. Fluidize easily and smoothly, forming only quite small bubbles not larger than a few cm, even in large beds. Geldart A particles often are the “best case”.
- Group B (“Bubbling”):
Sand-like particles. Fluidize well, but forming bubbles of considerable size that are growing and coalescing to virtually infinite size while rising in the bed. Vigorous bubbling encourages the gross circulation of solids in the bed. Geldart B particles are the most common case in fluidized bed technology due to the upstream processing of the feedstock.
- Group D (“Dense”):
Very large or dense particles, often referred to as “spoutable”. Difficult to fluidize, and only used if unavoidable, e.g. for food processing (roasting coffee beans...). Large quantities of gas are needed.

Fig. 31 shows the Geldart groups in graphical form. If the particle size and density are known for a given solid, then this diagram can be used to predict the fluidization behavior. It’s valid for air at ambient conditions. The Geldart classification is widely used because it’s clear and easy. The transition zone between C and A particles, the so-called AC-boundary (hatched area

in Fig. 31), is of special interest because it separates easily usable from difficult-to-use particles.

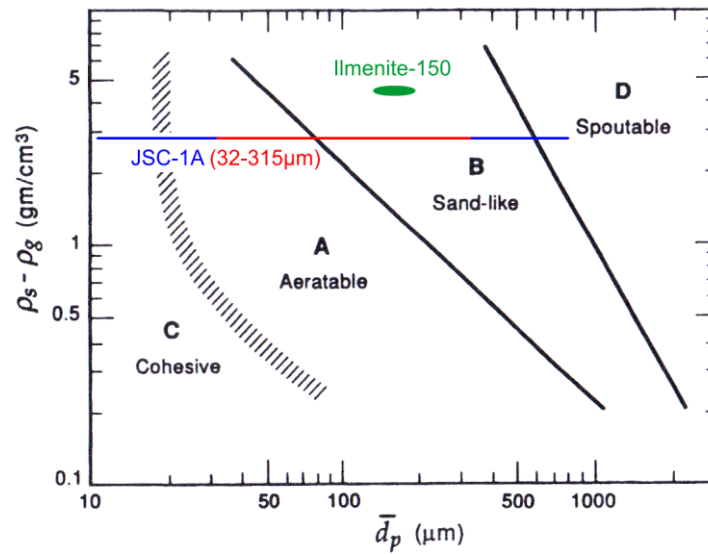


Fig. 31: Geldart classification for air at ambient conditions. Adapted from (Kunii & Levenspiel, 1991) and (Geldart, 1973). The lines and area plotted in color represent the particles used in this work (see chapter 3.3.2).

On the Moon

Still largely unknown is how the boundaries in the Geldart diagram shift when operating a fluidized bed on the Moon. (Shao, Williams, & Overfelt, 2006) tested the behavior of 8 different particle samples fluidized with nitrogen under different gravity levels on a parabolic flight. They compared the fluidization under 1.8 g (airplane recovers from the parabola), 1.0 g (Earth), 0.38 g (Mars), and 0.16 g (Moon). Four of the samples were glass spheres with a density of 2.5 g/cm³ and the other four were irregularly shaped aluminum oxide with 3.77 g/cm³. The main result of the work was that a shift of the Geldart AC-boundary towards increasing particle size with decreasing gravity was clearly observed. Although they got only a very limited quantity of data points, their investigation indicates that the Geldart AC-transition on the Moon can be expected to be between 50 and 60 μm for fluidization with air at ambient conditions. In any case, this is a very interesting area of research that deserves to be thoroughly explored in the future.

1.4.4 Gas-Solid Reactions

Gas Velocity vs. Gas Flow Rate

Fluidization requires a certain *gas velocity* (unit: distance/time) u_G for working well. But fluidization is not an end in itself, it is there to ensure good contact between the gas and the solids so that they can accomplish the actual task of the plant, the *chemical reaction*.

Neglecting inert substances, this reaction can be written in generalized form as:



with S... solid reactant(s), G... gaseous reactant(s), P... gaseous product(s), R... solid residuals, and ν_{index} the corresponding stoichiometric coefficients. This chemical reaction needs a certain molar feed gas flow rate to work as required, which can be converted into a *volume flow rate*

(unit: volume/time) \dot{V}_G . These two requirements (velocity, volume flow rate) finally can be put into agreement (“married”) by proper selection of the *cross section* A_{FB} of the fluidized bed⁴⁶:

$$\dot{V}_G = u_G \cdot A_{FB} \quad (25)$$

In the very common case of a cylindrical reactor with a vertical axis, and with the volume flow rate converted into a molar flow rate, eq. (25) becomes:

$$\dot{n}_G V_m \frac{T/T_0}{p/p_0} = u_G \cdot \frac{\pi}{4} d_{FB}^2 \quad (26)$$

with the molar volume of an ideal gas at ambient conditions $V_m = 22.414 \text{ dm}^3/\text{mol}$. Thereby, it is assumed that the gases involved can be described as ideal gases⁴⁷.

Only in rare cases the reactant is completely converted into the product. This is expressed by the *yield* of the product with respect to the feed gas (Müller-Erlwein, 2007):

$$Y_{PG} = \frac{\dot{n}_P \cdot v_G}{\dot{n}_G \cdot v_P} \quad (27)$$

The yield can range between 0% (no product obtained) and 100% (the complete feed reactant is converted⁴⁸ into the desired product). With the molar mass $M_P = m_P/n_P$ of the product, equation (26) becomes:

$$\dot{m}_P \frac{V_m}{M_P Y_{PG}} \frac{v_G}{v_P} \frac{T/T_0}{p/p_0} = u_G \cdot \frac{\pi}{4} d_{FB}^2 \quad (28)$$

Equations (25), (26) and (28) apply in this form only if solely the reacting gas G is fed into the reactor. If additional inert gas like argon or nitrogen is also involved, then the left sides have to be divided by C_G , the (molar or volume) proportion of the reacting gas G in the total gas volume. In this case, equation (28) is extended to:

$$\dot{m}_P \frac{V_m}{M_P C_G Y_{PG}} \frac{v_G}{v_P} \frac{T/T_0}{p/p_0} = u_G \cdot \frac{\pi}{4} d_{FB}^2 \quad (29)$$

For the determination of the gas velocity u_G according to chapter 1.4.2, the properties of the gas mixture have to be used. Equation (29) allows to estimate the product gas flow based on some process parameters and in particular the diameter of the fluidized bed. This topic will be addressed further in chapter 5.5.1.

⁴⁶ Strictly speaking, the “gas velocity” always used here only applies to the *empty* reactor (without particles). To obtain the real (mean) gas velocity, this value has to be divided by the porosity ε of the bed. Therefore, the true velocity, needed for example for gas residence time calculations, in first approximation is about twice as large. In reality, bubbles and dragging by the bulk particles make the calculation of the real gas velocity a complex thing.

⁴⁷ This is justified when the temperature is far above and the pressure far below the corresponding critical value of the gas. Under the conditions occurring in this work (reactor temperature 1073-1273 K, pressure 0.1 MPa), this is fulfilled for air (crit. temp 133 K, crit. press. 3.9 MPa), argon (151 K, 4.9 MPa), and hydrogen (33 K, 1.3 MPa). https://www.chemie.de/lexikon/Kritischer_Punkt_%28Thermodynamik%29.html#Tabelle_von_kritischen_Zustandsgr.C3.B6.C3.9Fen

⁴⁸ Yield = how much of the *desired* product is formed from the reactant. Conversion = how much of the reactant is consumed, *regardless* of whether into the desired product or an unwanted by-product. If no or only very small amounts of by-products are formed, then both terms have the same value.

Solids Flow

The mean *residence time* \bar{t} of the solids is determined by the mass inventory m_{FB} of the reactor and the rate \dot{m}_R of the outflowing particles (Kunii & Levenspiel, 1991):

$$m_{FB} = \dot{m}_R \cdot \bar{t} \quad (30)$$

Since the mass capacity of the reactor is defined by the volume, and the reactor diameter by the gas velocity, it's the *height* of the fluidized bed h_{FB} what ultimately determines the mean residence time of the solids:

$$(1 - \varepsilon_{FB}) \rho_s \cdot \frac{\pi}{4} d_{FB}^2 \cdot h_{FB} = \dot{m}_R \cdot \bar{t} \quad (31)$$

If no better value is available, then the void fraction ε_{FB} of the fluidized particles can be set roughly equal to the void fraction ε_{mf} under minimum fluidizing conditions. The outflow rate \dot{m}_R of the particles can be calculated from the inflow rate \dot{m}_S by the conservation of mass:

$$\dot{m}_S + \dot{m}_G = \dot{m}_R + \dot{m}_P \quad (32)$$

Analogous to eq. (27), the yield of the product *with respect to the solid feedstock* is given by:

$$Y_{PS} = \frac{\dot{n}_P}{\dot{n}_S} \frac{v_S}{v_P} \quad (33)$$

Supposing a pure solid feedstock with the molar mass $M_S = m_S/n_S$ gives:

$$\dot{m}_S = \frac{\dot{m}_P}{Y_{PS}} \frac{M_S}{M_P} \frac{v_S}{v_P} \quad (34)$$

Since the required solid raw material is practically never available in pure form, its proportion (by mass) C_S in the lunar regolith must be taken into account. Thus, the *inflow of regolith* required for the continuous operation of a lunar fluidized bed reactor becomes:

$$\dot{m}_{regolith} = \frac{\dot{m}_P}{C_S \cdot Y_{PS}} \frac{M_S}{M_P} \frac{v_S}{v_P} \quad (35)$$

Bed Height vs. Diameter

As can be derived from equations (23), (29) and (31), under otherwise identical conditions, a reactor that has the shape of a pot on Earth would take the shape of a pan on the Moon. This is because with decreasing minimum fluidizing velocity (due to lower gravity), the diameter increases, and with constant residence time (and therefore volume), consequently the height decreases. But a general rule for fluidized beds is that it should be $h_{FB}/d_{FB} \geq 1$ to achieve proper fluidization. Under lunar gravity conditions, this might result in large volumes and very long residence times for the solids of several hours. This is not necessarily a disadvantage, since it would mitigate the general problem of the very non-uniform residence time distribution of the particles in single-stage fluidized beds. The start-up time in the morning would increase somewhat because of the higher thermal mass, but due to the very long day on the Moon, this would also not be a really significant issue. In any case, there exists still the possibility to employ multistage fluidized beds, i.e. to arrange several smaller ones in series (serial staging), or at least to divide the gas distributor into several sections that can be fluidized individually (parallel staging).

2 The Project

2.1 Plataforma Solar de Almería

The Plataforma Solar de Almería (PSA)⁴⁹ is the largest and most complete development and test center for concentrating solar technology research in Europe. It is a dependency of the Centro de Investigaciones Energéticas, Medioambientales y Tecnológicas (CIEMAT)⁵⁰ and its activities are integrated in the CIEMAT organization as an R&D division of the Department of Energy. CIEMAT is a public research body assigned to the Ministry of Science and Innovation under the General Secretariat for Research. The PSA is officially considered by the European Commission as a Major European Scientific Facility and is also a Singular Scientific and Technical Infrastructure (ICTS) of the Spanish government.



Fig. 32: Location of the Plataforma Solar de Almería in the southeast of Spain⁵¹.

The PSA is located in southeastern Spain, in the Tabernas desert at 37°05'27.8" north and 2°21'19" west (Fig. 32). It receives an annual solar radiation of more than 1900 kWh/(m²·yr). PSA has 40 years of experience in the operation, maintenance and evaluation of concentrating solar power systems, their components, and different types of commercial applications. PSA currently has a variety of experimental facilities and R&D laboratories for CSP-related activities (Fig. 33). Among them are central receiver facilities with an 85 m / 7 MW tower and a 45 m / 2.8 MW tower, several parabolic trough and Fresnel collectors, three solar furnaces, some parabolic dishes, facilities for thermal storage, solar desalination, water treatment, and so on. The main focus of the work at PSA is on concentrated solar power technologies, but from time to time there are projects from other areas for which the use of concentrated solar energy is beneficial.

⁴⁹ www.psa.es

⁵⁰ www.ciemat.es

⁵¹ <https://www.google.es/maps/>



Fig. 33: Plataforma Solar de Almería, aerial view.

2.2 Oresol Background

The objective of the *European Research Area (ERA)* is to create a single, borderless market for research, innovation and technology across the EU. It helps countries to be more effective together, by strongly aligning their research policies and programs. In order to make these various policies supporting the development of aerospace applications coherent, the ERA-STAR Regions consortium has been formed to coordinate the efforts of the *regions* with European and national activities, with the objective of bringing together research institutions directly on regional rather than on national level.

In the years 2006 and 2007, the project *AMOR* (Acquisition of Moon Oxygen Resources) was carried out within the ERA-STAR Regions Program of the 6th Framework Programme of the European Commission. Within *AMOR*, institutions and companies from the regions Bremen in Germany and Andalusia in Spain made a preliminary design for an Earth Demonstration Facility (EDF) of a lunar ISRU plant to be built in the south of Spain. The work was divided into the following three “key modules” (Fig. 34):

1. Lunar regolith collection system (OHB, Bremen)
2. Oxygen extraction chamber (PSA/Solúcar, Andalusia)
3. Oxygen post processing system (IFAM, Bremen)

Within a trade-off performed mainly by the subcontracted Spanish *CSIC* from Sevilla, taking into account chemical, thermal as well as mechanical constraints, it was decided that the oxygen extraction process will be based on the reduction of Ilmenite (FeTiO_3) with hydrogen at a temperature of about $T = 1000\text{ }^\circ\text{C}$ using solar heat. The baseline target for the EDF was set to a production of 0.6 kg oxygen per hour (Romberg, Braukhane, Gonzalez-Elipse, Baumeister, & Spenneberg, 2007).

With the goal to continue the work and build the components designed in *AMOR*, a proposal for the ERA-STAR project *DeMoLOP*, (DEmonstration MOdules for Lunar Oxygen Production) was submitted in 2007. The consortium and distribution of the work (excavation, processing,

oxygen storage) were mostly the same as in the *AMOR* project, except that Solúcar did no longer participate.

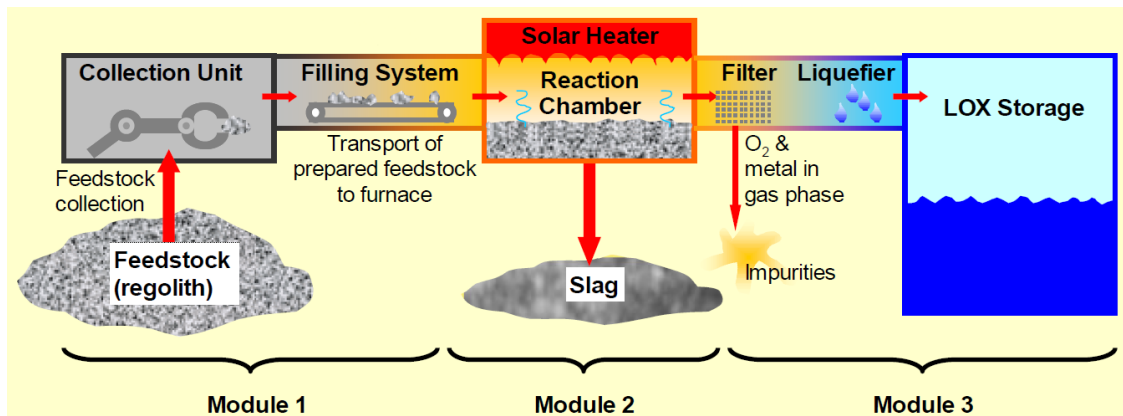


Fig. 34: Block diagram of a lunar oxygen production facility.

The ERA-STAR program does not fund projects directly, but serves to form consortia whose members are then funded by the national research ministries within the framework of sub-("complementary") projects. The sub-project concerning the solar reactor lead by PSA was granted by the Spanish Ministerio de Ciencia e Innovación (ref. ESP2007-29981-E) under the acronym *Oresol* (obtención de Oxígeno a partir de Regolita [sic!]⁵² lunar con Energía SOLar concentrada) (Fig. 35). The planned term of the project was from January 1 to December 31, 2008.



Fig. 35: *Oresol* Logo⁵³.

However, due to changes of key staff at OHB, the other project partners stepped out before the start of the project but after financing commitment, so that there were funds available for the execution of the project at PSA. Since the investigation of the processing step alone seemed promising, it was decided to go ahead with the project. A request to change the project timeframe could not be accepted, as the project was 70% financed by European

⁵² The correct Spanish word for "regolith" is "regolito" (male, ending in "o"). However, since this is a generally unfamiliar word, the (wrong) female form "regolita" (ending in "a") somehow slipped through when the project was applied for.

⁵³ Designed and illustrated by Tanja Denk during her internship in spring 2017.

structural funds. Long story short: At the beginning of 2008 I had available 100000 EUR to be spent within one year, a great project idea, but no partners remaining.

During the official project period in the year 2008, the process and the reactor were designed, and basic components like reactor steel parts, the ceramic inner wall and aperture, five quartz windows, insulation material, support structure material, a cooler, and the original particles separator were acquired. Furthermore, five flow controllers, the electrolyzer, and the particles themselves were purchased. A first, preliminary assembly of the reactor was carried out.

After the end of the official project period, PSA decided to continue the work with internal funding. This meant that only a few thousand Euros per year were available for additional hardware, and also that my working time had to be shared with other projects. Despite, or possibly precisely because of this, the plant was able to mature slowly over the years into a small but almost complete and very capable *chemical factory*.

2.3 Process Selection

One result of the precursor project *AMOR* was that the ilmenite reduction with hydrogen and concentrated solar power was supposed to be the most feasible concept. This was also a great fit with my own expertise in aerospace engineering, concentrated solar power (CSP), and fluidized bed technology. Nevertheless, the most important processes will be compared here once again in retrospect.

- *Polar ice*: Until the LCROSS mission in 2009, this was a rather hypothetical option. But even more than 12 years later, there is still far too little knowledge about the chemical and mechanical properties of the feedstock to build a meaningful demonstrator. And this will not change until the first soft landing by a space probe in the area. Furthermore, there is now so much activity on this topic elsewhere that there remains little to do for me. Design of solar concentrators might be a future contribution.
- *Vapor phase reduction*: Apparently a good process for Concentrated Solar Power, but the required very high temperatures pose huge technical challenges. This starts with the extremely high quality needed for the solar concentrator to overcome the thermal radiation losses associated to the high temperature, continues with the window of the solar reactor that acts itself as a cold trap and therefore must be kept clean somehow, and does not end with the requirement of fast quenching of the product gas and hence no possibility of recovery of some of the sensible heat.
- *Magma Electrolysis*: This concept also requires high temperatures. Furthermore, it works with electricity and therefore it's difficult to see how to operate it with direct concentrated solar power. Protection of a possible window appears problematic.
- *Molten Salt Electrolysis*: This process works at considerably lower temperatures than the magma electrolysis, but also works mainly with electric power and hence is difficult to integrate in a meaningful way into a CSP system. Saving electric power by solar preheating of the regolith and/or the salt might be worth some consideration, but adds complexity to the system. Moreover, this process was not widely known in the lunar ISRU community at that time, I myself became aware of it for the first time in 2015. Nevertheless, the probable need to preheat the regolith to drive out interfering volatile substances (Fereres et al., 2021), or the need to roast Sulphur minerals, or the possibility to modify the process to make it work with regolith molten by concentrated solar power (Schwandt et al., 2012) and in continuous mode could be interesting options for future work.

Ilmenite or glass reduction with hydrogen in a fluidized bed reactor was eventually selected. In hindsight I still think it was the right choice, for the following reasons:

- It's possible to heat a fluidized bed with *concentrated solar power*. If the reactor has a window, even *direct heating* is possible without the need of a heat transfer wall or system. The *operation temperature well below 1000 °C* not only *limits material problems* of the reactor walls but also the radiative losses, and the *good mixing properties of a fluidized bed* help to avoid melting or sintering of the particles due to hot spots in the system.
- The use of hydrogen as reducing agent has the advantage that there is a very *low quantity of involved different elements*, only Fe, H, and O. This leads to less byproducts and especially no solids, simplifying the recovery of the only substance to be brought from Earth, the hydrogen. Its actually disadvantageous high volatility is even a benefit here, since the hydrogen can be driven out of the tailings more easily than other substances such as CaCl_2 . If impurities such as sulfur were present in the raw material, then the possible products of the side reactions (especially H_2S) are volatile in nature and the recovery of the hydrogen shouldn't be too much of a problem. Elemental C, CO or CH_4 as reducing agents might create solid C, SiC or Fe_3C that would be well mixed into the particles and/or form solid deposits in the electrolysis cell and hence be extremely difficult to recover.
- *Continuous operation* is possible. This leads to a significantly better usage of the solar power. Furthermore, this is doable without the need for complex mechanical parts in the hot or dusty environment.
- Due to the presence of trace amounts of water and hydrogen in the regolith, it appears *possible to cover the inevitable hydrogen losses with local material*, thus avoiding the need to replenish consumables from Earth.

Nevertheless, the hydrogen reduction process also has *disadvantages* that shouldn't be swept under the carpet:

- *Low yield*. A lot of regolith has to be moved to achieve a modest amount of oxygen. Nevertheless, excavation systems like RASSOR (Schuler et al., 2019), developed by NASA, have shown the ability to excavate regolith with 1000x of their own mass within less than one lunar day. Even under the most pessimistic assumptions, the payback time (in terms of mass)⁵⁴ should be much shorter than one month⁵⁵. This is much less than what's expected for the reactor (estimated: 6 months).
- *Limited locations* for a lunar outpost. The site selection is driven by the ilmenite or FeO-content of the regolith rather than oxygen production-independent criteria like science requirements of a Moon Base etc.

⁵⁴ The concept of the payback time for process evaluation was already suggested by (Carr, 1963) under the denomination "weight payout time".

⁵⁵ RASSOR prototypes, aiming for a dry mass of 50 kg per unit (presently: 66 kg), have shown during 250 hours of operation the ability to excavate 50 tons of regolith. Even if only 1% (= 500 kg) of oxygen could be extracted from this material, this is still 10x the mass of the excavator during less than one lunar day. For example, a fleet of much less than 80 RASSORs (or up-scaled equivalents) with a total mass of 4 tons could provide the regolith needed to produce the oxygen to fuel one Starship (240 t) for the return trip to Earth every 6 months. And even if this were by a factor of 10 wrong (e.g., due to the need for power supply, thermal management, etc.), the excavation system would be able to provide its own mass in oxygen in still less than one month.

- *Difficulty of the operation of fluidized beds under lunar gravity.* It has to be found out if there is enough useful raw material on the Moon with properties (grain size) on the right side of the Geldart AC-boundary for hydrogen at 950 °C at 1/6 *g*, or alternatively if technical means in the reactor or pretreatment of the regolith can be sufficient to overcome the poor fluidization that has to be expected.

The question of whether it is better to use ilmenite (eq. (1)) or glass (eq. (3)) as a raw material probably cannot (and does not need to) be answered in advance on Earth. Experiments with real lunar stuff will eventually reveal where the best feedstock for hydrogen reduction is located and how it can be processed best on the Moon.

2.4 Goals

The testing campaign of the Oresol plant had four primary goals. They were in order of importance:

1. **Chemistry:** Demonstration of water production from the reaction of the ilmenite with hydrogen.
2. **Temperature:** Operation of the reactor at a minimum of 800 °C, heated exclusively with concentrated solar energy.
3. **Gas Flow:** Identification of the gas flow demand of the main fluidized bed in the reactor as a function of the temperature.
4. **Solids Flow:** Demonstration of continuous particle feed and discharge.

All these goals were achieved. A fifth goal arose late in the tests:

5. **Kinetics:** Gaining basic information about the maximum possible rate of the reaction.

Initial results about this were obtained, but deeper insight is yet to come. The results for all goals are discussed in Chapter 5.

3 The Solar Fluidized Bed Chemical Plant

3.1 General Considerations

3.1.1 Overall Facility Concept

Besides the reactor, a lunar oxygen production plant requires many peripheral components without which it could not function. In order to get an overview of the subtasks required for the solar-powered ilmenite-hydrogen process, a scheme was developed which shows the different components (or tasks) and the material and energy flows between them (Fig. 36).

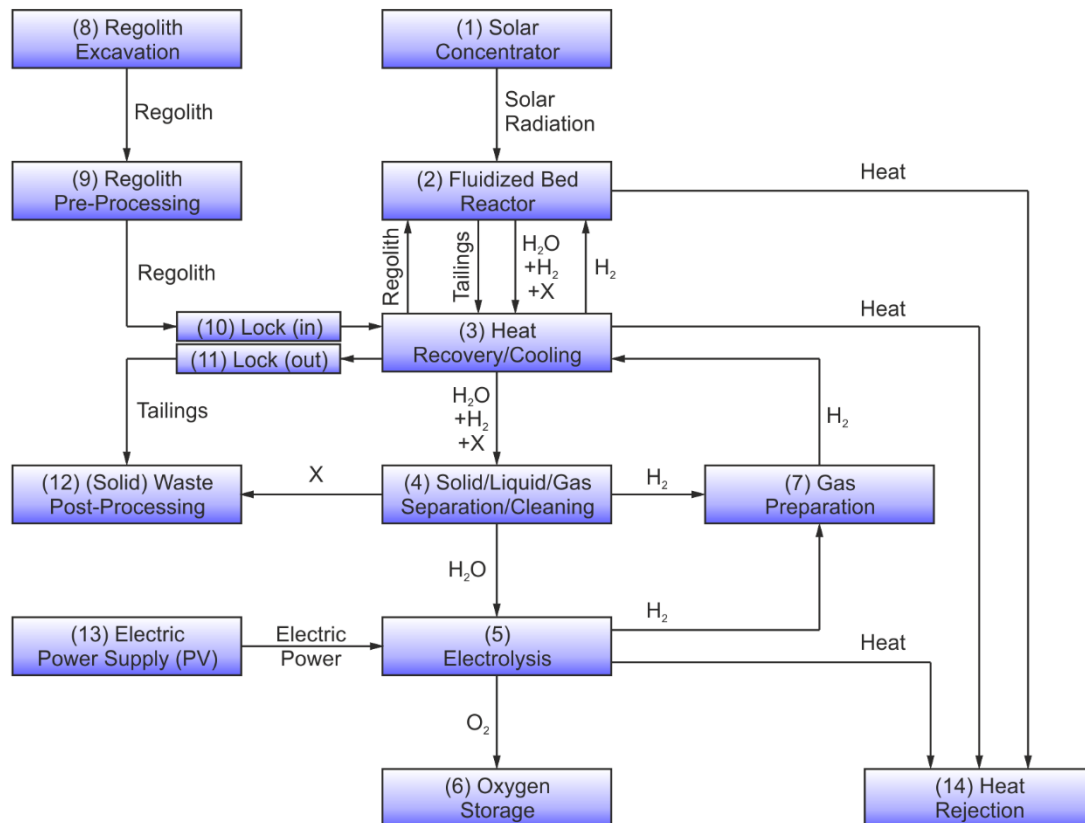


Fig. 36: Schematic overview of the components of a lunar oxygen production facility for the solar powered ilmenite-hydrogen process. For the numbers see explanation in the text.

The centerpiece is the Solar Thermal Reactor (2). The solar radiation energy is coupled in directly via the Solar Concentrator (1). The reactor has one inlet each for the solids (regolith) and one for the reaction gas (hydrogen, H_2). On the outlet side, solids and gas are already mostly separated within the reactor by gravity. Thus, there are also two outlets, one for the (solid) tailings and one for the product gas. The latter contains not only water vapor (H_2O) and excess hydrogen (H_2), but also stray particles and all kind of known and unknown volatile products originating from side reactions, summarized by the letter "X" in Fig. 36. The heat recovery/cooling step (3) is partially optional. For practical reasons (particle-particle heat exchangers are complex devices), in most cases, heat recovery or cooling will probably be limited to the product gas (more about this in Chapter 7.2). If surplus heat is present, it has to be radiated away via a heat rejection system (14). In step (4) the product water is separated from residual gas, residual solids, and the by-products, and also purified, since Electrolysis

requires very clean water (ASTM Type 2)⁵⁶. In practice, the steps (3) and (4) are combined and usually consist of much more than just two components. In Oresol, even without reactants pre-heating and water purification, there are at least five (see chapter 3.9). The electrolysis (5) splits the product water into hydrogen (H_2) and oxygen (O_2). It operates with electrical power generated by a PV system (13). The resulting oxygen, the desired end product, is stored (6), while the hydrogen, together with the recovered gas from step (4), is returned to the reactor. Gas preparation (7) includes mainly flow measuring and metering devices, a pump, pressure control, gas buffering, and chemical analysis.

On the solids side, the lunar feedstock (regolith) is excavated (8) (Just et al., 2020), and then pre-processed (beneficiated) (9). This includes sieving, crushing or other means to achieve a suitable particle size, possibly a gentle grinding to produce "rounder" particles. Furthermore, there can be, as far as feasible and reasonable, the enrichment of ilmenite with the aid of an electrostatic or magnetic separator or other means (Rasera, Cilliers, Lamamy, & Hadler, 2020), and finally the transportation to the reactor plant. Then the processed raw material is introduced into the reactor through a gas lock (10). After processing, the tailings must be continuously removed from the reactor. This also requires a gas lock (11). The tailings can then be carried away and disposed of directly (12). Alternatively, they can be stored in a well-insulated container to serve as a convenient heat source during the lunar night. The development of the necessary gas locks is particularly

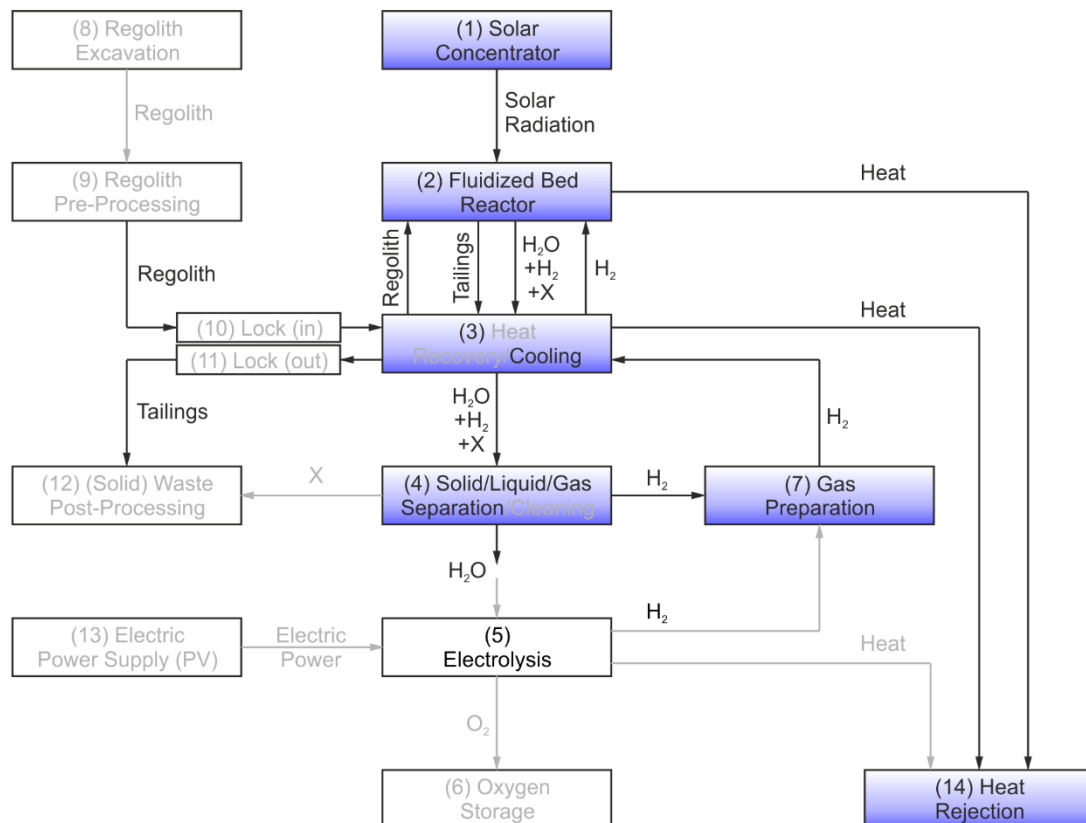


Fig. 37: Schematic overview of the components realized in the Oresol project with the not built or used components grayed out. (5) Electrolysis was partially used.

⁵⁶ The specification for electrical conductivity is $< 1 \mu S/cm$ at $25^\circ C$.

difficult as they must guarantee perfect hydrogen gas tightness despite the presence of very fine dust and the possibly very high temperature, especially at the outlet of the lock (11).

The steps from Fig. 36 *realized in this work* are shown in Fig. 37 with the omitted steps grayed out. Obviously, there was a solar concentrator (1) and a reactor (2), but no heat recovery (3). Cooling was limited to the off-gas, no reactant was pre-heated, and tailings were expelled hot. Solids, liquids and gas were separated from each other (4), but side products were not removed. The electrolyzer (5) wasn't fed from the product water due to the missing cleaning step. Moreover, for economic reasons, it was too small from the beginning. Also, it didn't work well and was eventually replaced by a gas bottle. Hence, there was also no oxygen storage (6). Recirculation of the working gas (7) was included, but not the solids pre- and post-treatment steps (8), (9) and (12). As the system works at atmospheric pressure, no special gas locks (10) and (11) were required. Power (13) came from the public grid, and surplus heat from the reactor and the off-gas was removed by a water cooling system (14). All the components will be described in deep detail in the following chapters.

3.1.2 Material Accumulation and Recovery

Regardless of the chosen process, a special and often sub-estimated problem are the possible by-products from the reaction, summarized by the letter "X" in Fig. 36. This can be e.g. compounds from traces of sulfur ($H_2S...$), or implanted solar wind (He) from the lunar soil. Together with the remaining solids, they must be removed from the product water or gas stream to avoid accumulation in the system and eventually stalling of the process.

The following two rules apply to *all kinds of lunar reactors or processing devices* and are not exclusively limited to the ilmenite process or oxygen production (see also Fig. 38):

- To avoid stalling of the process, substances that originate *from the Moon* must *not accumulate* in the loop. In fact, it is not necessary to keep the loop perfectly free of these substances. The point is that the removal process step is able to maintain them at a low and tolerable level.
- To minimize costly resupply from Earth, substances that are *not from the Moon* must *not be lost*. This means that they must not be found neither in the products nor in the residuals. The required resupply (in terms of mass, incl. spare parts) should be at least two orders of magnitude below the product output.

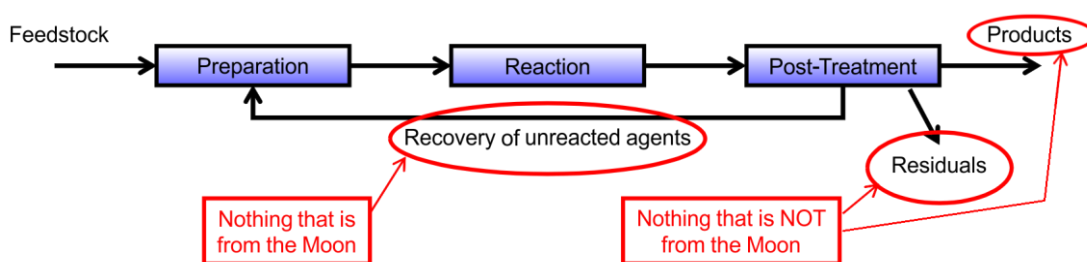


Fig. 38: General scheme of a chemical process with special requirements for operation on the Moon (adapted from (Müller-Erlwein, 2007)).

This means on the one hand that the cleaning steps must work quite well to avoid excessive accumulation of whatever unwanted substances in the system, and on the other hand that no hydrogen (or whatever other working substance the process requires) is allowed to escape through the gas locks or other leaks, even adsorbed, absorbed, or reacted with the tailings. In principle, lost hydrogen (in the case of the ilmenite/hydrogen process) has to be replaced

externally (from Earth), but it might also be possible that traces of water in the lunar regolith are sufficient to cover the losses or at least to alleviate the problem.

3.2 Process

The first step of the process used for the **Terrestrial Demonstrator** built in the Oresol project converts solid *ilmenite* (FeTiO_3 , a mineral from the lunar regolith) with gaseous *hydrogen* into solid *tailings* (the waste) and gaseous *water* (the desired *intermediate product*), see Fig. 39 top and eq. (1) on page 26. This chemical reaction happens within a **fluidized bed reactor** (net reaction volume about 10 liters) at 900 - 950 °C, heated by a beam of **concentrated sunlight**. The fluidization gas is *argon* (the reason will be explained in chapter 3.3.1). The process can be run in fully *continuous mode*. The second step (Fig. 39 bottom) is the conventional water electrolysis.

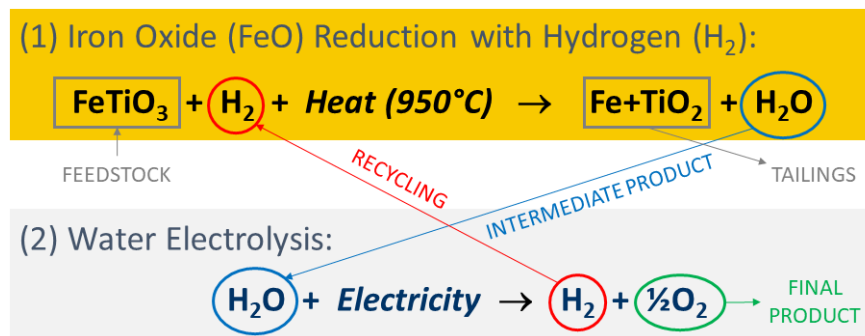


Fig. 39: Chemical reactions and material flows in the Oresol process.

3.2.1 Summarized Description

The process can be roughly broken down into the following sub-loops which converge within the reactor:

- Solids loop (open)
- Gas loop (mostly closed), with the sub-sections
 - Upstream (gas supply), and
 - Downstream (off-gas treatment)
- Hydrogen supply
- Solar power supply

Fig. 40 shows the simplified piping diagram.

The **solids** are manually filled into a hopper (“Moon”). From there, they flow downwards through the *standpipe* and then upwards through the riser (or “*Inpipe*”) into the fluidized bed reactor. Both pipes are fluidized to enable the particle stream. On the opposite side, the reactor has an overflow where the hot particles can leave. From there, they pass without cooling through a fluidized syphon, the so-called “*Outpipe*”, into the tailings container. The reason for the syphon is to avoid the process gas to escape from the reactor through this pipe. It even allows for a small overpressure (a few tens of millibar) within the reactor.

The **gas** loop (drawn in purple in Fig. 40) is mostly, but not completely, closed. Argon is externally supplied from a bottle. This gas is then dosed (flow controller FC01), mixed with the recirculated gas and the fresh hydrogen, and fed into the reactor, where it heats up immediately (within a few centimeters) by contact with the hot particles. The hydrogen reacts with the oxygen from the ilmenite to water. This gaseous water then leaves the reactor

together with the inert argon and (if present) unreacted hydrogen. The design of the gas outlet avoids mostly, but not completely, the entrainment of solids. The off-gas is pre-cooled (Cooler C1), the remaining particles are segregated (Particle Separator PS) and filtered (Filter F3), the gas is further cooled down (Cooler C2) to ambient temperature, and then, in the two-stage Water Separator (WS1 and WS2), the **product water** is separated from the gas stream, extracted from the loop (Pump P3), and stored ("H₂O"). Finally, a system of valves (GV and MV12) purges surplus gas, and the remaining gas is returned by a pump (P1) into the upstream section where its flow is measured (FT07) and it's mixed with fresh argon gas from the external supply before entering again into the reactor.

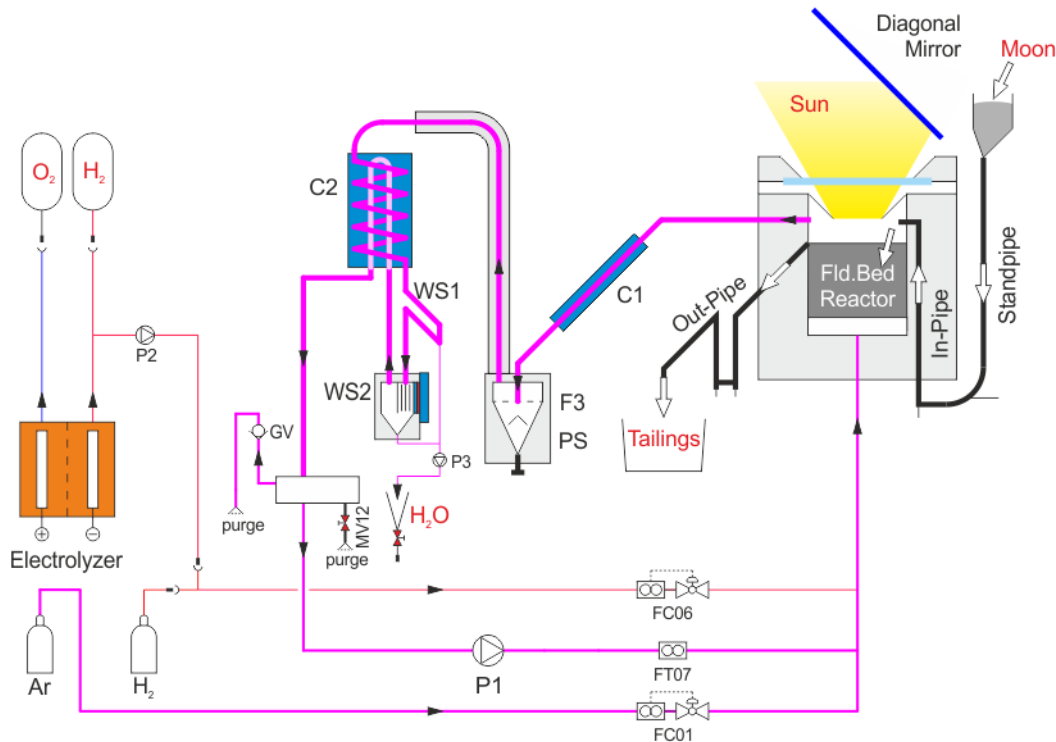


Fig. 40: Simplified Oresol Piping Diagram.

The **hydrogen** supply consists of an electrolyzer, gas storage bags, a pump (P2), and a flow controller (FC06). Alternatively, a gas bottle can be used instead of the electrolyzer. The pure hydrogen is mixed with the recirculated gas and the additional gas from the external supply before entering into the reactor.

The **solar power** ("Sun") enters the reactor from the top through a transparent quartz window. It's adjusted by the shutter of the Solar Furnace and heats directly the particles within the fluidized bed without need of any heat exchangers.

3.2.2 Piping and Instrumentation

While chapter 3.2.1 gave a general overview of the Oresol process, this chapter describes it in detail. Fig. 41 shows the complete piping of the Oresol process and the position of all sensors except most of the 80 thermocouples.

Starting bottom left in Fig. 41, there are two options for external gas supply: argon from a bottle or air from a compressor. The latter one is only intended for engineering pre-tests at temperatures below 400 °C, mainly to avoid the cost of elevated argon consumption. The manual valve MV25 is the main gas feed valve and is closed while the system is not in use. The

pressure of the feed gas is adjusted externally by solar furnace infrastructure and monitored by the pressure transmitter PT06. Then, at point (a), the gas stream is split into the main stream (main bed and window protection) and an auxiliary stream (solids supply and removal).

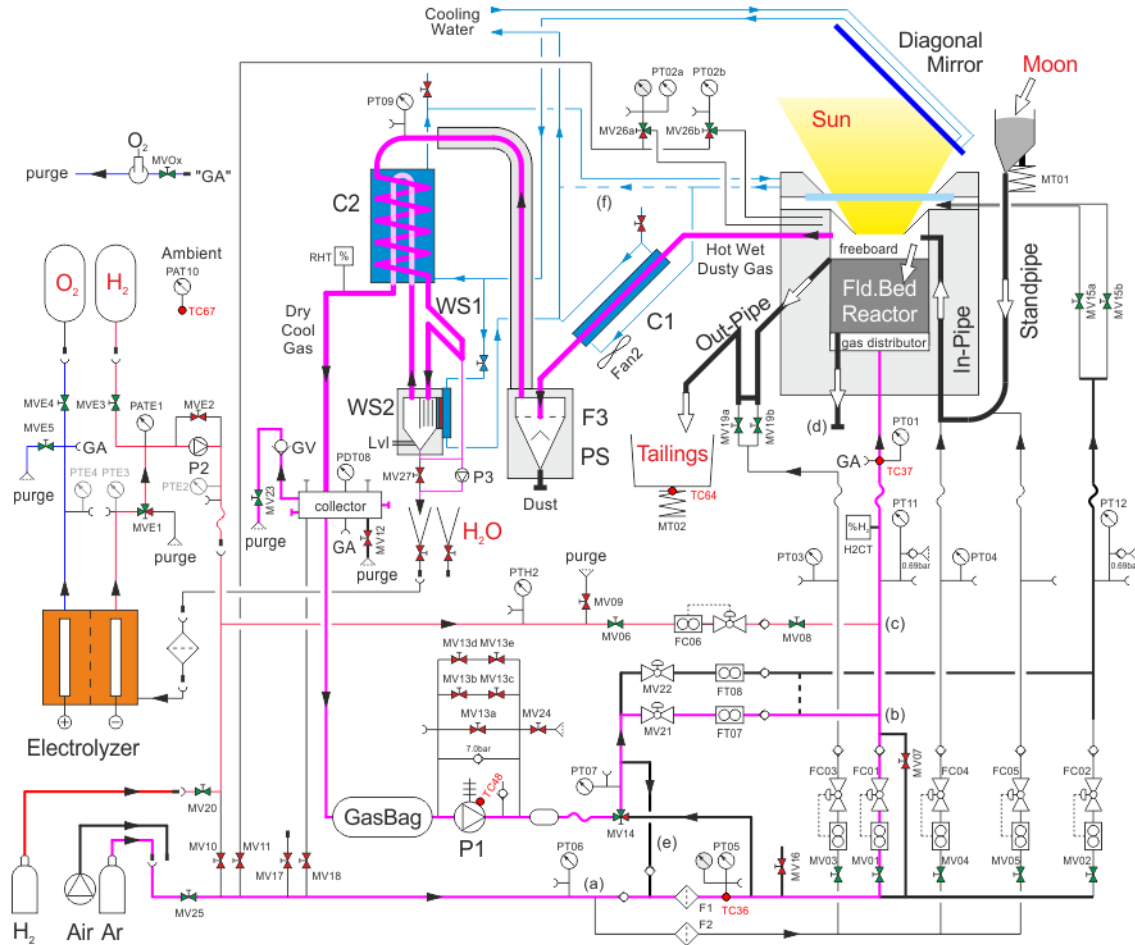


Fig. 41: Oresol Piping and Instrumentation Diagram⁵⁷. The purple lines represent the main gas loop and product water extraction described in chapter 3.2.1. The red lines show the hydrogen supply, the dark blue lines the oxygen pipes, and the light blue lines the cooling water. The thickness gives a hint about the pipe diameter. Valves drawn in red are usually closed during nominal operation, valves in green are (partially or completely) open. Only a handful of thermocouples are shown (red dots), the others can be found in Fig. 43, Fig. 44, and Fig. 45.

In the *main gas stream*, after the filter F1, the pressure is monitored again with the pressure transmitter PT05 and a pressure gauge with dial. MV16 (together with MV17) allows for pressure relief when the system is not operating. Then, the line splits into two branches with flow controllers. FC01 controls the main fluidized bed gas stream and FC02 adjusts the gas stream for the window protection. The pressures after the flow controllers (in the order of well below 100 mbar) are monitored with the pressure transmitters PT01, PT11, and PT12. In the main bed gas line, the manual valve MV07, connected in parallel to the flow controller FC01, allows for very high gas streams beyond the range of FC01 (this is usually only needed when operating with air near ambient temperature). In this case, the pressure drop between PT11

⁵⁷ Abbreviations: FC = Flow Controller, FT = Flow Transmitter, TC = ThermoCouple, PT = Pressure (Relative) Transmitter, PAT = Pressure (Absolute) Transmitter, MT = Mass Transmitter, RHT = Relative Humidity Transmitter, H2CT = Hydrogen Concentration Transmitter, Lvl = Level Sensors, P = Pump, F = Filter, MV = Manual Valve, GV = "Gravity" Valve, GA = Gas Analysis (connection point).

and PT01 is used to calculate the resulting gas flow. At the points (b) resp. (c), the recirculated gas and the hydrogen are mixed into the main gas stream. Finally, a hydrogen sensor H2CT informs about the composition of the reactor feed gas, and the quick connector “GA” allows for the connection of external, more sophisticated gas analysis equipment if desired. The main bed gas stream then enters the gas distributor within the reactor from the bottom and fluidizes the particles. The window protection stream enters at the top of the reactor just below the window through two lines with the manual valves MV15a and MV15b.

The *auxiliary gas stream* passes through the filter F2. Then, the line splits into three branches with the flow controllers for the auxiliary gases. FC03 controls the fluidization of the particle outlet pipe (“Outpipe”), FC04 is for the riser of the particle feed pipe (“Inpipe”), and FC05 doses the fluidization within the standpipe and hence the particle mass flow into the reactor (see chapter 3.7). The pressures in the different lines (in the order of around 100 mbar) are monitored with the pressure transmitters PT03 and PT04. The bellows valves MV19a and MV19b can help to better distribute the gas between the two legs of the Outpipe syphon if needed.

The mass flow of the unreacted *particles* (“Moon”) entering into the reactor is monitored by the strain gauge MT01. In a similar way, the solids that are leaving the reactor (“Tailings”) are continuously weighed by the sensor MT02. In case of maintenance, the reactor can be emptied manually through a pipe at the bottom (d).

In the volume above the surface of the fluidized bed, the so-called *freeboard*, four gas streams are joined: the main bed stream with changed composition due to the chemical reaction, the window protection stream, the fluidization gas of the Inpipe, and about half of the fluidization gas of the Outpipe. The other half, as well as the gas for the standpipe, are vented to the ambient and not recovered.

The *pressure in the reactor* (to be precise: in the freeboard) is monitored by two independent pressure transmitters, PT02a and PT02b (Fig. 42). As this pressure (the average of PT02a and PT02b is usually referred to as “PT02”) is considered to be the most important one in the system for operational and safety reasons, two redundant sensors were implemented. An

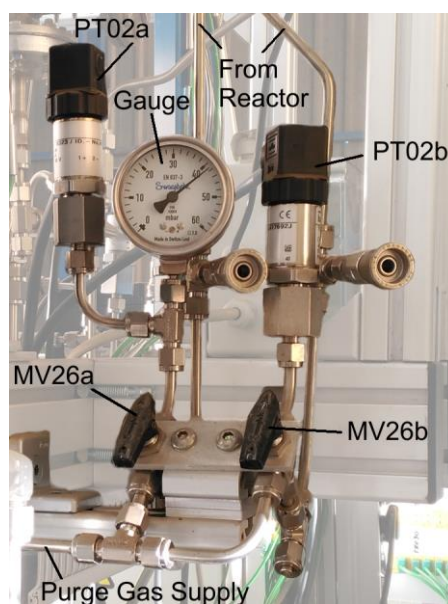


Fig. 42: Sensors for redundant reactor (freeboard) pressure measurement.

additional pressure gauge with dial allows manual adjustment of valves close to the system by an operator without surpassing a maximum reactor pressure. Normally, pipes that are in contact with a particle laden environment should always be installed with a physical inclination upwards to avoid settling of dust on the sensors. In the case of PT02a and PT02b, however, this was not possible because of interference with the concentrated sun beam. Therefore, in case of particle accumulation in the lines, the valves MV11, MV26a and MV26b allow for manual pneumatic cleaning of the pipes if needed.

The *hot, wet, and dusty gas* that leaves the reactor enters into the *downstream section*. The first element there is the Cooler C1, it reduces the off-gas temperature to a value low enough for easy subsequent treatment, but still well above the condensation point of water. The *Particle Separator* (PS) then removes most of the particles from the gas stream by inertia and gravity. The Filter F3 finally eliminates the remaining dust (the so-called “fines”). Due to the working temperature well above 100 °C (and pressure close to ambient), no product water condenses at the bottom of the particle separator. As the flow in the outlet pipe of the particle separator is upwards, it is insulated to avoid premature condensation and thus unwanted water backflow. The pressure transmitter PT09, together with the reactor pressure PT02, allows the continuous assessment of the state of the Filter F3.

The next step is the cooling of the product gas stream down to ambient temperature within the Cooler C2. A mix of gas saturated with water vapor and liquid water leaves this device at the bottom. There, a two-stage *water separator* extracts almost all of the precious water from the gas stream. The first stage (WS1) simply separates the already liquid water by gravity and inertia, while the second stage (WS2) uses a thermoelectric cooler (Peltier element) to further sub-cool the gas about 10 to 15 °C below ambient with the aim to condense most of the remaining water. The small peristaltic Pump P3, turned on and off by three level sensors (Lvl), extracts (valve MV27 is for maintenance only) and meters the water that finally is collected in two so-called Imhoff cones (“H₂O”).

The remaining gas, very cold and still saturated with water steam, leaves the Water Separator WS2 at its top and returns briefly into the Cooler C2, which is now working as a “re-heater”. The gas temperature increases back to mostly ambient, with the desired effect that it is no longer saturated with humidity. The humidity sensor RHT monitors this.

The gas, now mostly dry, cool (ambient) and clean, enters then into a multipurpose collector (“Out-Collector”) with several connections. If the pressure in the loop increases, a *gravity driven check valve* (“GV”) opens slightly to maintain the pressure and vents the surplus gas. If the gas flow is high (causing a too high pressure in the reactor), the manual valve MV12 can be partially or completely opened by the operator. This happens usually at the beginning of any test when the reactor is still cold. The valve MV18 is for maintenance, it allows for reverse flushing and cleaning of the Filter F3 (more about this in chapter 3.9.2). An oxygen sensor can be connected to the “GA”-port. Further ports are available for more sophisticated gas analysis if desired. The pressure at this place is monitored by the differential pressure transmitter PDT08. This sensor allows negative pressure (below ambient) because at the beginning of the project, this was considered a possibility at this point.

The major part of the gas however remains in the loop and flows into a buffer (“GasBag”). This buffer is a flexible gas bag and hence avoids that the pressure can easily fall below ambient. Then, the membrane *Pump P1 recirculates* the gas. Its pumping capacity can be reduced by the short-cut valves MV13a-e, and an adjustable check valve protects it from overpressure above

7.0 bar without venting gas to the ambient. A smaller buffer tank at the outlet dampens somewhat the pressure fluctuations caused by the Pump P1. After the valve MV14, this pressure is monitored by the sensor PT07.

Then, the line splits into two branches with flow transmitters. FT07 measures the gas stream pretended to be mixed into the flow for the main fluidized bed at point (b), and FT08 monitors the gas stream mixed into the branch for the window protection. The manual valves MV21 and MV22 help to correctly distribute the gas. For special purposes (basically when operating experimentally with air at high gas flows and without window), it is possible to quickly modify the plumbing so that both streams enter into the main fluidized bed (dashed line).

The *three-way valve* MV14 allows for operation with or without the Recirculation Pump P1. The latter one happened in particular during the pre-tests with air and is of limited importance. When operating with the Pump P1, the original idea to reduce the recirculated flow was to close partially the manual valves MV21 and MV22. The flow reduction results in an increase of the pressure at PT07. Once this pressure reaches the same value as the pressure from the external gas supply (PT06), the recirculated gas starts to flow also into the flow controllers FC01 and FC02 through line (e). However, after all, this never happened because the flow never was needed to be throttled low enough, and also because later during the tests, the MV13 valves b-e were added to better control the flow rate of the Pump P1 (for reasons and details see chapter 3.10). This made line (e) obsolete, nevertheless it was never removed.

The *electrolyzer* produces hydrogen (H_2) and oxygen (O_2). Both can be stored in separate gas bags. The pressure transmitter PATE1 allows determining when the hydrogen bag is full or empty. (PTE2, PTE3 and PTE4 were originally foreseen for further monitoring purposes but finally not purchased.) The membrane Pump P2 extracts the hydrogen from the gas bag when needed. As an alternative to the electrolyzer, an external hydrogen gas bottle can be used (bottom left in Fig. 41). In this case, the pressure is manually set by a pressure reducer that's part of the Solar Furnace installation, MV20 must be opened, and the pressure is monitored by the pressure transmitter PTH2. The flow controller FC06 sets the quantity of the hydrogen before being mixed into the main bed gas stream at point (c). The valve MV10 allows flushing of the hydrogen pipes for inertization with argon before use. This avoids mixing with atmospheric air and possible formation of an explosive mixture e.g. after a downtime. This argon is purged through MVE2/MVE1, MV09, and FC06.

In the ideal case, the *water* collected in the Imhoff cones can be fed into the electrolyzer. In practice, this water is strongly contaminated and must first be treated (see chapter 5.5.3). In Oresol, this was not done. Instead, the electrolyzer was fed by deionized water from a water treatment plant that's part of the infrastructure of the Plataforma Solar de Almería.

For the overall *mass balance of the gas loop* it's important to see that the main bed and the window protection in principle can be operated solely with the recirculation pump. In this case, the set points of FC01 and FC02 would be zero and all the flow passes through FT07 and FT08. Nevertheless, the auxiliary flows (FC03, FC04, FC05) are not recirculated, they are always fed from outside. The result is that there is always a small net gas inflow into the loop (from half the flow of FC03 and the full flow of FC04). This surplus gas volume finally leaves the loop through the gravity check valve "GV". On the Moon, this gas would also be collected and recycled. The reason why this is not done in Oresol is that this would have required additional flow metering and controlling devices able to work at low pressure, and it was simply considered not worth the additional complexity and to spend the extra money and time for

this. In addition, there is no need for an active pressure control due to the always present net inflow of argon. The hydrogen, at least if fully consumed, does not contribute to the balance, because its reaction product, the water, is mostly completely extracted from the system in equal molar quantity. The case where the hydrogen is not fully consumed will be discussed in chapter 5.5.1.

The water *cooling system* uses an existing installation of the Solar Furnace. The components to be cooled are largely connected in series, as parallel flows are difficult to control without additional costly equipment. The water flows first through the diagonal mirror, then the Cooler C2, then the window flange, and finally the Cooler C1. This cooler (C1) was later converted into an air cooler (Fan2) and therefore disconnected from the cooling water line and shortcut by the dashed line (f). Only the cooling of the Peltier element is connected in parallel. The possible absence of proper flow is detected by the thermocouple TC78 (see Fig. 45 in the next chapter).

A detailed technical description of all elements of Fig. 41 is given in the chapters 3.5 to 3.11.

3.2.3 Temperature Measurement

The Oresol system counts with a total of 80 thermocouples, numbered TC01 to TC80. The first 30 of them are within the reactor vessel of which 18 are located directly in the fluidized bed. 15 of them (TC01-TC15) are distributed evenly over the bed in three levels of five each (see Fig. 43 and Table 3), and another three measure the temperature close to the bottom (TC20) and to the surface (TC24+25) of the bed.

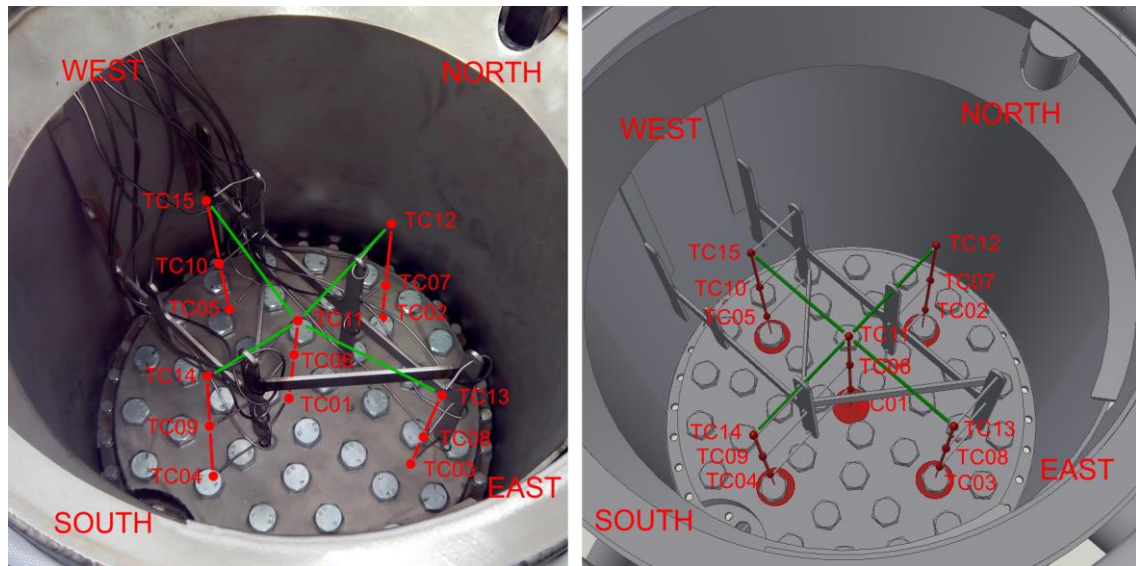


Fig. 43: Thermocouples (red dots) within the fluidized bed. Left: photo, right: CAD drawing. They are arranged in three “levels” (Bottom, Middle, Top) and five “columns” with the shape of a cross (Center, North, East, South, West). The columns are marked by red lines (including “footprints” at the bottom of the reactor in the CAD drawing), and the top level cross is drawn in green (middle and bottom crosses are omitted for clarity of the drawing).

The remaining 12 thermocouples within the reactor housing (see Table 3 and Fig. 44) measure the temperature of the inside (TC16-19) and the outside (TC21-23+26) of the aperture cone (see chapter 3.5.2), and the inside of the window flange (TC27-30).

Location	Center	North	East	South	West
Fluidized Bed – Bottom	TC01	TC02	TC03	TC04	TC05
Fluidized Bed – Middle	TC06	TC07	TC08	TC09	TC10
Fluidized Bed – Top	TC11	TC12	TC13	TC14	TC15
Inner Cone	-	TC16	TC17	TC18	TC19
Outer Cone	-	TC21	TC22	TC23	TC26
Flange Inside	-	TC27	TC28	TC29	TC30
Flange Outside	-	TC49	TC50	TC51	TC52
Wall Outside	-	TC53	TC54	TC55	TC56

Table 3: Numbering of the thermocouples arranged according to the "cross" system.

For TC01-TC15 see Fig. 43, for TC16 ff. see Fig. 44.

The locations of the temperature sensors outside but in the close vicinity of the fluidized bed are also shown in Fig. 44. The temperature of the feed gas within the gas distributor (see chapter 3.5.4) is measured by TC31+32. Further upstream, TC37 is installed together with the pressure transmitter PT01, and TC36 with PT05 (see Fig. 41). The outside of the window flange is monitored by TC49-52, and the outside of the reactor wall by TC53-56. All thermocouples "groups of four" are distributed following the north-east-south-west pattern (Table 3).

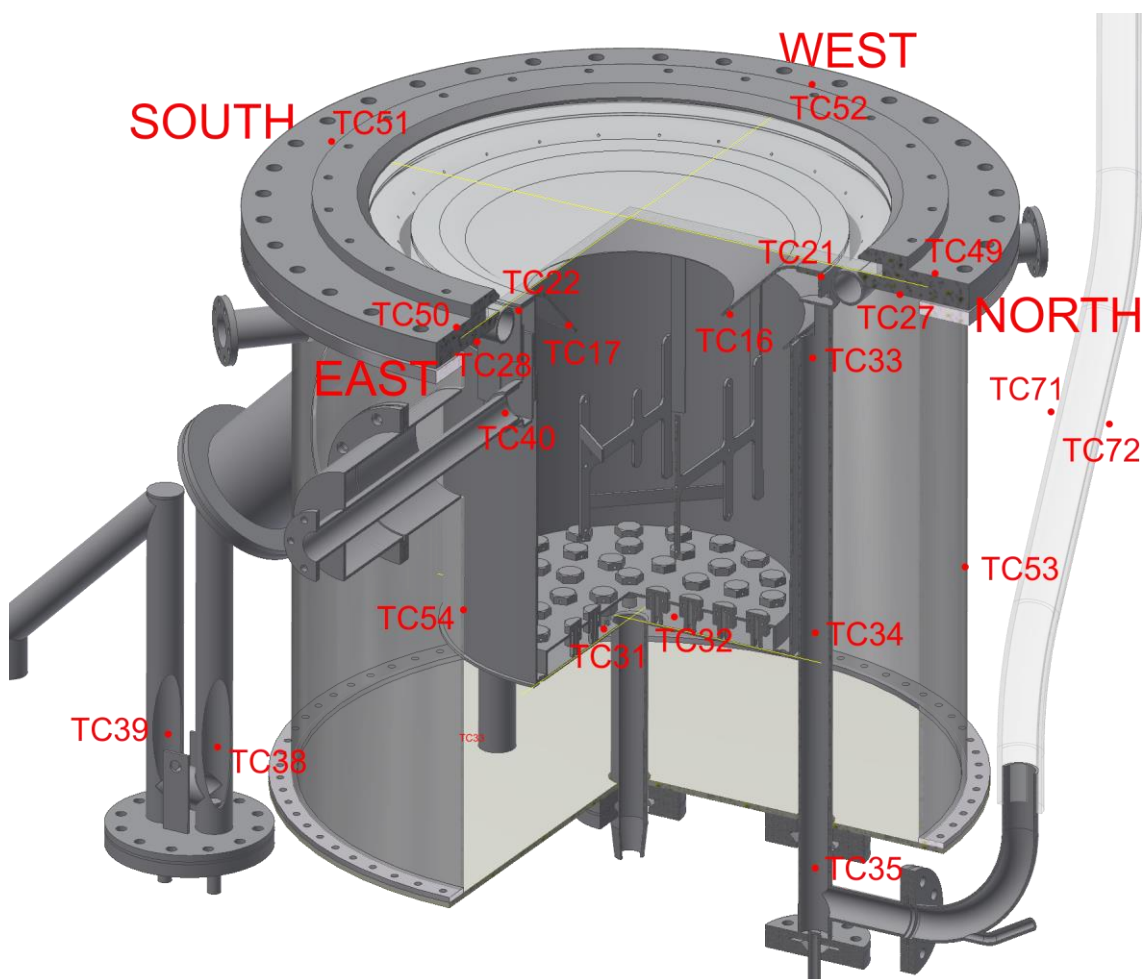


Fig. 44: Location of the thermocouples in the close vicinity of the reaction zone.

A total of 8 thermocouples are installed in the solids loop. TC35, TC34, and TC33 give information about the heat-up of the particles in the Inpipe when they flow from the bottom to the top, and TC38 and TC39 are installed in each branch of the Outpipe syphon. TC64 measures the temperature under the particle collector pot (see Fig. 41), while TC71 and TC72 monitor the temperature on the outside of the standpipe. The latter one has a certain importance because it's possible that this pipe receives (non-concentrated) solar radiation and/or residual heat from the reactor housing.

The thermocouples TC40-45, 48, and 57-63 are installed in the downstream section (see red dots in Fig. 45). Following the flow of the off-gas, TC40 measures the temperature of the gas in the pipe still inside the reactor housing (therefore also drawn in Fig. 44), TC41 at the entrance of the Cooler C1, and TC42 at the exit. TC43 measures at the bottom of the Particle Separator (PS), and TC44 at its outlet. TC43 is of special importance, because it informs when unwanted water condensation can occur at this place. Further downstream, the temperature drop in the Cooler C2 is measured by TC57 (inlet) and TC58 (outlet). The subsequent water separator has three thermocouples. TC59 and 63 measure the temperature at the internal heat exchanger

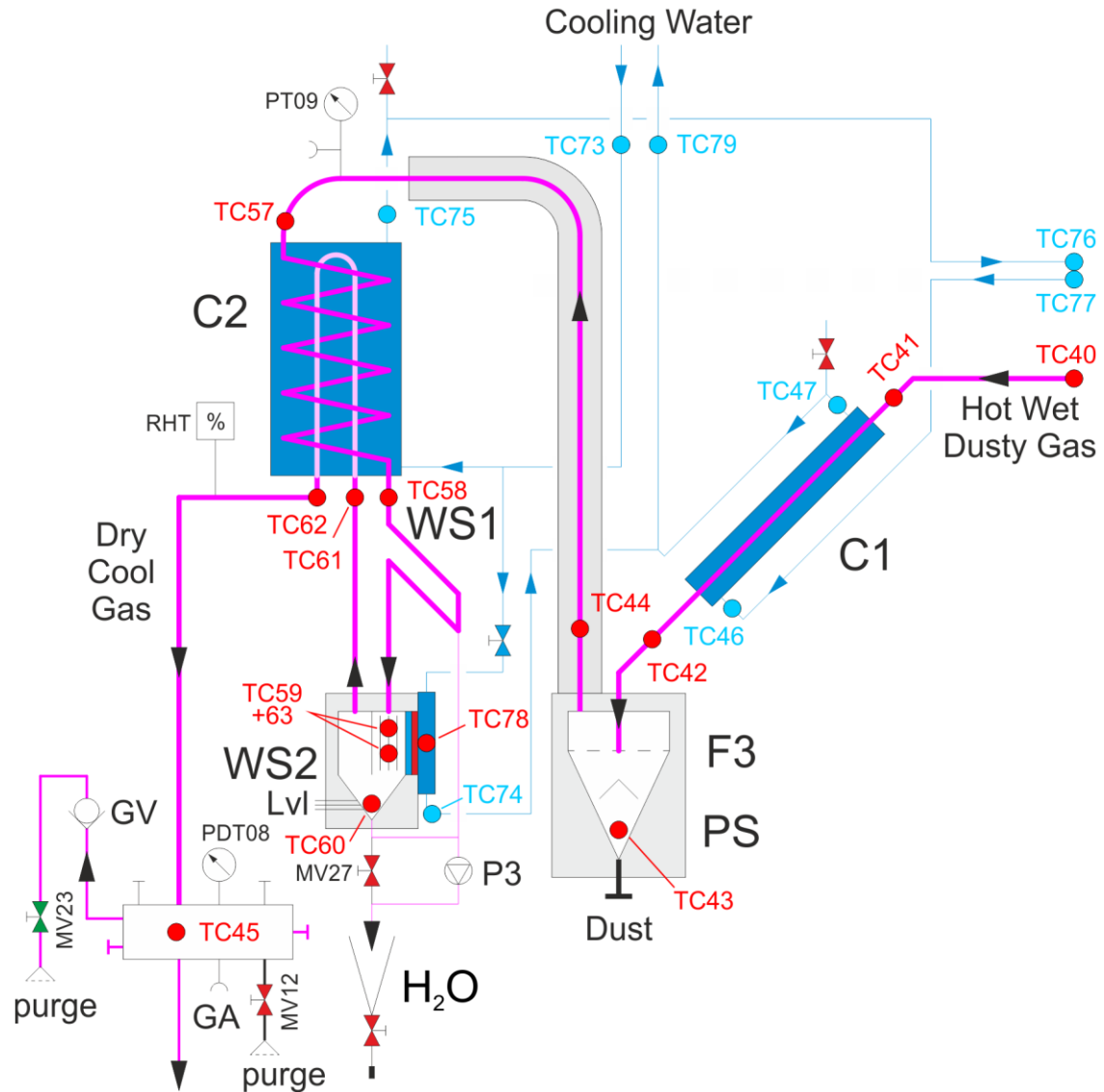


Fig. 45: Location of the thermocouples in the downstream section (red) and in the cooling water (blue).

fins. They are redundant to make sure that freezing of the product water is reliably prevented. TC60 measures the temperature at the bottom of the water collector of the water separator. Then, TC61 (inlet) and TC62 (outlet) measure the temperature increase in the re-heater section of the Cooler C2. Finally, TC45 is installed inside the “Out-Collector” tube close to the “Gravity-Valve”, and TC48 monitors the cylinder head of P1 (see Fig. 41).

The temperatures in the cooling water (see blue dots in Fig. 45) are monitored by TC73 (main feed in), TC75 (Cooler 2 out), TC76+77 (window flange in+out), TC46+47 (Cooler 1 in+out), TC74 (TEC out), TC78 (copper heat exchanger of the TEC), and TC79 (main feed out). After the modification of the Cooler 1 (see chapter 3.9.1), TC46+47 will be repurposed to measure the temperature of the cooling air.

The thermocouples TC65 and TC66 measure the temperature within the electronic boxes. Especially during operation in summer, these boxes have to be opened to avoid overheating of some electronics parts when the temperature exceeds 40 °C. TC67, together with the pressure transmitter PAT10, is used to determine the ambient conditions. The thermocouples TC68-TC70 and TC80 are multi-purpose (“joker”) sensors. They are used flexibly at places where a special interest for the temperature exists, like the inner surface of the radiation shield, the high temperature seal at the off-gas exit of the reactor, the seal of the particle separator, the particles coming out of the reactor, and so on.

3.2.4 Basic Design Parameters

Basis for the initial requirements for the system design was the “MoonROx Challenge”, part of the NASA Centennial Challenges program. This is a program that intends to directly engage the public in the process of advanced technology development offering prizes to generate solutions to problems of interest to NASA. There was never a plan to participate, because several of the participation conditions made it impossible (e.g., the demonstration had to be done at a location in the United States). But the challenge gave valuable hints for the dimensioning of the system. The central requirement was the production of 2.5 kg of oxygen in 4 hours (NASA, 2007). In addition, the [electric] power consumption should not exceed 10 kW and the overall system mass had to stay below 50 kg. While it is easy to meet the electric power requirement when using concentrated solar energy, the system mass requirement is hopeless from the beginning. Nobody was able to come even close, and hence the challenge was closed with no winner.

The oxygen production requirement is equivalent to a plant capacity of 700 g of water within one hour. This value was adopted for Oresol, but all the time only considered orienting, since the main goal of the project was in the first place to demonstrate the fact in itself that oxygen in the form of water can be extracted from ilmenite with concentrated solar power in whatever meaningful amount.

3.2.5 Operation Parameters

During operation, many system parameters have to be monitored or controlled. The variables in the following list *can be actively adjusted* by setting directly themselves or by adequately adjusting a related actuator. Except when specifically mentioned, this is done remotely from the data acquisition and control program (more about this in chapter 3.14):

- **Reactor temperature:** Measured by TC01-TC15. Probably the most important parameter, and finally a question of power balance. During stationary operation, *energy sinks* are mainly thermal radiation losses through the window, feed gas

heating, and particle feed heating. The sole *energy source* is the incoming solar radiation. Before entering the Solar Furnace (on Earth), this radiation (expressed as DNI = direct normal irradiation) depends mainly on the weather and also to some extent on the elevation of the Sun in the sky. In the solar furnace, the minor weather influences (thin clouds etc.) can be eliminated very well with the help of the shutter. The reactor temperature remains constant when the incoming power equals the sinks. The temperature *control* is done manually by the operator, because the Oresol control program never achieved permission for remote control of the set point of the shutter in the control program of the Solar Furnace. The response of the bed temperature to changing conditions is quite slow (in the order of one to several minutes) due to the rather high mass (better: thermal inertia) of the particles. Therefore, keeping the temperature constant at a desired value requires certain experience of the operator.

- **Main bed gas flow⁵⁸:** There must be enough flow to guarantee a vivid mixing of the particles in the bed, but not too much in order to avoid excessive entrainment of the particles. The flow usually has to follow a pre-programmed pattern in function of the fluidized bed temperature (inversely proportional to the absolute temperature; more about this in chapter 5.1). It comes from four sources: FC01 (argon), FC06 (hydrogen), FT07 (recirculated gas), and MV07 (high flow valve). As FC01 is the only remote controlled element of them, it is programmed to adjust the flow in a way that the overall flow (sum of all four) meets the requirement. The main bed gas flow is the second most important parameter of the system after the reactor temperature.
- **Window protection gas flow:** There is no hard criterion for the set point. Somewhat arbitrarily, it was usually chosen to $\frac{1}{4}$ of the main bed gas flow, but not lower than 10 l_n/min. This flow comes from two sources: FC02 (argon) and FT08 (recirculated gas). Similar to the main bed flow, FC02 controls the overall stream taking into account the measured data from FT08.
- **Outpipe gas flow:** This flow must guarantee proper fluidization of the particles in this pipe. The set point of FC03 is set automatically in function of the lower one of the two temperatures in the syphon (TC38, TC39). The proper gas distribution between the two legs was done manually in a pre-test with the valves MV19a and MV19b.
- **Inpipe gas flow:** In the same manner as the Outpipe flow, the Inpipe gas flow is set automatically in function of the lowest one of the temperatures in the riser (TC33, TC34, TC35).
- **Particle feed:** This flow is *measured* by the change of the strain gauge MT01 and *controlled* by the partial fluidization of the standpipe by the flow controller FC05. As the trial of a determination of a direct relation between the particle flow and the gas flow failed, the control is done by an automated adjustment of the gas flow every three minutes in order to get the particle flow as close as possible to the set point. More about this in chapter 3.7 and 3.14.
- **Recirculated gas flow:** The Pump P1 can be turned ON and OFF from the control computer, but the flow cannot be adjusted remotely. Instead, the four manual short cut valves MV13b-MV13e are used. MV13b and MV13d are ball valves with the positions open/closed, while MV13c and MV13e are adjustable bellows valves. Once the bellows valves are pre-set, three different flows can be chosen in a rapid and repeatable way by simply opening or closing of the ball valves. The valves can be accessed by the operator without interruption of the solar operation. (The valve

⁵⁸ About units and conversions see Appendix A.2.

MV13a is only opened when turning on the Pump P1 to avoid a sudden surge of the gas flow in the main fluidized bed.) The distribution of the recirculated gas between the main bed (FT07) and the window (FT08) was manually set to about 2.5:1 by partial closing of the manual valve MV22.

- **Water extraction pump:** This Pump P3 is switched on automatically when the water level sensors in the lower part of the water separator indicate that the water level has risen, and off again when it has fallen.
- **Thermoelectric cooler (TEC):** Once switched on manually from the control computer, it usually remains ON all the time. There are two exceptions. When operating in winter at cold ambient conditions and low gas flow, it is possible that the temperature of the water separator (the lower value of TC59 and TC63) comes close to 0 °C. To avoid the formation of frost in the water separator, the cooler is automatically turned off below 3 °C and turned on again at 4 °C. The other exception is when the temperature of the hot side of the TEC becomes too high (TC78 > 45 °C). This indicates some kind of failure of the cooling water system and requires the immediate shut off of the TEC to avoid damage.
- **Electrolyzer:** The electrolyzer is turned off remotely when the pressure sensor PATE1 detects a strong rise. This indicates that the hydrogen gas bag is full. On the other hand, when this sensor detects a strong pressure drop, the bag is empty and the Pump P2 is turned off. This control is inactive when the hydrogen is supplied from a bottle.
- **Hydrogen share:** The flow controller FC06 adjusts the hydrogen flow into the main fluidized bed. It can be set a fixed value (in l_n/min) or a fraction (in %) of the main bed gas flow (the remainder is argon). When operating with the electrolyzer as hydrogen source, FC06 sets to zero when the Pump P2 turns off, and vice versa: when FC06 is set zero, P2 switches off.
- **Cooler 1 temperature:** Originally designed as a water cooler, in autumn 2018 the Cooler-1 was converted into an air cooler (more about this in chapter 3.9.1) to allow for control of the gas outlet temperature and reduced heat-up time of the subsequent particle separator. When a certain temperature is exceeded (usually TC42 > 300 °C), the fan F2 is switched on. Once below 290 °C, it turns off again. The final purpose of this control is to keep the temperature of the particle separator (TC43 and TC44) well above 100 °C to avoid condensation of water at this place.

The following parameters *cannot be actively adjusted*, or only in a limited way. In case they leave their safe range, the operation must be suspended.

- **Reactor pressure:** The third most important parameter after reactor temperature and gas flow. Measured by PT02a and PT02b. This is the pressure in the volume above the fluidized bed (the “freeboard”). It depends on the pressure drop in the different components of the downstream section, in particular the Filter F3, and the gas purge through the “gravity valve” GV and the purge valve MV12. Comparing the data of PT02, PT09 and PDT08 allows for easy distinguishing between the two cases (filter vs. GValve). In case of high gas flow, the valve MV12 can be manually opened (partial or entirely) to relieve pressure from the reactor. This is a standard procedure during start up. But if the reason for high reactor pressure is a clogged Filter F3, then there is no further way to reduce it. This becomes a problem if the Filter F3 gets clogged too fast. More about this in chapter 5.4.
- **Pump P1 intake pressure:** Because of the gas bag, the pressure at the Pump P1 intake cannot fall easily below atmospheric pressure (relative pressure = zero). This is

monitored with the pressure transmitter PDT08. The drop of this value below 3 mbar triggers an alarm, and the operator has to decide rapidly what to do. In the best case, this can be a slight manual adjustment of some valves (usually closing MV12). In the worst case, this means the suspension of the operation by defocusing the heliostat and stopping the Pump P1 before the gas bag becomes empty within about 20-30s.

- **Solids outflow:** Measured by the change of the strain gauge MT02. In theory, this value should be almost the same as the solids inflow. Nevertheless, in practice, differences in the balance of more than 1 kg were often observed. The reason is not completely clear, but it is believed that, even if there is no inflow, that particles spout into the Outpipe and therefore the bed level drops slowly with time. When starting inflow, this has to be refilled first before a substantial outflow will be detected. Nevertheless, a mismatch between MT01 and MT02 can also be an indicator of clogging of the Outpipe. If no measures are taken, the reactor can be overfilled and the particles would then flood the downstream section. However, that never happened during Oresol operation.
- **Argon bottle pressure:** This pressure is calculated by integration of the argon inflow into the system. If it becomes low, a new argon bottle has to be used. Fortunately, the argon supply system of the Solar Furnace allows for “hot-swap”, this means bottle exchange can be done without interruption of the supply. With an available stock of up to four bottles, it never happened that a test had to be suspended due to argon shortage.

3.3 Feedstock

3.3.1 Gas

The gas supply of a fluidized bed reactor has two purposes. On the one hand it serves to fluidize the solids, on the other hand it is a partner in the chemical reaction. For the first task, a certain *gas velocity* is necessary, while the second task requires a certain *molar (or mass) flow*. The two requirements can be brought into agreement by a suitable choice of the reactor cross-section (for more details see chapter 1.4.4). If possible and necessary, the operating pressure can also be appropriately chosen (this option was not available in the Oresol experiment).

Originally, operation in Oresol was planned with pure hydrogen. This was rejected very quickly, because safety concerns came up. Instead, argon with a limited amount of H₂ is used (Fig. 46). For this purpose, a bottle with a mix of 95% Ar and 5% H₂ was purchased, as 5% was considered a safe fraction. However, this bottle was never used. Instead, argon and pure hydrogen are metered individually and mixed together in the upstream section of the system (see chapter 3.6). This way, the hydrogen fraction in the gas can be freely adjusted as needed.

Argon was chosen over nitrogen for two reasons. The first was to avoid possible chemical reactions of the nitrogen at high temperatures with whatever component in the reactor, the solid feedstock, or the gas. The other one was to allow control for leaks. Detection of nitrogen would be a sign that some atmospheric air is remaining or somehow entering into the reactor, containing also oxygen that would increase the water production of the reactor and therefore distort the results.

Furthermore, especially for technical pre-tests at the beginning, air from a compressor was also used for fluidization (Fig. 46 top left).

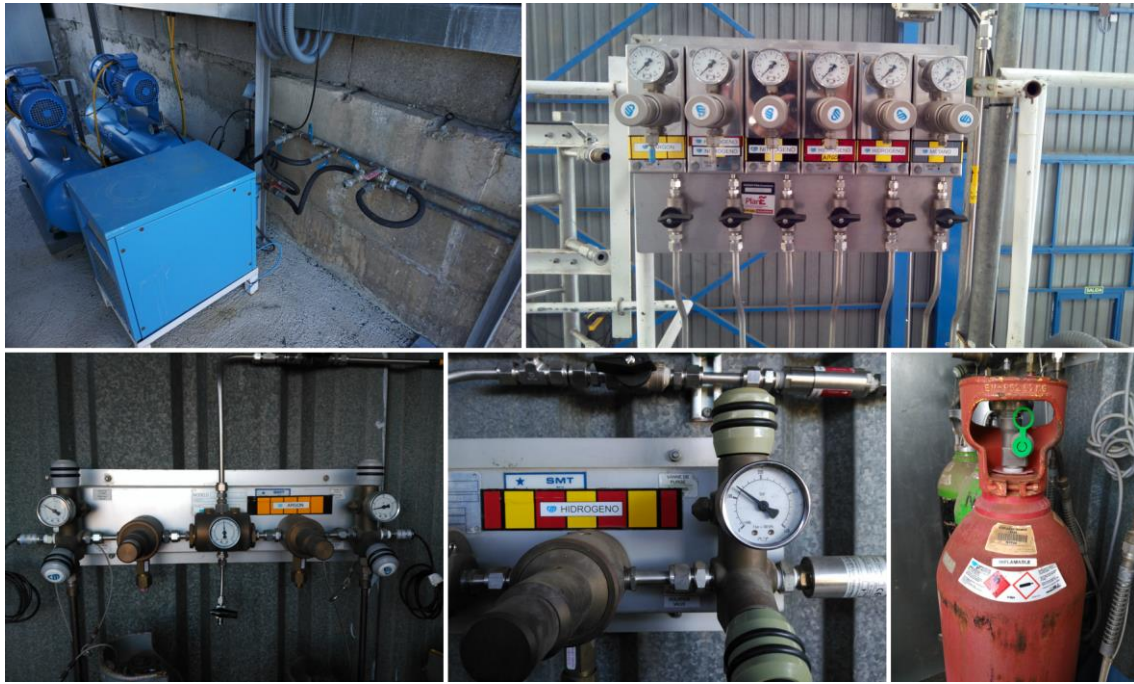


Fig. 46: Gas supply installation of the Solar Furnace. Top left: Air compressor. Bottom left: Argon supply with “hot-swap” valve for change of the bottle without interruption of the operation. Bottom center and right: Hydrogen supply. Top right: Panel for gas distribution and pressure adjustment close to the test platform.

3.3.2 Particles

For obvious reasons, at the present time, it is not possible to carry out the experiments with real lunar material at an Oresol-like scale (dozens of kilograms). Therefore, so-called *lunar soil simulants* are offered by various manufacturers. An overview can be found in (Taylor, 2015) or in the online database (Colorado School of Mines, 2021). One of the most famous ones is the NASA-produced JSC-1A (Fig. 47). It has a broad particle size distribution from a few microns to over 1 mm. The density is $\rho_s = 2900 \text{ kg/m}^3$. Fluidized with air at ambient temperature, unscreened, and under terrestrial gravity, it belongs to the Geldart group C. Screening to between $32 \text{ }\mu\text{m}$ and $315 \text{ }\mu\text{m}$ recovers about 60% of the material and shifts it to the Geldart Group A (see blue and red line in Fig. 31 on page 57). The absorption coefficient is about 0.7. For the Oresol project, 101 kg were purchased. However, this material is a simulant for Ti-poor lunar highland soil with a TiO_2 content of only 1-2%. This makes it suitable for studying the fluidizability of lunar dust in general (see Fig. 111 on page 139) and of screened particle size fractions, but not for hydrogen reduction.

For this purpose, the company Tioxide from Huelva (Spain) kindly provided us with a metric ton of pure ilmenite (Fig. 48). The material originates from the company Kenmare Moma Processing Ltd. in Moma (Mozambique). It normally serves as raw material for titanium dioxide pigment manufacturing and for synthetic rutile and titanium slag production. The ilmenite has a relatively narrow particle size range around $d_p = 150 \text{ }\mu\text{m}$ and a grain density of $\rho_s = 4300 - 4600 \text{ kg/m}^3$ (bulk density $2400 - 2700 \text{ kg/m}^3$). The sphericity of the particles was determined to $\phi_s = 0.66$ and the void fraction to $\varepsilon_{mf} = 0.48$. This material clearly behaves like particles belonging to the Geldart group B (see green dot in Fig. 31 on page 57). Its absorption coefficient is about 0.8. So far, only this ilmenite has been used in the Oresol solar experiments. Since tests with other grain sizes are planned for the future, this material is often referred to as “Ilmenite-150” in this text.



Fig. 47: JSC-1A Lunar Soil Simulant.



Fig. 48: Kenmare Moma Ilmenite, grain size 150 µm. Left: In the storage box. Right: Magnified.

3.4 Solar Concentrator

From the beginning, the Oresol reactor was designed for operation in the large solar furnace of the PSA, the SF-60 (Rodriguez, Cañadas, Monterreal, Enrique, & Galindo, 2019). This solar furnace (Fig. 49) consists of a rectangular, flat heliostat with a surface of 130 m² on the outside. It reflects the sunlight into a large hall with an attenuator (“shutter”) at the north side, a fix, parabolic concentrator with a 100 m² mirror surface at the south end, and a test platform at a height of four meters from the floor in the middle. The optical axis is 6.123 m above the ground. On this test platform, the Oresol (or any other) experiment is placed during the tests.



Fig. 49: Solar Furnace SF-60 of the Plataforma Solar de Almería. Left: View from outside. Right: View from inside. (1) Heliostat. (2) Shutter. (3) Concentrator. (4) Test platform with Oresol reactor. (5) Diagonal mirror. For a schematic view see Fig. 25 left on page 48.

Since the reactor requires a vertical beam, there is a water cooled, 45° inclined "diagonal" or "redirection" mirror located 50 cm in front of the focal plane, which deflects the beam 90 degrees down. Originally, for Oresol, there was constructed a rectangular, 1.4 m by 1.0 m sized, thin mirror with an air cooling system (Fig. 50 top). But during the reconstruction of the testing platform of the Solar Furnace (more about this see chapter 3.12), a slightly smaller (1.2 m x 0.8 m), heavy, water cooled diagonal mirror was built by the Solar Furnace team (Fig. 50 bottom). Despite the smaller size, this mirror since was always used in the Oresol test runs, because the water cooling promised to be safer than the air cooling.



Fig. 50: Diagonal Mirrors of the Oresol project.

Top: Air cooled. Bottom: Water cooled. Left: Oblique front view. Right: Oblique rear view.

The test platform provides all required consumables. Those are pressurized air, argon, and hydrogen with adjustable pressure up to 10 bar, alternating (230 V) and three-phase (400 V) current, cooling water (up to 1.8 m³/h), observation and thermal cameras, data connections (Ethernet), and easy access for operation and maintenance.

The active part of the operation is performed by two components, the heliostat and the shutter. The heliostat automatically tracks the (calculated) position of the Sun in the sky, with

the normal vector of the mirror being the bisector between the solar vector and the horizontal coordinate axis pointing south (northern hemisphere!). Manual fine adjustment ("offset correction") is possible and is also usually done several times a day. The required power is then adjusted gradually by the opening angle of the shutter. The latter is done manually by the operator during operation.

3.5 Reactor

The reactor (Fig. 51) is the heart of the Oresol test facility. It is a fluidized bed reactor which is operated in stationary, isothermal and fully continuous mode. It produces water (H₂O) from the heterogeneous gas-solid reaction of hydrogen with ilmenite. Its nominal operating temperature is between 900 and 950 °C.

It has the shape of a short, vertical cylinder with internal insulation, and flanges welded to both ends. The overall outer dimensions (without connectors and legs) are a maximum diameter of 550 mm (window flange) and a height of about 460 mm (including gaskets). The outer wall of the cylinder is made of 4 mm thick stainless steel EN 1.4301 (AISI 304) with an outer diameter of 478 mm. The flat base plate on the bottom and the window flange on the top are screwed onto the flanges. An inner cylinder with an inner diameter of 260 mm and a height of 240 mm is the recipient for the particles. The filling height is about 175 to 180 mm, which results in a net reaction volume of 9.5 dm³ or a particle capacity (ilmenite-150) of about 22 kg.

The reactor has the following connections to the outside. The numbers in parenthesis refer to the numbering in Fig. 51 and the numbers with asterisk to Fig. 53 on page 89:

- Base plate:
 - Main gas supply for the fluidized bed (*1)
 - Particle supply (for continuous operation) (*2)
 - Particle drain (for maintenance) (*3)
- Cylinder circumference (middle):
 - Particle removal (for continuous operation) (1)
 - W-Rh (type C) thermocouple (not used) (2)
- Cylinder circumference (top):
 - Off-gas outlet (3)
 - 2x Window protection gas (4)
 - 2x Reactor pressure measurement (5)
 - 30x NiCr-Ni (type K) Thermocouples (6)

The energy source is the beam of concentrated solar radiation entering vertically from above through an opening with a diameter of 370 mm into the interior of the reactor. There it hits and heats the surface of the fluidized bed directly and without the need for further components such as heat exchangers or similar. The excellent mixing properties of the fluidized bed, especially in the vertical direction, ensure a fast and even distribution of the heat within the reactor. The opening is covered by a transparent quartz window.

Most parts of the reactor were manufactured by the company Imecal S.A.⁵⁹ in Valencia (Spain). Stainless steel 1.4301 (AISI 304) is the primary material grade. The pieces in the hot area are mostly made of Inconel-600, a nickel-chromium alloy suited to service in high temperature

⁵⁹ <https://www.imecal.com/>

environments. To keep the cost low, standardized dimensions of the Inconel pieces were used. All Inconel sheets are 2 mm thick, and all tubes have an outer diameter of 27.6 mm and a wall thickness of 2.0 mm. The original technical drawings can be found in the Appendix A.4.

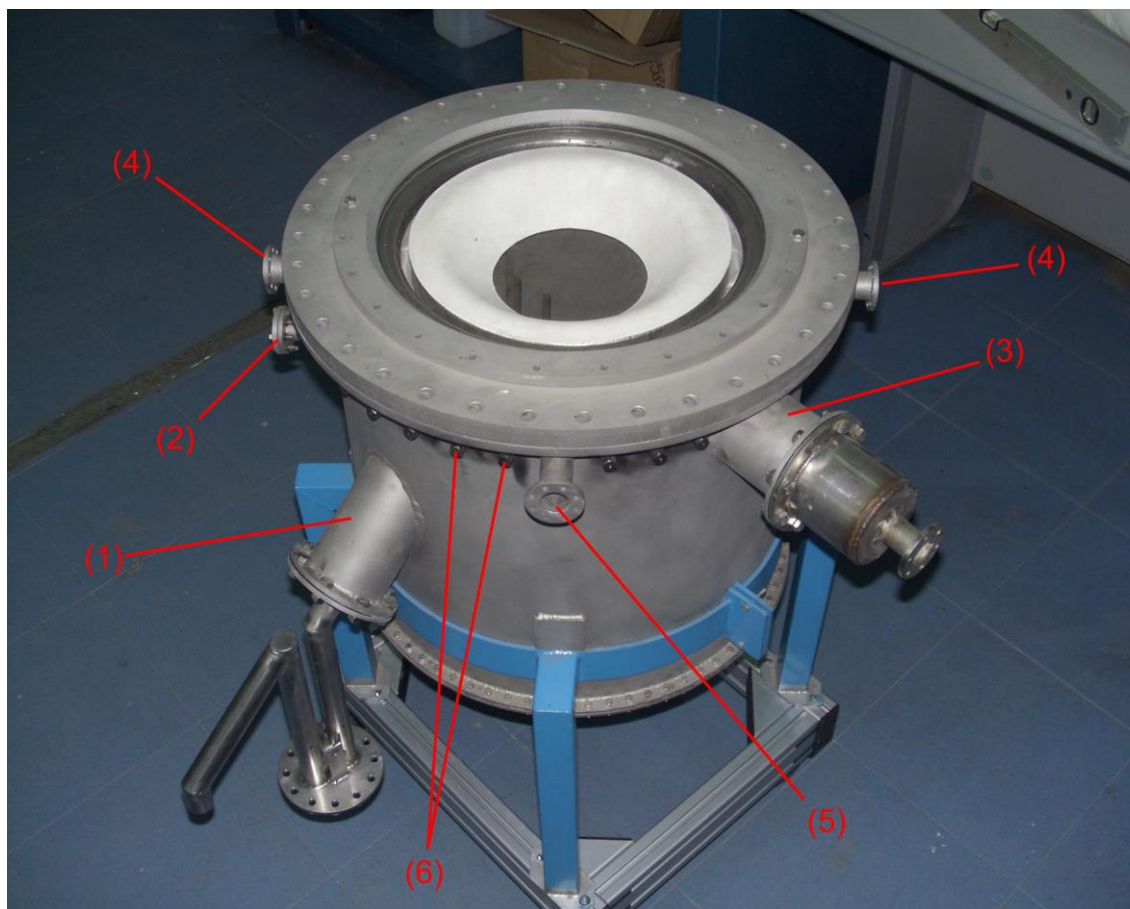


Fig. 51: Oresol reactor. For the numbers see the list in the text.

3.5.1 Window

At the top, the reactor is closed by a 20 mm thick flange with a large, flat window (diameter 400 mm, thickness 8 mm). Five windows were purchased from the company LSP Quartz B.V.⁶⁰, from Wijchen (The Netherlands). The window is made of amorphous silica (“quartz-glass”) GE124. This material has an excellent thermal shock resistance due to its extremely low thermal expansion coefficient ($4.8 \cdot 10^{-7} \text{ K}^{-1}$ at 900°C), and simultaneously a very low optical absorbance (“no appreciable absorption [between 245 nm and 4500 nm] for a 1 mm thick sample”⁶¹). The fabrication must be “electrically fused” (and not with a flame) to keep the OH content low (GE124: <33 ppm). This avoids absorption bands in the infrared at 1390 nm and 2200 nm, and reduces notably the depth of the band at 2720 nm. These properties make quartz-glass an ideal material for the coupling of highly concentrated solar radiation into the reactor.

The window is held in place by an additional clamp ring and two gaskets made of “expanded pure graphite”, fixed by 24 screws. Through this window, the concentrated solar radiation reaches the inside of the reactor, and at the same time it prevents the gas in the reactor from escaping to the outside. The flange is water cooled to minimize its thermal expansion, this way

⁶⁰ <http://lsp-quartz.com/>

⁶¹ Supplier information by e-mail from June 2nd, 2009.

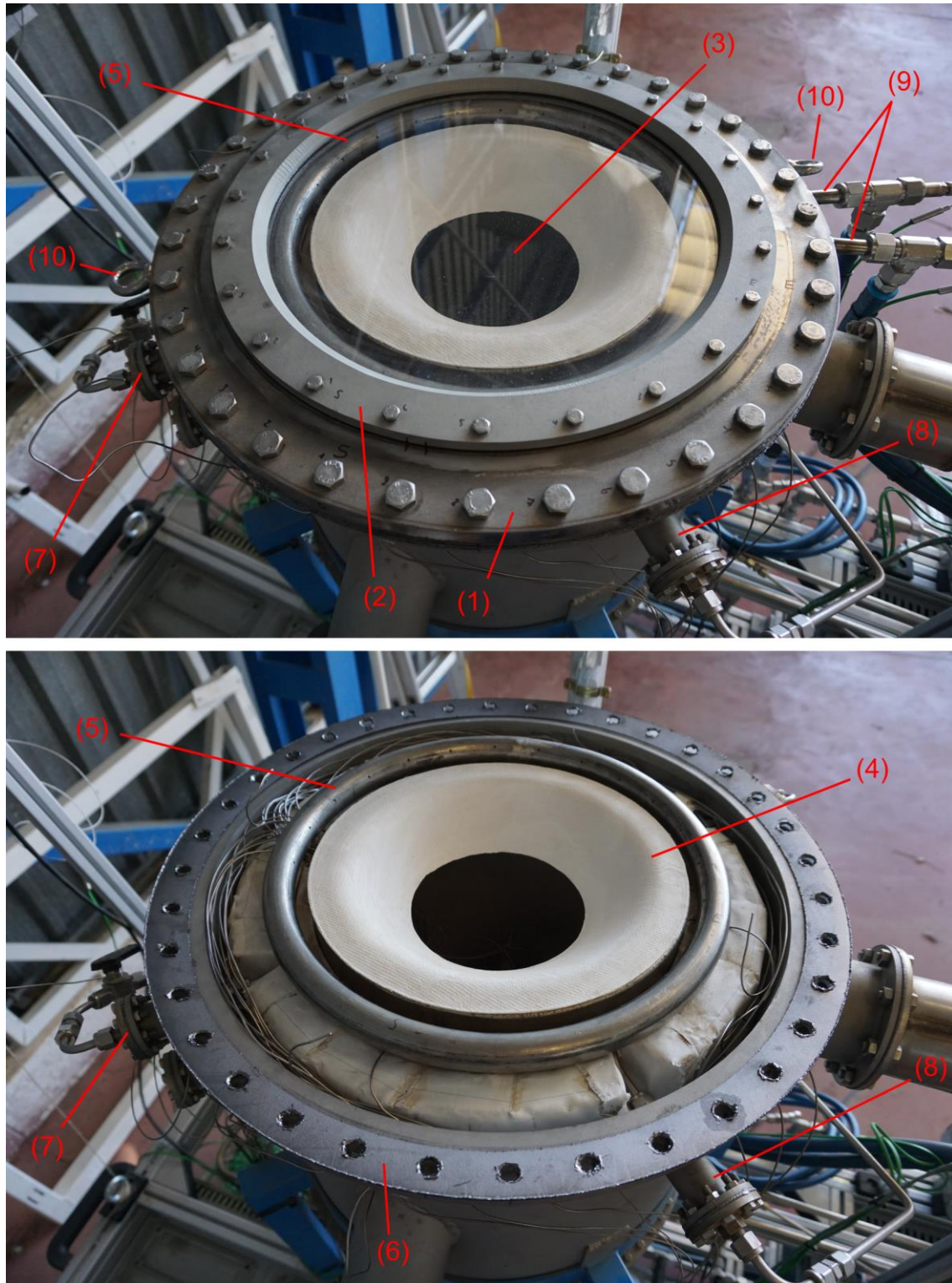


Fig. 52: Oresol reactor with (top) and without (bottom) the window flange. (1) Window flange. (2) Clamp ring. (3) Quartz window. (4) Ceramic aperture cone. (5) Window protection gas distributor ring. (6) Graphite seal of the window flange. (7) Window protection gas connection. (8) Line to pressure sensor. (9) Cooling water connections. (10) Eyes for flange lifting.

avoiding warping and possible damage of the window (anyway this happened once, see chapter 5.6). As the reactor is a demonstrator working on Earth at nearly ambient pressure, the window can be quite thin. The differential pressure it can withstand was calculated to be at

least 100 mbar⁶¹. All the mentioned details of the window section of the Oresol reactor can be seen in Fig. 52. Two auxiliary connections close to the top of the cylindrical wall of the reactor are used to supply protective gas for the window (the other two are to connect two redundant pressure sensors). The window protection gas flows into an annular pipe with 24 small radial bores (\varnothing 2 mm each) with the purpose to distribute the gas as homogeneously as possible below the window.

3.5.2 Aperture Cone

Under the window, there is a truncated cone ("aperture cone") made of 1 mm thick so-called "sheet ceramic" AvA-Z-ISC⁶² (item (4) in Fig. 52). This is a white material that has basically the common properties of ceramics, like e.g., good heat resistance, but contrary to common ceramics it allows at least slight bending flexibility. This makes handling and operation much easier than for use of "normal" ceramics. With a diameter of 150 mm of the aperture opening, its purpose was to reduce the thermal radiation from the fluidized bed (but this didn't work exactly as planned, see Chapter 5.3). A further task is to partially prevent particles from spouting against the window from the bottom. Moreover, it channels the downwards flow of the window-protection gas through the aperture opening, preventing this way that in particular very fine particles can reach and contaminate the window.

3.5.3 Base Plate

On the bottom, a flat, 4 mm thick, flat plate closes the reactor. It has three ports (Fig. 53). The first one in the center is for the main bed fluidization gas (see Chapter 3.5.4); the second one is for the particle feed (see chapters 3.5.6 and 3.6). In the original design, the third port was

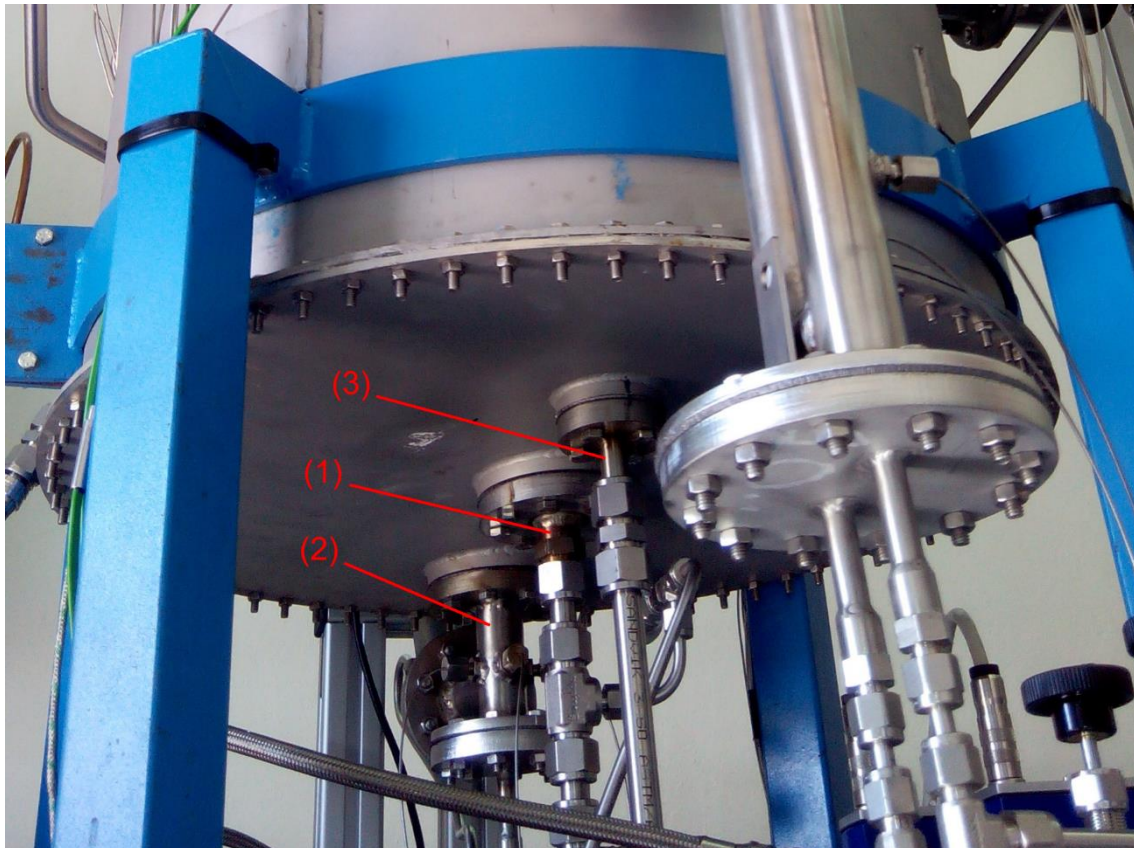


Fig. 53: Reactor base. (1) Main bed gas supply. (2) Particle feed. (3) Particle drain.

⁶² <https://www.keramiklech.com/en/>

intended for the gas supply of the riser of the particle outlet pipe. But as this did not work very well, the design was modified (see chapter 3.8) and the port was repurposed for the particle drainage of the reactor needed in case of maintenance or modifications.

3.5.4 Gas Distributor

The fluidization gas is introduced centrally from below into the reactor. At the bottom of the fluidized bed sits a drum-shaped component with a diameter of 236 mm and a height of 20 mm (Fig. 54). This is the gas distributor. It contains 40 screws, each with a central, vertical bore in the shaft, which communicate with three small, horizontal bores in the head (Fig. 55). Through these holes, the gas is distributed evenly at the bottom of the fluidized bed, while this geometry also prevents particles from entering into the gas distributor. The screws reach to the floor of the gas distributor, providing this way mechanical support for the top plate. This avoids a possible collapse under the weight of the particles of the fluidized bed when the material is weak due to elevated temperature. The whole gas distributor including screws and nuts is made of the austenitic nickel-chromium-based superalloy Inconel 600.

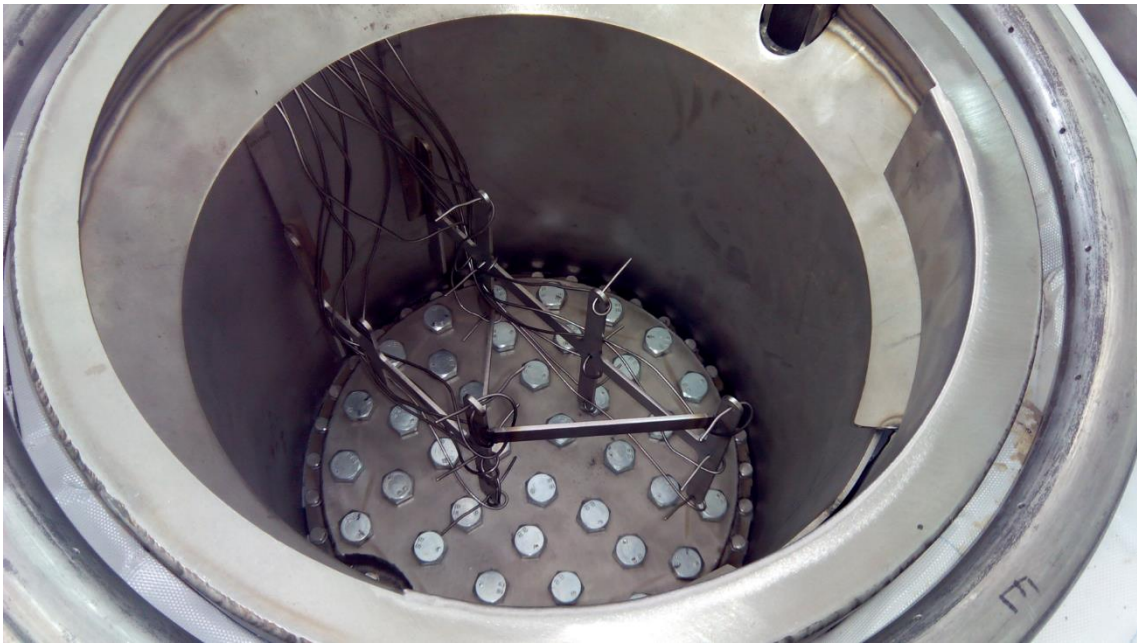


Fig. 54: Gas distributor at the bottom of the empty reactor.

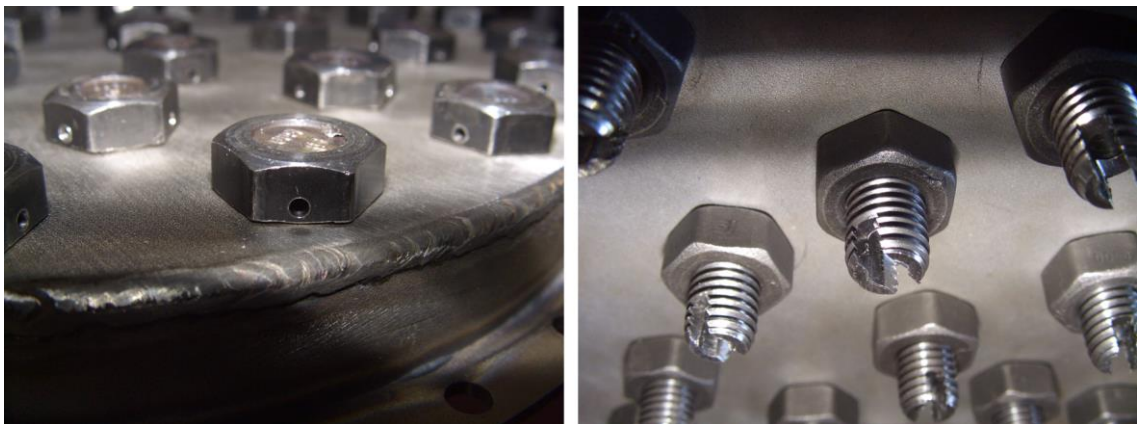


Fig. 55: Gas distributor screws (tuyere type). Left: View from above. Right: View from below.

Some other configurations of the gas distributor were tried, in particular one dubbed “annular fluidization” or “9/2”, because it used only 9 of the 40 screws with only 2 orifices each instead of 3, all located on the outer perimeter creating an annular shaped fluidization pattern. This configuration finally didn’t work satisfactory. It is described in more detail in chapter 4.1.1 and 4.1.2. In contrast, the original configuration is sometimes denominated “40/3”.

3.5.5 Reaction Volume

The space above the gas distributor represents the net reaction volume of the reactor (Fig. 54). In the original design, this wall was made of the above-mentioned “sheet ceramic”⁶² with a thickness of 2 mm. It was later replaced by a cylinder of Inconel 600 with the same dimensions.

Among the most important parameters of the whole system is the temperature in the fluidized bed. It is measured by the thermocouples TC01-TC15. 30 fittings located around the circumference of the upper part of the outer reactor shell allow the gas-tight introduction of thermocouples into the reactor (see Fig. 51 item (6) on page 87). The thermocouples are distributed within the bed in the shape of a cross in three levels, called bottom (TC01-05), middle (TC06-10), and top (TC11-15), see chapter 3.2.3. Each level has a thermocouple for north, east, south, west, and center. This way, a rather good resolution of the temperature distribution within the bed is achieved. The thermocouples are held in their place by a specially designed “holder-piece” submerged in the bed (see Fig. 54). During the tests, it turned out that not always all parts of the bed were well mixed, resulting in a lag of the temperature at these places. To avoid that these temperatures pull down the average temperature in an inadequate way, there is the possibility in the data acquisition program to “deactivate” (exclude) thermocouples individually from the averaging calculation (more about this in chapter 5.3).

3.5.6 Solids In- and Outlet

The particles enter into the reactor through a vertical, fluidized pipe, a riser, in the Oresol project also called the “Inpipe” (item (3) in Fig. 56). They enter this pipe at the bottom from the outside of the reactor and leave it through an opening on the top at the inside (“Solids In” in Fig. 57), from where they fall into the main fluidized bed of the reactor. More about the particle feed can be found in chapter 3.7.

The removal of the particles is done by a simple overflow located on the top of the inner reactor wall (“Solids Out” in Fig. 57), connected to a pipe with a 45° downwards slope (item (4) in Fig. 56). In the Oresol project, this line is denominated “Outpipe”. A double walled tube with inner insulation reduces the conductive heat losses at this connection. A syphon at the outside of the reactor avoids that the gas follows the same path. More about the particle removal can be found in chapter 3.8.

The photo in Fig. 56 was taken during the preparation of a cold test with a provisional reactor vessel with the reactor wall still removed. It gives a good impression of the mutual arrangement of the feed and discharge pipes for particles and gas. With the reactor fully assembled, it’s no longer possible to see all these parts from one single viewpoint (compare to Fig. 113 on page 140).

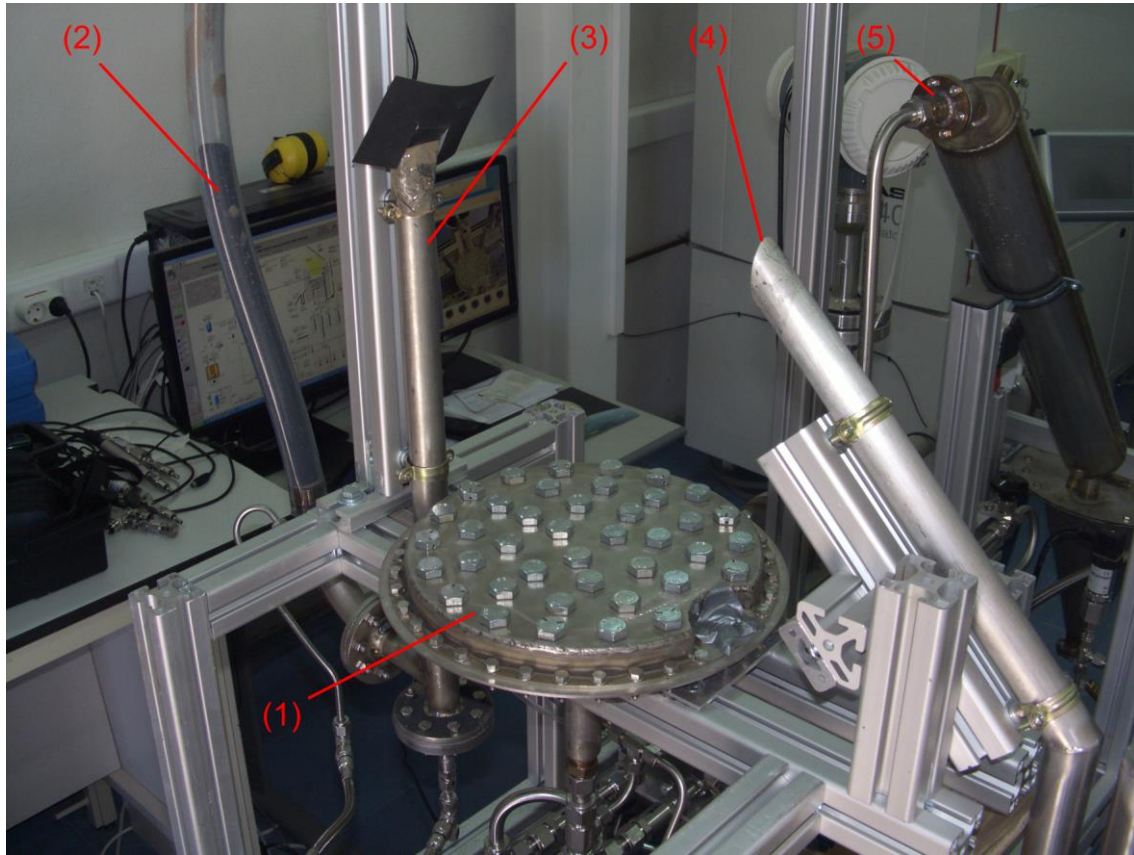


Fig. 56: Arrangement of the feed and discharge elements of the reactor. (1) Gas distributor. (2) Standpipe. (3) Particle feed ("Inpipe"). (4) Particle outlet ("Outpipe"). (5) Gas outlet pipe (the $\frac{1}{2}$ "-pipe with the 90° arc is not part of the final assembly).

3.5.7 Gas Outlet

To keep the quantity of particles that leave the reactor together with the product gas as low as possible, a first separation of particles and gas already takes place within the reactor. A general problem of fluidized bed reactors with direct coupling of concentrated solar radiation is that there is very little height available for the freeboard (the volume above the surface of the fluidized bed). This means that no internal cyclones can be used and that the gas outlet is practically always below the disengaging height. Nevertheless, by incorporating baffles, a rather good separation of the solids from the gas can be achieved.

In the Oresol reactor, two baffles are integrated at the upper circumference of the reactor ("Gas Out" in Fig. 57). They each form a channel and together span an angle of 120°. The cross section of the channels is relatively large, so that due to the low gas velocity, the particles still can sediment and trickle back into the reactor through a narrow slit. The cross-section of the adjacent outlet pipe is smaller, so that, due to the now higher gas velocity, possibly still present particles are entrained in any case. As a result, a blockage of the tube due to unwanted particle accumulation is avoided.

Finally, the gas leaves the reactor through a horizontal pipe (named "GasOutPipe" in Oresol) located near the top of the reactor (see item (3) in Fig. 51 on page 87). 80 mm of the pipe outside the reactor are double walled with insulation in between. This helps to reduce conductive thermal losses through this connection.

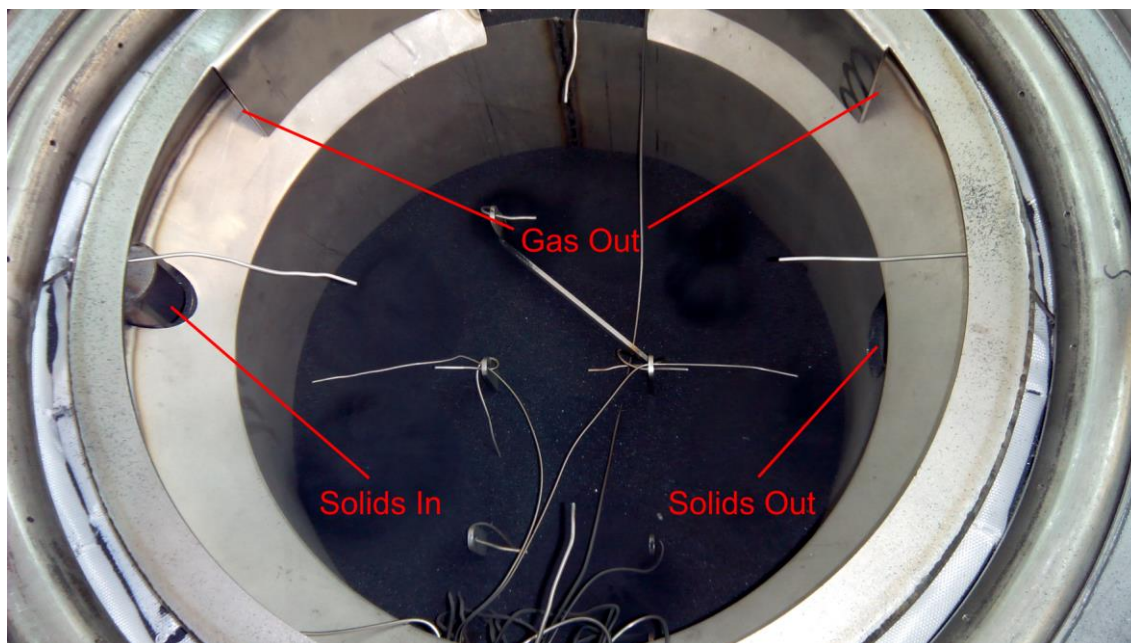


Fig. 57: Fluidized bed reactor with feed and discharge connections. As it is not completely filled, some of the thermocouples are visible.

3.5.8 Thermal Insulation

A very important detail of any reactor working at high temperature is the proper selection of the thermal insulation. Oresol uses microporous material from the “Microtherm” brand⁶³. This is a fine grained material with the effect that thermal conduction is minimized due to the small contact area between the grains, and at the same time, the small size of the pores suppresses heat transfer by convection of gas. The used material has a thermal conductivity of 0.049 W/(m·K) at 800 °C.

The material was purchased in prefabricated sheets with a thickness of 25 mm (bottom) and 10 mm (wall). Furthermore, half-shell parts were used to insulate the outlet pipes for the solids and for the gas. All these sheets can be cut with a saw or a knife and this way be adapted to the exact geometry of the reactor, including bores for feedthroughs. Fig. 58 shows some stages of the manufacturing process.

The plates are arranged in a stepped geometry (Fig. 59) to avoid convective gas flow through the gaps between the different layers. The thickness of the insulation of the Oresol reactor was chosen to 100 mm. This turned out to be sufficient; the outside of the reactor could be touched with the bare hands at any time without being burned.

Initially, there was no insulation directly under the window flange. However, as this caused problems during the initial phase of the tests including a crack in the window, the gaps in this area were filled with alumina wool (see Fig. 58 bottom right and chapter 5.6).

⁶³ <https://www.promat.com/en/industry/technologies/microporous/>

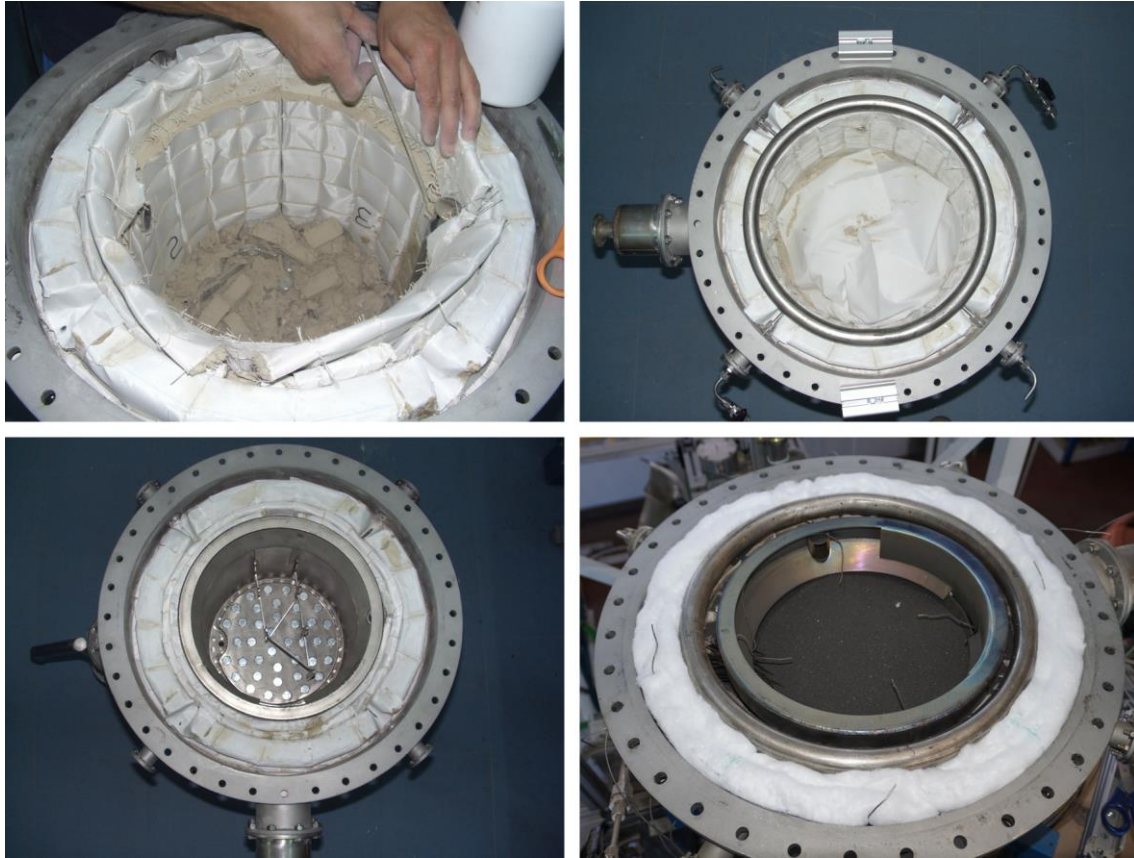


Fig. 58: Different stages of the manufacturing of the insulation of the Oresol reactor.

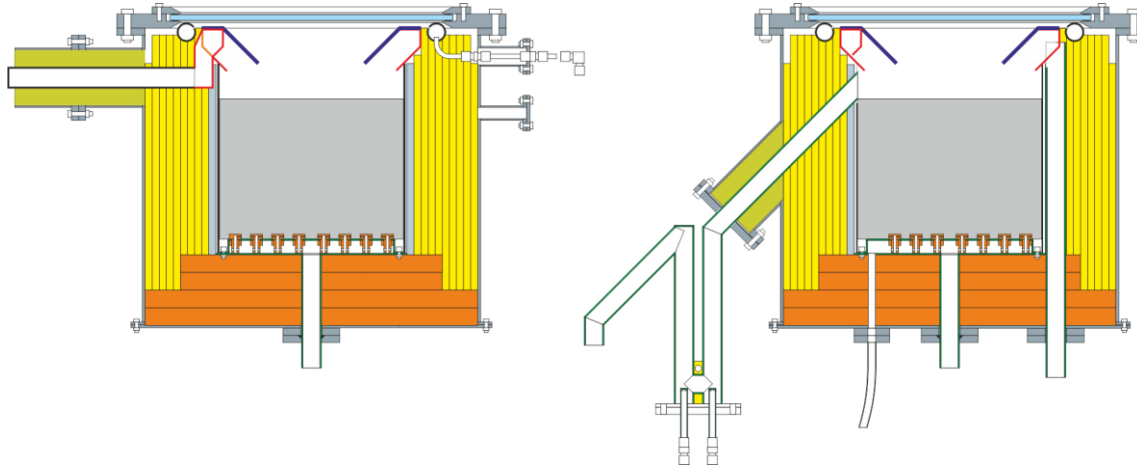


Fig. 59: Insulation of the Oresol reactor. Orange: base sheets (25 mm thick). Yellow: wall sheets (10 mm thick). Yellow-green: half shells (25 mm thick).

3.5.9 Radiation Shield

To protect the outside of the reactor from the fraction of the highly concentrated solar radiation that misses the window, a radiation shield is needed. It consisted initially of a total of 7 CAD-designed alumina pieces⁶⁴ (Fig. 60 left and Fig. 61 center), but it turned out quickly that the large diagonal piece was not needed and hence it was discarded (Fig. 60, right). The conical central holes of the two horizontal pieces are adapted to the shape of the vertical radiation cone (Fig. 61 right), while the remaining pieces provide general protection from the radiation

⁶⁴ Kaowool 1400 (1000 x 1000 x 25) <https://www.morganthermalceramics.com/>

coming from the concentrator of the Solar Furnace. The radiation shield has its own support structure that allows dismounting within a few minutes in case access to parts covered by the radiation shield is needed for inspection, maintenance, or repair.

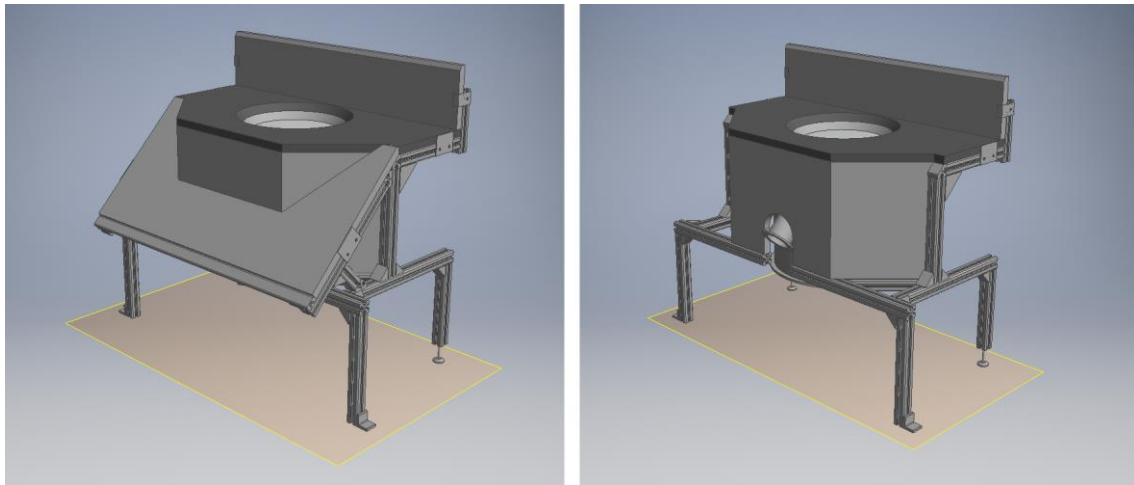


Fig. 60: Radiation Shield CAD drawings. Left: initial version. Right: final configuration.



Fig. 61: Radiation shield hardware. Left: Manufacturing at the PSA Solar Furnace workshop. Center: Initial version still with the diagonal shield. Right: Conical central opening, adapted to the shape of the concentrated solar ray.

3.5.10 Further Details

An important problem during the design process was to make the reactor completely dismountable, in case a major problem occurs that requires repair or modification. This means that many pieces could not be welded, but simply were stuck together. This caused, among

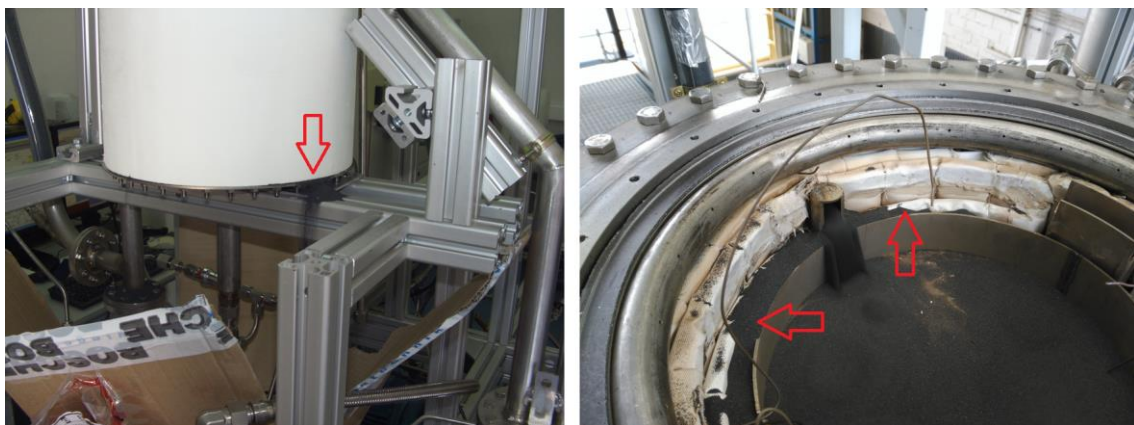


Fig. 62: Left: Leak between gas distributor and inner reactor wall. Right: Gap between inner reactor wall and insulation, filled with particles to “close the gap”.

others, a problem of tightness at the bottom of the inner cylinder (the actual wall of the fluidized bed). The fluidization gas preferred the way through the small gap between the inner wall of the reactor and the gas distributor plate to the outside of the inner wall (Fig. 62 left) rather than the desired way through the fluidized bed. The problem was solved by simply filling the gap between the inner reactor wall sheet and the insulation with particles (Fig. 62 right). This way, the hydrostatic load in the gap was increased and this path no longer provided a short-cut.

Another (fairly big) problem for the disassembly are the thermocouples. Since they are rather stubborn wires, they should be moved or bent as little as possible. In order to nevertheless allow disassembly of the reactor's internal components, they are first all collected on the outer perimeter of the reactor and then from there routed to the interior all together from one side. Since the north side of the reactor already contains the particle feed, the south side the particle removal, and the east side the off-gas removal, the west side was used for this purpose. Fig. 63 shows how the thermocouples with their holder are carefully bent out of the reactor and fixed with a cord, so that access to the parts further down is possible without having to dismantle or even destroy the thermocouples.

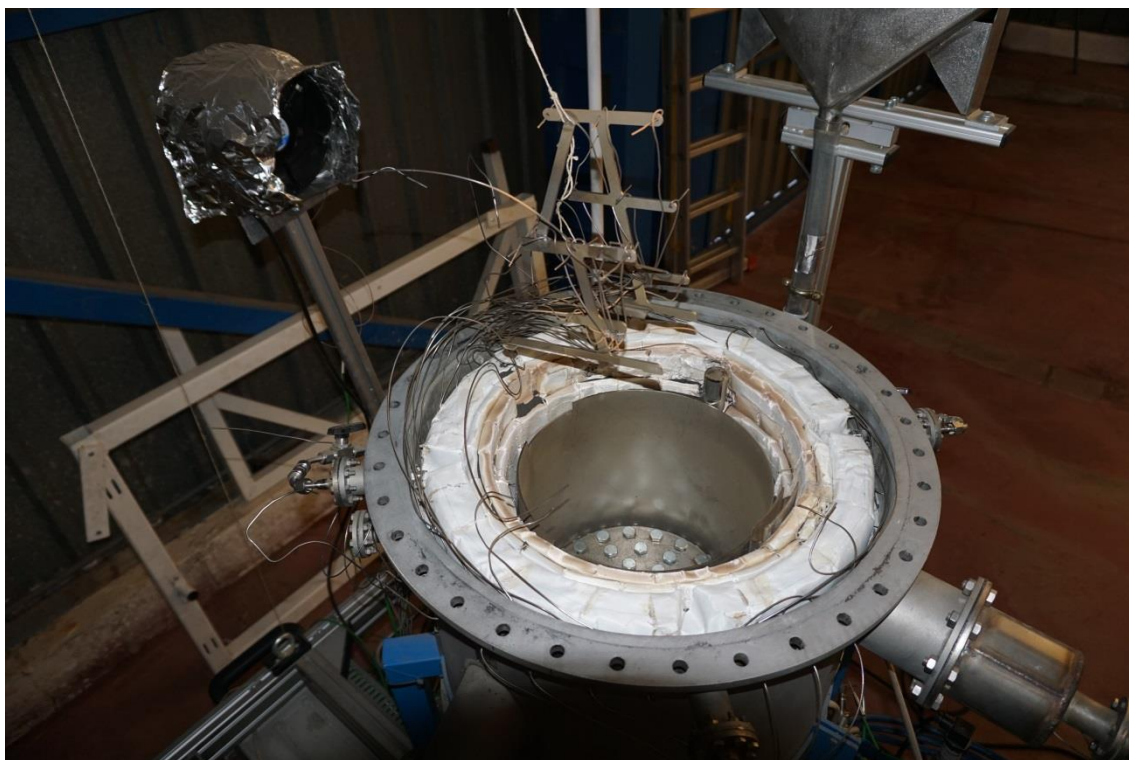


Fig. 63: Fluidized bed thermocouples lifted out of the reactor to enable dismounting of internal components.

A further point to consider was that when operating fluidized beds, the particles in permanent movement can generate static electricity by friction among themselves or the reactor wall. To minimize possible problems, all equipment is properly grounded.

3.6 Gas Supply ("Upstream")

The gas supply is rather conventional plumbing compared to other parts of the installation. It occupies a large part of the space below the reactor (Fig. 64). All pipes and connectors are from the commercial brand Swagelok. Pipes are $\frac{1}{2}$ " or $\frac{1}{4}$ " (outer diameter), depending on the

expected flow. Center piece of the gas supply sub-system are six flow controllers and two flow transmitters. Five of the controllers work with argon. They adjust the gas flow of the main fluidized bed (FC01), the window protection gas (FC02), the Outpipe syphon (FC03), the Inpipe (FC04), and the Standpipe (FC05). The sixth flow controller (FC06) doses the hydrogen share of the main gas into the reactor. The pressure from the external argon supply is usually set to around 5 bar, according to the requirement of the flow controllers. The hydrogen supply has a pressure of 2 bar. A manual valve (MV10) allows flushing the hydrogen pipes with argon before use, so that the possible formation of an explosive mixture with ambient air can be reliably avoided.

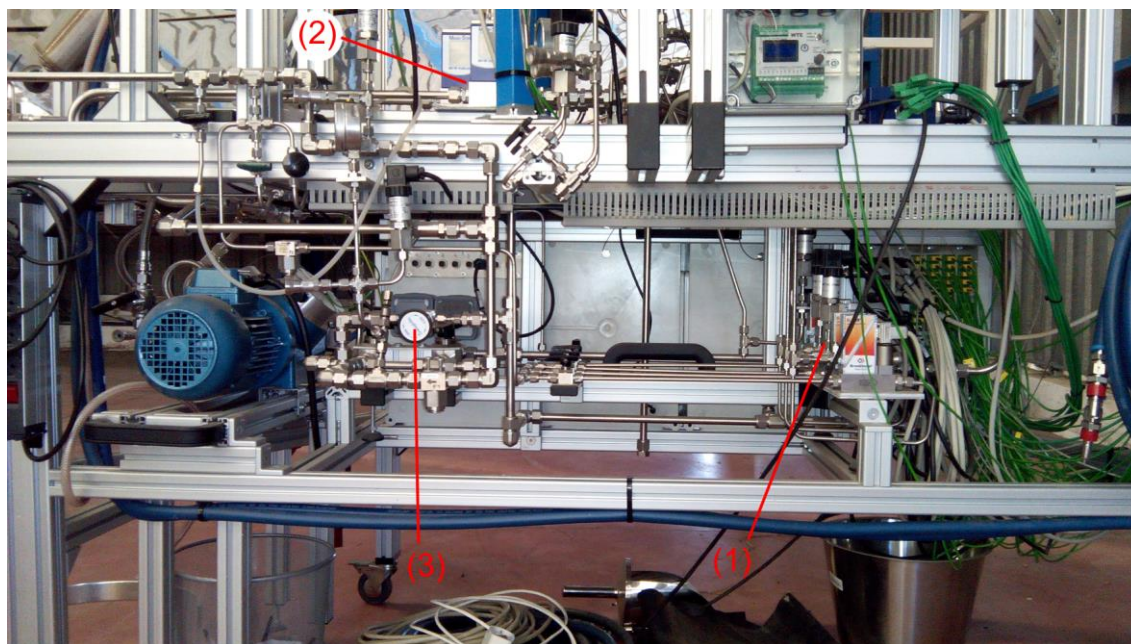


Fig. 64: Gas supply (“upstream”) section of the Oresol experiment. (1) Flow controllers. (2) Flow transmitters. (3) Manual Valve MV07.

The two flow transmitters are to measure the recirculated gas flow. One of them (FT07) is to return the gas directly into the main bed. The other one (FT08) is usually connected to the window protection gas line, but the plumbing and the control software can be easily modified to use it for the main bed too if required (this was helpful during the pre-tests with air). Two manual valves (MV21 and MV22) serve to adjust the flows.

If a main bed gas flow beyond the range of the flow controller is needed, and no or not enough recirculated gas is available (this happens when operating with air at or near ambient temperature), a manually operated valve (MV07) can be opened to supply additional gas. In this case, the flow is provisionally calculated with the help of the difference of two pressure sensors (PT01 and PT11). The data needed by the valve-operator for proper adjustment is transmitted to a mobile phone via Bluetooth.

3.7 Particle Supply

The particles are fed into the reactor by a combination of two pipes, the riser (in Oresol called “Inpipe”) that enters the reactor from the bottom and where the particles flow upwards, and a so-called standpipe on the outside of the reactor where the particles flow downwards. On the top of the standpipe sits a feed hopper with a capacity for up to 8 kg of solid feedstock. (The capacity is limited by the range of the strain gauge MT01, not by the volume of the hopper.)

The two vertical pipes are both fluidized, and are interconnected at the bottom forming a kind of siphon (U-tube). Like explained in chapter 1.4, the fluidization causes the particles in the tubes to behave like a liquid in a pipe. Since the level in the hopper (Fig. 65) above the standpipe is well above the level of the overflow at the top of the riser, an almost continuous particle flow into the reactor is created (Fig. 66 right). “Almost”, because the fluidization regime in the Inpipe is “slugging” due to the long and slim shape. This means that the rising gas bubbles grow to the size of the diameter of the pipe and the particles enter the reactor in pulses with a frequency somewhat below 1 Hz rather than in an uninterrupted flow. However, this is of little importance for the proper functioning.

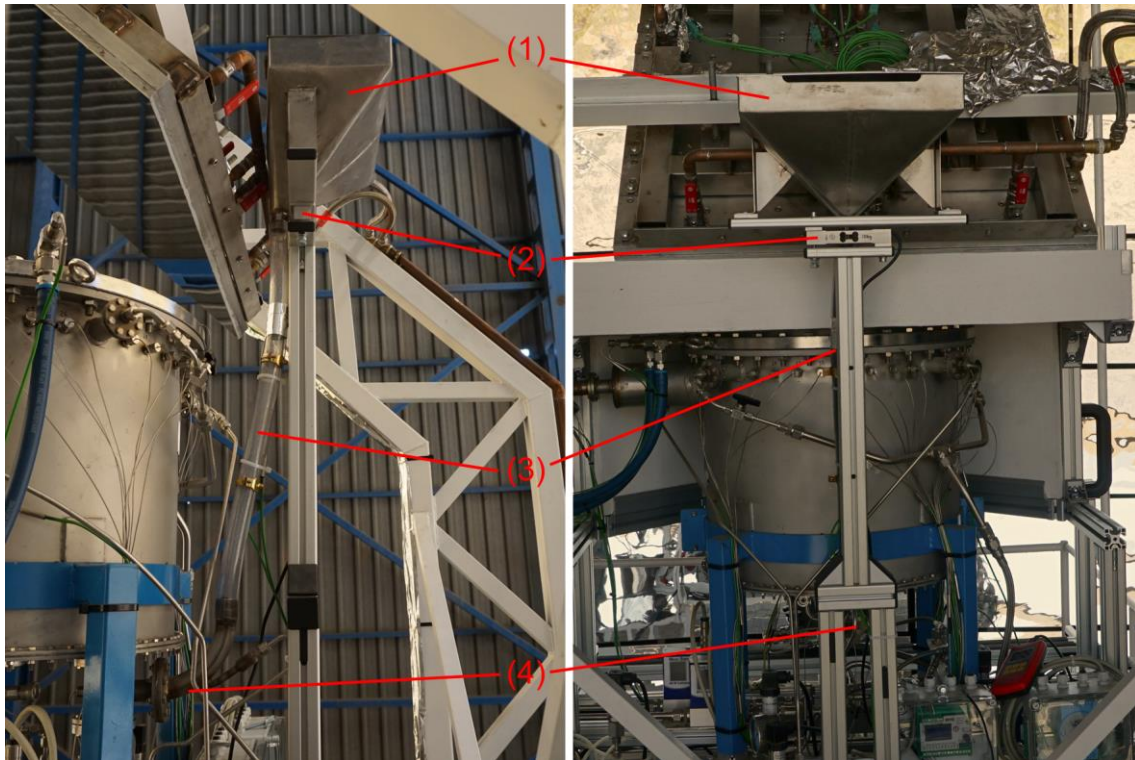


Fig. 65: Particle supply: (1) Hopper, (2) Load Cell (MT01), (3) Standpipe, (4) L-Valve.

To control this particle flow, the lower end of the standpipe is designed as a so-called L-valve (Fig. 66 left) (Koenigsdorff, 1994). This consists of a 90° bent pipe with a connection for the fluidizing gas. Unlike the riser which is fully fluidized directly from the bottom (by FC04), the amount of gas supplied to the standpipe (by FC05) is rather low. It is generally near or even below the minimum fluidizing velocity. By careful choice of this gas flow, the particle mass flow can be adjusted. The enormous advantage of this concept is that it works without any moving parts in the hot or dusty area of the system.

A load cell (MT01) installed directly below the hopper measures its weight (mass) with the particles contained therein (Fig. 65). This is possible because the standpipe is made of soft, transparent, rubber-like material that hardly absorbs forces. This is necessary because the mass of the hopper and the particles only can be properly determined when the scale is the only mechanical support of the hopper. The used hose for the standpipe is a cheap piece of plastic purchased by a local supplier. It was initially thought only as a provisional solution, but during the whole time of the project, it worked fine and no better solution was neither searched nor found nor needed.

The particle mass flow is *measured* simply by subtracting the current hopper mass from the mass measured one minute ago. The difference gives the particle mass flow in the unit grams (or kilograms) per minute.

The particle mass flow is *controlled* by a software code that adjusts the standpipe fluidization gas flow according to the particle mass flow set point and the measured value. For a more detailed explanation of the code see page 133 ff. in chapter 3.14.2.

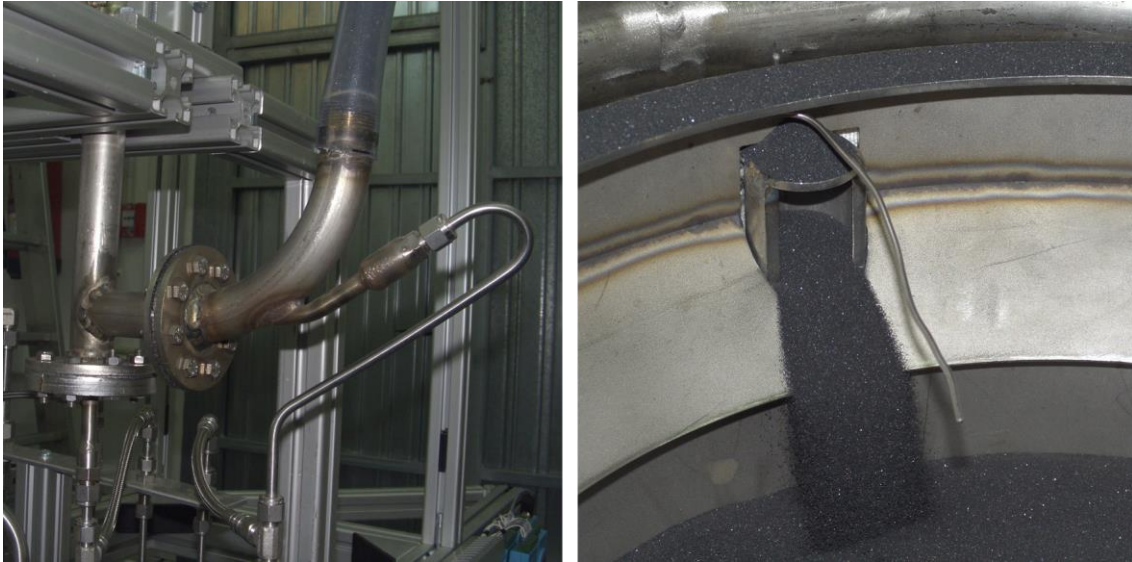


Fig. 66: L-Valve (left) and solids inflow into the reactor (right).

3.8 Particle Removal

The original design of the particle outlet was a tube with the shape of the number “1” with the vertical leg submerged in the main fluidized bed (see description in appendix A.3 and technical drawings in appendix A.4). As this did not work well, it was soon replaced by a better design.

The new design is more similar to the particle feed, and, like this, consists of a fluidized U-tube (in Oresol called "Outpipe", Fig. 67 left). But in contrast to the feed, flow control is not needed here. The purpose of this siphon is to avoid the gas escaping from the reactor through this opening. A simple overflow at the inner cylinder of the reactor is defining the bed level (Fig. 67 right top). If the amount of particles in the reactor increases, particles from the reactor automatically pour into the Outpipe.

The two legs of the syphon are fluidized individually from the bottom, but they share a common flow controller (FC03). The proper distribution of the gas between the two legs is adjusted by two manual valves (MV19a and MV19b).

The length of the two legs of the Outpipe allows for a pressure difference up to 40 mbar between the reactor and the environment, a value that the window easily withstands (see chapter 3.5.1). In principle, one can say that the Outpipe can act like a pressure relief valve. If this happens, all particles remaining in the Outpipe are instantly blown out, the pressure in the reactor drops to near ambient, all the gas also leaves the reactor through this opening, and the operation should be interrupted immediately. This unwanted failure mode is called “*solids blow-out*”.

The particles flowing out of the Outpipe (Fig. 67 right bottom) fall into a collecting container, which also stands on a balance (MT02). This allows the particle outflow to be recorded in the data acquisition as well. The range of the scale originally was the same as for the feed hopper, 8 kg. But as the container often became full during operation and needed to be replaced by a human, and this action required an interruption of the solar power supply to avoid roasting of this human, later in the project the scale was replaced by a bigger one able to measure up to 80 kg, enough even for an extremely busy testing day.



Fig. 67: Particle removal from the reactor. Left: Siphon shaped Outpipe. Right top: Overflow inside the reactor. Right bottom: Solids outflow.

The solids coming out of the reactor carry a large amount of heat with them. As already mentioned in chapter 3.1.1, this surplus heat is not recovered in Oresol. A possible future use is discussed in chapter 7.2.

3.9 Off-Gas Treatment ("Downstream")

The off-gas from the reactor not only contains the desired product (water), but also all sorts of other substances, such as fluidization gas (argon, see chapter 3.3.1), unreacted hydrogen, coarse and fine stray particles from the fluidized bed, and also contaminants from the solid feedstock and products from side reactions thereof. In addition, it comes out at almost the reactor temperature. Bluntly spoken, the off-gas is "hot, wet and dirty". Hence, to obtain pure product water, cooling, drying, and cleaning of the gas is essential. This part of the plant is summarized in Oresol under the term "downstream section". It can be considered as a small, but rather complete chemical factory.

It's physically located on the east side (on the right when looking from the concentrator) of the installation. Fig. 68 shows the major subcomponents, Fig. 69 the CAD drawings which include the latest modifications (see chapter 7.1). It is noticeable that the components are arranged almost completely vertically (in "columns"), i.e. one above the other. This is typical for

chemical plants that treat liquids or solids, because the gravity is used for transportation and segregation. The Oresol downstream section consists of two vertical columns, this can be recognized well, for example, in the middle view of Fig. 69. The first column includes (the numbers in parenthesis refer to the numbers in Fig. 68) the reactor gas outlet (3), the first

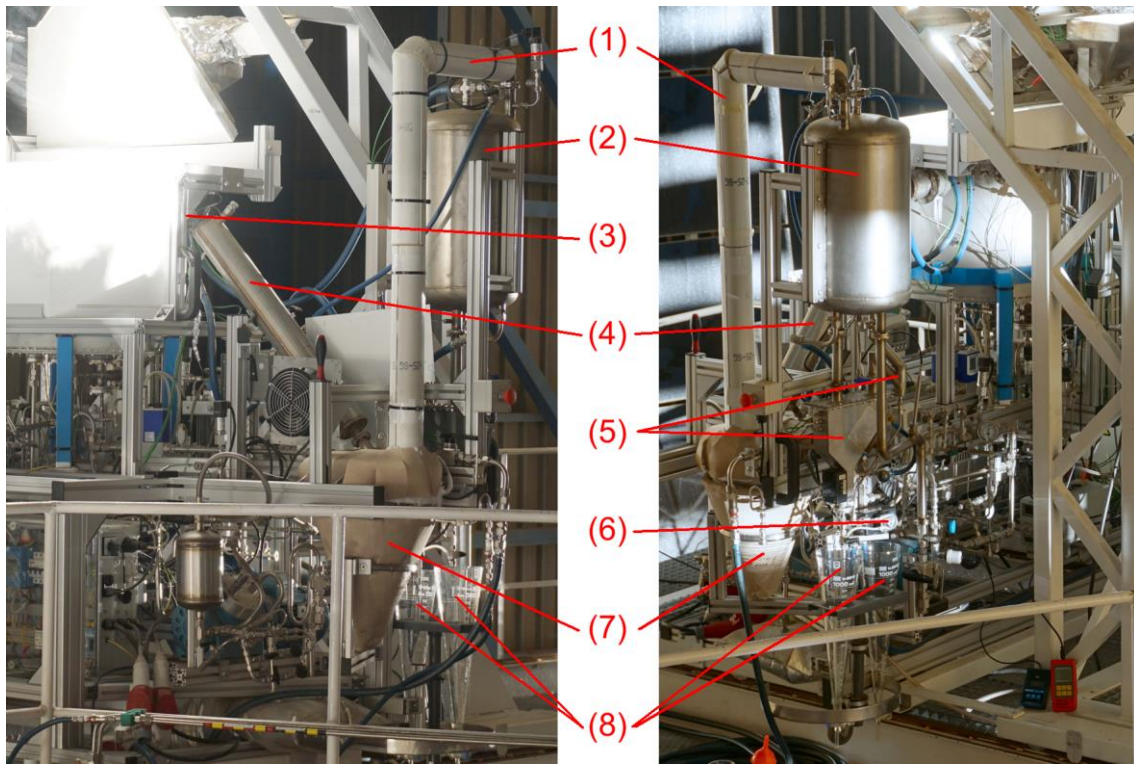


Fig. 68: Downstream section of the Oresol experiment. (1) Insulated pipe. (2) Cooler-2. (3) Reactor gas outlet. (4) Cooler-1. (5) Pre- and Main-Water Separator. (6) Water Extraction Pump. (7) Particle Separator. (8) Product Water Storage (Two Imhoff Cones).

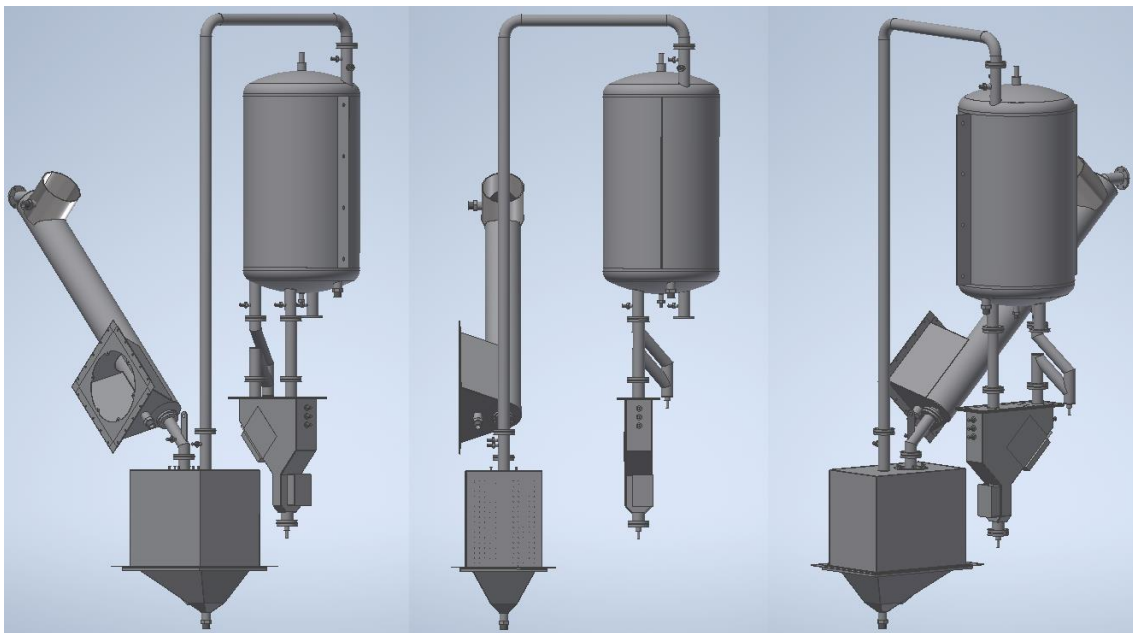


Fig. 69: Latest CAD drawings of the Oresol downstream section, with new air cooled Cooler-1 and enlarged Filter F3 (for details see chapter 7.1).

cooler (4), and the particle separator (7). At its lower end, the solids present in the off-gas are extracted. The gas then flows back up through an insulated pipe (1) to the second column. This comprises the second cooler (2), the two-stage water separator (5) including the Pump P3 (6), and ends at its bottom with the product water storage (8), so-called Imhoff cones, where the product water is collected.

3.9.1 Pre-Cooling

The gas leaves the reactor at around 750 °C. This temperature is somewhat lower than the reactor temperature of 950 °C, because above the fluidized bed, the window protection gas is mixed into the main gas stream and does not heat up entirely to the reactor temperature.

After a 260 mm long, internally insulated section, the further course of the gas outlet pipe is no longer insulated (Fig. 70 and Fig. 71 item (1)). Therefore, the temperature there drops to about 500 °C. Since the gasket in this area (Fig. 71 item (2)) is exposed to this temperature on the one hand and to atmospheric oxygen on the other, it is made of mica, unlike all other gaskets in the Oresol system. This pretends to prevent possible oxidation, which occurs with graphite gaskets from about 400 °C on.



Fig. 70: Piping between the reactor (right) and the Cooler-1 (left).

Nevertheless, the off-gas temperature is still too high for the subsequent cleaning steps, so the first component in the "downstream"-section is a cooler. This cooler, denominated Cooler-1 in Oresol (Fig. 68 item (4) and Fig. 71 item (3)), was originally a water cooler with an internal, 700 mm long gas pipe, and an external water sheath. It is a remnant of the original design from 2008 (see Appendix A.4) which had only a very rudimentary downstream section. The gas leaves the bottom end of the (water cooled) Cooler-1 at around 200 °C. During the test campaign in autumn 2018, the Cooler-1 was converted into an air cooler (Fig. 71) with a fan. This new configuration allows for much better control of the temperature of the downstream components by simply turning on and off the fan. The outlet temperature of the Cooler-1 was then adjusted to about 320 °C. The purpose of the higher temperature is that this reduces substantially the time the subsequent downstream components need to reach their operational temperature. The modification was done rather provisionally by removing the water connections and simply adding a fan (Fig. 71 item (4)) and a baffle (Fig. 71 item (5)) to the lower part of the Cooler-1. The baffle is there to protect the cables of thermocouples etc. which would otherwise be in the warm air stream from the fan. At the moment of the writing

of these lines, the pieces of a better design were already purchased and fabricated but not yet installed.

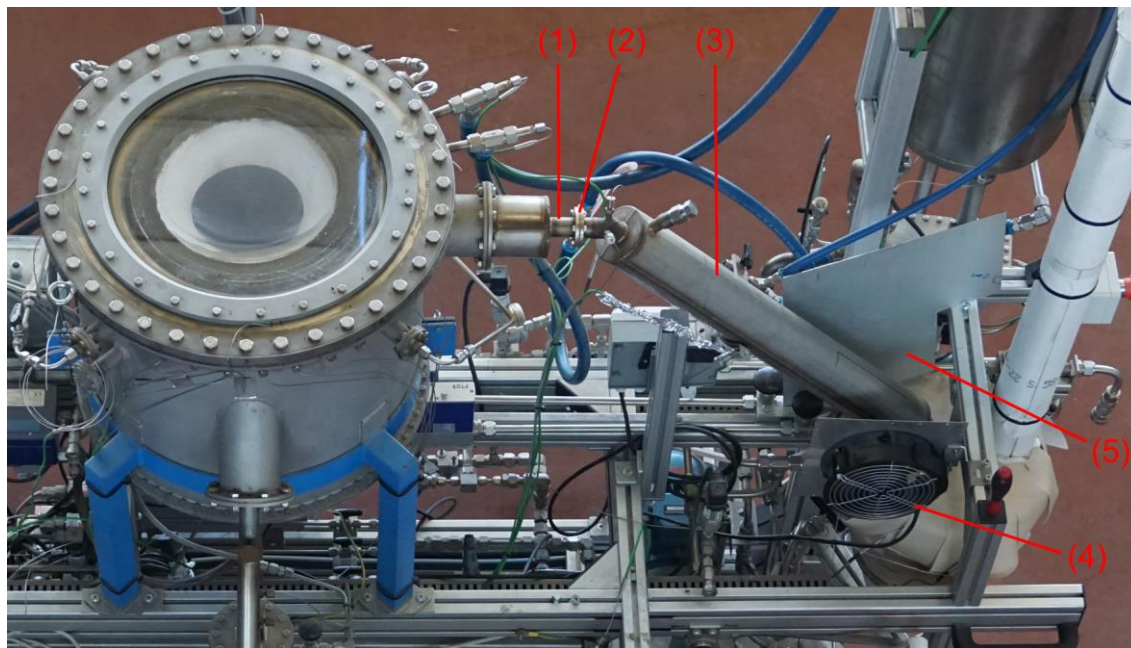


Fig. 71: Cooler-1, configuration with provisional air cooling. (1) Gas outlet from reactor. (2) Mica seal. (3) Cooler-1 / water sheath. (4) Fan. (5) Provisional baffle.

3.9.2 Solids Separation

The particle separator (Fig. 72) is the next element in the off-gas stream after the Cooler-1. In principle, it consists of a conical recipient where the particle-laden gas enters vertically from the top through a pipe at relatively high speed (in the order of 1 to 4 m/s). At the end of this pipe, the abrupt cross-sectional enlargement (by a factor of about 60), along with a 180 degree deflection, causes the gas to move slowly upwards, while the particles, due to their inertia (supported by gravity), settle at the bottom of the recipient. Only the very fine ones remain suspended in the gas stream. A cone shaped baffle at the bottom of the particle separator prevents the gas jet from stirring up the settled particles again. The installation of a cyclone was not considered because the operating conditions are too variable for efficient design.

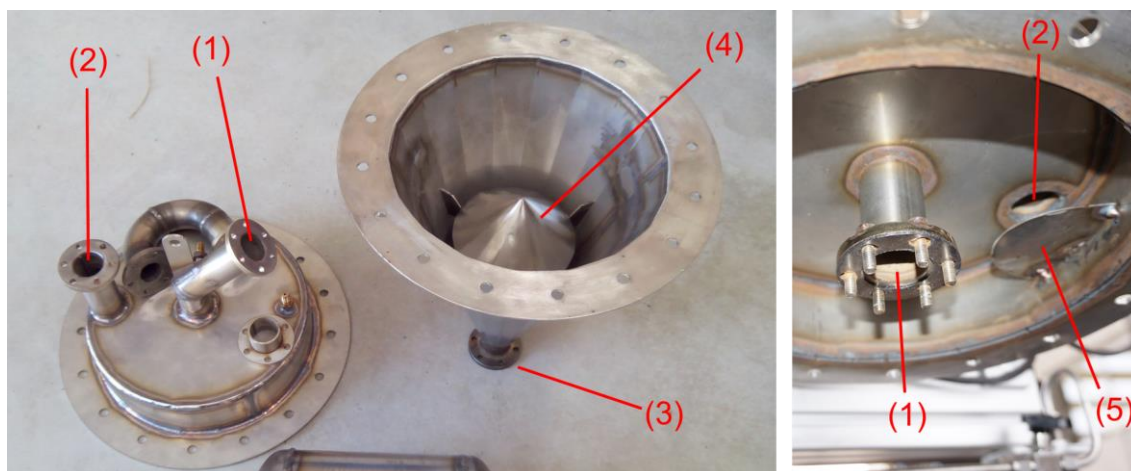


Fig. 72: Particle separator: (1) Gas inlet. (2) Gas outlet. (3) Solids extraction point. (4) Cone. (5) Baffle.

Close to the upper end of the particle separator is the fine Filter F3 (Fig. 73). It spans the entire cross section of about 2.8 dm^2 . It is made of fiberglass felt⁶⁵ so that it can be used for a gas temperature of up to $500 \text{ }^{\circ}\text{C}$. Above the filter, the now particle-free gas leaves the device through a pipe.

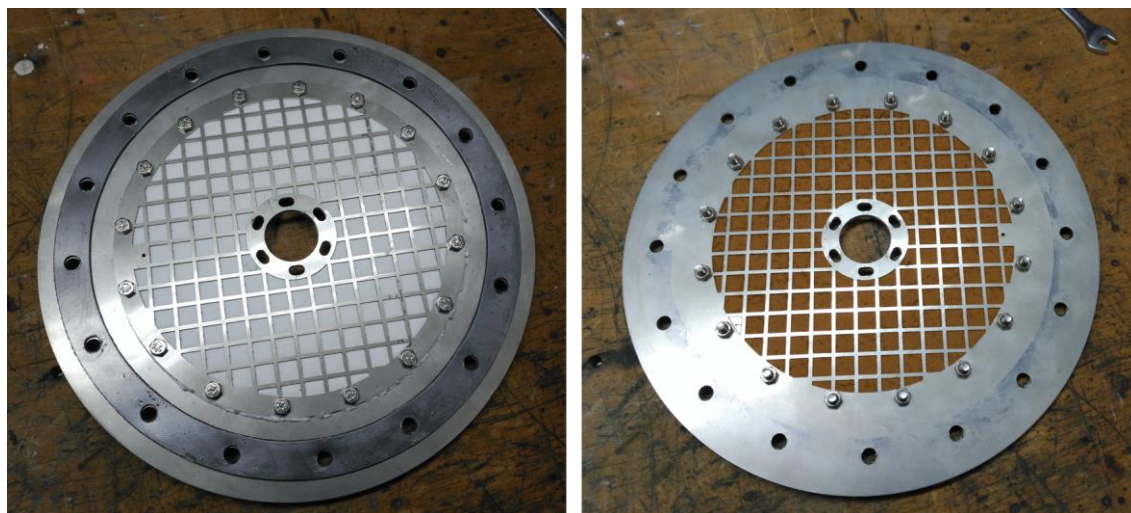


Fig. 73: Off-gas main filter after use. Left: Top side (clean). Right: Bottom side (dirty).

An important operating condition for the particle separator is that its *temperature* never must fall below the evaporation point of water. In the case of Oresol this is near $100 \text{ }^{\circ}\text{C}$ because the operation pressure is near ambient. This avoids that the product water condenses and settles at the bottom of the conical recipient. To keep the temperature high, the particle separator is wrapped in thermal insulation⁶⁶ made of two layers 25 mm thick each (see Fig. 74). During operation, it always took a relatively long time for the entire particle separator to reach the required temperature. This was the main reason why the Cooler-1 was modified to air cooling. This way, the time to reach $100 \text{ }^{\circ}\text{C}$ could be reduced from two to one hour after start of solar operation.

Another important side effect of the filter of the particle separator is that it is the most important contribution to the *pressure loss* in the downstream section and hence determines strongly the pressure in the reactor. This pressure never should become so high that a particle blow-out of the Outpipe occurs (see chapter 3.8 and 5.4). Especially during the tests with increased hydrogen share in the gas flow (see chapter 4.1.5), the load of fine particles in the gas stream was so high that the filter often clogged early. The tests then had to be aborted to avoid a blow-out. To solve this problem, a new filter with a 20x increased filter area was designed and purchased. As this new filter was not yet tested at the moment of the writing of this text, its detailed description can be found in the outlook, chapter 7.1.

For quick and efficient *emptying* of the particle separator and *cleaning* of the filter, the lower part of the insulation can be removed easily and installed again very quickly (Fig. 74). Once removed the outer layer of the insulation, there is access to the cap at the bottom of the cone. When unscrewed, the separated particles fall out. Then, with the help of a manual valve (MV18) in a short-cut line particularly installed for this purpose, a *reverse* flow through the filter is applied that blows out a large part of the so-called filter cake, the dust accumulated on

⁶⁵ Whatman GF/D $\phi 257$ www.dicsa.es

⁶⁶ Superwool 607 HT Blanket (128 kg/m^3) <https://www.morganthermalceramics.com/>

the bottom side of the filter cloth. A baffle (Fig. 72 item (5)) protects the filter cloth from being damaged by the resulting gas jet. This maintenance process became part of the system preparation protocol in the morning before operation and could be done rather fast in less than five minutes. It avoids the laborious work of dismounting of the filter for replacement of the cloth.

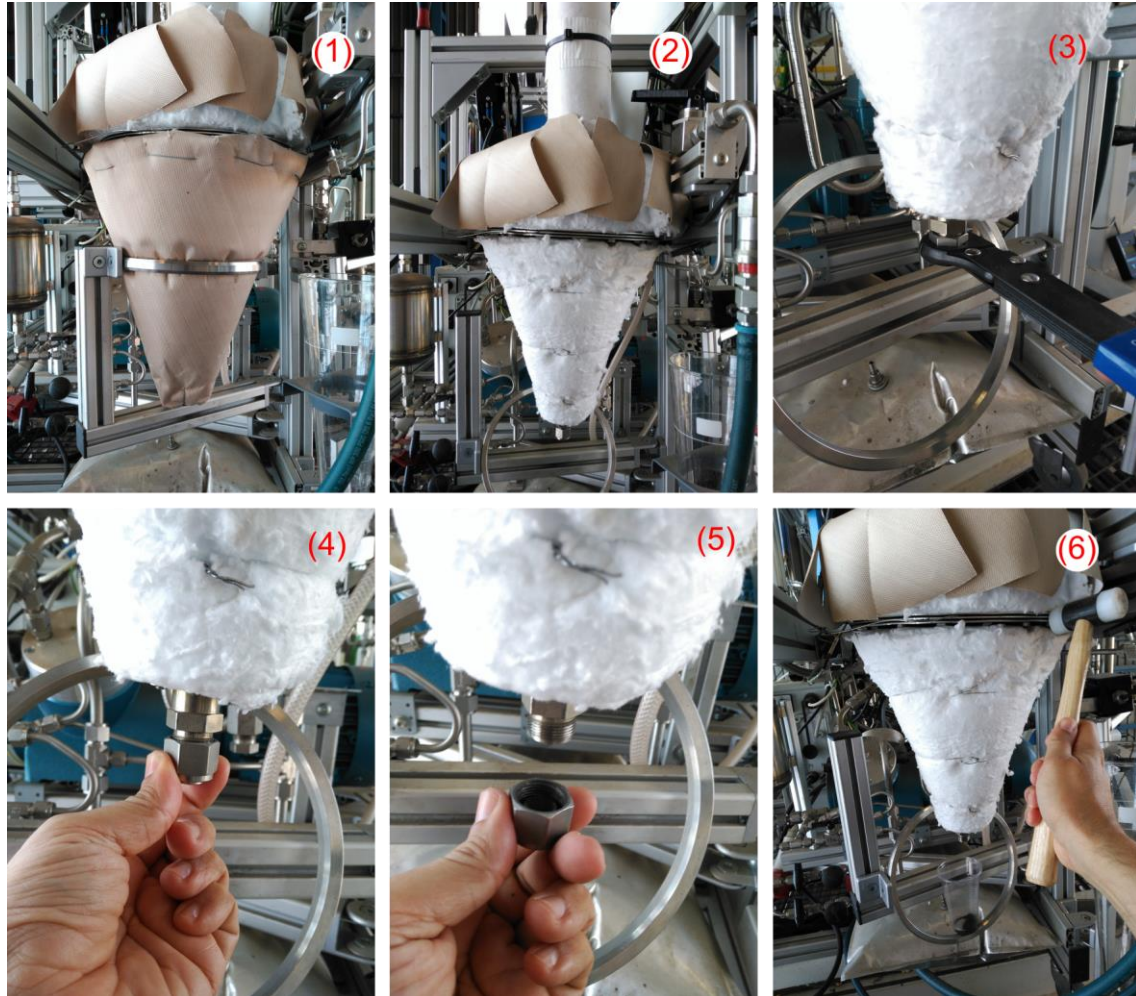


Fig. 74: Cleaning of the Particle Separator / Filter F3 by reverse flow flushing: (1) Particle separator fully insulated. (2) Outer insulation layer removed. (3)+(4) Opening of the bottom cap. (5) Removal of the cap with the accumulated particles. (6) Removal of the filter cake by reverse gas flow (by opening of MV18, see Fig. 41), supported by hammer strokes.

The cap at the bottom of the particle separator is the lowest point of the *first column* of the Oresol downstream section. This is where the residual solids are taken out of the off-gas stream.

3.9.3 Water Condensation

After leaving the filter, the gas is particle-free and still hot enough so that the water is only present in the gas phase. This means that the gas can be moved upwards through a long, thermally insulated pipe (item “(1)” in Fig. 68 on page 101) to the top of the second column of the downstream section without danger of segregation of one or several of its components. There it enters from the top into the second cooler (Fig. 75).

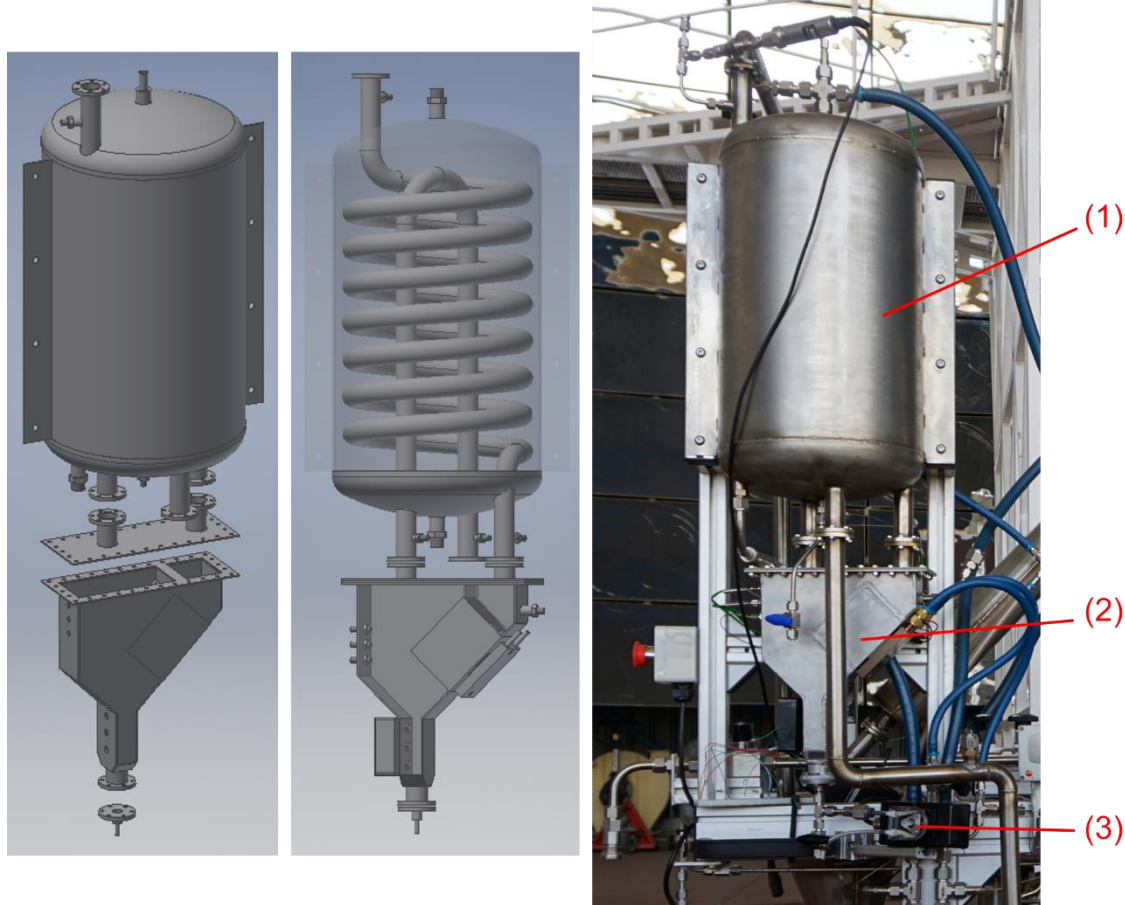


Fig. 75: Cooler-2 and water separator. Left: CAD model. Right: The hardware: (1) Cooler-2. (2) Water Separator. (3) Water Extraction Pump. The orientation of the pipes at the bottom of the Cooler-2 differs due to an error during fabrication (the mounting plates were welded to the housing at an incorrect angle).

This Cooler-2 (Fig. 76) consists of a 5-meter long, coiled tube, which is located inside a tank filled with cooling water. In this component, the off-gas is completely cooled down to ambient temperature (to be precise: to the temperature of the cooling water) and its water content is condensed. Since the entire piping system always maintains a downward slope, the water can nowhere accumulate undesirably. It leaves the Cooler-2 on the bottom along with the remaining gas.

The cooling water is injected tangentially at the bottom, so that it flows with a spin upwards through the water tank. Additional blades ensure that the water follows the gas pipe in countercurrent flow and prevent a short-circuit flow from forming. The water outlet at the highest point allows complete venting of air. An additional connection at the lowest point of the tank allows complete drain of the water if needed (e.g. to reduce weight when lifted with the crane).

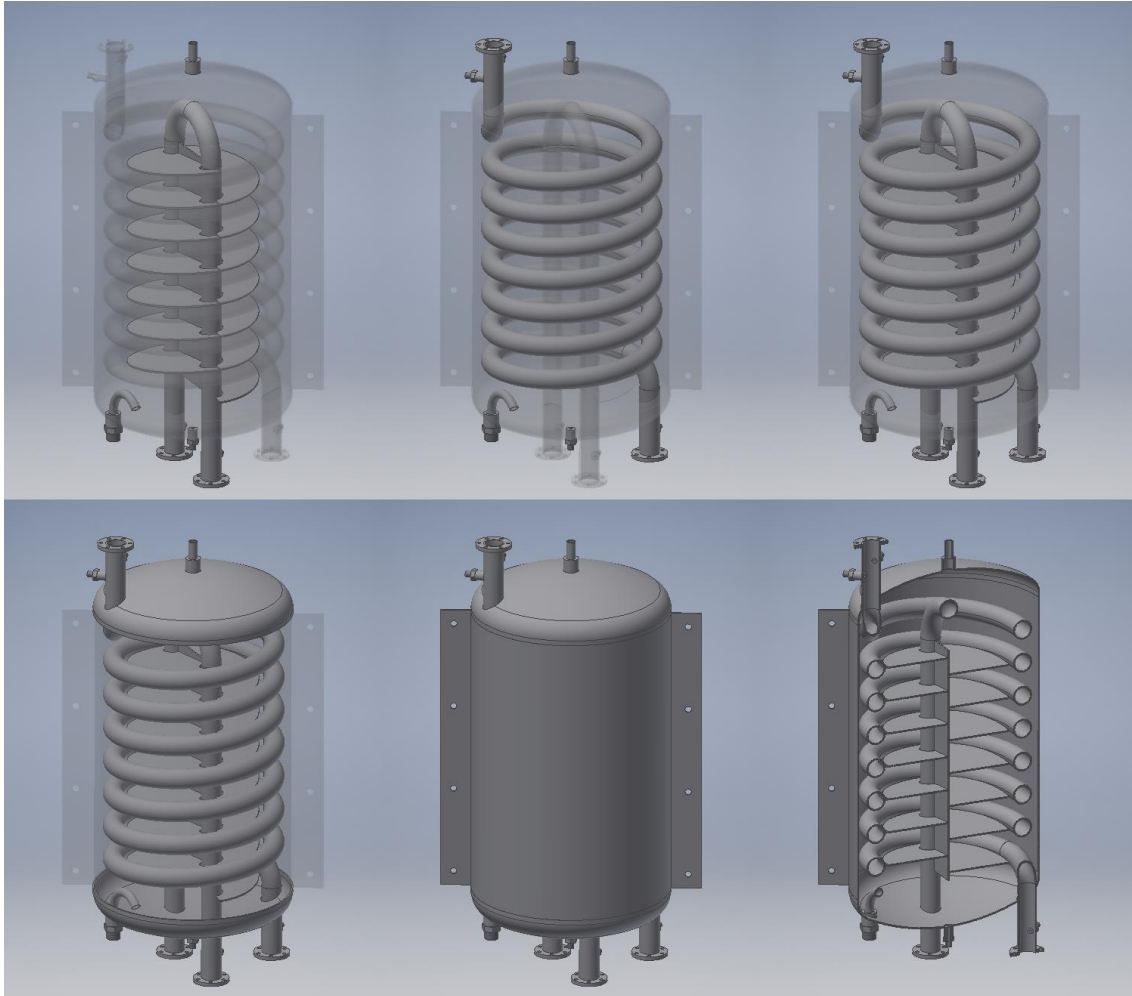


Fig. 76: CAD drawings of the Cooler-2. There are shown:

Top left: Reheater tube with water guiding blades.

Top center: Coiled off-gas tube with flange connectors and thermocouples fittings.

Top right: Reheater tube and coiled off-gas tube.

Bottom left: In addition top and bottom cap (torispherical (Klöpfer) heads).

Bottom center: Housing with mounting plates and gas tube connections.

Bottom right: Sectional view of the Cooler-2.

All views contain also the cooling water in- and outlet, and the water drain connector.

3.9.4 Water Separation

The water separator is located under the Cooler-2 (Fig. 75 in the previous chapter). Its working principle is separation by gravity of the denser (liquid) water from the much lighter gas. The design is shown in Fig. 77. The gas enters through a pipe from above, changes the direction of flow by 180°, and leaves the water separator through the other pipe on the top. Meanwhile, the liquid water settles in the lower part of the apparatus (arrows in Fig. 77). In order to extract the maximum amount of water from the gas stream, it contains an additional, thermoelectric cooling (TEC), realized by a Peltier element (Fig. 78 item (1)). The heat transfer from the gas is maximized by the use of a piece with cooling fins made of aluminum, normally applied for heavy duty cooling of computer CPUs (Fig. 78 item (3)). In fact, the Oresol water separator was designed literally around this commercially available heat sink. The heat generated at the hot side of the TEC is removed by a water cooler made of copper (Fig. 78 item (2)), also commercially available and normally intended for very high performance computer

cooling. As a result, the gas temperature can be lowered an additional 10 to 15 °C. This leads to somewhat increased water separation, and, more importantly, eliminates problems with condensing water in and after the Recirculation Pump P1.

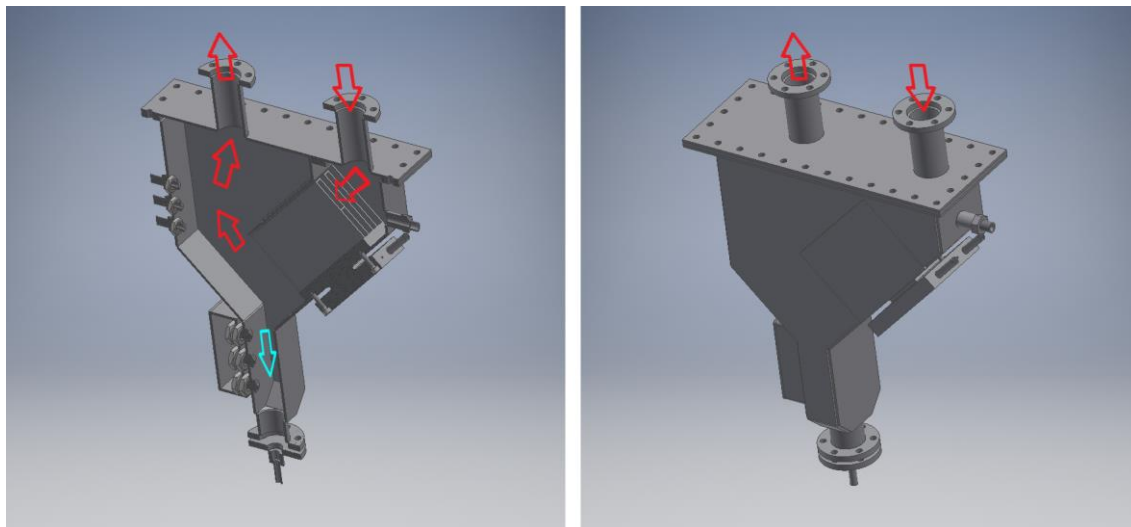


Fig. 77: Water Separator (CAD drawing). The two pipes on the top are the gas inlet (right pipe) and outlet (left pipe). The pipe on the bottom is the water outlet. The box on the bottom left contains the water level sensors. The three connectors on the left (top) are for thermocouples. The red arrows indicate the gas flow, the blue arrow represents the condensed water.

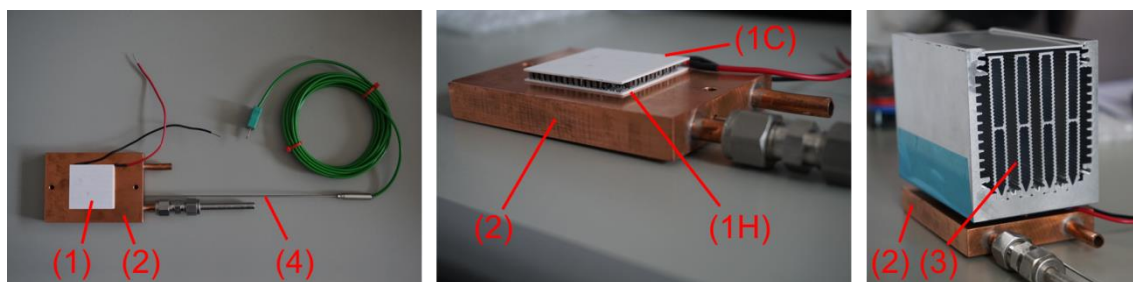


Fig. 78: Components of the active cooling of the water separator. (1) Peltier Element, with (1H) hot side and (1C) cold side. (2) Copper water cooler. (3) Radiator. (4) Thermocouple.

Fig. 79 (left) shows the device on the workbench during assembly. While the residual gas leaves the water separator cold (below ambient temperature) and saturated with water vapor (100% RH) at its top, the condensed water is collected in the lower area. There, three level sensors (Fig. 79 item (4) and Fig. 80 left) detect the presence of water. If a certain water level is exceeded, a small peristaltic pump (Fig. 79 right and Fig. 80 left) starts turning and extracts the product water to the outside. At this point, the lowest one of the second column of the downstream section, the water is collected in two so-called “Imhoff cones” (Fig. 80 right). Imhoff cones have a graduation that allows to reliably measure both large (up to 1 liter) and very small (under ½ ml) water quantities. The use of two cones enabled the separate collection of the product water from different phases of the test operation (e.g., heat up w/o H₂ vs. production w/ H₂). The quantity of product water is already determined during operation from the operating time and the flow rate of the pump (10.8 ml/min). The calculated values always matched better than 2% with the values read after the tests on the Imhoff cones.

During the measurement campaign in 2017, it turned out that the thermoelectric cooling system was somewhat overloaded when large quantities of water were produced. For this

reason, a passive pre-separation stage was designed, which was inserted between Cooler-2 and the original water separator. It consists of a simple, roughly Y-shaped gas guide, with the lower leg connected to the water outlet of the primary water separator. The already liquid water coming from the Cooler-2 can then flow directly into this pipe due to its higher density, while the remaining, moist gas takes the “normal” way into the original, actively cooled water separator for extra water extraction. This way, the unnecessary sub cooling of the already liquid water is avoided. Fig. 81 shows all components of the improved water separation unit.

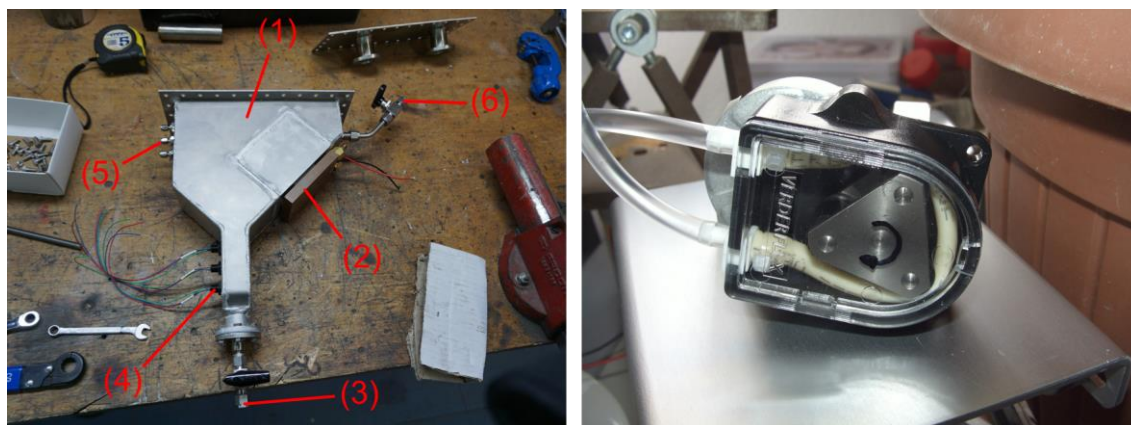


Fig. 79: Left: Water Separator. (1) Housing. (2) Copper water cooler. (3) Water extraction point. (4) Level sensors. (5) Thermocouples fittings. (6) Water feed (for testing purposes). Right: Peristaltic product water extraction pump.

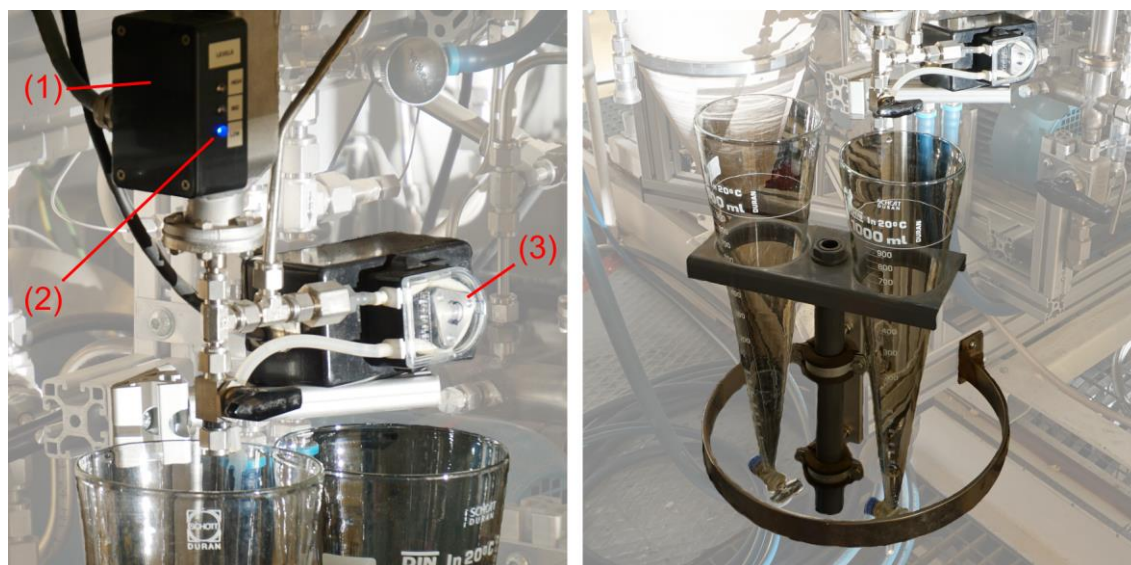


Fig. 80: Left: Level sensors housing (1) with indicator LEDs (2). Peristaltic product water extraction pump (3). Right: Product water deposits (“Imhoff cones”).

The valves of the Imhoff cones under the water separator are the lowest point of the *second column* of the Oresol downstream section. This is where the product water is taken out of the off-gas stream.

The cold, residual gas from the water separator, still saturated with water vapor, is returned to a pipe with the shape of the letter “U turned upside down” within the tank of the Cooler-2 (see Fig. 76 top left on page 107). This time, the aim is *re-heating* of the gas back to ambient temperature. This decreases the relative humidity in the gas to well below 100% (usually to

around 50%), with the important effect of reducing the risk of undesirable formation of water droplets in the components further downstream.

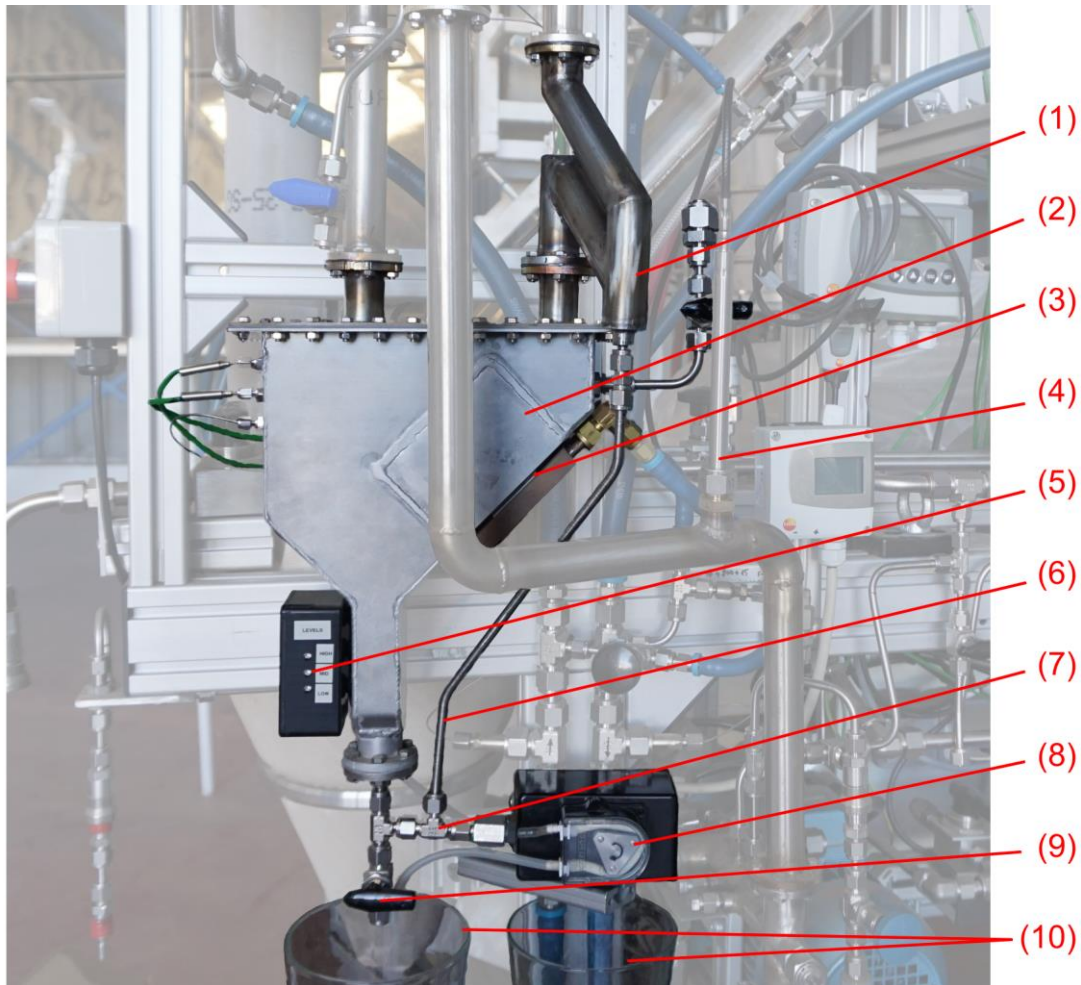


Fig. 81: Close view of the two-stage water separation system. (1) Water Separator Pre-Stage. (2) Water Separator. (3) Thermoelectric Cooler (Peltier Element). (4) Humidity Sensor. (5) Level Indicators. (6) Pre-Stage Water Line. (7) Water Lines T-Connector. (8) Water Extraction Pump. (9) Manual Drain Valve. (10) Water Collectors (Imhoff Cones).

3.9.5 Gas Analysis, Pressure Control, and Venting

Following the product water extraction part of the downstream section, various monitoring and control tasks of the now “dry, cool, and clean” gas are performed. These include:

- Measurement of relative humidity (since 2018)
- Measurement of the residual oxygen content
- Measurement of pressure
- Venting of surplus gas to the environment
- Recirculation of the gas (see chapter 3.10)

The measurement of the relative humidity (sensor see Fig. 81 item (4)) serves to monitor the effectiveness of the “reheater” and to predict possible problems further downstream. If the data differs from the calculated value, it’s a hint that something is going wrong with the water separation, and (in some cases) that the gas flow measurement of the recirculated gas has to be taken with care (more about this see chapter 3.10).

The residual oxygen content in the gas is measured with an oxygen partial pressure probe (Greisinger electronic GOX100), see Fig. 88 (left) on page 116. It's only read from time to time by the operator on a handheld display (and not automatically logged) to ensure that no (or few) residual atmospheric air is remaining in the system. As air contains nitrogen and oxygen that both can react with hydrogen, it could falsify substantially the results of the tests. For the future, it's planned to connect a gas chromatograph at this point to get detailed information about the gas composition at the exit of the downstream section.

To avoid air intrusion into the system, every part of the gas loop must work above ambient pressure. This is accomplished by the installation of a pressure control device at the gas vent. It turned out that an active pressure control, typically made with a sensor and a valve, is very hard to realize (and hence expensive), mainly because of the very low overpressure (a few millibar) that has to be maintained together with a gas flow variable over a wide range.

Therefore, a passive approach combined with manual intervention was chosen. It consists of a manual valve (MV12) in parallel with a check valve⁶⁷, see Fig. 82. In Oresol-jargon, this check valve was called "Gravity-Valve" or short "GValve", because it works with the help of gravity. This was chosen because ordinary check valves that work with springs were not available for a minimum opening pressure under 300 mbar. The pressure drop of the Oresol GValve is 10 mbar at an air flow of around 20 l_n/min and goes down to around 6 mbar when the flow approaches zero. (A reminder that this pressure is not equivalent to the pressure inside the reactor; to this, the pressure loss in the downstream section and especially in the filter has to be added.)

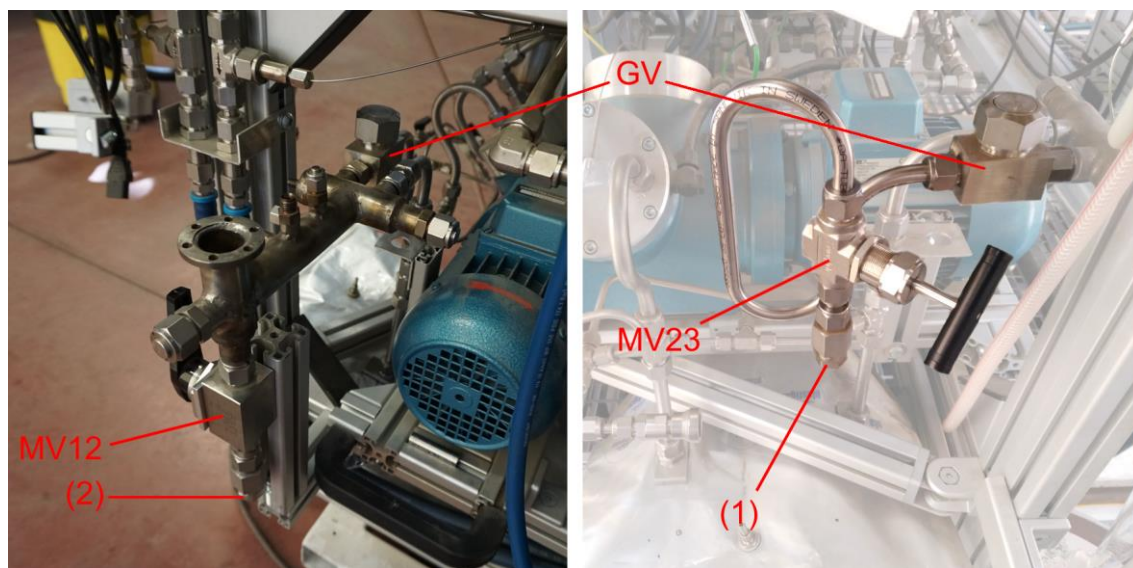


Fig. 82: Gas Vent (left: during assembly). GV: Check Valve ("Gravity Valve"). (1) Primary Vent with Manual Valve MV23. (2) Auxiliary Vent with Manual Valve MV12.

While the gas out flow is high (especially during start up with the system still cold), the additional manual MV12 valve must be open to avoid overpressure in the reactor. This valve can also be semi-closed to adjust the pressure during intermediate flow phases. A manometer with a dial close to the manual valve helps the operator to easily adjust the pressure to the desired value. Once the flow is low enough, the manual valve is closed completely. From this

⁶⁷ Swagelok SS-5858 Stainless Steel Lift Check Valve, 2.20 Cv, ½"

moment on, the pressure before the vent is passively determined by the drag coefficient of the gravity valve.

The vent itself is a simple $\frac{1}{2}$ "-pipe that is, like all other gas vents of the system, pointing downwards and equipped with a mesh to avoid the intrusion of dirt, insects, and all other kind of unwanted things.

3.10 Gas Recirculation

During the initial phase of the Oresol project, due to simplicity, gas recirculation was not foreseen. But rather soon it turned out that the consumption of gas other than air would be prohibitively high, in the order of one gas bottle with a capacity of 10 m³ of argon per testing day. Therefore, recirculation was included into the system.

The Recirculation Pump P1 (Fig. 83) is a diaphragm pump type PM26138-186 from the company KNF Neuberger (Freiburg, Germany)⁶⁸. This type of pump was chosen because it is hermetically sealed and therefore allows the safe displacement even of explosive gases such as hydrogen. To reduce the influence of the pressure surges of the pump on the rest of the system, a small buffer tank with a volume of 2 liters was attached to the pump outlet.

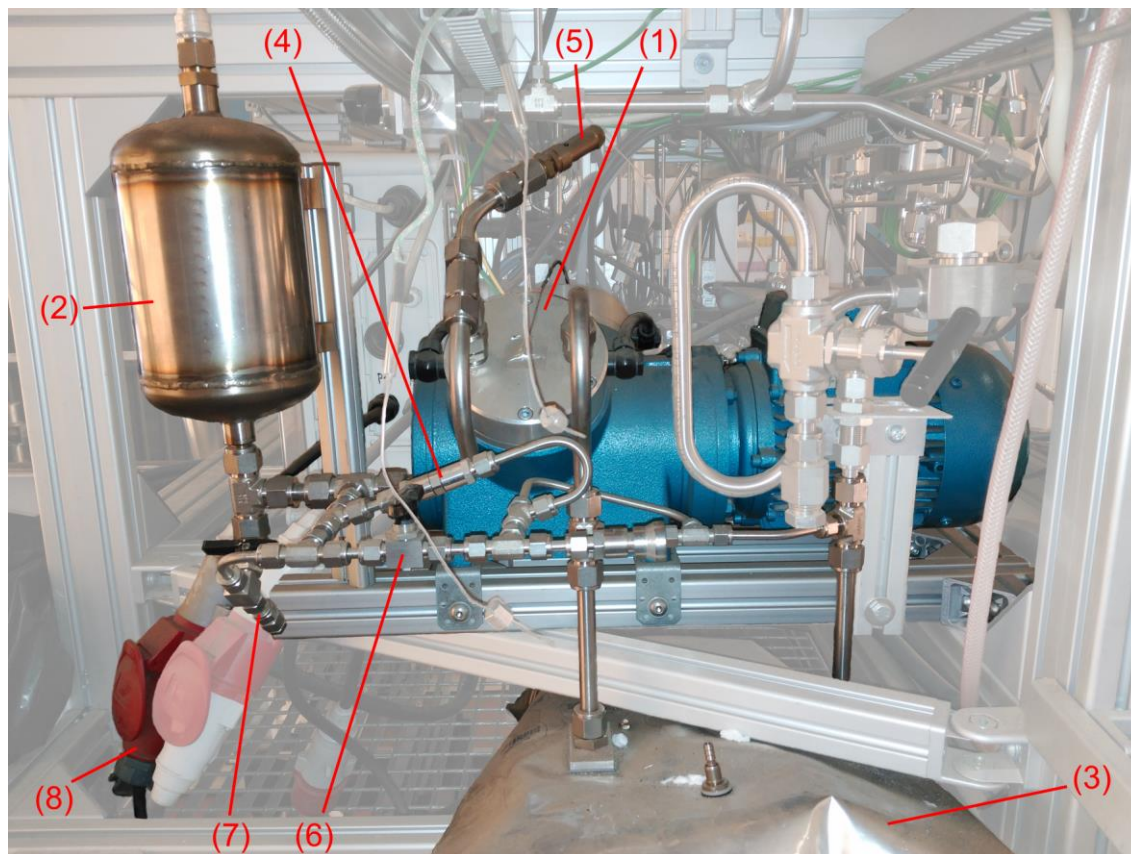


Fig. 83: Components of the gas recirculation. (1) Diaphragm Pump P1. (2) Buffer tank. (3) Gas bag. (4) Adjustable overpressure protection valve. (5) Emergency pressure relief valve. (6) Manual shortcut valve MV13 (updated version see Fig. 86). (7) Vent. (8) Three-phase power supply.

⁶⁸ <https://knf.com/en/global>

At the inlet there is a 27-liter gas bag (Fig. 84). Since this bag has a variable volume, this way, undesirable negative (below ambient) pressure is avoided during nominal operation. In fact, the gas bag is usually inflated like a balloon with the pressure established by the “GValve” described in chapter 3.9.5. In case of an emergency, for example when the gas flow from the downstream section stalls due to an Outpipe particle blow-out (see chapter 3.8), it takes more than 20 seconds for the pump to empty the gas bag, enough time to detect and identify the problem and to take adequate measures (e.g., turn off the pump). This reliably prevents air from entering the system.

The pump has a maximum capacity of 50 l_n/min in the case of operation with no counter pressure. The maximum operation pressure is 7 bar, in this case the flow is reduced to 10 l_n/min. This means that during start up (with high gas flow demand), the flow from the pump is not sufficient and must be supported from the external source. Once the fluidized bed has reached operation temperature, the opposite happens; the flow from the pump must be throttled (see chapter 5.1).

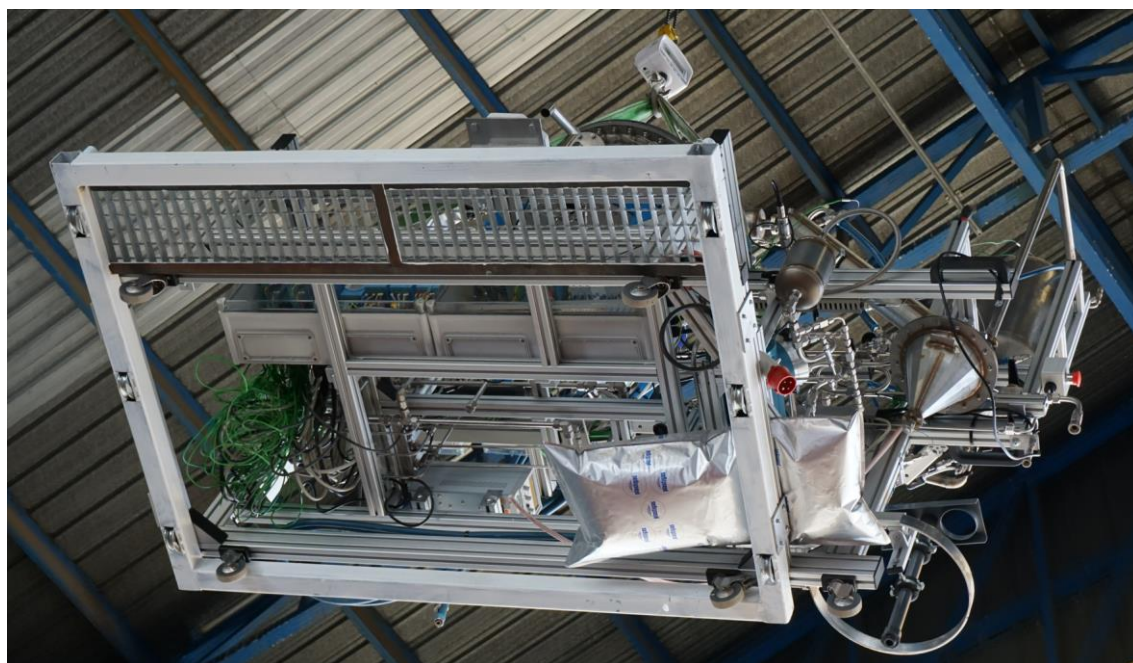


Fig. 84: Bottom view of the Oresol system. This unusual view of the system hoisted by the crane for installation shows nicely the position and dimensions of the buffer gas bag.

This brings two problems with it. The first one is that the low pressure gas flow is not suitable for the flow controllers, they need a supply pressure of 4 to 5 bar. Therefore, two additional flow sensors (Fig. 85) with negligible pressure drop but no control ability were installed. One of them (FT07) measures the gas flow from the pump to the main fluidized bed and the other one (FT08) the flow to the window protection system.

The other problem was more subtle. It has to do with the residual humidity in the recirculated gas. The original way to throttle the flow were two valves (MV21 and MV22) connected in series in front of the flow sensors. These valves were manually adjusted to the desired flows, at the expense of an increased pressure between the pump and the valves. It results that the *partial* pressure of the water vapor in the gas increases proportional to the pressure increase of the gas. But the *saturation* pressure for steam does NOT increase (it depends only on the temperature) and hence, when exceeded in the pump, droplets of liquid water form. These

droplets then do not evaporate fast enough after having passed through the valves and enter into the flow sensors, where they cause wrong readings.



Fig. 85: The two flow transmitters (blue) for the recirculated gas.

The solution for this problem was implemented at the end of the 2017 test campaign. It consists of a modification of the way how the gas flow of the pump is reduced. The two manual valves in front of the flow sensors remained, but are used now solely to fine tune the distribution of the flow between the two lines. In fact, MV21 is always completely open, while MV22 adjusts the window protection gas stream to the desired fraction. The total flow is adjusted now by a series of short cut valves installed close to the pump (Fig. 86). This way, the output of the pump can be regulated manually without increasing the pressure and provoking the saturation of the residual water vapor in the flow. Four valves allow the pre-adjustment of two different reduced flow rates through the bellows valves MV13c and MV13e; and during operation they can then be adjusted quickly and repeatedly by simply opening (or closing) the ball valves MV13b and MV13d. The access to the short cut valves is possible and safe even during solar operation. Another possible option to solve this problem, the regulation of the

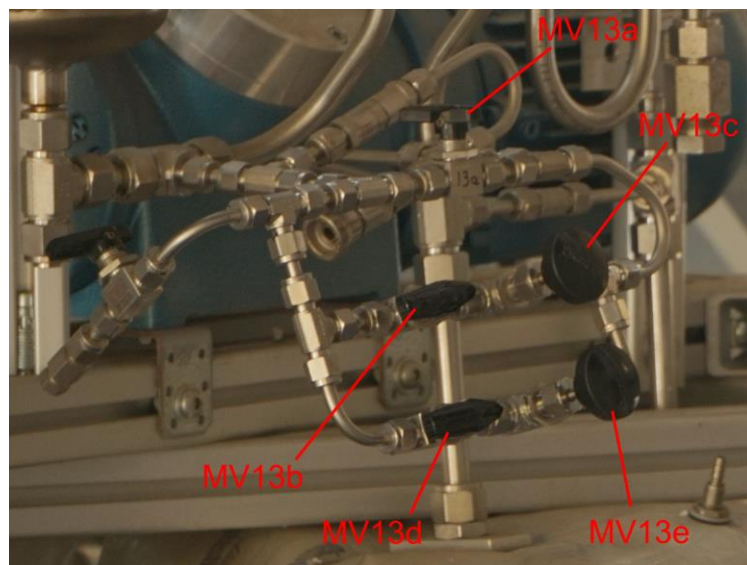


Fig. 86: Short cut valves for rapid and repeatable adjustment of the recirculated gas flow.

flow by reducing the pump speed, was not recommended by the manufacturer, because then the proper cooling of the electric motor by the fan mounted directly on the motor is no longer guaranteed.

The recirculated gas is used for the main fluidized bed and for the window protection gas. The other auxiliary gas streams are always supplied from the external gas installation of the Solar Furnace. The reason is, besides additional cost and complexity for more low pressure flow sensors, that this way, there is at all the time a slight excess of gas in the system, making the passive pressure control with the check valve possible.

3.11 Electrolyzer

At the very beginning of the Oresol project, an electrolyzer (Fig. 87) was purchased. Its task is to split the product water from the solar reactor into hydrogen and oxygen according to eq. (2) on page 26. For budget reasons, however, it was not possible to buy a device with the full capacity required. Instead of the 16 l/min hydrogen production originally expected for nominal operation, the unit delivered only one. Nevertheless, it was considered useful for end-to-end demonstration of the entire process. A special feature that was particularly taken into account was that the oxygen produced could also be collected.

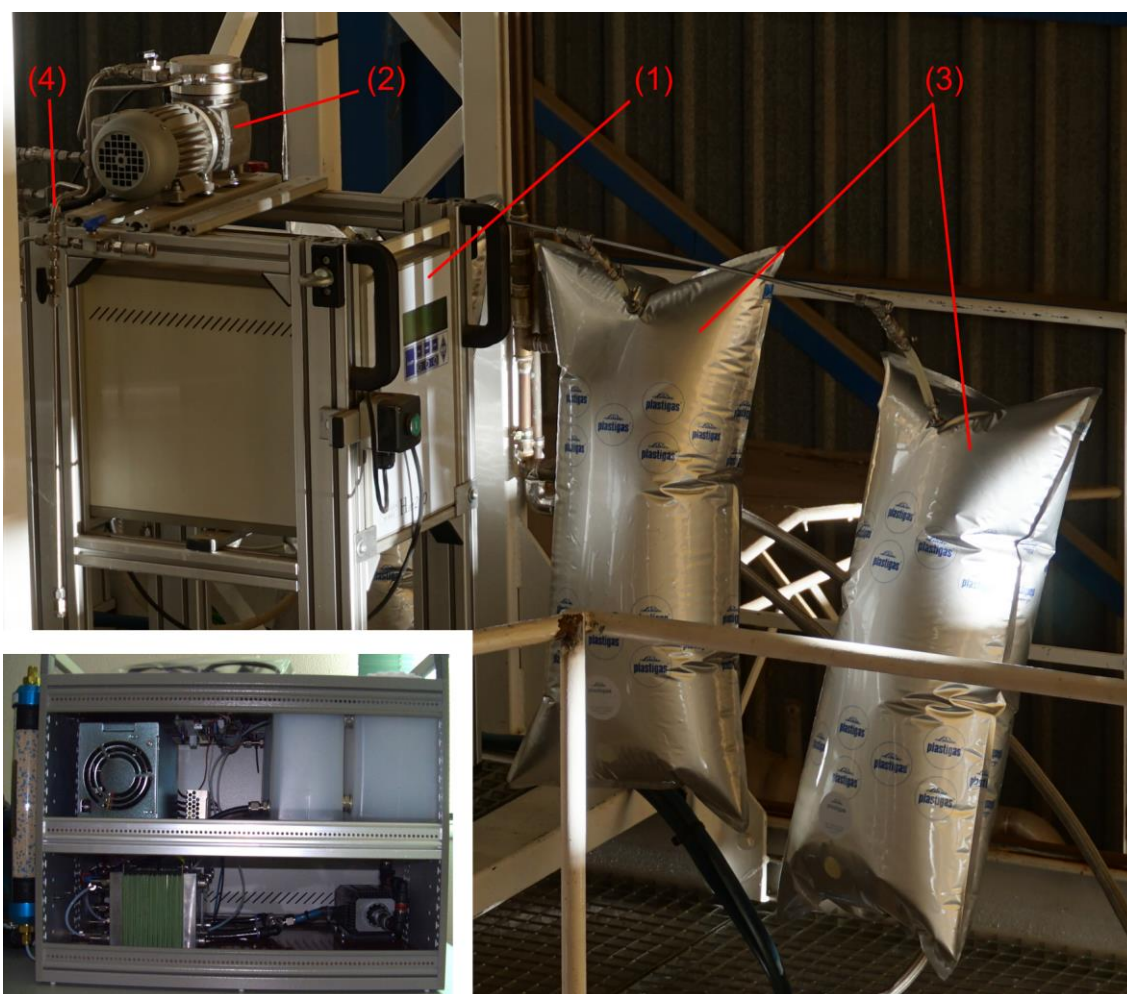


Fig. 87: (1) Electrolyzer. (2) Hydrogen pump. (3) Hydrogen storage (gas bags). (4) Oxygen outlet. The inset on the bottom left shows the inside of the electrolyzer.

Since the electrolyzer releases the hydrogen at near ambient pressure, a small diaphragm pump (type PM26139-022 from the company KNF Neuberger, Freiburg, Germany⁶⁸) was installed. Initially one, and later up to three gas bags, with a volume of 27 liters each, were used to store the hydrogen. The oxygen was fed directly from the electrolyzer into a gas bag or alternatively vented to the ambient air. While pure oxygen was detected by the measuring device mentioned in chapter 3.9.5 (Fig. 88 left), purity of hydrogen was simply tested by means of small balloons (Fig. 88 right). If they rose upwards, then it was (mostly) pure hydrogen!



Fig. 88: Sensors for oxygen (left) and hydrogen (right).

Nevertheless, the electrolyzer did not produce the expected amount of hydrogen and oxygen, probably due to the storage time of several years, and additionally because of an operating error at the beginning. In order to still be able to carry out reasonable experiments, the electrolyzer was finally replaced by a gas bottle.

3.12 Support Structure

The support structure of the whole experiment is made by an aluminum profiles building kit system from the company item Industrietechnik GmbH (Solingen, Germany)⁶⁹. This system allows for a fast and very flexible construction of the supporting structure.

The biggest challenge at the beginning was the presence of the old, massive 3-axes testing table that was used since decades for smaller solar experiments in the Solar Furnace. As this table was not removable, the Oresol experiment had to be designed “around” it. The center of the table marked the focal plane of the concentrator. As Oresol uses a diagonal mirror with a vertical ray path of 500 mm, it had to be installed 500 mm in front of the table (in the direction of the concentrator). Fig. 89 left shows the first fit test of this configuration.

However, due to increasing technical problems and the high age of the test table, the management of the solar furnace decided to remove the table and replace it with a modern construction. But as the construction of the Oresol experiment was already very advanced, no significant changes were made to the frame. When the experiment was placed on the test platform for the first time (Fig. 89 center), another problem arose: the steel plates under the wheels gave way slightly under the weight, which, as long as work was being carried out on the

⁶⁹ <https://www.item24.de/en/index.html>

system, led to constant slight swaying. Although the problem was tolerable in principle, the solar furnace management decided to radically modify the test platform. The result were two ultra-stable rails on which future experiments can be moved easily back and forth on wheeled carts with high precision. In addition, the working platform has been extended both to the north and south, this way providing better access to the experiment and storage room for temporarily unused devices. A new, modern three-axis table has also been integrated. It is now fully retractable, so that larger experiments no longer collide with it. The support structure of the Oresol experiment then obviously had to be adapted to the new geometry, in particular the system had to be "lowered". This was finally achieved without dismantling the components (Fig. 89 right).



Fig. 89: Evolution of the test platform. Left: Original state with the old 3-axes table (Feb 2011). Center: Flat surface still with the steel sheet floor but the table dismantled (May 2015). Right: Current state with robust precision rails (March 2017).

Fig. 90 shows the evolution of both the support structure and the test plant over the years. On the left, the structure is still clearly visible below the reactor with the original rudimentary downstream section. On the right, one can see that the main trusses are still largely identical, but that the now complete downstream section has extra support, and in particular that the legs have been replaced by the white cart.

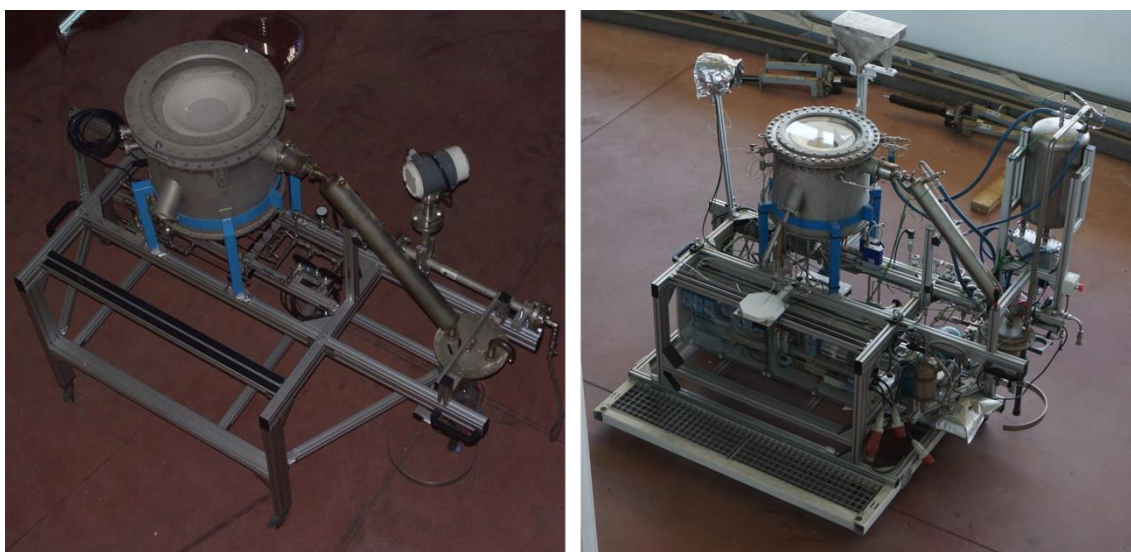


Fig. 90: Support structure of the Oresol experiment. Left: end of 2011, right: 5 years later.

The entire system weighs about 450 kg and can be lifted onto the test platform (and down again) by the crane of the solar furnace building within a few minutes (see Fig. 91 and Fig. 84

on page 113). In fact, the complete setup including diagonal mirror and connection of all water, gas, power and data lines can be completed within half a work day.



Fig. 91: Lifting of the entire Oresol experiment onto the test platform of the Solar Furnace

3.13 Instrumentation

The Oresol test facility is equipped with more than 100 sensors. It contains a total of 80 thermocouples, 6 flow controllers and 2 additional flow transmitters, 2 load cells, 15 pressure sensors, 1 humidity sensor, 1 hydrogen sensor, 3 water level indicators, and 7 digital outputs for the control of 3 pumps (recirculation, hydrogen from electrolyzer, and water extraction), 2 fans, the electrolyzer, and the Peltier element (TEC). In addition, the Solar Furnace infrastructure provides data for solar radiation (DNI), weather (temperature, pressure, wind speed and direction), and the position of the shutter. For a complete list see Appendix A.5.

3.13.1 Temperature

All 80 thermocouples are of type K (Ni-CrNi) with a temperature range for continuous operation from 0 °C to 1100 °C and a sheath diameter of 1.5 mm. Exception are TC20, TC24, and TC25 with a diameter of 1.0 mm due to a manufacturing error when welding the fittings to the reactor housing. The thermocouples were purchased from the Spanish company SEDEM and the British suppliers ThermalComp and CAAFT. Fig. 92 shows the connections on the electrical cabinet. A list of all thermocouples can be found in Table 16 in the Appendix A.5.



Fig. 92: Sockets for 80 thermocouples and 27 analog sensors on the backside of the electrical cabinet.

3.13.2 Gas Flow

The six gas flow *controllers* (Fig. 93) are from the EL-FLOW® series of the company Bronkhorst. They are Thermal Mass Flow Meter/Controller for Gas working with a by-pass design⁷⁰. In thermal instruments based on the bypass principle, only part of the gas stream flows through the sensor. The (bypassed) gas stream through the sensor is warmed up by two heaters and the temperature of the tube is measured at two points. When the flow increases, the temperature at the first measuring point will decrease, as the fluid carries away the heat. At the same time the temperature at the second measuring point will increase as the fluid carries heat to it. The resulting temperature differential is directly proportional to the mass flow. This signal is then compared with the set point and the subsequent valve is adjusted accordingly within a few milliseconds. These sensors have a high accuracy of $\pm 0.2\%$ FS (full scale) and need a working pressure on the supply side in the order of 5 bar.

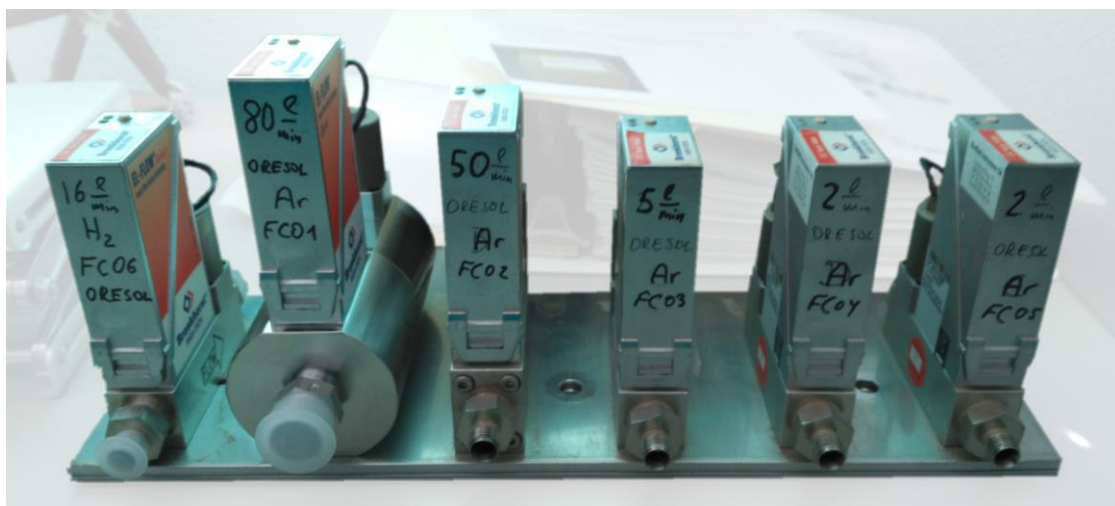


Fig. 93: The Oresol flow controllers

The two gas flow *transmitters* (Fig. 85 on page 114) are from the Mass-Stream® series of the company M+W Instruments, member of the Bronkhorst Group. They are also thermal mass flow meters, but working with a direct through-flow measurement following the constant temperature anemometer principle. The main difference is that the flow is measured directly in the main gas stream without bypass, and instead of evaluating the temperature difference,

⁷⁰ <https://www.bronkhorst.com/int/service-support-1/technologies/thermal-mass-flow-sensor-for-gases-bypass-principle/> <https://www.youtube.com/watch?v=G62ma2IFh9o>

the heating power is adjusted to keep the temperature difference constant. These devices have a moderate accuracy ($\pm 2\%$ FS), but their huge advantage is that their pressure loss is mostly negligible.

All flow sensors except FC06 are calibrated for argon. For operation with air, a conversion factor has to be applied, resulting in a reduction of the available range of the flow sensors. Before October 2017, FC01 was calibrated for a mix of 95% argon with 5% hydrogen (for the reason see chapter 3.3.1). Therefore, an additional conversion factor had to be used during this period when working with pure argon. All these factors were provided by the manufacturer. Table 4 lists the flow sensors purchased for the Oresol plant.

Name	Gas	Range (l _n /min)	Conv. Factor (Ar → Air)	Description
FC01	Argon(*)	2-100 (95%Ar5%H ₂) Since Oct2017: 1.6-80	1/1.38	Main bed fluidization gas
FC02	Argon	1-50	1/1.38	Window protection gas
FC03	Argon	0.04-2.0 Since Aug2014: 0.1-5.0	1/1.38	Outpipe fluidization gas
FC04	Argon	0.04-2.0	1/1.38	Inpipe fluidization gas
FC05	Argon	0.04-2.0	1/1.38	Standpipe fluidization gas
FC06	Hydrogen	0.04-2.0 Since Oct2017: 0.32-16	N/A	Main bed hydrogen supply
FT07	Argon	1.2-60	1/2.1	Main bed fluidization gas (recirculated)
FT08	Argon	1.2-60	1/2.1	Window protection gas (recirculated)

Table 4: The Oresol flow controllers (FC01-FC06) and transmitters (FT07-FT08).

(*) Before October 2017, FC01 was calibrated for a mix Ar+5%H₂. For operation with pure argon, the flow had to be divided by 0.874. Hence, the maximum range was 114 l_n/min.

3.13.3 Solids Flow

The flow rate of the solid particles is determined with the help of two “mass transmitters” made out of single point load cells integrated into the support structure of the particle containers. As load cells, the model H10A from the company Bosche⁷¹ was used. These load cells work on the principle of a double bending beam with the help of strain gauges. The mass flow rate is determined by the difference between two measurements taken one minute apart (see chapter 3.7 and page 133 ff. in chapter 3.14.2). Table 5 lists the mass sensors installed in the Oresol plant.

Name	Range	Description
MT01	0-10 kg	Particle Feed Hopper
MT02	0-10 kg. Since Jan2018: 4x 20kg.	Particle Outlet Bucket

Table 5: The Oresol mass sensors.

⁷¹ <https://www.bosche.eu/waagenkomponenten/waagezellen/plattform-waagezellen/plattform-waagezellen-h10a>

3.13.4 Pressure

A total of 15 pressure sensors are installed in the Oresol plant. All but one of them are the model 8323 from the company Bürkert⁷². All parts of these sensors that are in contact with the measured fluid are made of stainless steel 1.4571 (AISI 316Ti) and are completely welded (no seals). This allows operation with most fluids, including hydrogen. The accuracy is $\pm 0.5\%$ FS (full scale). Twelve of them, named “PTxx”, measure relative pressure (against the atmosphere), the other two, named “PATxx”, absolute pressure (against vacuum).

The remaining sensor (PDT08) is a differential pressure transmitter model Testo 6321⁷³. The accuracy is $\pm 1.2\%$ FS. It was chosen because initially it was believed that at its location at the inlet of the Recirculation Pump P1, a negative (below ambient) pressure could occur. Finally, due to the installation of the buffer gas bag (see chapter 3.10), this was not necessary. Furthermore, it has a display mounted directly on the sensor, which helps for adjustment of the manual purge valve MV12. Table 6 lists the pressure sensors installed in the Oresol plant.

Name	Range	Description
PT01	0-160 mbar	Pressure Main Bed Fluidization Gas
PT02a	0-100 mbar	Pressure Reactor Freeboard (Sensor a)
PT02b	0-100 mbar	Pressure Reactor Freeboard (Sensor b)
PT03	0-160 mbar	Pressure Outpipe Fluidization Gas
PT04	0-250 mbar	Pressure Inpipe Fluidization Gas
PT05	0-10 bar	Flow Controllers Supply Pressure
PT06	0-10 bar	External Gas Supply Pressure
PT07	0-10 bar	Recirculation Pump Discharge Pressure
PDT08	-100-100 mbar	Recirculation Pump Inlet Buffer Bag Pressure
PT09	0-100 mbar	Cooler2 Inlet Pressure
PAT10	0-1000 mbar(a)	Ambient Pressure
PT11	0-250 mbar	Pressure for HiFlowCalc Main Bed Fluid. Gas (*)
PT12	0-160 mbar	Pressure Window Protection Gas
PATE	0-1000 mbar(a)	Electrolyzer Hydrogen Bag Pressure
PTH2	0-10 bar	External Hydrogen Supply Pressure

Table 6: The Oresol pressure transmitters. (*) For the use of PT11 see page 72.

3.13.5 H₂O and H₂

The *water extraction Pump P3* (Fig. 79 right on page 109) is a peristaltic pump that also serves to *measure* the extracted product water. The model M045 from the manufacturer Verderflex⁷⁴ was acquired. While the nominal value is 12 ml/min, a real flow rate of 10.8 ml/min was determined by preliminary tests. The pump is activated when the level within the Water

⁷² <https://www.buerkert.de/de/type/8323>

 <https://www.burkert.com/en/Media/plm/DTS/DS/DS8323-Standard-EU-EN.pdf?id=DTS00000000000000001000011112ENS>

73 <https://www.testo.com/en/testo-6321-differential-pressure-transmitter-accuracy-1-2/p/0555-6321> <https://static-int.testo.com/media/73/ca/2872fcfe4234/testo-6321-EN.pdf>

⁷⁴ <https://verderflex.com/en/peristaltic-oem-pumps>
https://www.verderflex.com/fileadmin/files/verderflex/documents/Verderflex_Technical_Datasheet_s/OEM/PDF/M045.pdf

Separator (WS2) rises above an optical liquid level switch. These level switches are very compact and have no moving parts. Simply by measuring the operation time of the pump, it is possible to follow the water production quite accurately during the experiments.

A *humidity sensor* RHT (relative humidity transmitter) is located at the exit of the reheater pipe of the Cooler C2 (see chapter 3.9.4 and 3.9.5). It's the model testo 6651 with the cable probe 6605⁷⁵. The probe contains a capacitive humidity sensor contained in a stainless steel shaft directly immersed in the gas stream. The measurement uncertainty is $\pm 1.7\%RH$. It was available as of October 2017, but broken since mid-2019.

The *hydrogen sensor* H2CT (H_2 concentration transmitter) was intended to measure the hydrogen concentration in the feed gas of the fluidized bed reactor (Fig. 94). With its help, the hydrogen fraction that was not consumed in the reaction should be determined. For this, the model BlueSens BCP-H2 was purchased⁷⁶. The measuring principle is a thermal conductivity detector calibrated for the binary gas argon/hydrogen. The range of the sensor is from 0 to 50 % (vol) with an error $<0.2\%$ (full scale) $\pm 3\%$ (reading). Unfortunately, the sensor never gave satisfactory results. It only returned readings when the (calculated) hydrogen proportion was above about 7%, and it remained unclear to what extent the data could be trusted and how they might be interpreted (see also chapter 4.2.7).



Fig. 94: Hydrogen sensor in the reactor feed gas line.

3.13.6 A/D-Converters

Analog-digital converters are necessary in order to send the data of the measuring instruments to the control computer. For Oresol, the ADAM-4000 Remote Data Acquisition Module Series from the company Advantech⁷⁷ was chosen, mainly for its relatively inexpensive price. Modules for thermocouples signals, for analog input (4-20mA) signals, for analog output (4-20mA) signals, for digital in- and output, and for the conversion of the serial communication

⁷⁵ <https://www.testo.com/en-US/testo-6651/p/0555-6651>

<https://static-int.testo.com/media/ea/eb/f0b618a31bc7/testo-6651-EN.pdf>

⁷⁶ <https://www.bluesens.com/products/gas-analyzers/hydrogen-sensor-bcp-h2>

https://www.bluesens.com/fileadmin/user_upload/downloads-products/BCP-H2/BCP-H2%20Data%20sheet%20EN.pdf

⁷⁷ <https://www.advantech.eu/>

<https://www.advantech.eu/search/?q=ADAM%2B4000&st=product&sst=Products>

among the modules to the Ethernet standard for communication with the control computer are installed. The electrical cabinet is shown in Fig. 95, the A/D-converters are listed in Table 7.

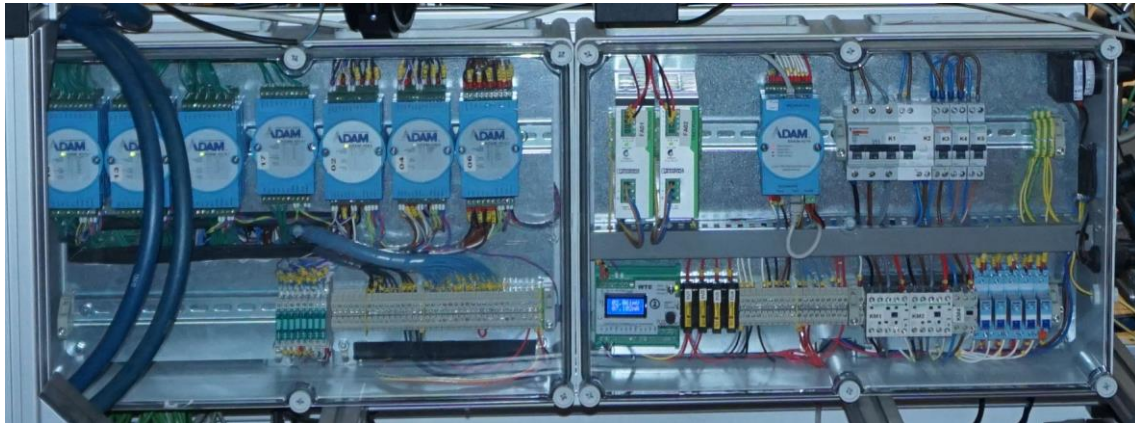


Fig. 95: Electrical cabinet ("EBox") of the Oresol plant. In the left box the A/D-converters, in the right box the DC-power supply, the digital I/O and the Ethernet module, relays for the pumps and the electrolyzer, fuses, and the electronics for the load cell MT02.

Qty.	Name	Sensors	Description
4	4017+	FCs, FTs, PTs, MTs, RHT, H2CT	8x input 4-20mA analog signal
10	4018+	TC01-TC80	8x input thermocouple type K signal
2	4024	FC01-FC06 set point	4x output 4-20mA analog signal
1	4055	Output: P1-P3, Ely, Fans, TEC Input: Level switches, Ely, E-Stop	8x output digital signal 8x input digital signal
1	4570	N/A	Serial to Ethernet Interface

Table 7: A/D converters of the Oresol data acquisition system.

Due to the large quantity of sensors and the low prize of the modules, the data transmission rate was relatively low, about one data set every 2-3 seconds. This is no issue during normal operation, but in case of an emergency, especially if a rapidly changing value is involved, a faster data transmission would be helpful.

3.14 Control Software

The transmission of the data from the experiment to the computer in the control room (Fig. 96) is done via Ethernet cable. The data acquisition and control program is programmed in the visual programming language *LabVIEW* developed by the company National Instruments⁷⁸. *LabVIEW* is the acronym for **L**aboratory **V**irtual **I**nstrument **E**ngineering **W**orkbench. A *LabVIEW* program is termed *Virtual Instrument* or short *VI* (pronounced: /'vi: 'aɪ/). This is because the programs consist of two components comparable to an ordinary physical measuring instrument: The *Front Panel* that contains the user interface (the "buttons and dials and displays"), and the *Block Diagram* with the graphical program code that contains the functionality (the "inside of the instrument" with "electronics and cables"). Furthermore, a *VI* can also call other *VI*s, which are then referred to as sub-*VI*s. A *LabVIEW* *VI* is not processed by an interpreter, but compiled, which makes the performance comparable to other high-level languages.

⁷⁸ <https://www.ni.com/> <https://www.ni.com/labview>

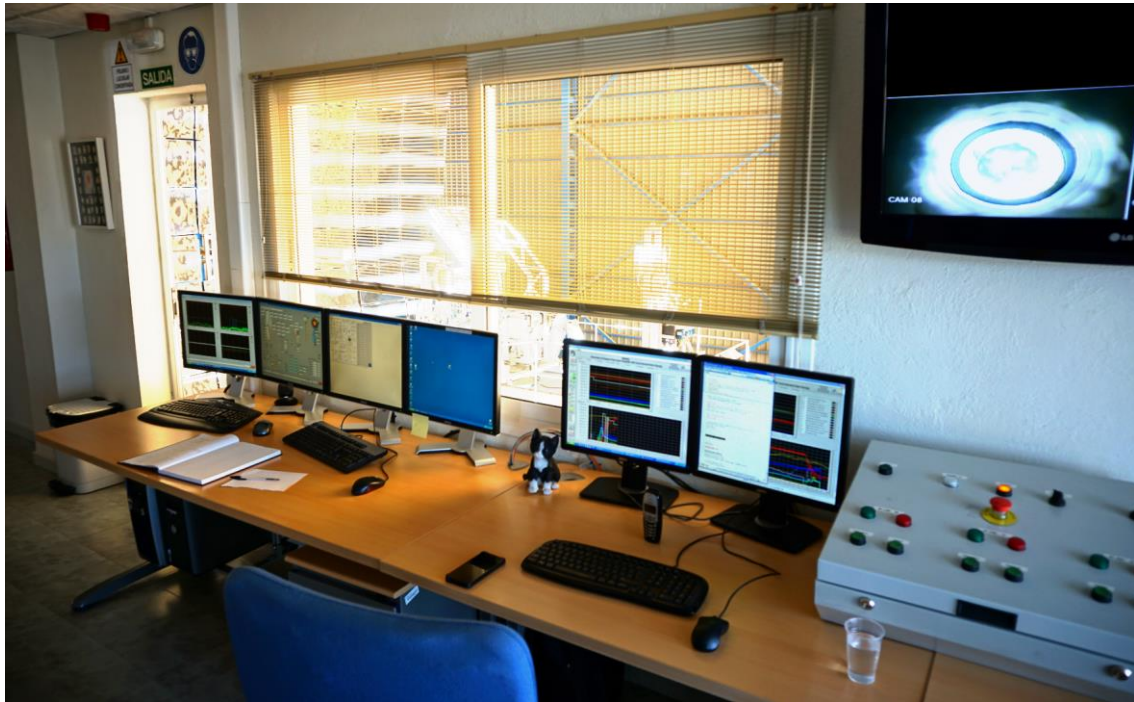


Fig. 96: View of the control room of the PSA Solar Furnace SF-60. The screens on the left are for weather, shutter, and heliostat, the two screens in the center are for the Oresol system. On the top right a camera view of the experiment.

The Oresol process is controlled by the master-VI named "*Oresol.vi*", together with 22 sub-VIs and 19 VIs for the transfer of the global variables from the A/D-converters and the Solar Furnace computer. The program fulfills the following tasks:

- Numerical and graphical visualization of the data.
- Calculation of additional useful data, such as average, minimum and maximum temperatures, gas, liquid and solids flows and consumption, solar power, gas concentration, product water quantity, reaction progress, and so on.
- Manual setting or automatic calculation of the set points of the flow controllers, on/off switching of pumps and fans.
- Alarms handling.
- Data logging.
- ... and many more.

Furthermore, the *Oresol.vi* offers a simulation mode. The development of the complete Oresol control software was an important part of this work.

3.14.1 Front Panel

The Front Panel of the Oresol VI (Fig. 97) consists of two parts. On the left, under the picture of the Moon, is a quite narrow stripe with permanently visible data. The remaining, major part of the screen contains a tab sheet with 8 tabs (pages).

The permanent stripe includes the Emergency Stop button, a display of date and time (in UT), alarm information and acknowledgement, the logger and simulator-mode status, and numerical displays for solar radiation (DNI), average temperature of the reactor, freeboard

pressure (PT02) and calculated gas velocity over minimum fluidizing gas velocity (u/u_{mf} , see chapter 1.4). Furthermore, there is the master button for automatic operation, a Quick-Status text field, and buttons for the automatic cool down, plant shut down, and VI exit sequences.

The 8 tabs have the following content:

Main View

This tab (Fig. 97) contains a simplified piping diagram with the most important temperatures, all flow and pressure data, weather and astronomical data, shutter position (from the Solar Furnace computer via an Open Platform Communications (OPC) server), and several further information like valve positions, solids and product water amounts and flow rates, information about the chemical reaction like a comparison of the molar water production with the molar hydrogen inflow, status of the gas supply (air, argon, hydrogen, electrolyzer), and so on. Furthermore, all manual controls of the system are done here, in particular the set points of the gas flow controllers, and activation of pumps, fans, and the TEC. Finally, the theoretical set point for the shutter position depending on a desired value for the solar power and the actual DNI is displayed. This is the tab that's normally selected during operation.

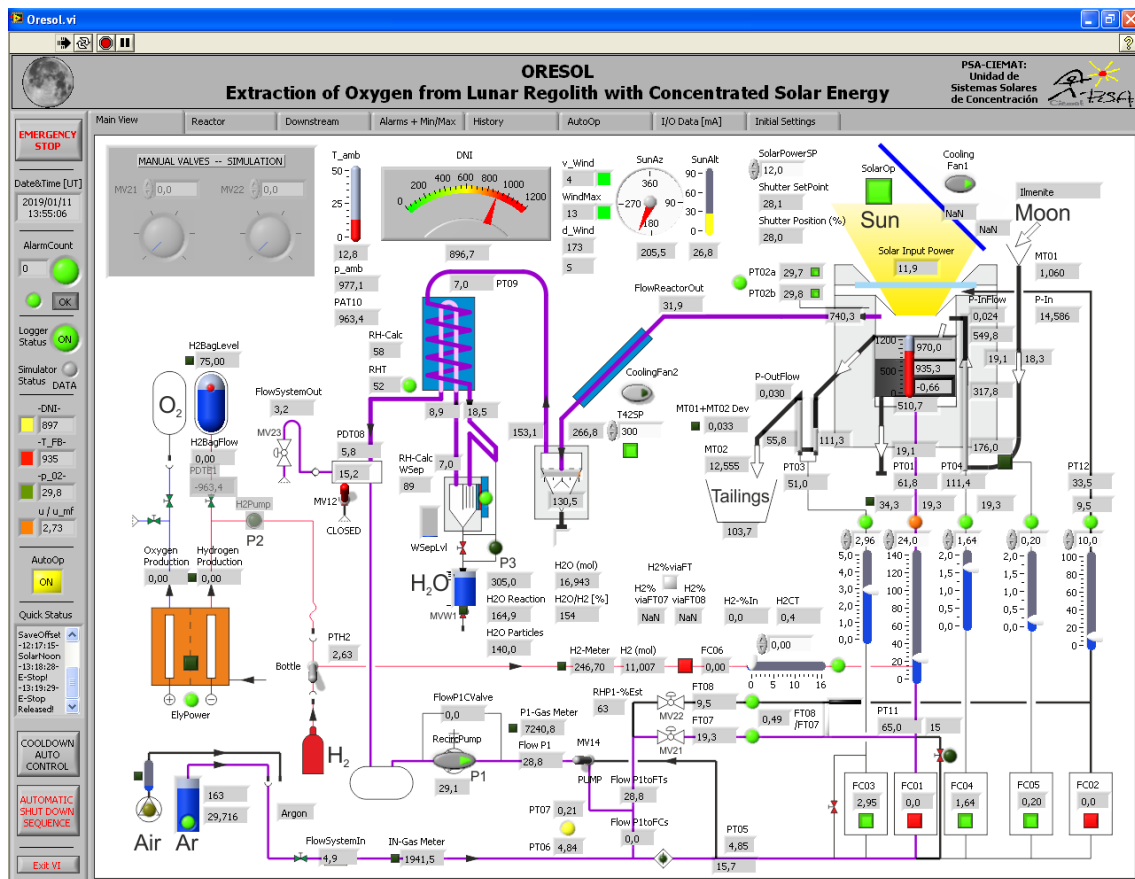


Fig. 97: Front panel of the Oresol.vi with the “Main View” tab selected.

Reactor

This tab displays all temperatures within and around the reactor, and especially within the fluidized bed. The minimum, average, and maximum temperature in the reactor are displayed. To get a quick intuitive impression of the temperature distribution within the bed, the measurements are color coded, from blue at minimum, over purple when at average, to red

when at maximum temperature. To avoid miscalculation, every value in the fluidized bed (TC01-TC15, see Fig. 43 on page 76) can be *activated or deactivated individually*. When this work refers to it, "reactor temperature" always means the value calculated with the "activated" thermocouples. This is useful in the case if an area of the bed is poorly fluidized, or simply if a thermocouple fails.

Downstream

This tab contains a cutout of the piping diagram with the downstream section from the reactor gas outlet, over Cooler C1, Particle Separator PS, Filter F3, Cooler C2, and Water Separator WS1 and WS2, to the "Out-Collector" with the "Gravity-Valve" GV (for a detailed description of these components see chapter 3.9). All temperatures in this area are displayed. Also, the TEC and the water extraction Pump P3 can be manually activated from here, including two drain modes for the water pump. Furthermore, all cooling water temperatures including the window flange are displayed here. A graphical representation of the temperature and pressure profile over the entire gas loop completes the tab.

Alarms + Min/Max

On this tab, all data that can enter into an alarm condition is listed. The threshold values that trigger the alarms are set here. Moreover, the maximum (or minimum if meaningful) values reached during the testing day are displayed. In the left column, most of the pressure sensors, the two load cells (mass sensors), the hydrogen sensor, and the solar input power can be found. The right side includes 10 temperatures, bad fluidization (u/u_{mf} low), inconsistent particle flow (outflow \ll inflow), low hydrogen level in the gas bags of the electrolyzer, and low argon level in the supply bottle. Besides the "normal" alarm (warning) that requires action from the operator, some of the values can trigger an emergency alarm that automatically interrupts the operation. While an emergency of one of the values in the right column only requires closing of the shutter, an emergency in the left column stops everything, especially flow controllers and pumps (except cooling water). From time to time, it happens that the data transmission from the A/D-converters is corrupted for a few seconds, with the possibility to trigger a (false) emergency stop. To avoid this annoying situation, a consistency check was included. It continuously compares the data from the two pressure sensors PT02a and PT02b, and while a difference > 1.5 mbar is detected, the emergency stop function is disabled. Finally, the alarm-log display and the control of the acoustic alarm beeper are placed in this tab.

History

This tab (Fig. 98) shows two identical diagrams with 15 graphs each, including shutter position, fluidized bed temperatures and pressures, gas and solids supply flow rates, extracted product water, and so on. The only difference between the two diagrams is that the upper one displays the curves for the past 15 minutes while the lower one spans over 6 hours. This way, it's possible to observe simultaneously the development of these values in short term and over the entire operation day. The diagrams have 4 different scales. If a value exceeds the maximum of its assigned scale, it automatically switches to the next one.

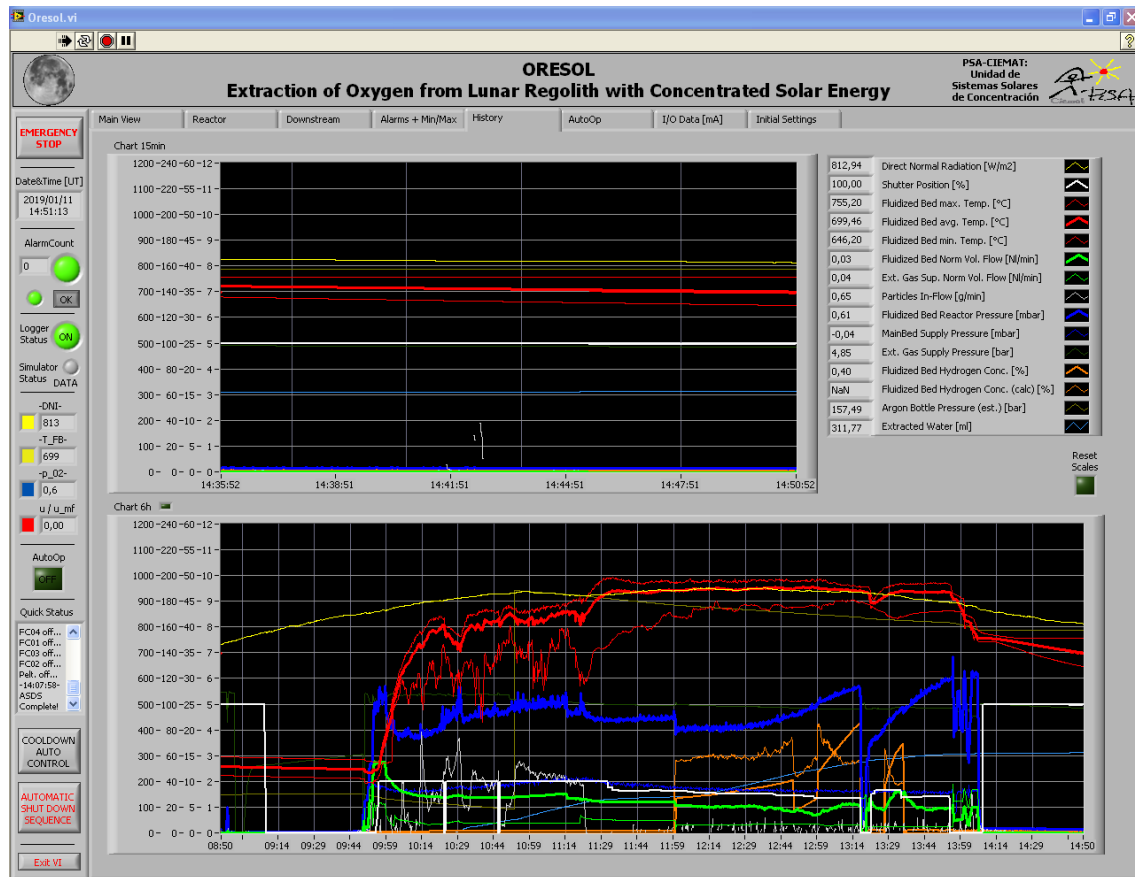


Fig. 98: Screenshot of the front panel of the Oresol.vi with the “History” tab selected.

AutoOp

This tab (Fig. 99) contains all the input needed for the automatic operation functions. They are:

- Adjustment of the main gas flow rate as a function of the mean fluidized bed temperature. There are two sub-modes, called “ u/u_{mf} ” (= constant), and “*empiric*”. The first one follows a $\dot{V}_N \sim 1/T^{1.7}$ law, while the second one adjusts the fluidization gas flow rate inversely proportional to the temperature ($\dot{V}_N \sim 1/T$). A detailed explanation for this is given in chapter 5.1.
- Alternatively, a down-up cycle of the gas flow can be performed fully automatically to determine the minimum fluidization point for the current fluidized bed temperature (see chapter 1.4.2 and Fig. 30 on page 55). The order “down-up” (instead of “up-down”) was chosen because this way it can be integrated into the ordinary fluidized bed operation with only a short interruption of the solar power supply. A practical example for this is shown in chapter 4.2.10.
- Setting of the window protection gas flow rate as a fraction of the main gas flow rate. A minimum flow limit can be included. During most of the tests, a fraction of 0.25 and a lower limit of 10 l_N/min was used.
- Setting of the fluidization gas flow rate for the particle Outpipe as a function of its temperature. The lower value of TC38 and TC39 is used. The calculation follows the $\dot{V}_N \sim 1/T^{1.7}$ law.



- Setting of the fluidization gas flow rate for the particle Inpipe (riser) as a function of its temperature. The lower value of TC33, TC34 and TC35 is used. The calculation also follows the $\dot{V}_N \sim 1/T^{1.7}$ law.
- Setting of the gas flow rate for the L-Valve (standpipe). This automatic function is of special importance because it is used to adjust the inflow rate of the particles into the reactor. Its working procedure is described in chapter 3.14.2.
- On/off-control of the water extraction Pump P3. The pump turns on when the lowest one of the level sensors in the Water Separator WS2 becomes wet; it turns off again when the level sensor falls dry.
- On/off-control of the TEC (Peltier cooler). When one of the two thermocouples TC59 or TC63 falls below a certain threshold (usually 3 °C), the TEC power supply is coerced to turn off. It only turns on again if the temperature has risen a certain amount (usually 1 °C) and the copper cooler (TC78) is not too hot (below the alarm-temperature). The purpose of this automatic mode is to avoid freezing of the product water.
- Control of the hydrogen feed flow rate. When this mode is on, the hydrogen flow rate, instead of being manually adjusted with FC06, is automatically calculated as a percentage of the total main gas flow into the fluidized bed. A minimum bed temperature can be set to avoid the introduction of hydrogen when the reactor is too cold. A late addition to the control program is the calculation of the supposed

optimum hydrogen fraction as a function of the bed temperature. More about this on page 187 in chapter 5.5.1.

- Control of the electrolyzer operation including the hydrogen pump (P2). This mode basically manages the hydrogen in the gas bags connected to the electrolyzer. When the pressure transmitter PATE1 detects a sharp rise of the pressure, the electrolyzer is turned off because the bags are full. If the pressure suddenly drops below ambient, then the bags are empty and the flow controller FC06 and the Pump P2 are turned off.
- Calculation of the shutter position as a function of the solar radiation (DNI) to maintain a constant fluidized bed temperature. So far, this value could not be transmitted automatically to the control computer of the shutter. A thinkable option for the future is that the computer of the Solar Furnace will perform this task.

The functions of this tab turned out to be extremely useful. Basically, they save from the need of up to nine extra operators! Presently, only two persons are necessary to operate the Oresol “chemical factory”, one for the Solar Furnace (heliostat and shutter), and one for general oversight of the activities, like choosing the temperature, activation of the particle inflow, supervision of all data, and so on.

I/O Data [mA]

All sensors, except thermocouples and digital sensors, return their values as “4-20mA” analog signals, and that are the values that are passed digitally from the A/D-converters to the control program. The VI then converts them into the “real” readings. These 4-20mA values are displayed on this tab. In theory, for sensors with zero as minimum value, a value of 4.000 mA corresponds to 0.0 [unit]. In practice, there is always a small offset. The Oresol.vi allows for correction of this offset. For this, the system must be turned off, all pressure released, and then by pressing the “Get Offsets” button, the offsets will be averaged over 3000 measurements for each sensor. This process lasts a little bit more than one minute. The offsets are then saved in the file “OresolOffsetValues.csv” and applied to the conversion into the displayed data.

Initial Settings

This final tab is a little bit something like a “catch-all” page. Everything that doesn’t logically fit into one of the other tabs is put here. When the Oresol.vi is started, several initial values have to be set. Some of these values, including “Logger ON” and “Simulator ON”, can be accessed on this tab, therefore the name. Further content are some error status displays, an array for wind speed tracking, and the button for the activation of the Bluetooth transmission.

3.14.2 Block Diagram

The block diagram of the Oresol.vi has a size of 7085 pixels (width) x 16690 pixels (height). As LabVIEW is a graphical programming language, it is not possible to give a “number of code lines” or similar information. The programming follows the general rules of structured programming, this means it is composed of sequences, conditionals, and loops. Furthermore, LabVIEW allows the pseudo-parallel execution of program blocks.

The outermost structure of the program is a sequence consisting of three blocks: Initialization, Execution, and Exit. The Initialization Block, as its name obviously indicates, initializes variables, charts and so on. It is executed only once when the program is started. The second block, the Execution Block, is the core of the program and contains 33 parallel loops executing

all the tasks that are necessary for the proper operation of the Oresol plant. This block is not terminated until a special flag ("ExitVI") is set TRUE by pressing the ExitVI button. Then, when all loops are properly left, the Exit Block terminates the run.

Initialization Block

This block contains a sequence of six steps. First, "everything is turned off", this means, all flow controllers, pumps, the electrolyzer etc. are forced OFF to categorically exclude any unintentional start of any physical component. Then, after writing a welcome message into the quick-status field, all gas meters and levels are reset. In the fourth step, the sub-VI "Oresol-Init.vi" is called and a pop-up window appears (Fig. 100). In this window, very basic parameters like fluidization gas (argon vs air), particle type (ilmenite, JSC-1A...), hydrogen supply (electrolyzer vs bottle), envisioned operation temperature etc. can be selected. In the final two steps of the block, some values for the simulation mode are preset in case it is used, and the history charts and the wind speed tracking array are initialized.

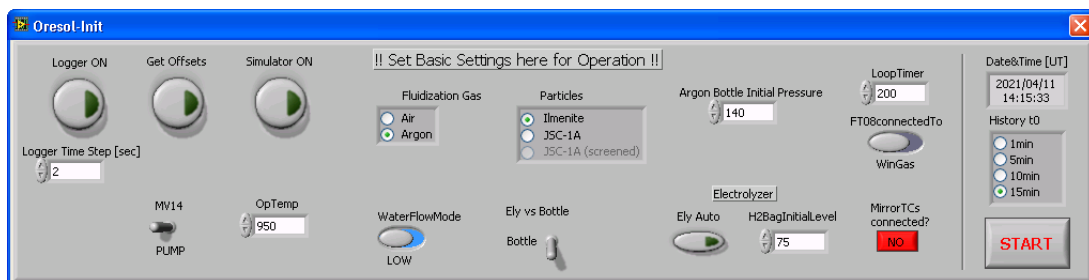


Fig. 100: Oresol-Init.vi pop-up window for the initial selection of basic operation parameters.

Execution Block

This is the place of the code that's repeatedly running during the operation. Besides of one short sequence that completes the initialization, there are a total of 33 loops running in parallel executing different tasks. As the vertical space in the LabVIEW IDE (integrated development environment) is limited, the loops are arranged in four columns (Fig. 102).

All these loops have the same basic structure (Fig. 101). The integer variable "LoopTimer" determines the minimum time needed for one loop pass. Its value is usually set to 200 ms. This way of "slowing down" the execution of the program is common practice in LabVIEW programming. It avoids that the CPU is running all the time at its limit. The Boolean variable "StopVIFlag" has normally the value FALSE. When the "Exit VI" button at the bottom-left of the front panel (see Fig. 97 on page 125) is pressed, then first an automatic shutdown routine is executed. This routine turns off all flows, pumps and other components in a cautious manner and in the right order. Only when that routine has finished, "StopVIFlag" is set to TRUE. This allows the program to leave all the 33 loops and the Execution Block can be exited.

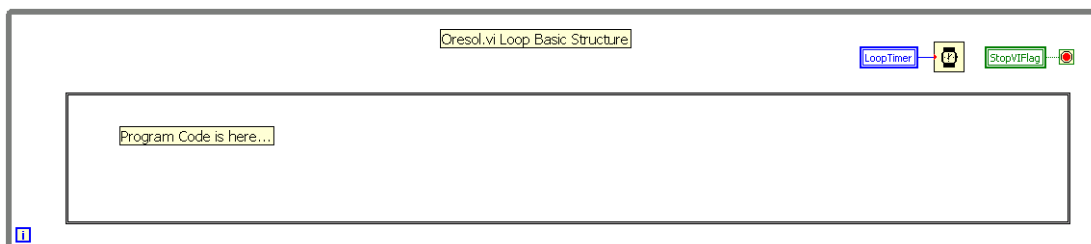


Fig. 101: Basic structure of every loop in the Oresol.vi execution block.

Only a few of the 33 loops are presented here, whether because they are important to the overall functionality of the program, because they have special properties, or because they are simply a curiosity.

The most important loop is the one for *Data I/O or Simulation*. Its task is to pass the measured data into local variables and send back the set points to the hardware. Besides calculation of the real time in UT, it only contains one conditional block, with the two alternatives simulation mode or operation mode. While the simulation mode generates the data with some simplified models, the operation mode receives them from the global variables of the OPC server of the data acquisition hardware; and vice versa, the set points, switch positions and so on are sent to the external hardware or to the simulator sub-VI.

Another important loop is the one for the *Calculation of Flow and Metering*. Like explained in chapter 3.2.5, the gas flow rate for the main fluidized bed can come from up to four sources. As the hydrogen (from FC06) does not count here, it's the sum of FC01 (argon), FT07 (recirculated gas) and MV07 (high flow valve). But from all these branches only FC01 has control ability. So, the set point for FC01 is calculated by subtracting $(FT07 + MV07)$ from the total set point. As there is no flow sensor in the pipe with the valve MV07, the flow rate through this valve is calculated in a somewhat provisional way by the pressure drop over a hose between the sensors PT11 and PT01. The flow rate is roughly proportional to the square root of the pressure drop. In practice, before opening MV07 during operation, the proportionality factor is determined with the help of FC01 and FT07.

For the flow rate of the window protection gas, the procedure is quite similar. To get the set point for FC02, the FT08 data is subtracted from the overall set point.

Additional tasks of this loop are the proper handling of the on/off button of each flow controller, the calculation of the flow in several pipes that do not have a flow sensor (e.g. reactor gas outlet pipe), the integration

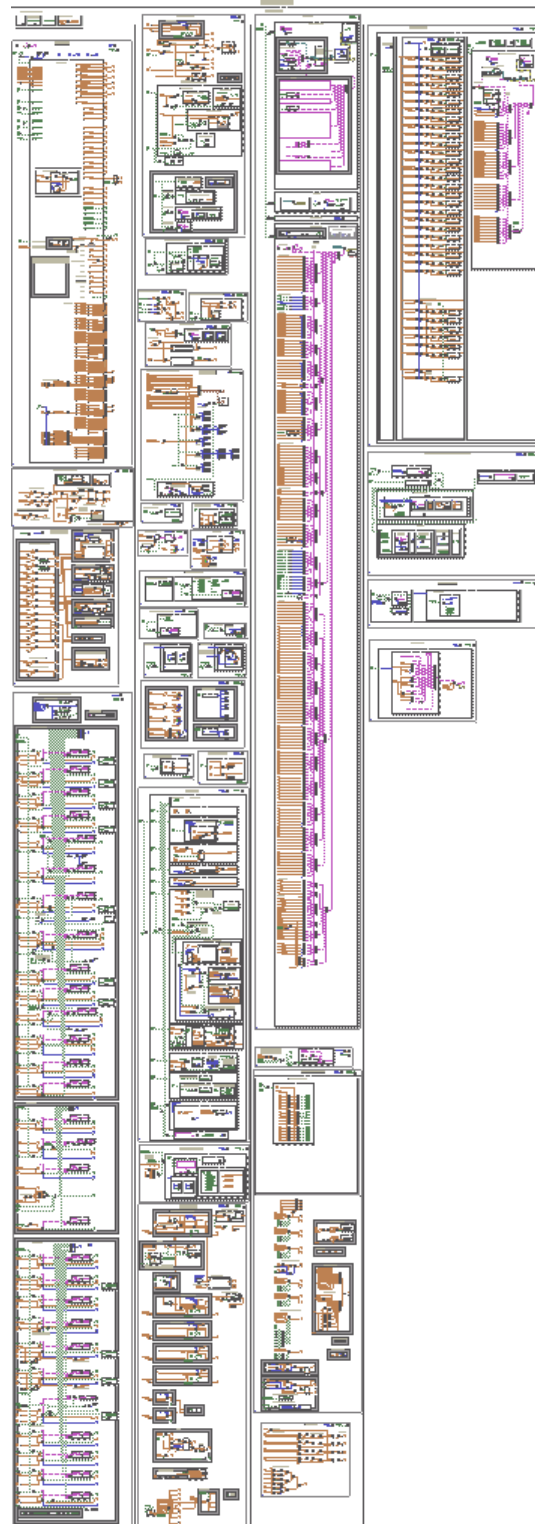


Fig. 102: Block Diagram of the Oresol.vi Execution block.

of the flow over time to determine the total consumption of argon (or air), and the calculation of the theoretical minimum fluidizing gas velocity under the given conditions (temperature, gas and particle type).

Obviously very important is the storage of all data generated during the tests. This is the task of the loop for the *Logger*. When the “*Logger ON*” button is pressed, the program generates automatically a file name including date, particle and gas type (for example “Oresol-20190111-IlmAr.csv”) and checks if this file already exists. In case of yes, an empty line is added, if not, a new file with a header line is created. Each field of the header line includes the corresponding sensor tag, the name, and the unit of the data (e.g. “TC14 FB-Top-South [°C]”). Then, every e.g. two seconds (can be adjusted in the VI), a line with a complete data set of 219 values including date and time is written to the file. When the “*Logger ON*” button is pressed again or deactivated during the Exit-VI sequence, the data file is properly closed.

The automatic shutdown sequence is initiated by pressing of the “*AUTOMATIC SHUT DOWN SEQUENCE*” button at the bottom-left of the front panel. The sequence consists of 15 frames. They are (in this order): closing the shutter of the Solar Furnace, stopping of the hydrogen supply (FC06 and P2), shut down of the electrolyzer (only if in Exit-VI mode, see next paragraph), stopping of the standpipe gas flow (FC05) and the Inpipe gas flow (FC04), manual closing of MV21 and MV22 (only if MV14 is not in recirculation position), turning off the Recirculation Pump P1, stopping the main bed gas flow (FC01), the Outpipe gas flow (FC03) and the window protection gas flow (FC02), deactivation of the TEC (Peltier), and draining of the remaining product water with the Pump P3 until the lowermost level-sensor falls dry. As far as possible, all steps are executed gradually, and are accompanied by text messages in the Quick Status field.

The same loop also handles the Exit-VI sequence, activated by pressing of the “*Exit VI*” button. This sequence first runs through all the steps of the Automatic Shutdown Sequence. Once completed, the fans are turned off, and then, after waiting a few seconds, the logger is turned off and the “*StopVIFlag*” is set TRUE to enable all loops to be terminated.

The loop for *Solar Input and Shutter* (Fig. 103) might be interesting for the reader because it includes the concentrated solar power supply, a rather special feature of the Oresol plant among the lunar oxygen production plants. It makes two opposite calculations. The first one is to calculate the available solar power from a given shutter position. Therefore, the current solar irradiation (DNI), the shutter position, and the nominal power of the Solar Furnace have to be known. The shutter position is given in % from fully closed (0%) to fully open (100%). As

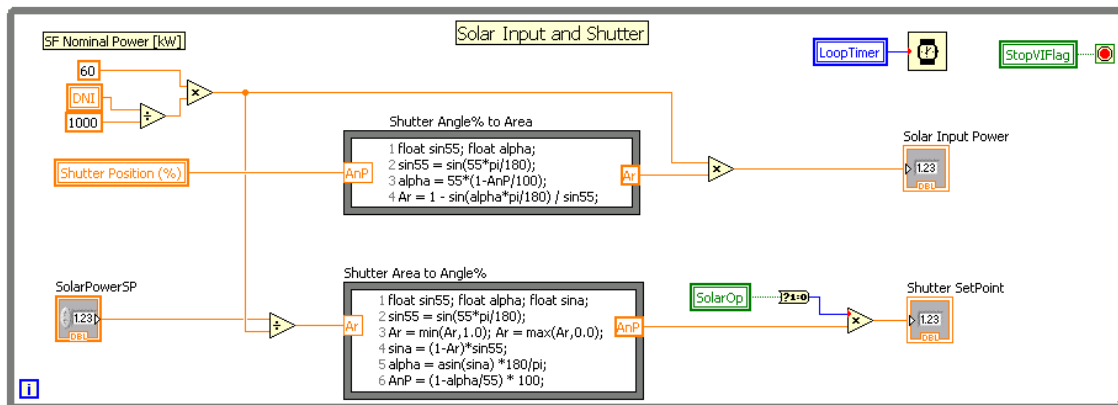


Fig. 103: Loop for Solar Furnace Shutter calculation

the percentage refers to the angle of the slats (fully closed = 55° , fully open = 0°), a conversion from angle to projected surface has to be done. A so-called formula node is used for this. The result, multiplied by the nominal power (60 kW) and the DNI normalized to 1000 W/m^2 , gives the current solar input power. The second calculation simply inverts these steps; a desired value for the solar power together with the current DNI gives a required set point (in angular %) for the shutter. It must be mentioned that the “solar power” calculated here is an ideal value because it refers to the nominal power of the Solar Furnace. In reality it’s lower, due to several reasons, mainly the intercept of the diagonal mirror and the shadow of the experiment (more about this in chapter 5.3). In principle, it could be determined with the help of a flux measurement campaign in the focal plane of the Oresol reactor, but this was not yet done.

As the displacement of solid particles through fluidized pipes is a somewhat unusual feature of the Oresol plant, its handling by the software will be explained here. As already mentioned in chapter 3.7, the *particle mass flow rate* is adjusted by the level of fluidization in the standpipe with the flow controller FC05. Three loops participate in the solids mass flow rate control.

The first loop (Fig. 104) is to calculate the flow rate. There are two flows. The flow into the reactor originates from a hopper (see Fig. 65 on page 98) whose mass is measured with the load cell MT01. The flow out of the reactor is collected in a saucepan (see Fig. 67 on page 100) whose mass is measured with the load cell MT02. The signals enter the VI in the 4-20mA format and first are converted into kilograms. The range of MT01 is 10 kg and that of MT02 is 80 kg. Then, the tare mass of the containers is subtracted. For MT01 this is about 2.54 kg, for MT02 about 2.89 kg. The next step is to compare the current value with the value recorded one minute ago. The difference gives directly an unfiltered value for the particle mass flow rate in the unit kg/min.

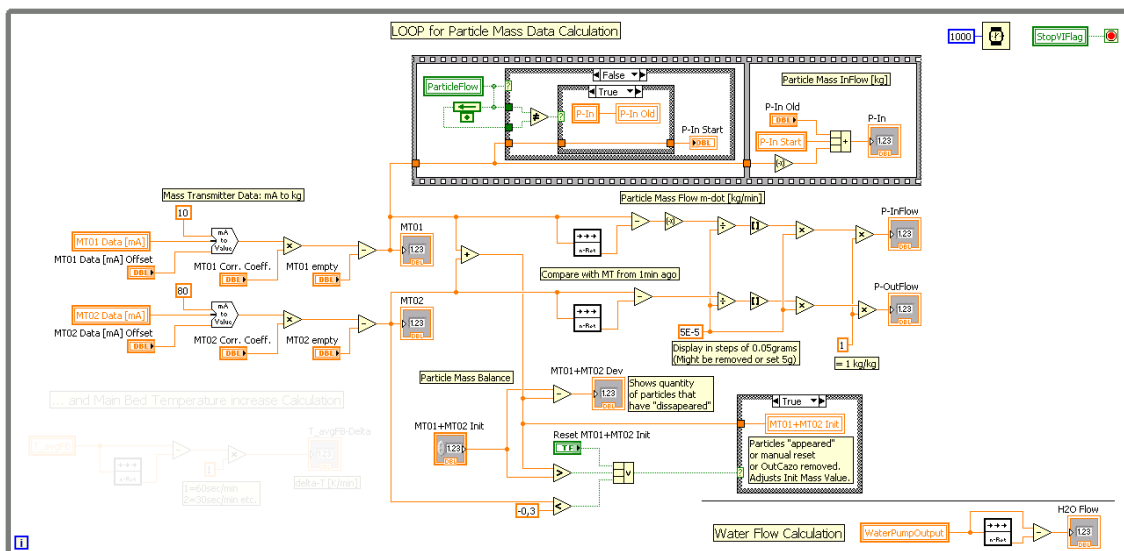


Fig. 104: Loop for particle mass and flow rate calculation

Furthermore, several particle mass balances are calculated in this loop. One of them is the difference between the inflow and the outflow. It usually happens that the outflow starts with a major delay, giving the impression that some particles “disappear” in the reactor. This difference is monitored in the variable “MT01+MT02Dev”. When it exceeds a pre-set value (e.g. 1 kg), an alarm is triggered. When refilling of the inlet-hopper or replacement of the outlet-container is detected, the difference is automatically reset to zero.

The second loop handles the On/Off-button on the Main Screen (Fig. 105). It simply switches the set point for FC05 between two pre-set values, where the value belonging to OFF is so low (e.g. 0.2 l_N/min) that the particle flow will cease. The construction with the unequal-comparison and the feedback-node causes the true path of the outer branch to be executed only at the moment when the push button for the particle flow is pressed. Therefore, the manual modification of the set point for FC05 remains always possible.

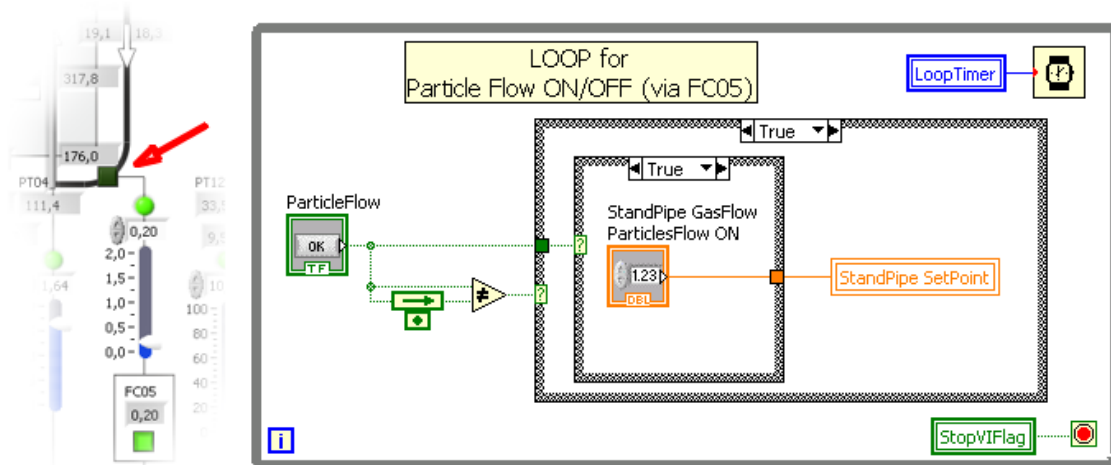


Fig. 105: Manual particle flow rate setting. Left: Front Panel with On/Off-button (red arrow) and slider for FC05. Right: Corresponding loop in the Block Diagram. The Boolean variable “ParticleFlow” corresponds to the On/Off-button.

The third piece of code dedicated to particle flow control is part of the *Loop for Automatic Operation* (Fig. 106). A first attempt to link the particle mass flow rate to the FC05 set point with a fixed, empirically obtained, quadratic relation had failed. The particles are wayward. Therefore, a control algorithm was developed that works with a two-minute cycle. For the first 1.3 minutes, the system simply waits for the particle flow to stabilize. This time includes the one-minute lead time required for the mass flow measurement with MT01. Then, for the remaining 0.7 minutes, the actual solids flow rate is averaged. If the result differs from the set point, the set point of the flow rate of the flow controller FC05 is proportionally modified in the needed direction. This routine includes several safeguards. To keep the particle flow running, the main bed gas velocity (u/u_{mf}) must be above a pre-set value, a minimum quantity of particles must remain in the feed hopper, the fluidized bed temperature should be above a desired value, and the deviation between the inflow and the outflow must not be too large. These safeguards mainly serve the purpose to avoid unintentional solids pile-up in the reactor and complete drain of the inlet hopper.

A cool feature of the Oresol.vi is the ability to send some data to a smartphone via Bluetooth. This was implemented, because the adjustment of the valves MV07, MV21 and MV22 has to be done manually directly at the plant. With the flow rate data on the smartphone, this can be done comfortably and with sufficient accuracy.

Another particular feature is the Control for Automatic-Cool-Down. This loop oversees the cooling down of the system after the defocus at the end of the day. This fully autonomous mode monitors the particle flow and activates the shutdown sequence when a preselected temperature (e.g. 200 °C) is reached. Finally, it switches the logger to night mode (data logging every 30 sec instead of every 2 sec). This loop was implemented to allow the system to run without supervision and the operator to finally go for lunch after a long solar testing day.

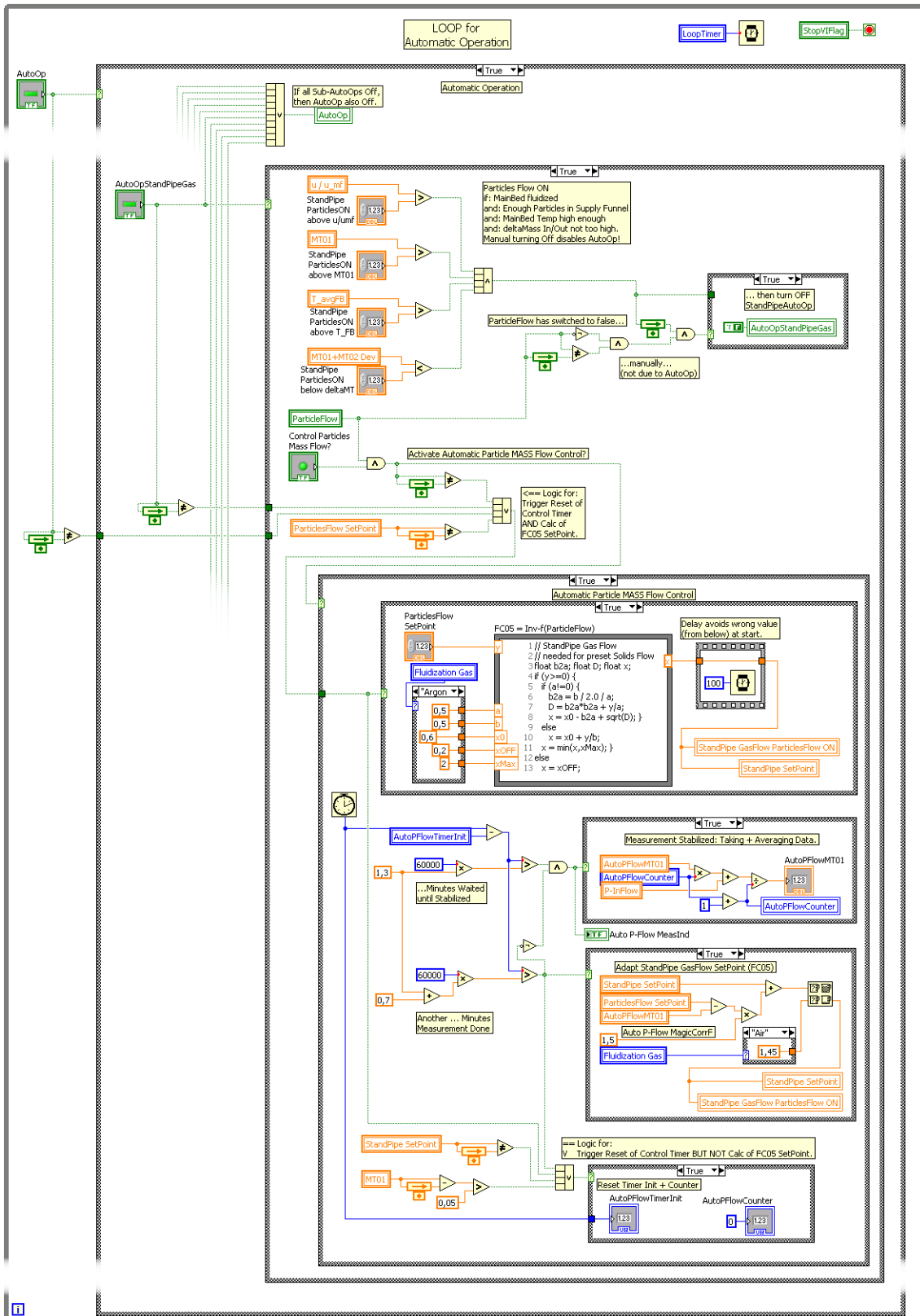


Fig. 106: Automatic Particle Mass Flow Control handling detail within the Loop for Automatic Operation.

Exit Block

When all loops in the Execution Block are left, the VI enters into the Exit Block. Its almost only task is to write a goodbye-message into the Quick Status text panel.

3.14.3 Sub-VIs

Functions and procedures that are needed frequently at different places of the main VI are implemented in sub-VIs. They have the same structure as a “normal” VI, which means they consist of a Front Panel and a Block Diagram. Furthermore, the variables in the Front Panel can be connected to a connector block that defines the interface to the calling VI.

Among the 22 sub-VIs that are executable, six are dedicated to temperature and gas flow related calculations, e.g. “T_avg-Sub.vi” calculates the average value of up to 8 input parameters taking into account whether the corresponding sensor is “activated” or not. Three sub-VIs are made explicitly for the generation of data when running in simulator mode. Another five help for some special functionality of the program, like the sub-VI for minimum and maximum values and alarms, the “Oresol-Init.vi” (see Fig. 100 on page 130) or the Bluetooth control, and eight are more generic routines for things like mathematics, the calculation of the color coded displays, or the conversion of mA into the actual value. As can be seen in Fig. 107, the subroutine “mA to Value-Sub.vi” does not only the trivial math, but also assigns automatically the value “zero” to the lower range if not specified otherwise in the calling program, subtracts the offset from the input value, and checks if the result is valid. If it isn’t, the value “NaN” (Not a Number) is assigned.

Finally, there are 19 VIs for the transfer of the global variables from their OPC servers to the Oresol.vi. 18 of them are for each one of the I/O-modules, and one is for the data provided by the computer that controls the shutter of the Solar Furnace.

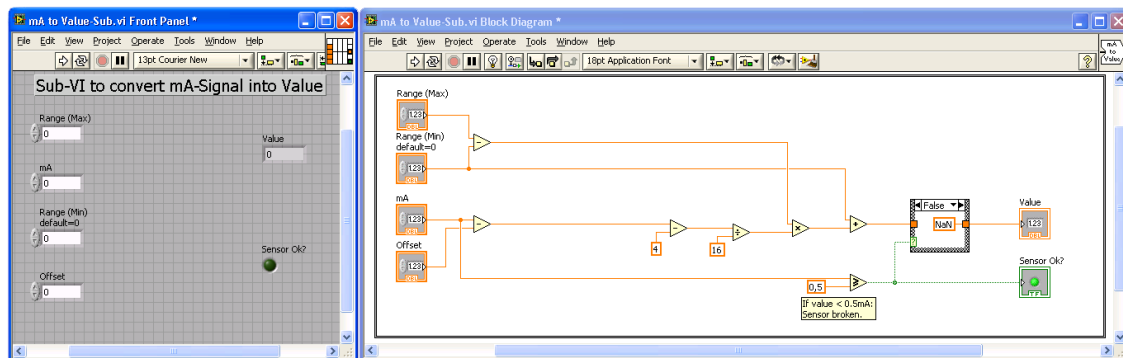


Fig. 107: mA to Value-Sub.vi. Left Front Panel, right Block Diagram.

3.14.4 Simulation Mode

The Oresol.vi also offers a simulation mode. Instead of receiving the data from the hardware, simplified mathematical models of the system generate the data. A sub-VI for upstream simulation provides flow data based on flow controller set points, the characteristics of the Recirculation Pump P1 (flow vs pressure), and two dials that simulate the valves MV21 and MV22. A sub-VI for power simulation generates a DNI and calculates temperatures from shutter position, absorptance and heat capacity of the particles, infrared radiation, etc. A third sub-VI for pressure simulation creates readings for the pressure transmitters based on fluidized bed behavior depending on flow rate, particle and gas properties. The simulation mode was initially implemented as a debugging help during development of the program, but it turned out to be also an excellent tool for the training of the operator.

4 Solar Chemical Reactor Operation

4.1 Test Campaigns

So far, three solar experimental *campaigns* have been carried out with the Oresol reactor in the Solar Furnace SF-60 of the Plataforma Solar de Almería (Fig. 108, Fig. 109). Thereby, the fluidized bed accumulated a total of 201 operating hours, 150 of them with solar power. The first solar campaign took place in July 2016, the second and longest one lasted from December 2016 to June 2017, and the third one with the highest quantity of solar tests was spread over four weeks in October/November 2018, four days in January 2019, and another one and a half weeks in September/October 2019. They were preceded by installation and non-solar pre-tests. The first campaign worked almost exclusively with air, while the second campaign saw the transition from air to argon and to hydrogen. In the third campaign, operation with a higher hydrogen share in the feed gas was attempted.

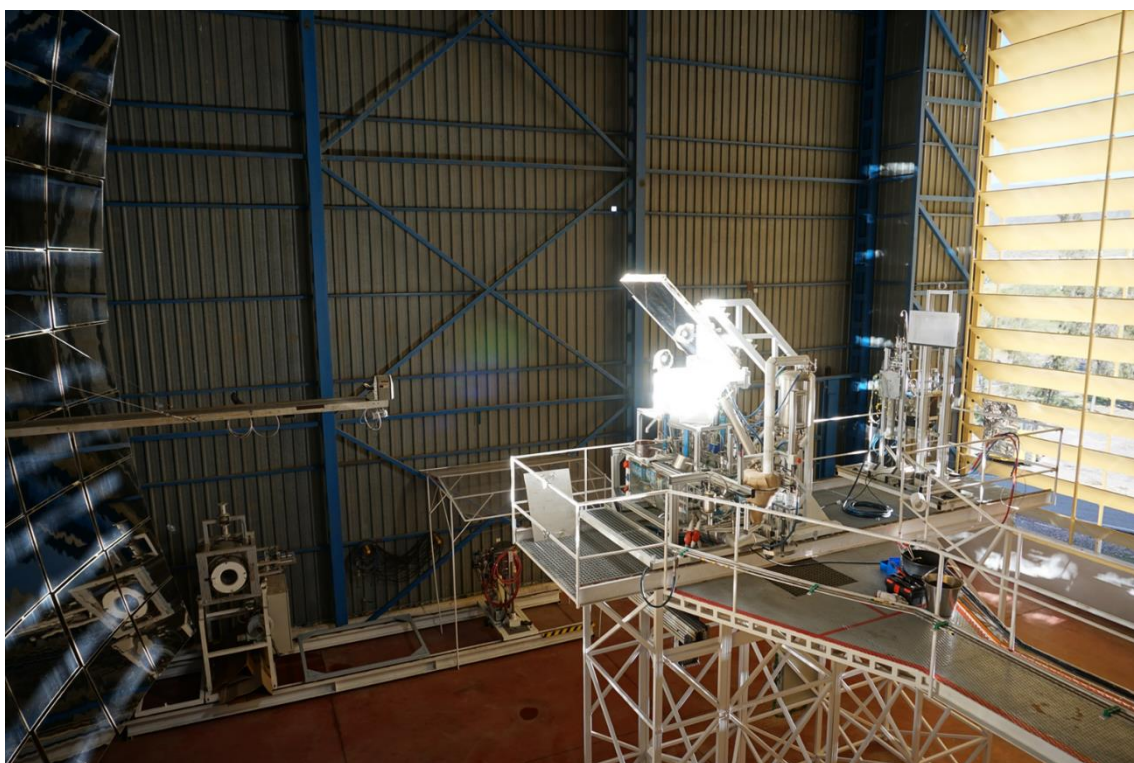


Fig. 108: Solar test of the Oresol experiment in PSA's Solar Furnace SF-60.

Therefore, instead of dividing the activities by test campaigns, a more targeted approach is to group them into *phases*, defined by the feed gas composition. After a lengthy phase of installation intertwined with non-solar testing of components and parts of the system at ambient temperature (chapter 4.1.1), solar testing started in July 2016 with *air* and up to 400 °C in the reactor (chapter 4.1.2). The goal here was to learn about the behavior of the system as a whole, identifying the characteristics of the fluidization at elevated temperature, testing of the interaction of the peripheral components, optimization of the data acquisition program, and finally the development of procedures for a fast passing through the low temperature range. This was important for minimizing argon consumption during start-up (for more about this see chapter 5.1). Then, on the last day of January 2017, testing switched to *argon* and the temperature was increased up to 800 °C (chapter 4.1.3) to demonstrate the minimum temperature target. After two months of tests with pure argon, *small amounts of*

hydrogen were added to the argon feed gas (up to 2 l_N/min or 8%vol.), accompanied by further temperature increase up to almost 1000 °C (chapter 4.1.4). This phase was to demonstrate the chemistry and the thermal limits. Finally, *more hydrogen* was added (chapter 4.1.5) to increase the product water yield and to determine the chemical limits of the system.

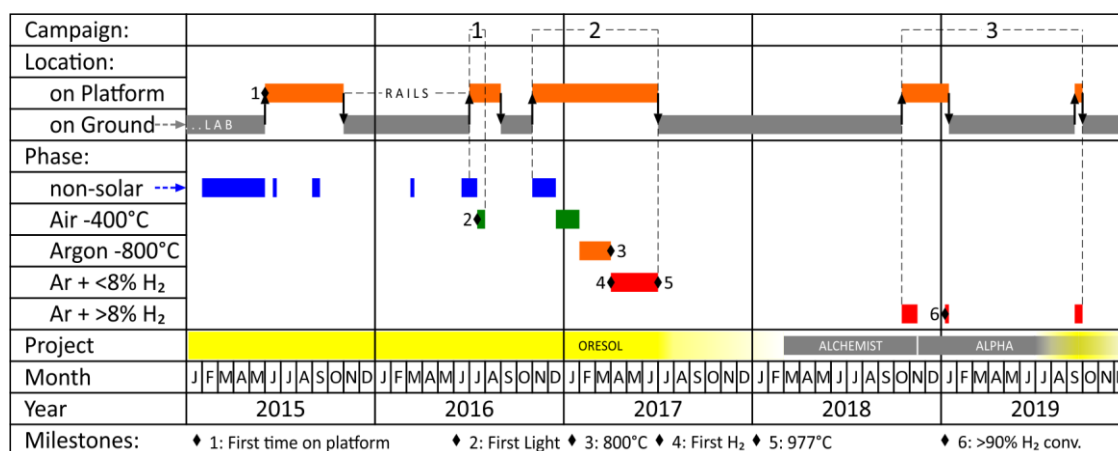


Fig. 109: Timeline of the campaigns and phases of the Oresol experiment including some major milestones between 2015 and 2019. Non-solar tests in the laboratory started well before 2015. For Alchemist and ALPHA see page 30.

All solar test campaigns and almost all pre-tests used ilmenite with a mean grain size of 150 µm (“Ilmenite-150”) as the solid feedstock. A list containing all solar tests of the Oresol project is given in Table 17 in the Appendix A.6.

4.1.1 Installation and Non-Solar Pre-Tests

During the official project period in the year 2008, the process and the reactor were designed, and basic components like reactor steel parts including outer housing, gas distributor, Inpipe and Outpipe, the ceramic inner wall and aperture, quartz windows, insulation material, support structure material, the Cooler C1 and the original Particle Separator were acquired. Furthermore, five flow controllers, the electrolyzer, and the particles were purchased. A first, preliminary assembly of the reactor was carried out, followed by the acquisition of more parts, assembly of the initial downstream parts and the supporting frame. The reactor housing got connectors for 30 thermocouples and the inner insulation. On February 10, 2011, a first, still pretty provisional fluidization test was performed (Fig. 110).

More tests with air and argon were done in the following months. Therefore, the provisional fluidized bed was included into the initial support frame of the Oresol system. In parallel, particle properties like grain density, bulk density, and grain size distribution were measured. In May of that year, the sphericity ϕ_s of the Ilmenite-150 was determined with the help of the Ergun equation (eq. (18)). On June 02, 2011, the first and so far only fluidization test with particles from NASA’s “official” *lunar soil simulant JSC-1A* using the Oresol gas distributor was executed (Fig. 111). The particles showed Geldart class C behavior, something to be expected for material with a high fraction of fines (fine particles). In Fig. 111 left, the dust plume above the bed made by the rather large quantity of fines entrained by the gas stream can be easily discerned. Screening to a narrower grain size distribution⁷⁹ improves significantly the fluidizability (Geldart class A). But due to the limited presence of reducible iron oxide in the

⁷⁹ About 60% of the mass of the JSC-1A is found between 32 µm to 315 µm.

material and the availability of only 100 kg of JSC-1A at PSA, further tests so far were limited to a small experimental fluidized bed operating at ambient conditions (see page 30, “Alchemist”).



Fig. 110: Very first fluidization test with Ilmenite-150. The 40-screws gas distributor “40/3” (see chapter 3.5.4) was used. The red instrument is a handheld display for pressure sensors that later could be attached with quick connectors to various points of the system.



Fig. 111: Fluidization test with JSC-1A. Left: System setup. Right: View into the fluidized bed.

During the tests, the idea of the “*annular fluidization*” came up. This means that only an outer ring of the bed is fluidized, while the center is not. The vigorously bubbling gas flow was thought to move the particles upwards there, while creating a countercurrent downward flow in the center of the bed. The advantage would have been to increase the horizontal mixing of the particles within the bed and to move the “wildly splashing” surface area of the bed to the zone below the aperture ring, this way minimizing direct particle contact with the quartz window. To test the idea, a provisional ring made of copper tube with several small bores was built and operated as gas distributor (Fig. 112). The test was considered promising and the idea was pursued further.

In the meantime, the assembly of the Oresol system continued. The provisional fluidized bed was put at the location of the future reactor (Fig. 113). The piping of the gas upstream section including the flow controllers was installed. The downstream section got the Cooler C1, the original particle separator, and the Imhoff cones to collect the product water. The electrolyzer together with the hydrogen Pump P2 was integrated into a separate frame. A still fairly rudimentary data acquisition system, limited to four flow controllers and four pressure sensors, was included. Furthermore, a very detailed excel table was developed based on the

book (Kunii & Levenspiel, 1991) that allowed to predict many aspects of the Oresol solar fluidized bed.



Fig. 112: “Annular” fluidized bed trials. Left: Provisional gas distributor made of a copper ring. Right: Annular bubbles distribution on the surface of the fluidized bed.

In spring and summer of 2012, a longer series of tests was executed with the then available hardware, with special emphasis on the main fluidized bed and the continuous in- and outflow of the particles. Like expected, the Ilmenite-150 gave the bed a Geldart class B behavior with bubbles growing to a large size before leaving the bed. The particle inflow worked well, the outflow not so much. It turned out that the fluidization gas of the old Outpipe only partially entered into this pipe and that the remainder of the gas preferred the easier bypass through the main bed. Moreover, the consumption of argon to be expected was determined to about one bottle of 10 m³ per testing day, a value considered as too high. Therefore, two major modifications were implemented into the system: the inclusion of a recirculation pump (P1) and a new Outpipe with the syphon completely outside of the reactor (Fig. 113 left).

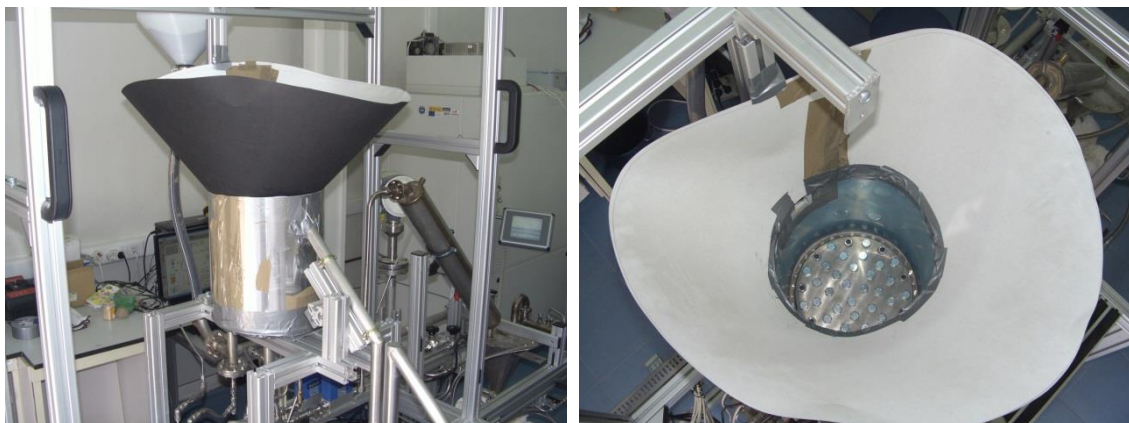


Fig. 113: Arrangement for cold fluidization and solids feed and discharge testing with a provisional reactor vessel wall. Compare also with Fig. 56 on page 92. The conical “collar” is to recover particles splashing out of the fluidized bed.

As a side note, the measurement of the optical properties of the particles, in particular the absorptance, turned out to be more difficult with the existing equipment at the PSA than expected. The reason was that this equipment requires the samples in a vertical position, something that cannot be done with particles because they simply fall down. As high precision was not needed, my son helped me out with his sophisticated equipment (Fig. 114). The absorptance (in red light) of the Ilmenite-150 turned out to be 80%, while the somewhat

brighter JSC-1A still has 70% (values rounded to one-digit precision). This data was used as input for the simulation mode of the Oresol.vi (see chapter 3.14.4).

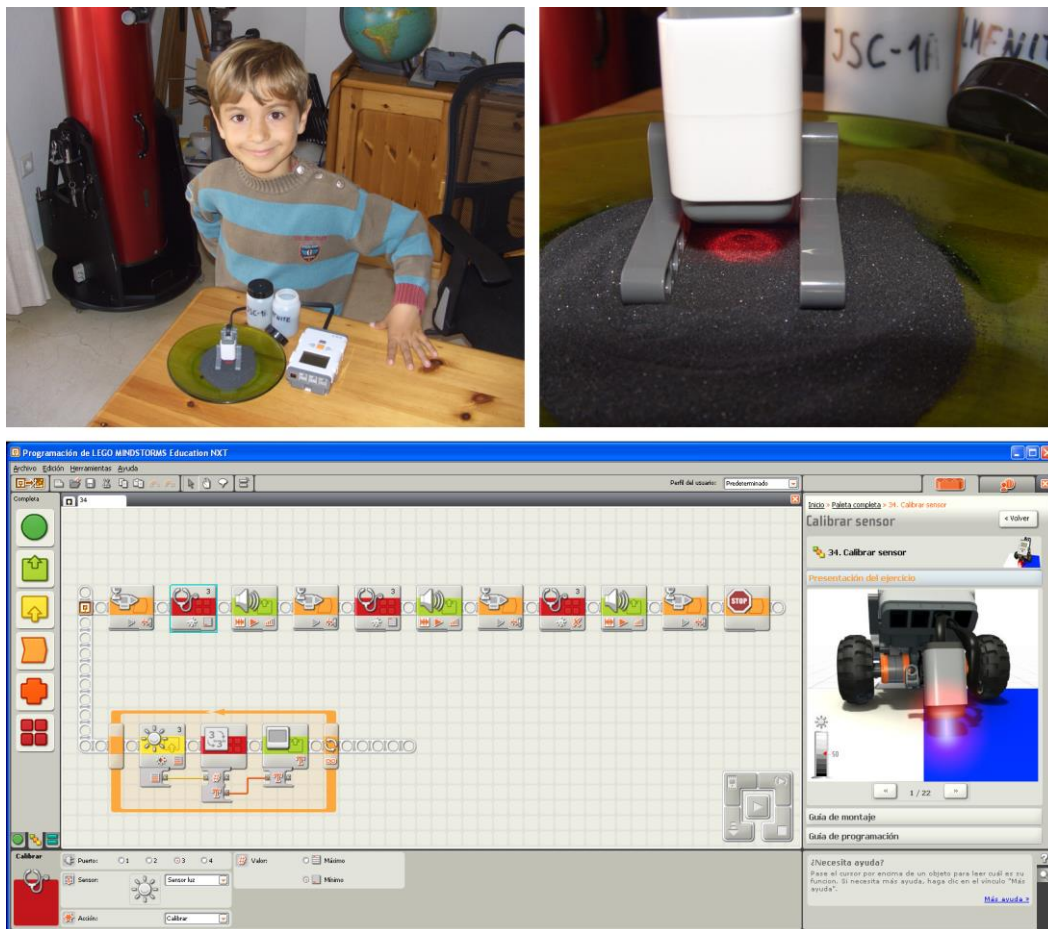


Fig. 114: Particle reflectance measurement. Top left: Lead investigator with the test setup. Top right: Close view of the sensor on Ilmenite-150. Bottom: Control program for the sensor written with Lego Mindstorms NXT-G.

After delivery of the new pump and the new Outpipe, the hardware allowed for execution of a variety of tests concerning fluidization and particle in- and outflow. Moreover, the new Recirculation Pump (P1) was tested and installed. The initial version of the control program Oresol.vi was developed, implemented, and tested. The requirements for the mass sensors (MT01 and MT02) were determined and the load cells acquired. The electrolyzer was tested frequently in parallel to other experiments, but its production rate was usually only about 1/3 to 1/2 of the expected value. The gas distributor got new screws, with only nine of them on the outer perimeter having two bores each (configuration “9/2”). As the first solar tests were planned to reach only 400 °C, no special and expensive screws made of high temperature steel were needed for this. Fig. 115 gives an impression of the resulting “annular” fluidization pattern.

In May 2014, the assembly of the reactor insulation (see Fig. 58 on page 94) was terminated and the first cold tests with the “real” reactor could be done. Further assembly work involved the air-cooled mirror including the fan duct, the standpipe, the window protection gas supply, the welding of the flanges of the In- and Outpipe to fix them in their definitive position, the installation of the new gas outlet ring and pipe in the reactor, the assembly of all missing upstream pipes including the hydrogen sensor H2CT, and the extension of the range of the



Fig. 115: Bubbling of the fluidized bed with “annular” fluidization

flow controller FC03 from 2 to 5 l_N/min. A special milestone was reached when the electronic boxes were ready for use with now all of the data channels available. In January 2015, the thermocouples within the reactor and the window were installed. This was the first time since the beginning of the project that the reactor was gas tight.

The first tests were performed with the empty reactor. The pressure losses of several components, especially the “Gravity Valve” GV and the purge valve MV12 were determined. An important experiment executed on April 06, 2015 was the comparison of the flow sensors FC01, FC02, FT07 and FT08. Therefore, first, the flow rate through FC01 was set to 60 l_N/min. Then (with GV capped), MV12 was carefully closed until the pressure PT02 in the reactor reached 25 mbar. Then, all the four mentioned sensors were operated one after the other with flow rates between zero and 60 l_N/min. The resulting more than 1000 data points for pressure drops over MV12 measured with PDT08 can be seen in Fig. 116 left. While FC01 and FC02 both follow a clean although different $p \sim \dot{m}^2$ curve, FT07 and FT08 more or less wind around the FC02 curve. The interpretation of this data is as follows:

- FC02 (black dots) is a high quality sensor calibrated for argon and measures correctly. Its data follows well the thick, yellow parabola.
- FC01 (red dots) is a high quality sensor too, but it follows another (the thin, orange) parabola. The fact that the data from FT07 and FT08 was close to FC02 (and far from FC01) suggests that FC02 measures right and FC01 does not. FC01 originally was calibrated for a mix of 95% Ar with 5% H₂, but now it was operated with pure argon. This had already been taken into account in the data acquisition system, but it’s very possible that something went wrong on the way. This deviation could be corrected with a simple factor.
- FT07 (green dots) and FT08 (purple dots) are identical, cheaper sensors. They were calibrated for argon too, but it cannot be ruled out that the manufacturer calibrated them with air and then applied a pre-calculated correction factor, neglecting more subtle non-linear effects. This is also supported by the observation that the deviation was very similar for both sensors.

The correction of FC01 with a factor and the FTs with two linear terms lead to the pressure drops shown in Fig. 116 right. All data points now follow the thick, yellow parabola. It should be emphasized that it’s not that important to get the absolute values for the flow rates right, but the relative ones, because during operation, flow can swap from one sensor to the other. With the sensors consistent among each other, the transitions between the sensors will always be smooth. A further confirmation that the corrections were right came from the observation that the calculated argon consumption (36 bar or 1.9 m³; w/o correction it was 1.75 m³) now matched very well the observed consumption (38 bar or 2.0 m³).

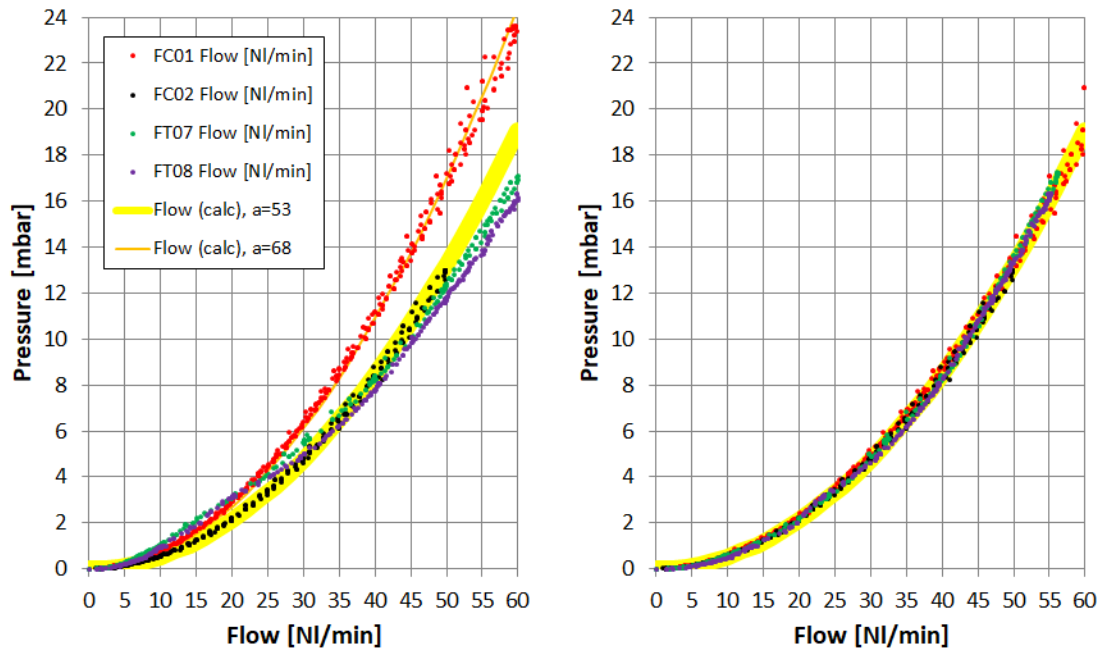


Fig. 116: Pressure drop over the valve MV12 measured against the flow data of four different flow sensors. Left: Before correction. Right: With correction applied.

Another important test was performed on May 05, 2015 and repeated one week later. From the (open) reactor, now filled with particles, 5 kg of Ilmenite-150 were extracted and put into a muffle furnace at 500 °C. Then, these hot particles were poured into the running fluidized bed (Fig. 117 left) and the behavior was observed. The mixing of the hot and cold particles was extremely fast. Within less than one minute, the temperatures in the bed had levelled off (Fig. 117 right) with the exception of a few temperatures close to the bottom of the bed. The measurement of the minimum fluidizing gas flow (see chapter 1.4.2) for several different temperatures mostly matched the expected values. The automatic flow reduction with increased temperature worked flawlessly. The same was valid for the In- and Outpipe when the particle flow was activated. All in all, a wealth of new information could be derived from this test, because it was the first time the fluidized bed operated above ambient temperature.

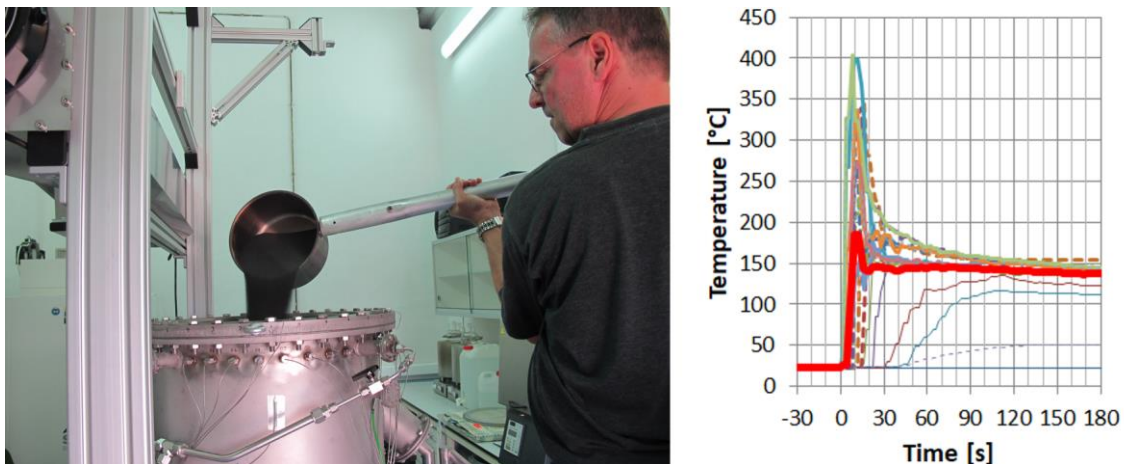


Fig. 117: Left: Pouring particles pre-heated to 500 °C into the running fluidized bed. Right: Temperature distribution in the bed within the first 3 minutes. The red line represents the average temperature.

A few more tests on the ground demonstrated that the window remained clean despite the bubbling and splashing fluidized bed below. The maximum continuous solids flow that could be achieved was 500 g/min. The particle losses through the particle separator were in the order of 5 - 20 g/h.

Then, on May 27, 2015, the time finally had come for the relocation from the lab room to the focal platform of the Solar Furnace (Fig. 118, milestone (1) in Fig. 109).



Fig. 118: Relocation from the lab room to the focal platform of the Solar Furnace.

A few more non-solar tests were performed, but then the activity had to be abruptly suspended because a compressor caught fire. The air consumption of the fluidized bed system was too much for it. Fortunately, a new, much larger compressor was scheduled to be installed anyway, so after a bit more than two months, the work could continue. During the downtime, the frame for the radiation shield was built and the air cooled mirror installed.

As the particle separator was not able to remove all the fine dust from the gas stream, a test was made with a rather small filter taken from model car accessories supply. This worked, but the pressure drop was quite high. Therefore, a larger filter system was designed and ordered.

Another problem had appeared immediately after lifting the system on the focal platform. The steel sheet floor was not stable. Especially when working (humans physically standing) on the frame of the Oresol system, it felt like being on a ship, not so nice when standing 5 meters above the ground. All kinds of attempts to stabilize the floor brought little success. Finally, the Solar Furnace team made a drastic decision: The floor was completely removed and replaced by a system with robust rails. This implied a downtime of another 9 months, but the result was well worth it. For more information about this see also chapter 3.12 and Fig. 89 on page 117.

The downtime was made use of for the installation of the new Particle Separator PS with the Filter F3, a small buffer tank at the outlet of the Recirculation Pump P1, a new window flange with integrated water cooling, for initial tests with the Peltier element, and for the erection of a large canopy that covered the entire plant to protect it from bird poop. Furthermore, a water

cooled diagonal mirror was built by the Solar Furnace staff (see Fig. 50 on page 85). A major challenge was the adaption of the support structure to the new rails, what, basically, meant that the legs had to be shortened. With the system suspended from the crane and replacing one leg after another, it finally was possible (Fig. 119).



Fig. 119: Replacement of the legs of the support structure.

After 6 months, in March 2016, the system was operated on two days on the ground. Then, the radiation shield was fabricated, and after another 3 months, two more ground tests to test the new Particle Separator PS and the Filter F3 were done without problems. The new components appeared to work fine, between 6 and 12 g/h of particles were collected in the particle separator, and virtually no particle had passed the Filter F3. The pressure PT02 in the reactor slowly increased during the tests, but this was not taken seriously at that time.

On July 06, 2016 the system was lifted again onto the test platform of the Solar Furnace SF-60. After three more non-solar tests there dedicated to particle flow, air supply, cooling water, and some fluidization tests, the facility was finally ready for solar operation (Fig. 120).

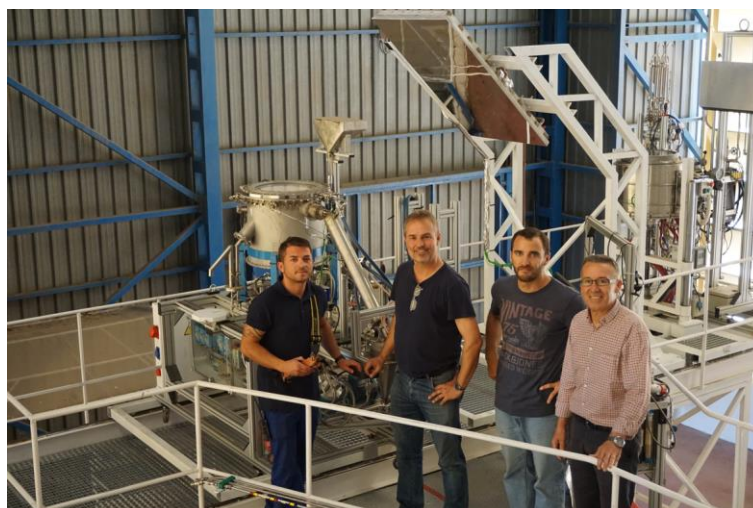


Fig. 120: Solar Furnace staff in front of the Oresol reactor on the SF-60 focal platform.

4.1.2 Ilmenite with Air

In this first *solar* test campaign of the Oresol system in July 2016, a total of 8 experiments were carried out. The downstream section was not yet complete, in particular the Cooler-2 and the

water separator were still missing. Hence there was no gas recirculation. During the first tests, the gas left the system through the bottom opening of the particle separator. Fluidizing gas was, with one exception, air from the compressor of the Solar Furnace. The setup of the gas distributor remained the annular “9/2”-configuration (9 screws on the outer ring with 2 orifices each). The fluidized bed operated for 28 hours, 19 of them with solar power.

The main objective of the campaign was to find out how the individual components of the plant behave at elevated temperature and how they can be controlled. Therefore, the facility was operated with air at up to 400 °C. The temperature was limited to this value because the oxygen in the air might have been a threat to some graphite seals or other pieces of the system. Air was chosen as fluidization gas because the gas consumption needed for proper fluidization at low temperatures is notably higher than at high temperatures and hence consumption of argon would have been excessive, even more taking into account that the gas loop was not yet closed. The plan was to learn as much as possible about operation with air, and then, after switching to argon, being able to pass quickly through the low-temperature / high-gas-consumption regime of the operation.

The Oresol reactor saw its first light⁸⁰ on July 13, 2016 (Fig. 121, milestone (2) in Fig. 109). The solar operation time was two and a half hours. The maximum shutter opening was 15%, but most of the time it remained below 10%. The maximum mean temperature in the bed was 168 °C, and the most surprising result was that there were no surprises. Everything worked as expected.

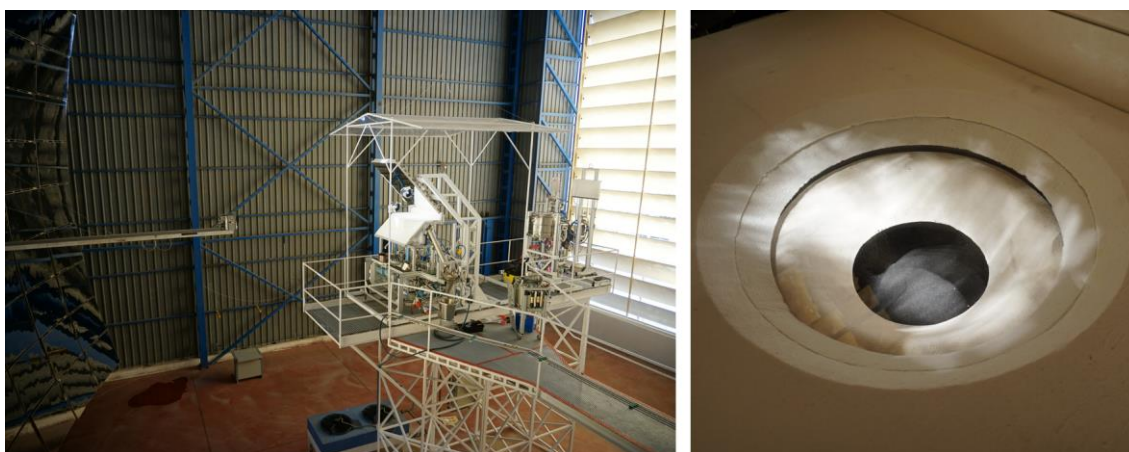


Fig. 121: First solar operation of the Oresol reactor on July 13, 2016.

The targeted 400 °C in the fluidized bed were already reached on the third day of the solar campaign. The particle in- and outflow was successfully tried, data about the minimum fluidizing gas velocity were obtained, and the window protection gas was tested. On the fourth day, 2 hours of stable operation with a constant particle inflow were demonstrated. The goal “4 - Solids Flow” was achieved (see chapter 2.4).

On the fifth day, the Filter F3 was “activated”, this means that the outlet at the bottom of the particle separator was closed, forcing the gas to leave the system now through the outlet on the top after having passed through the particle Filter F3. It turned out that the Particle Separator PS and the Filter F3 worked fine and didn’t cause any problems.

⁸⁰ This expression is commonly used in astronomy when a new telescope mirror is exposed to starlight for the first time. But it also fits quite well to solar energy installations.

On the sixth day, the Recirculation Pump P1 was used for the first time during solar operation. Due to the lack of some parts of the closed loop, the intake was simply connected to the ambient. During this test, some problems occurred. Comparison showed a new deviation between FC01 and FT07 that was difficult to explain. Also, the temperature TC11 on the center-top of the fluidized bed became with 750 °C unduly high. In fact, the particles began to sinter slightly at the site, forming a small "sandstone" (Fig. 122).



Fig. 122: Slightly sintered material in the center of the reactor (the red dot is from a laser for calibration).

The next day, after crumbling the “sandstone”, the first and only test with argon was done. The goal was to gather some experience with this fluidization gas and to narrow down some of the parameters of the control program. After two and a half hours and up to 400 °C, more than 6 m³ of argon or about 60% of the gas bottle were consumed. Like mentioned before, this high value was expected due to the increased argon consumption at lower temperatures. The data from the fluidization tests was only of limited usefulness.

The final day of this campaign went once again with air and without the Pump P1. It showed 4 hours of continuous particle inflow, again a high temperature of TC11 (the thermocouple on the top in the center), and several measurements of the minimum fluidizing gas velocity that gave higher values than calculated. After termination of the solar tests, the particles were drained from the reactor and the whole system lifted down from the test platform.

This first Oresol testing campaign in July 2016 can be summarized as follows. On the positive side, heating of the particles solely with concentrated solar radiation worked with no issues. Continuous particle inflow including flow rate control was possible. The peripheral components, namely the entire upstream, the Cooler C1, the Particle Separator PS with the Filter F3, and the Recirculation Pump P1 did their job. On the downside, the temperature at the center-top of the fluidized bed (TC11) was sometimes so high that even slight sintering occurred. This could be attributed to the “annular” fluidization regime that finally did not allow the particles in the center to sink down fast enough to avoid overheating from the solar beam. The solution was to return to the initial configuration of the gas distributor of 40 screws with 3 orifices each. The other problem was the new inconsistency of the flow rate measurements, especially comparison of FC01 with FT07, and the minimum fluidizing flows notably higher (up to 50%) than the theoretical predictions. This problem found its solution during the subsequent non-solar sub-campaign.

In the following months, the missing components of the downstream section were acquired and installed, in particular the Cooler C2 with the Reheater, and the Water Separator WS2 with

the thermoelectric cooler (Peltier element, TEC). Furthermore, the original gas distributor, consisting of 40 screws with 3 orifices each, was installed again (see chapter 3.5.4).

At the beginning of November 2016, the now complete facility was hoisted again on the test platform (Fig. 123), followed by a series of non-solar tests with the empty reactor. Besides the functionality tests of some new components like the TEC or the buffer gas bag at the intake of the Pump P1, the main goal was to measure the pressure drops of the components.



Fig. 123: Lifting of the Oresol plant onto the test platform of the Solar Furnace SF-60 for the second test campaign.

But very soon, the mismatch between FC01 and FT07 showed up again. Therefore, a special test, similar to the one on April 06, 2015 (see page 142) was done to find the root cause of the problem. The test again consisted in running the four flow sensors FC01, FC02, FT07 and FT08 individually one after the other with the same flow rate of 30 l_N/min. For each sensor, the pressure in the reactor (PT02) caused by the pressure drop in the downstream section was measured. It turned out that the pressure was the same for all sensors, except for FC01, where it was significantly lower. Only the increase of the flow rate set point to almost 50 l_N/min resulted in the same pressure in the reactor. The conclusion was clear, something was wrong with this sensor. A detailed comparison of the data of the former tests from July led to the conclusion that the problem occurred for the first time on July 26. This was the day when the Pump P1 was used for the first time. Therefore, it seems plausible that some dirt or residuals from the manufacturing or whatever was blown into the flow controller FC01, causing some obstruction, and therefore a modification in the behavior of the sensor. Cleaning attempts were unsuccessful. After several further tests, finally a reduction of the range of the sensor to 56.5% of its initial value was determined. The control program was modified to take this change into account. The best solution for the problem of course would have been to send the sensor to the manufacturer for cleaning and recalibration. But this would have meant another interruption of the test campaign for several months. As the correction factor appeared stable, and because the goal of the test campaign was to demonstrate that the system works and not the gathering of high precision data, this was postponed to summer 2017 after termination of the second test campaign. It turned out that the decision was correct; there never occurred any situation that appeared inconsistent with the “new range” of the sensor.

With the flow sensor problem sorted out, the next step was the determination of several pressure drop coefficients in the system. Therefore, the whole range of gas velocities was run through in automatic mode, with air, with argon, with the valve MV12 open and closed, and the pressures were recorded. This way, relations of the type $\Delta p = a\dot{m}^2 + b\dot{m} + c$ were

established for the gas distributor, the “gravity” valve GV, the valve MV12, and the downstream components. The obtained values matched quite well with similar measurements from nearly two years before.

The remaining non-solar tests were dedicated to the checkout of the Recirculation Pump P1 and a dress rehearsal for the gas flows expected for a heating cycle including the handling of some manual valves. Then the reactor was filled with ilmenite. Finally, the coefficient for the flow rate measurement with PT11 and PT01 in case of high flow operation with MV07 open was determined.

On December 14, 2016, the *first solar operation with the complete downstream section* was performed. The test with air as the fluidization gas and Ilmenite-150 as particles went smoothly. After one hour of heating and one hour of very stable particle feed with 100 g/min, a cloud terminated the solar test. As already observed in former tests, the gas demand expressed as u/u_{mf} seemed to increase with temperature. The second and final solar test in December 2016 went quite similar to the one before. Main difference was that the Recirculation Pump P1 was now used. Heating up was done with more solar power and went quite fast, it took only half an hour to reach 400 °C. Before the next test in January 2017, the Particle Separator PS and the pipe to the Cooler C2 were insulated. This way, water condensation in these places is avoided. During that test, the reactor pressure was with about 40 mbar quite high, and indeed, an Outpipe blow-out happened. As such a blow-out (see chapter 3.8) is a somewhat undesirable situation, an automatic detection and warning was programmed in the VI. The next day, this warning was triggered several times. The reason was obvious, the Filter F3 needed cleaning. As at this time the filter was not yet prepared for easy cleaning, it had to be dismantled and the filter cloth was replaced by a new one (Fig. 124). Finally, on January 30, the final test with air was done. Heating up to 400 °C needed only 27 minutes, followed by one and a half hours of smooth operation. The reactor pressure was low again, but it was rising from 13 mbar to 19 mbar over the day. Moreover, a few milliliters of water came out of the water separator, but no further attention was paid to this at first. After 19 operating hours of the fluidized bed, 12 of them with solar power, the system was now ready for operation with argon!

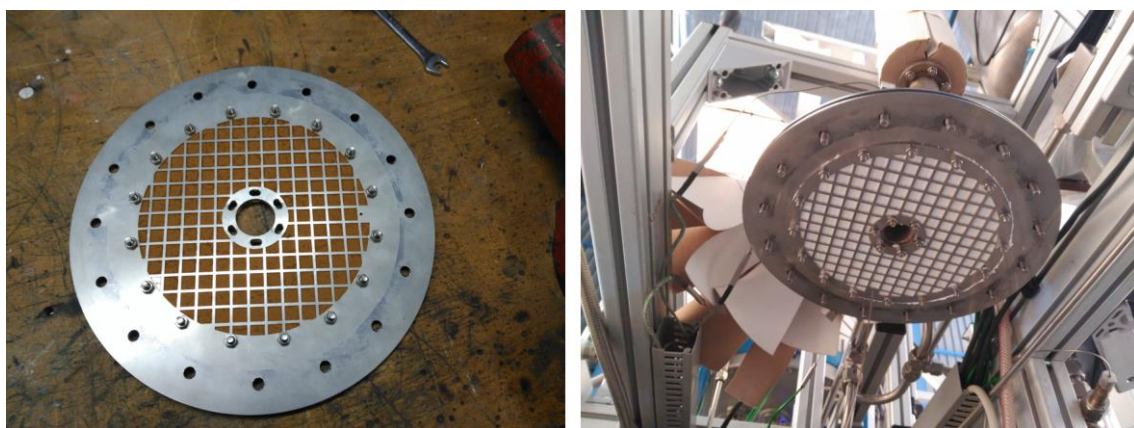


Fig. 124: Filter F3. Left: Dirty, dismantled. Right: With a new cloth, mounted again.

4.1.3 Ilmenite with Argon

The following day, January 31, gas supply was switched to argon. The day was somewhat cloudy; nevertheless, two hours of solar operation were possible. The temperature of the reactor was up to 550 °C like planned. 110 g/min of ilmenite went into the reactor, and a total

of 18 ml of water came out. Like hoped and expected, the overall argon consumption was with 1.9 m³ quite low, the practicing with air at lower temperatures paid off now. The developed operation procedures worked but needed some refinement.

The next day, February 01, the envisioned 700 °C were reached in the fluidized bed. Another goal this day was to adjust frequently the gas flow parameter u/u_{mf} during heat-up with visual help from the observation camera. This worked unexpectedly well, and the important result was that the flow rate requirement depending on the temperature follows a $1/T$ -law rather than a $1/T^{1.7}$ -law (more about this in chapter 1.4 and 5.1). This was then used to include the new “empiric” mode into the automatic gas flow control section of the control program. After only one and a half hours of operation, the automatic blow-out detection interrupted the operation. This was strange, because the reactor pressure PT02 was only about 21 mbar. A thorough revision of the data revealed that the reason was a data transmission glitch. Apparently, from time to time, the (relatively cheap) data acquisition modules mix up some values and the VI on the control computer receives wrong data. To avoid this problem in the future, a consistency check was included in the VI. It simply compares the data from the two redundant pressure sensors PT02a and PT02b. When there is a difference of more than 1.5 mbar, all automatic emergency and shut down routines are disabled until the data is back to normal. The inconsistency is indicated to the operator by a red LED on the front panel of the Oresol.vi. It turned out that this trick worked quite nicely, benefiting from the smart move that the two redundant pressure sensors were connected to different A/D converters. Finally, a small quantity of water (14 ml) also came out of the plant again.

One week later, the goal was to reach between 750 °C and 800 °C. But when the temperature was about 770 °C, suddenly, a suspicious “crack”-sound could be heard. After the defocus, a crack crossing the whole window was visible (Fig. 125). So, this day had mixed results. On the positive side, the thermoelectric cooler and the new “empiric” mode worked very well. The next one of the testing goals, “3 - Gas Flow”, was achieved (Fig. 126 left). Also, the source of the water became more and more clear, it must have been the water content of the material (see chapter 5.5.1). On the negative side, the reactor pressure PT02 was again above 30 mbar, indicating that the Filter F3 once more started to clog. And, like mentioned, a crack in the



Fig. 125: Crack in the window on February 09, 2017.

window appeared, and this even below the nominal operation temperature. More details about that only failure of the window during the whole project and the measures taken to solve this problem can be found in chapter 5.6.

The following days, repairs and improvements were made. The insulation of the window flange was improved, and a new window was installed. The cloth of the Filter F3 was replaced once more, and the insulation of the particle separator was modified in a way that it became much easier to be removed than before. Furthermore, the level sensors in the water separator were finally connected to the data acquisition system.

After one month, solar testing was resumed. Heat-up to 700 °C went quite fast in only 54 minutes. Operation lasted 3½ hours, a maximum of 730 °C was reached, and everything went rather smooth. Solids inflows of 110 and 220 g/min were tested. Maybe the most interesting result was, thanks to the newly installed level sensors, that *the water production* (total of 40 ml) *could be observed in real time* now. It turned out that it followed nicely the particle inflow. This made it definitely clear that the water came from the particles and not from any other obscure source like a small internal cooling water leak or whatever.

Another half a month later, on March 29, a very successful test completed this operation phase. 3½ hours of solar operation, with 1½ of them near or above 800 °C went smoothly without significant problems. The protection against data glitches worked, and despite quite high temperatures under the window flange (especially TC30), the window didn't break again. Immediately after the defocus, the orange glow of the hot particles could be seen for the first time (Fig. 126 right). With this test, the goal "2 - Temperature" was achieved (milestone (3) in Fig. 109), and it was time to start operation with hydrogen.



Fig. 126: Left: Well fluidized particles. Right: Red hot glowing particles at 800 °C.

This second testing phase can be summarized as follows. During the six days with solar operation, argon was the feed gas. The fluidized bed ran for 27 hours, 15½ of them with solar power. At the end, 814 °C were reached in the fluidized bed, slightly exceeding the target temperature of 800 °C. The parameters for the automatic gas flow controls were determined and the continuous supply and removal of particles was once more successfully demonstrated. The window broke once due to insufficient insulation under the large flange. Occasional problems with the data transmission were solved by a software upgrade. The Filter F3 clogged faster than desired; an improvement of the insulation simplified the cloth replacement work. The connection of the level sensors allowed the tracking of the water production in real time. This revealed immediately the source of the water as water of hydration from the particles.

4.1.4 Ilmenite with Ar + <8% H₂

The next day, on March 30, the first cautious operation with hydrogen was made (milestone (4) in Fig. 109). To avoid confusion of product water with water of crystallization, operation above 600 °C was extended for more than one hour, to ensure that no more water was extracted during this time. Then, when at about 840 °C, 1 mol of hydrogen was added (Fig. 127 left) within 15 minutes (reminder: 1 mol of an ideal gas has a volume of 22.4 dm³ under standard conditions). With a delay of also 15 minutes (perceived time: eternal), water started to come out of the system. The quantity was rather low, 4.5 ml or 25% of the possible quantity (Fig. 127 right). Technically spoken, the most important goal, “1 - Chemistry”, was achieved (see chapter 2.4). But the result of course was not yet very satisfactory. Where did the other three quarters of the hydrogen go?

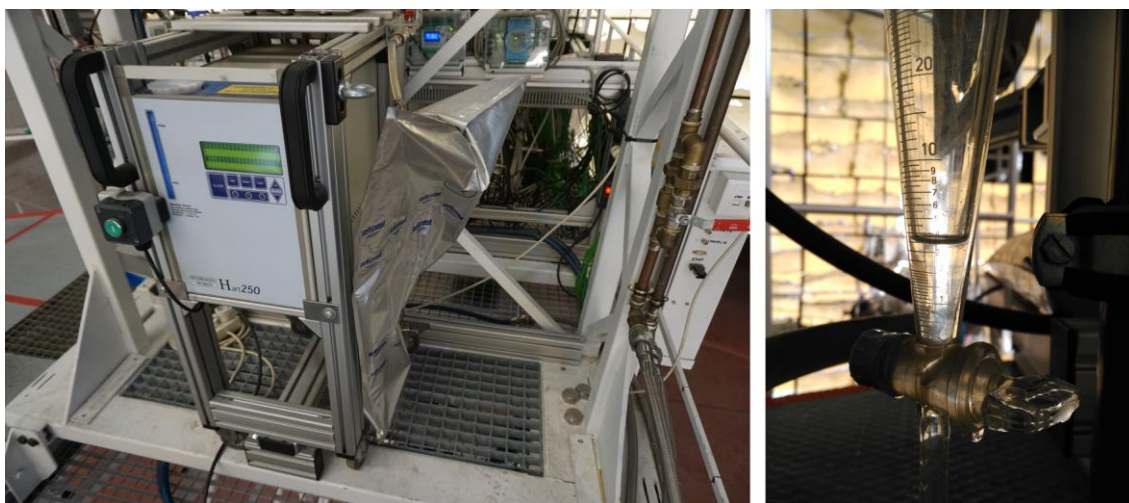


Fig. 127: First operation of the Oresol reactor doing solar thermochemistry on March 30, 2017. Left: Electrolyzer with mostly empty (and somewhat crumpled) hydrogen bag. Right: Product water from the chemical reaction (the first “lunar gold”).

In the following days, several different parameters were tried. H₂-injection at low flow rate (0.5 l_N/min) gave no water at all. Another test with the maximum flow rate of 2.0 l_N/min converted less than 10% of the hydrogen. Due to the ongoing weakness of the electrolyzer, every second day was needed to refill the hydrogen bag. Another day was used to replace the particles in the reactor, with the hope that the reason for the low yield was maybe that the old ones were already “exhausted” by too many heating cycles. Furthermore, the hydrogen storage was increased to 3 bags of 27 liters each to increase the total gas feed (Fig. 128). Nevertheless, the water production remained between 10 and 20% of the possible maximum. The *mystery* was not so much the low production rate but the question where the unreacted hydrogen had gone. It should have been detected in the recirculated gas, but this was apparently free of hydrogen, the flow transmitters FT07 and FT08 didn’t show any deviation. The delay between start of hydrogen feed and start of water discharge was always about 20-25 minutes. In parallel, during the tests, the reactor temperature was steadily increased to above 900 °C.

To overcome the difficulties with the electrolyzer and the low hydrogen storage capacity of the gas bags, a connection to the hydrogen supply line of the Solar Furnace was installed. This required some formal paperwork and the acquisition of a hydrogen bottle, but thanks to the help of the safety responsible at PSA, this went remarkably fast. On April 25, the first test with hydrogen from the gas bottle was executed. 5 mol of hydrogen produced 26 ml of water, 27%

of the theoretical maximum. This was better than before, but still far from “good”. The next test on May 18 with 10 mol (224 liters) of hydrogen produced 60 ml or 33% of water. Step by step, things became better. This was also the first test operated at more than 950 °C.



Fig. 128: Electrolyzer with three hydrogen bags.

In the following weeks, there were only limited opportunities for testing. In particular, due to the presentation of the work on the Fifth European Lunar Symposium (ELS 2017)⁸¹ in Münster (Germany), three TV teams⁸² visited the project within two weeks. Then, with only one day remaining in the test window, it was tried to squeeze out once more the maximum from the system (Fig. 129). The maximum average temperature was a record breaking 977 °C with local peaks above 1000 °C (milestone (5) in Fig. 109). 180 liters or 8 mol of hydrogen produced 80 ml of water, or 56% of the possible quantity. After this test, the system was removed from the testing platform to clear the Solar Furnace for other projects.

This third testing phase can be summarized as follows. The fluidized bed was in operation for a total of 60 hours, $\frac{3}{4}$ thereof heated with concentrated solar radiation. At 9 of the 14 experimental days, a mixture of argon with hydrogen was used, adding up to 8.3 hours. During the first 4 of the tests, the hydrogen came from the electrolyzer. Its continuous production rate should have been 1 l_N/min, but in practice it was much less. There were at first one, later three storage bags for the hydrogen with a capacity of 27 liters or 1.2 mol each. Due to the ongoing problems with the electrolyzer, the hydrogen source was changed to a bottle. The amount of supplied hydrogen was, for the reasons mentioned in chapter 3.3.1, with a maximum of 2 l_N/min relatively low, so that only moderate amounts of water were produced. During the tests, the reactor temperature was increased gradually, from 814 °C at the end of the previous test phase up to 977 °C at the end of this phase, without any damage to the

⁸¹ <https://els2017.arc.nasa.gov/>

⁸² Canal Sur (Andalusia), RTVE (Spain), and Cosmos Factory Filmproduktion (Austria). The documentary “The Moon – Our Gateway to the Universe” (2017) by Cosmos Factory won several awards: New York Festivals: Gold World Medal. US International Film and Video Festival: Silver Screen Award. International Nature Film Festival, Gödöllő/Hungary: Bronze Award.

reactor. A total of 336 ml of water were extracted from the reactor, 85 ml of them from the mineral and 251 ml from the chemical reaction.

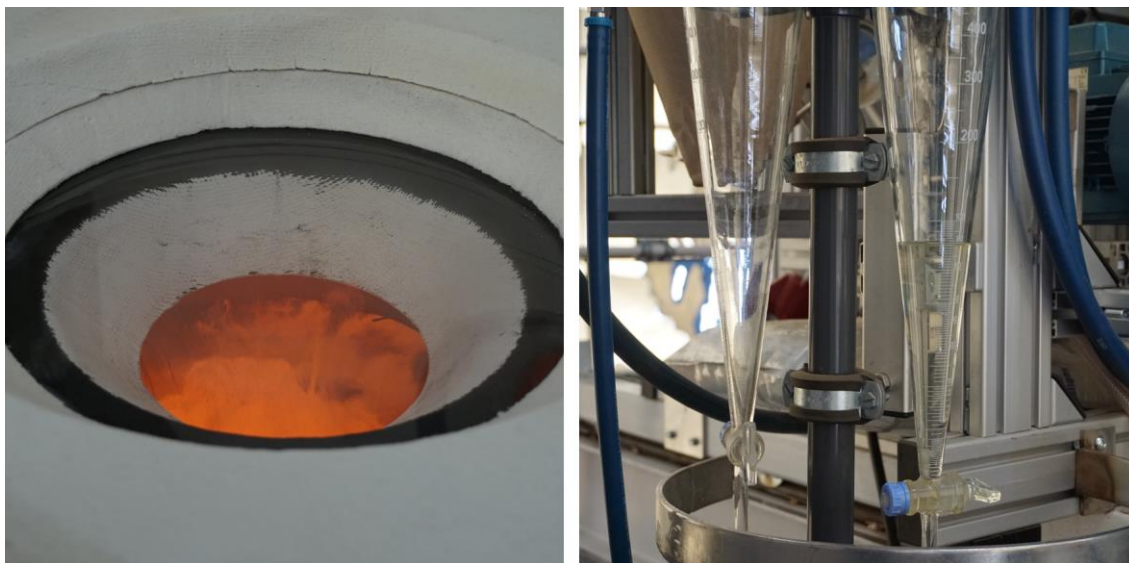


Fig. 129: Final test of the second test campaign on June30, 2017. Left: Fluidized bed at 950 °C. Right: Product water (80 ml).

At the end of this testing phase, the first four goals outlined in chapter 2.4 were achieved. Particle in- and outflow was demonstrated, the gas flow rate parameters were determined, a reactor temperature above 950 °C was achieved, and water produced by the chemical reaction came out of the system. Several technical problems, like cleaning of the Filter F3 or humidity in the flow sensors FT07 and FT08 were solved. The product water appeared always with a large delay of 20 to 30 minutes after start of the injection of the hydrogen. Only the two final days were an exception, where the delay was only 3 min. But the product water yield was well below the expectations, in the best case it reached 56%. The *mystery* of the fate of the unreacted hydrogen remained.

To be able to increase the hydrogen share of the feed gas in future tests, the flow controller FC06 was sent to the manufacturer in summer 2017 for recalibration to 8x the range, allowing then a hydrogen flow rate of up to 16 l_N/min. But during disassembly of the device, it was noticed that two fittings were not properly tightened. The location (Fig. 130) was extremely

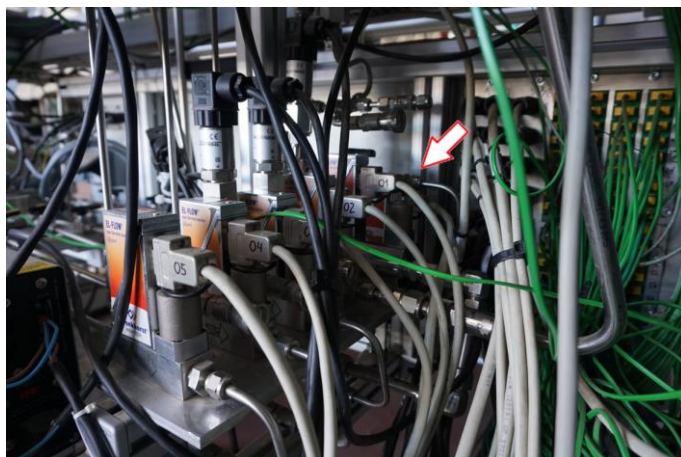


Fig. 130: Location of the leak.

unfortunate, it was after the flow controller FC06, but before the junction with the argon feed line, and possibly among the most inaccessible places of the whole installation while on the focal platform. This immediately solved the *mystery* of the missing hydrogen. The positive side of that “discovery” was that it didn’t invalidate the qualitative results of the test campaign. And the quantitative results, the conversion rates, now promised to become better.

4.1.5 Ilmenite with Ar + >8% H₂

Due to heavy utilization of the Solar Furnace, the subsequent test campaign could only be carried out after more than one year in autumn 2018. Despite the long break, there were no problems with the restart. The most important changes made to the system in the meantime were the installation of a pre-stage for the water separator (see chapter 3.9.4), a new scale for the used particles (MT02) with a range of up to 80 kg (instead of 10 kg before), the installation of the humidity sensor RHT (after more than one year [sic!] of procurement time), the cleaning and recalibration of the Flow Controller FC01 for use with pure argon now, and especially the recalibration of the hydrogen flow controller. Instead of up to 2 liters per minute, its range was now up to 16 liters per minute.

The campaign was divided into three sub-campaigns, with the first one in autumn 2018, the second in January 2019, and the last one in autumn 2019.

The aim was to determine the behavior of the plant with higher hydrogen content in the feed gas. In particular, the production of at least 100 ml of water should be demonstrated on a single testing day.

Although the first sub-campaign lasted four weeks, only a total of 6 days of operation were usable due to the mostly bad weather and various technical problems with the shutter and the hydrogen supply of the Solar Furnace. The first two of the tests were dedicated to the determination of the release of water of crystallization from the particles at 660 °C and 930 °C, and therefore without hydrogen. In both cases, the fraction of water of crystallization was 0.84%, more than the 0.24% indicated in the data sheet.

October 31 was the first day with hydrogen in the feed gas. The flow rate was set to 2.0 l_N/min to allow comparison of the results with the previous test campaign in 2017. After half an hour and 2.5 mol at about 930 °C, a cloud forced the end of the operation with hydrogen. Nevertheless, the results looked promising. 31 ml of water were produced by the chemical reaction, corresponding to 68% of the possible yield. The water appeared with a delay of 22 min. An interesting observation was that the humidity sensor RHT reacted practically immediately to the hydrogen injection with an increase from 40% to 60%.

But with the increase of the hydrogen flow to first 5 l_N/min and then 4 l_N/min the following two testing days, the problems began. The yield remained comparable (about 65%), but the pressure loss through the Filter F3 rose much faster than in previous experiments. Especially the second day, the pressure in the reactor PT02 became so high that operation with hydrogen had to be suspended after 40 min. Moreover, the Particle Separator PS no longer reached the necessary working temperature above 100 °C, in particular the sensor TC43 at the bottom. For some reason, possibly the increased water steam content and/or the possible presence of unreacted hydrogen in the off-gas, the cooling efficiency of the Cooler-1 was better than before. After replacement of the filter cloth, the fourth day with hydrogen didn’t show any improvement. Due to the low temperature in the particle separator, it was suspected that the

Filter F3 was too humid and therefore better retained even the coarse dust that normally would have fallen down.

To overcome this problem, a radical solution was adopted. The water cooler C1 was converted into an air cooler (Fig. 131). The cooling water was disconnected and drained, and a fan was installed at the bottom end of the cooler. Two subsequent tests showed that the temperature in the particle separator could be well controlled now. It surpassed the 100 °C after only one hour of solar operation, compared to at least two while working with water cooling. But due to clouds, no further operation with hydrogen was possible. This left this part of the test campaign without meaningful completion.



Fig. 131: Cooler C1 converted into an air cooler with fan.

Thanks to a rearrangement in the test schedule of the Solar Furnace, advantage of a good weather period in January 2019 could be taken. 4 runs on 4 consecutive working days were possible in this second sub-campaign. At temperatures around 950 °C, quantities of water up to 150 ml and more per testing day were generated only from the hydrogen reaction, corresponding to a hydrogen conversion above 90% (milestone (6) in Fig. 109). This demonstrated that the Oresol system in fact is able to convert almost all of the hydrogen into water. The water appeared with a delay of 10 to 15 minutes. However, the fast filter clogging was an ongoing problem, and all attempts to control it by varying operating parameters or other measures failed. Even a method with hammer strokes against the filter during operation led only to short-term relief. The course of one of the days (January 11) of this sub-campaign is described in deep detail in chapter 4.2.

Another problem that latently accompanied the experiments was a somewhat insufficient fluidization of the eastern side of the fluidized bed. Around noon on the last day of this sub-campaign, the upper layer of the fluidized bed became hotter than usual, reaching 1007 °C in the center (TC11). The temperature on the eastern surface probably was even higher, resulting in slight sintering of the particles at that location (Fig. 132). The consistence of the sintered material was very similar to the one during the first campaign, comparable to wet sand used to build castles on the beach, and decomposed immediately when touched with the fingers. This event was a gentle reminder that there is definitely an upper temperature limit for operation.

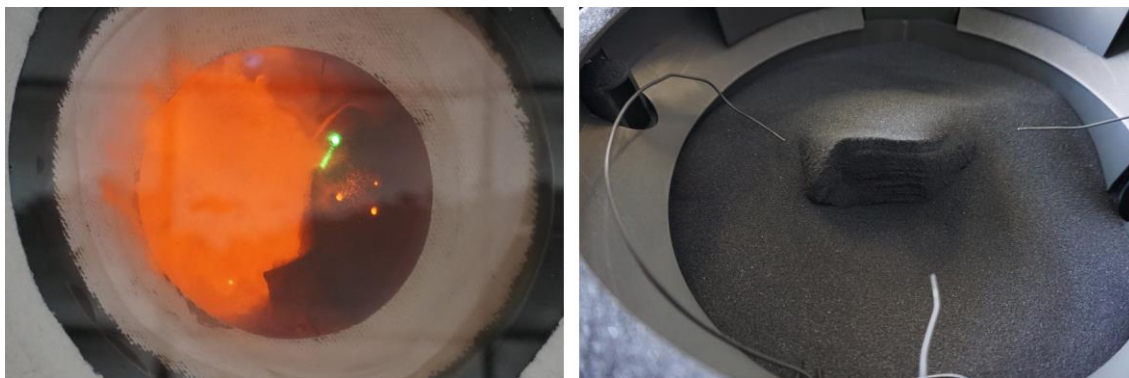


Fig. 132: Sintered particles due to overheating. Left: with the hot fluidized bed still running (north on top). Right: After opening of the reactor (north on left).

To overcome the filter problem, a new filter with 20x increased filter area was designed (see chapter 7.1) and purchased with the goal to use it during the third sub-campaign in September 2019. Unfortunately, the acquisition of the filter was delayed due to ongoing administrative problems. As it was not ready on time, the two weeks of testing had to be done with an unchanged configuration.

Five solar tests could be done during this short final sub-campaign. The goal was to find out if there is something like an upper limit for the hydrogen supply that allows operation without fast clogging of the Filter F3. The tests were done at temperatures between 870 °C and 950 °C. The first day on September 24, a total of 5.1 mol of hydrogen was injected with between 1.6 and 2.2 l_N/min. The machine produced 93 ml of water, this means on this day, all hydrogen was converted (see also page 187 in chapter 5.5.1). The reactor pressure went up only moderately, from 12 mbar at the beginning to 19 mbar at the end. The next three days, however, the Filter F3 again was uncooperative. On all these days, between 5 and 6 mol of hydrogen were fed at about 2 l_N/min into the reactor. The hydrogen conversion became worse from day to day, dropping from 89% to 71%. The reactor pressure always started around 15 mbar and ended around 35 mbar. The last day of the campaign didn't even see hydrogen feed, because the pressure PT02 already started to rise during the heat-up phase from 15 to 35 mbar within one hour. The next logical step might have been to replace all particles in the reactor by fresh ones, but there was not enough time left for this in the given short slot of this test campaign.

This fourth and so far final testing phase can be summarized as follows. The fluidized bed was operated for a total of 66 hours during the three sub-campaigns, of which just under 60 hours were with solar energy. The significantly higher solar share compared to the previous test campaigns was mainly due to the fact that the active cooling of the plant after the tests was mostly omitted. The hydrogen feed with now tight piping led to an immediate increase of the conversion. During slightly more than 13 hours of operation with hydrogen, a total of 1069 ml of water were produced. Rates of around 100 ml/h and more were achieved on several days. In addition, the plant extracted 581 ml of water of crystallization from the ilmenite. The hydrogen conversion ranged from 60% to 100%, with 90% being a frequent value. After the modification of the Cooler C1 into an air cooler, the heating time of the Particle Separator PS dropped to about one hour. But the clogging of the Filter F3 still went far too fast. Operation with hydrogen was hardly possible for much more than one hour. A new filter with 20x the filtering area was designed and purchased, but not ready in time. Trials to find an upper limit for the hydrogen feed flow without filter clogging did not give conclusive results.

After these tests until the writing of these lines at the end of 2021, no further solar or non-solar tests were carried out with the Oresol system (Fig. 133).



Fig. 133: Oresol system in summer 2021 awaiting future testing. In the background the recently replaced, brand-new concentrator of the PSA Solar Furnace.

4.2 Example of a Test Day

The choice of the most suitable testing day to be presented in this chapter was not easy, because there was no single testing day that could be considered as completely “flawless” or “perfect”. The shortlist finally narrowed down to the four days in January 2019. They all had good meteorological conditions, operated with sun for more than four hours (except the last day, only three), all worked around 950 °C in the reactor and well above 100 °C in the particle separator, had phases with particle inflow, produced quite large quantities of product water, but had difficulties with the clogging of the Filter F3. Finally, January 11 was chosen because, despite the somewhat bumpy start, it shows in a nicely separated way the effects from the particle and the hydrogen feed. Moreover, it had a successful minimum fluidizing velocity measurement at the end, and it produced the highest quantity of water of all testing days.

4.2.1 Protocol and Check-List

During all testing days, notes were taken continuously in a *protocol-document* in parallel to the operation. To prepare the following day, these notes usually were simply copied, cleaned up, and modified according to the foreseen goals of the test ahead. This means that the document had a double task: On the one hand, it served as a *check-list* for all events to be *expected ahead*, and on the other hand, over the course of the day, it turned into a *protocol* documenting all events that had *occurred in the past*. The conversion of the old protocol into a new check-list was usually done the evening before a test.

That document starts with a table including basic information like a very short summary, reactants used, maximum temperature reached, water production, involved staff, and detailed information about the currently used hardware including sensors and information about recent modifications and anomalies. The subsequent main section is basically a chronologic list including the timing of all major and minor events that occurred during the day. Important events like start/end of reactor fluidization, operation with solar radiation, or feed with reactants (particles, hydrogen) are highlighted. Finally, at the end, there's a quick summary, some initial evaluation, and spontaneous thoughts about what should/might be done in the near future. The language used is a vivid mix of English, Spanish, German, and *Schwäbisch*⁸³, because there's usually very little time the operator can dedicate to this document, especially when things go awry. The times of the events are always put in UTC (Universal Time Coordinated), because it better reflects the geographical location of the Plataforma Solar de Almería (Longitude 2.4° West) than the official time (UTC+1h, corresponding to 15° East), and it also avoids confusion caused by change to daylight saving time (UTC+2h).

4.2.2 Preparation

The preparation of the system mostly follows the same procedure every day. This includes start of the control program (Oresol.vi), start of the cooling water pump at 5% speed, check of the available gas bottles pressure (argon and hydrogen) and opening of the argon bottle (hydrogen remains closed), switching on of the power supply for pumps and TEC, emptying of the bucket for the spent particles and refilling of the funnel with fresh particles, filling of the water separator with deionized water and drain with Pump P3 until the low level sensor falls dry, and connection and calibration of the oxygen sensor. Also the cover of the reactor window is removed and the window cleaned if necessary. The heliostat, the concentrator, and/or the diagonal mirror are cleaned from time to time when needed. Furthermore, the dust accumulated in the Filter F3 is removed according to the procedure described in chapter 3.9.2 and Fig. 74 on page 105. In addition, the logger is turned on, and all remaining pressure is released from the system to allow for the automatic offset calibration. Then, all manual valves are switched into their correct position. Finally, the shutter of the Solar Furnace is closed, the heliostat is set into sun tracking mode, and the cooling water pump is set to 25%.

In the case of 2019, Jan 11 (the day detailed here), relatively recent modifications of the hardware were change of the Cooler C1 from water to (provisional) air cooling, and the installation of a new "gravity" check valve (GV). All sensors were installed and working, only TC16 and TC18 (thermocouples under the aperture cone) were somewhat displaced and therefore expected to give wrong (too high) readings due to being no longer protected from direct solar radiation by the cone. Operator of the Solar Furnace was José Galindo, replaced if necessary (lunch!) by Mario Cano, and the operator of the Oresol plant was me, assisted by the student Andre Adämmer. The weather was sunny ($\text{DNI} = 850 \text{ W/m}^2$), the wind speed low ($< 10 \text{ km/h}$), and the ambient temperature quite cold (8°C). Due to the heat retained in the reactor from the previous day, the temperature of the particles was still around 250°C .

An unusual holdover from the previous day was that it had ended with a "*solids blow-out*" (see chapter 3.8). As the Outpipe could not easily be refilled with particles, this required a special measure. To avoid the gases to leave the system through this wrong path, the outlet port of this pipe simply was plugged by a scrunched up piece of paper.

⁸³ Dialect spoken in some regions in the south of Germany.

The course of the most important data of the 2019Jan11-test is shown in Fig. 135. The diagram on the top includes data which has to do with the operation of the fluidized bed, like available solar power (DNI: yellow, shutter: black curve), temperature (min, avg, max; red lines), flow rate (green; set point: light green), and pressure (blue). The graph on the bottom shows the data related to chemistry, which means particle feed (black, thick is smoothed data, gray is set point), hydrogen feed (red: in-flow; dark orange: calculated concentration, light orange: H₂CT), and water production (blue). The arrows and numbers “(X)” in red refer to events that happened during the day and are explained in the following chapters. The events (10), (11) and (26) are marked by ovals instead of arrows since they refer to longer periods of about 1 hour and not only to single events. To fully understand all actions and occurrences, the piping diagram (Fig. 41 on page 72) is repeated here (Fig. 134), with the sensors, valves, etc. mentioned in the subsequent chapters highlighted with a light yellow background.

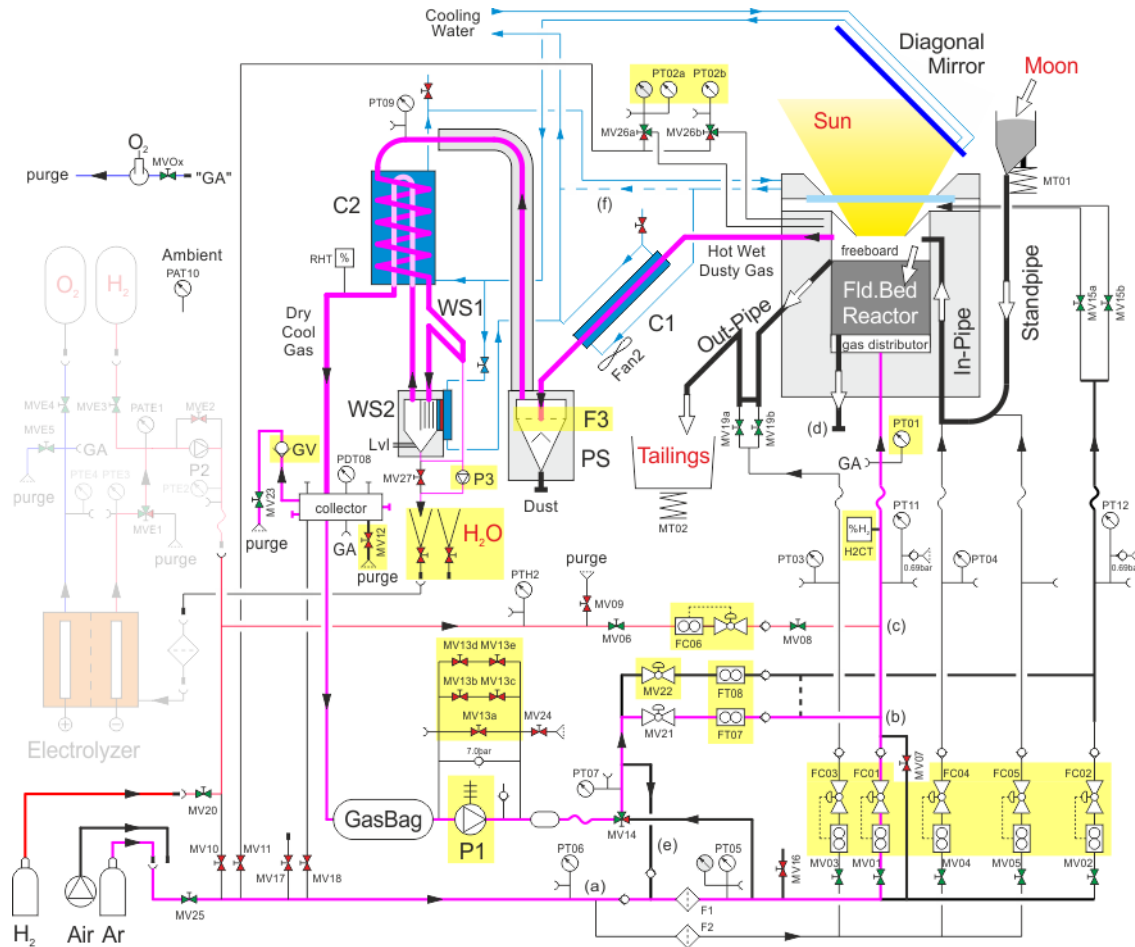


Fig. 134: Oresol piping diagram (Fig. 41, page 72) repeated, with the sensors, valves, etc. mentioned in the subsequent chapters highlighted with a light yellow background. The electrolyzer was not used.

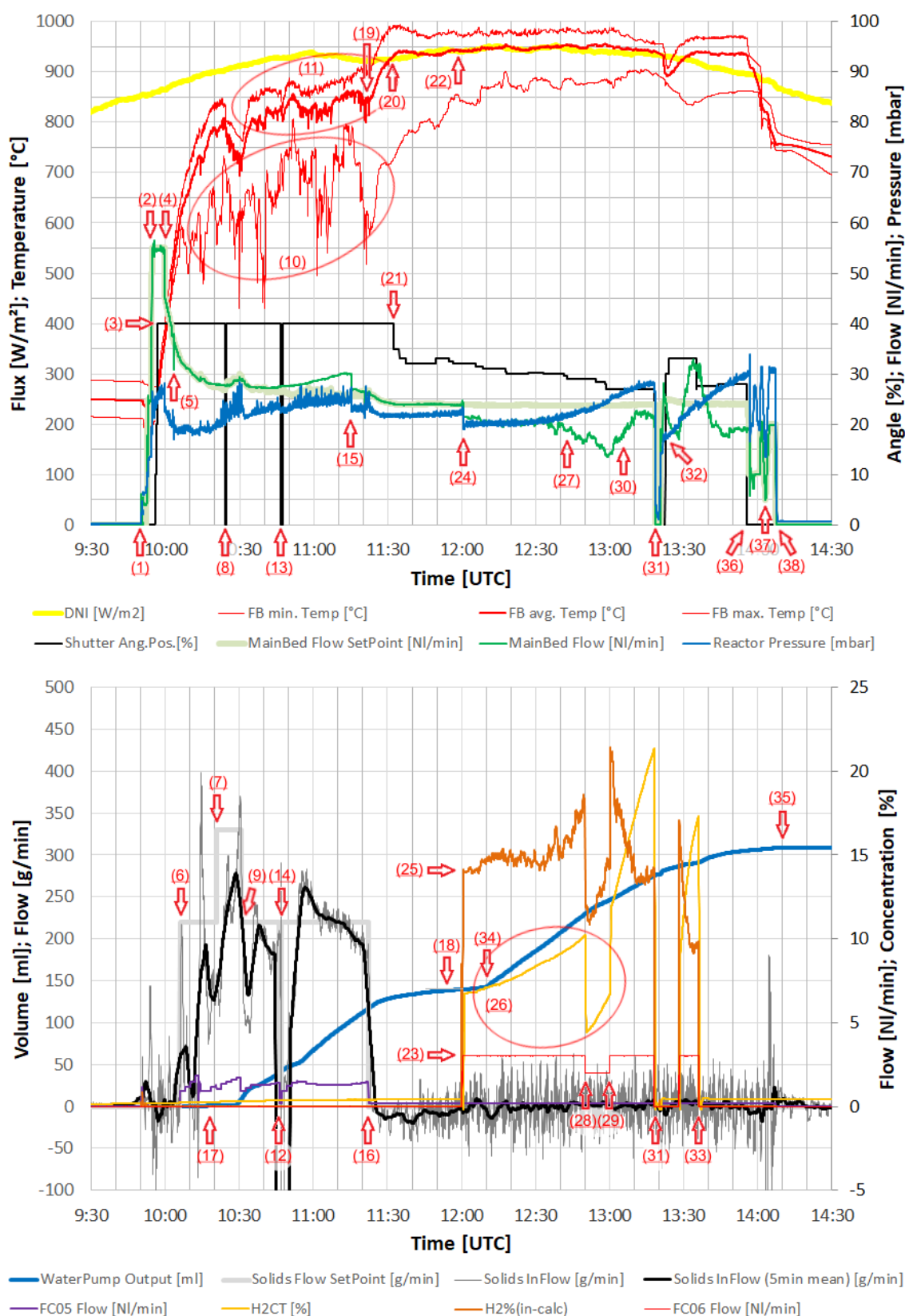


Fig. 135: The most important data from the test on 2019 Jan 11. Top: Fluidized bed related data: DNI (yellow), temperatures (red), gas flows (green), pressure (blue). Bottom: Chemistry related data: Water production (blue), particle inflow (black) and hydrogen feed (reddish). In both graphs, the first four items in the legend refer to the left axis and the second four to the right axis. The events marked by numbers in parenthesis “(X)” are explained in the text.

4.2.3 Fluidized Bed Operation

Operation always begins with the activation of the gas flows, also called *Fluidized Bed Startup*, marked as (1) in Fig. 135. First, all flow controllers except FC06 (for hydrogen) are switched on, making them run on their minimum possible flows (2% of the full range). Then, the nominal flows are set in the proper order, starting with the window protection gas (FC02), followed by the Outpipe (FC03) and the main fluidized bed (FC01 + Pump P1). The reason for this order is to avoid unwanted accumulation of particles in the reactor or the Outpipe. On the given day, FC03 initially was left off deliberately due to the mentioned problem with the blow-out. Furthermore, FC01 is always set first to a rather low value (25 l_N/min) to avoid uncontrolled splashing of the particles when the Pump P1 is turned on. To further minimize this effect, the short cut valve MV13a is open while P1 is switched on, and then carefully closed. Once P1 is running and MV13a closed, the set point for the main bed gas flow rate is increased again until it matches with the demand required for the current bed temperature. When the system starts from completely cold, this can be up to 100 l_N/min and more. To avoid a too high pressure drop over the “gravity” valve GV, the purge valve MV12 is normally open during start-up. In case of the given day, due to the residual heat in the bed from the day before, a main bed gas flow rate of 55 l_N/min was sufficient (2). This flow was also low enough to allow keeping the valve MV12 closed from the beginning. Once the main bed is properly fluidized, the remaining flow controllers for the Inpipe (FC04) and the standpipe (FC05) are set to their initial values. To complete the start-up of the fluidized bed, the automatic operation modes were activated. On this day, due to an error while preparing the check-list, the gas flow for the main bed remained at first in manual mode and hence constant ((2)..(4)). Furthermore, like mentioned, the Outpipe gas flow (FC03) was still left off due to the “blow-out” situation.

4.2.4 Solar Operation

About five minutes after the beginning of the fluidized bed operation, the *Solar Operation* was enabled. The first step there is a slight opening of the shutter to 10% to allow for fine tuning of the heliostat tracking. Once done this, the shutter was opened stepwise up to 40% (3) and the temperature in the reactor started rising quickly. A few minutes later, the error with the Main Bed Automatic Operation was noticed and corrected making the flow rate instantly drop to the correct value (4). After just 7 minutes of solar operation, the reactor temperature had increased to 500 °C, time for the first reduction of the flow of the Pump P1 by opening of the bypass-valve MV13b (5). This work is done directly at the system, but the position of the valves allows access without interruption of the solar operation. The transmission of the most important flow data to the smartphone via Bluetooth helps with the fine-tuning of the MV13c adjustment if necessary. Furthermore, a check of the oxygen sensor (that is not connected to the control room computer) confirmed that the system was well purged with argon and practically free of atmospheric oxygen.

4.2.5 Particle Inflow

The subsequent continuation of the heating is normally a more or less relaxed phase of the operation, but on this day, because of the “blow-out” event the day before, the *Particle Inflow* was initiated early. The plan was to “overfill” the reactor to a certain extent with particles to guarantee that the north-branch (the one on the reactor side) of the Outpipe syphon became as full as possible. For saving time, the rather high value of 220 g/min (6) was set. But the particles were not very cooperative this day, the flow started slowly and unstable. After 10 minutes and some hammer strokes, the particles finally poured into the reactor and the automatic mode was resumed at the unusually high set point of 330 g/min (7).

Now it was time to reactivate the Outpipe. Therefore, in rapid succession, the shutter of the furnace was closed (8) and Andre (the student) removed the plug in the Outpipe. After a quick check of the reactor pressure (PT02) confirmed that it was stable (did not plunge to zero), the Outpipe gas flow (FC03) was turned on, carefully increased, then switched to automatic mode, and the shutter was opened again to 40%. This way, the interruption of the solar operation did last only 40 seconds.

With the Outpipe fully operative again, the operation with particle inflow continued with the set point back to 220 g/min (9). As the particles enter cold into the reactor and in form of slugs, they cause a certain disturbance of the temperature distribution within the fluidized bed, easily visible in the graph of the bed temperatures and in particular the minimum temperature (10). Especially TC07 and TC12, the mid and top thermocouples located on the north side of the reactor just below the mouth of the Inpipe (see Fig. 43 on page 76) showed strong fluctuations.

Normally, when operating with particle inflow, the power input is increased a few kilowatts to compensate for the additional heat sink. But in this case this was not done because the system still was in the heat up phase and strict temperature control was not necessary. This resulted in an unusually flat curve of the reactor temperature during heat-up and a somewhat increased heating time compared to other days (11).

After 40 minutes of operation with a rather high but unstable particle inflow totaling in 6.8 kg, the feed funnel was empty and the inflow was halted automatically (12). In a similarly coordinated action as with the plug in the Outpipe, the shutter was closed (13), the funnel was refilled with a particle quantity already weighed out beforehand, and the shutter reopened to 40%. Again, less than 1 minute of solar operation was lost during this action. The automatic particle inflow was set once more to 220 g/min (14).

The following about 35 minutes of operation with particle inflow were mostly uneventful. An Argon-Low alarm was resolved by hot-swapping of the bottles, and the gas flow into the main fluidized bed had to be reduced for a second time (15), now by opening of the valve MV13d. In the 30 or so minutes before (15), a certain misbalance developed between the flows through FT07 and FT08 with FT07 slowly increasing. This was solved by further opening of the final remaining bypass valve for the Pump P1, MV13a. The flow to the window through FT08 was then somewhat low, but as this flow is not critical and also can be compensated easily by FC02 (at the expense of slightly higher argon consumption from the external supply), it was decided not to interrupt the solar operation for refinement of the position of the valve MV22. When the funnel of the particle feed was empty again, the particle flow was stopped one last time by reducing the gas flow into the standpipe to 0.2 l_N/min (16). The total amount of particles refilled into the reactor was 14.6 kg or about ⅓ of the capacity of the reactor.

4.2.6 Water of Crystallization

Contrary to the operation on the Moon, most solid feedstock from Earth is to some extend hydrated, meaning that it contains at least some small amounts of so-called water of crystallization that is stripped from the mineral when exposed to elevated temperatures. For the water separator of the Oresol system it's an easy task to extract this water from the gas stream. The first drops appeared (17) about 10 minutes after the start of the solids inflow, and at the end, nearly 140 ml of water (18) were extracted from 14.6 kg of ilmenite, resulting in a fraction (by mass) of the water of crystallization of 0.96%. This value can be input into the

control program to enable a proper real time calculation of the progress of the chemical reaction later in the day.

In the meantime, the reactor temperature had risen further, and at the moment of stopping of the particle inflow it had already reached 850 °C (19). With the now missing particle inflow heat sink, the pace of the temperature rise went up again. Only 10 minutes later, it had reached 930 °C (20) and it was time to reduce the solar input power (21) to stabilize the operation conditions. This is a process that takes some time, because there are always some thermocouples in the bed dragging somewhat behind, and also there still “disappears” some energy into heating of the insulation of the reactor. Finally, the mean reactor temperature levelled around 950 °C (22), the target temperature for the day.

4.2.7 Chemical Operation

Now it was time for *chemical operation* with hydrogen. First, the second Imhoff cone was placed under the product water outlet. This way, the two different waters (crystallization vs chemical reaction) remain separated and possible differences in the chemical or physical properties can be detected. Then, the valves of the hydrogen bottle and the piping system are opened, the supply pressure adjusted, and the system access gate closed to comply with internal safety regulations. The final preparation step is to press the “Calibrate-for-H₂-sensing” button in the control program. This is a somewhat peculiar and highly experimental feature of the Oresol control VI. The idea behind it is that the flow transmitters are calibrated for argon, but during operation with hydrogen it has to be expected that the gas composition changes and therefore the sensors will give wrong readings. It’s supposed that the real volume flow does not change, because the Recirculation Pump P1 works with volumetric displacement and hence doesn’t care about the composition of the gas. In other words, any change in the data from FT07 and FT08 can possibly be attributed to additional hydrogen in the gas flow and therefore be used to estimate the hydrogen fraction in the recirculated gas.

At exactly 12 o’clock, FC06, the controller for the hydrogen, was set to 3.0 l_N/min (23) and the operation with hydrogen started. The external argon supply to the fluidized bed, already at its minimum, was completely stopped by turning off FC01 (24). The fluidized bed was now running exclusively on recirculated gas and without active flow control. In Fig. 135 top it can be seen how the gas flow was then somewhat below the set point and for more than 30 minutes without significant variation. The pressure in the reactor (PT02) was with 20 mbar encouragingly low (24). The *calculated* hydrogen share (from FT07 and FC06) in the gas was 14-15% (25), well above the 8% that were used in most of the previous tests. Like mentioned earlier (chapter 3.13.5), there was a hydrogen sensor (H2CT) in the reactor feed line that didn’t work properly. Normally it returned zero, but when the hydrogen flow rate was higher than about 2 l_N/min, a signal (26) appeared that seemed to follow more or less the calculated value only with an offset of approx. 7%. This measured value showed a slow but rather steady rise during the first 50 minutes of the operation with hydrogen. It’s not clear if this is real or a sensor artefact or both.

About 40 minutes after the start of the hydrogen operation, the data from the flow transmitter FT07 started to drop significantly (27), indicating that something had changed in the composition of the gas. It has to be reminded that from this moment on, the absolute value of the graph for the calculated hydrogen share no longer makes sense, because it’s based on the now unreliable data source FT07. Around the same time, the reactor pressure started to rise slowly (27), indicating the beginning of the clogging of the Filter F3. About ten minutes later, at 12:50, the hydrogen feed (FC06) was reduced to 2.0 l_N/min (28), with the hope that this would

slow down the pressure rise of PT02. Interestingly, both, the calculated and the measured hydrogen share, dropped practically instantly for about the same amount, indicating that H₂CT at least measured “something” meaningful. But the deviation of FT07 continued in the same direction, and the rise of the reactor pressure remained unaffected. Therefore, after another 10 minutes, the hydrogen flow was restored again to the initial value of 3.0 l_N/min (29). The hydrogen shares (calculated and measured) returned instantly to their original trends, but surprisingly, the trend of the deviation of FT07 now had changed its direction (30). Long story short, the interpretation of the data is difficult. A more reliable hydrogen sensor and a bigger filter would help.

4.2.8 Filter Cleaning

As the reactor pressure continued to rise, and also based on the experience from earlier tests, it was decided to interrupt the operation for a rapid filter cleaning. Opening of the system to apply the reverse flow method used in the morning before the start of the system was not an option, because the particle separator was hot (>100 °C) and because this would mean to allow air with oxygen to enter into the system. The alternative was the brute force method, some hammer strokes against the filter. Therefore, the hydrogen feed was turned off, the shutter closed, and all flows and pumps stopped simultaneously (31) by pressing the Emergency-Stop button. The hammer strokes were applied, the flow controllers and the Pump P1 turned on again, and the shutter opened again to 33%. About ten minutes later, the operation temperature (950 °C) was recovered and the hydrogen feed activated again. The result of the operation was overwhelming; the pressure drop over the Filter F3 had fallen 10 mbar (32)! Unfortunately, that didn’t remain a long time this way, PT02 now rose even faster than before, and about another 10 minutes later it was decided to end the operation with hydrogen supply (33). The total hydrogen feed of the day was 11 mol or a little bit less than 250 dm³.

4.2.9 Water Production

Already about 10 minutes after the start of the operation with hydrogen at 12:00, the first product water was extracted from the system by the water separator and the Pump P3 (34). The outflow then remained rather constant with only slight variations that even can be attributed to the variations of the hydrogen feed rate. After stopping of the hydrogen feed (33), the water production continued for 10 to 20 minutes. This delay of water extraction with respect to the hydrogen feed was observed in all tests and varied apart from a few exceptions

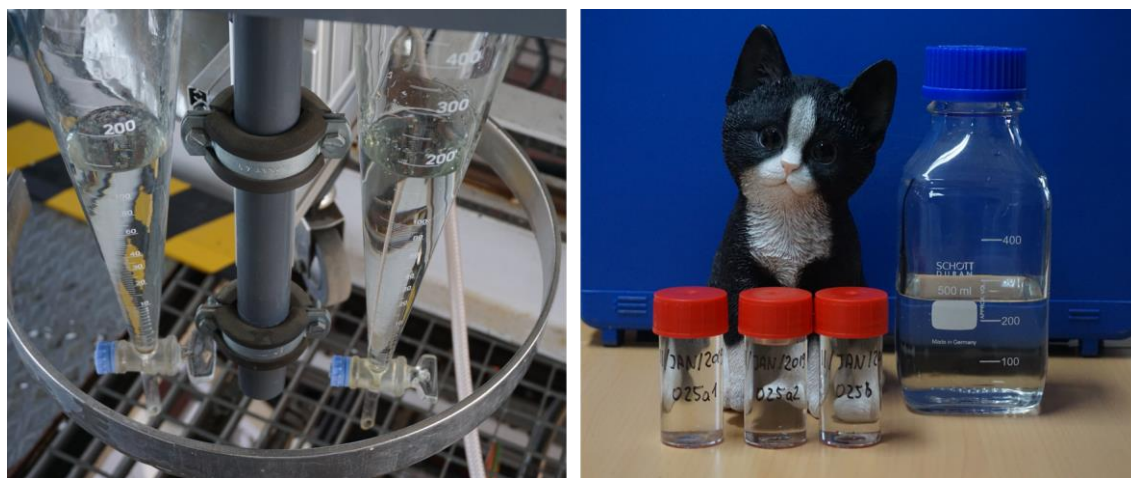


Fig. 136: Water produced during the operation on January 11, 2019.

from about 10 up to 25 minutes. At the end of the day, a total quantity of 312 ml of water was produced (35), see also Fig. 136. Subtracting the 140 ml from the water of crystallization extraction, 172 ml or 9.6 mol of water were produced by the chemical reaction. Comparison with the hydrogen feed of 11.0 mol gives a yield of 87%, an interesting and encouraging value due to its proximity to 100%. This will be further discussed in chapter 5.5.1.

4.2.10 Minimum Fluidization

When the water production had definitely ceased about 20 minutes after the cut of the hydrogen supply, the solar operation was ended by simply closing of the shutter (36) and moving the heliostat to the standby position. Before terminating the day, a measurement of the minimum fluidizing gas velocity at high temperature was successfully attempted (37). A similar test failed the day before because the switch between recirculated (P1) and external (FC01) argon flow was not made with the necessary care, and the pressure within the reactor spiked high enough to provoke the particle blow-out from the Outpipe. This time, it was made with more care.

Therefore, first the automatic operation mode for the main bed supply was switched off and the flow set point was reduced to only 10 l_N/min. Then, the Pump P1 was switched off. This caused a slight rise of the pressure because now all the gas was leaving the system through the “gravity” valve GV. Partial opening of MV12 contributed to pressure relief. Finally, the flow rate set point was carefully increased up to 20 l_N/min, the starting point for the subsequent test.

This test consists of automatically decreasing the fluidization gas flow rate, starting from 20 l_N/min, in steps of 0.5 l_N/min every 3 seconds. When reaching the minimum of 5 l_N/min, the action is reversed and the flow is now increased for 0.5 l_N/min every 3 seconds. The experiment ends when the initial 20 l_N/min are reached. It lasted about 3 minutes, is executed in a completely automatic way by the program, and was logged in a total of 98 data sets.

An extract from the data needed to evaluate this little experiment is shown in Fig. 137. The last

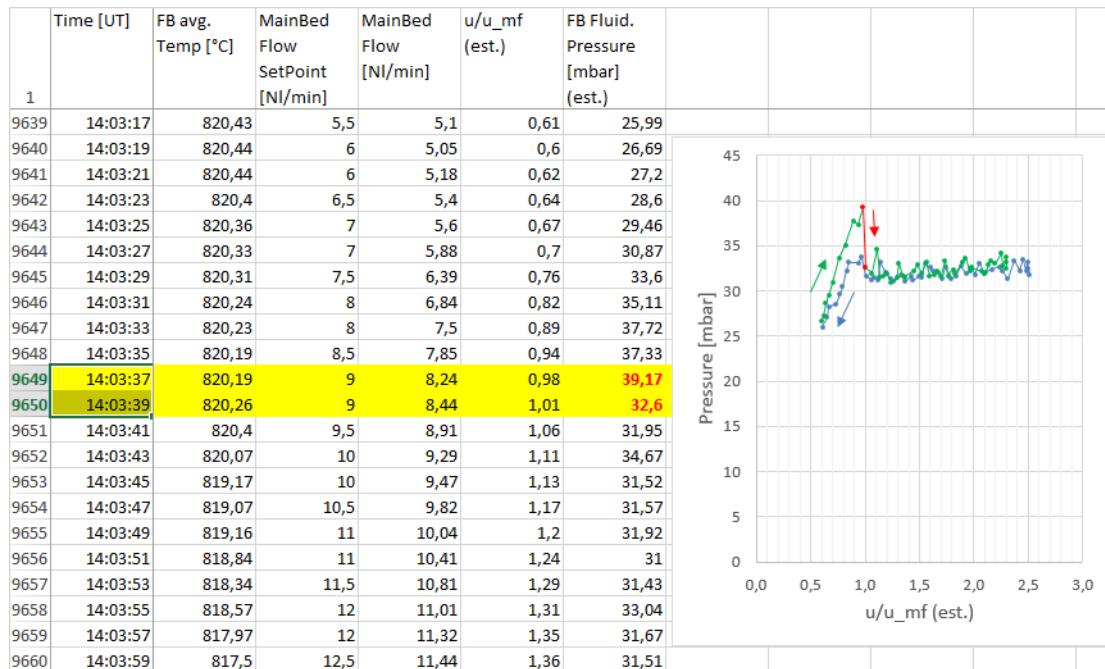


Fig. 137: Extract from the data file showing the inset of fluidization.

column is called “FB Fluid. Pressure [mbar] (est.)”, this means “Fluidized Bed, Fluidization Pressure in mbar, estimated value”. This is the difference between PT01 in the feedline and PT02 in the freeboard of the reactor. “Estimated”, because the correct point for the measurement of the higher pressure would be on the bottom of the fluidized bed, a place that is very difficult to access. The “estimation” includes an experimentally determined coefficient that removes the pressure loss in the gas distributor determined in previous tests with the empty reactor (see page 148 in chapter 4.1.2). The highlighted lines in Fig. 137 (left) and the red line (right) show clearly the sudden pressure collapse typical for the onset of fluidization. The associated gas velocity fits perfectly with the theoretical prediction (see column “ u/u_{mf} (est.)”). The column “FB avg. Temp [°C]” tells that this data point is valid for the temperature of 820 °C.

4.2.11 Wrap-Up

A few minutes after the termination of the minimum fluidization experiment, the Automatic Shutdown Sequence was activated which ended the fluidized bed operation (38). The remaining activities are closing of valves and bottles, check of the gas consumption (argon: 50 bar, hydrogen: 5 bar), turning off the power supply, and covering the window with a stainless steel plate to protect it from dust and dirt. The cooling water keeps running on a low level (5%) until the next morning to avoid damage due to remaining heat in the reactor. Furthermore, some product water and particle samples are taken, the conductivity of the water is measured (see chapter 5.5.3), a screenshot from the History tab of the Oresol.vi is taken (Fig. 98 on page 127), and a backup copy from the logger data is made.

5 Data Evaluation and Discussion

This chapter gives insight into the results of the tests and their interpretation. Chapter 5.1 deals with the fluidization gas demand, which decreases strongly with increasing operating temperature. An inversely proportional relationship between the gas flow and the (absolute) temperature was determined. In section 5.2, the continuous solids supply and removal is discussed in more detail. Since a direct correlation with the gas flow in the standpipe could not be established, an automatic control system was developed that proved to work acceptably. In chapter 5.3, the temperature distribution and the energy balance in the reactor is analyzed. The incident solar radiation must cover all useful and dissipated power, including transient heating. For this purpose, the actual available solar power is first determined with the help of a steady-state operation point. Then, with the help of the heat balance, all relevant heat flows are determined over the course of a test day, including heating up and cooling down. Chapter 5.4 analyzes the pressure profile over the gas loop. A distinction is made between start-up of the system with high gas flow, and operation at nominal temperature with reduced gas demand. Finally, it is shown how the increasing clogging of the Filter F3 prevents prolonged operation. Chapter 5.5 is dealing with the actual purpose of the system, the generation of the product water. The three subchapters are about the water quantity produced, the efficiency of the separation from the gas stream, and the impurities found in the water. For the production, it is noticeable that the rate-controlling step must be the diffusion of the product water out of the particles and not the diffusion of the hydrogen into the particles or the reaction itself. The water separator is capable of separating at least 90% of the water carried in the gas stream. The remaining vapor amount is with 50 - 70% well below the saturation point, so there is no concern for condensation during recirculation. The recovered water is very acidic and contains significant impurities of chlorides, sulfates and ammonium. These substances must be separated, e.g. by distillation, before the water can be used in the electrolyzer. Finally, in chapter 5.6, some minor details are discussed, in particular the solar-specific quartz window and the argon savings due to recirculation.

January 9 or January 11, 2019 are usually used as example days in the diagrams. In the graphs that show the course of variables over a complete day, the curve of the reactor temperature is always included as a thin red line. This serves for easier orientation and understanding. In the chapter about water separation (5.5.2), the amount of water produced is also included as a dashed blue line.

5.1 Gas Demand

An important engineering question before the start of the test campaigns was how the gas demand (mass flow or norm-volume flow) of the fluidized bed would change with increasing temperature. It was clear that it would decrease as the gas density decreases and the dynamic viscosity of the gas increases. An inverse proportionality to $T^{1.7}$ (T ... absolute temperature) was calculated for the gas flow for the minimum fluidization (see chapter 1.4.2). In Fig. 138, the blue line shows the calculated curve for air and the green line the one for argon, both for ilmenite particles with a mean diameter of 150 μm . Please note that in this figure, in contrast to the diagram in Fig. 29 on page 54, the norm volume flow is plotted on the y-axis and not the gas velocity. The circles in Fig. 138 are minimum fluidization measurements made with air during two different campaigns, and the diamonds represent measurements while operating with argon. All these data points show a reasonable agreement with the predictions (the solid lines).

As minimum fluidization is not enough for proper operation, the calculated gas flow has to be increased. The initial idea was to do this by simple multiplication with a fixed factor. This was programmed into the control software and provided with an (adjustable) “multiplication factor” to be able to push the gas flow well beyond the minimum fluidization point. As an example, a value of 1.6x is displayed for both gases as dashed lines in the diagram.

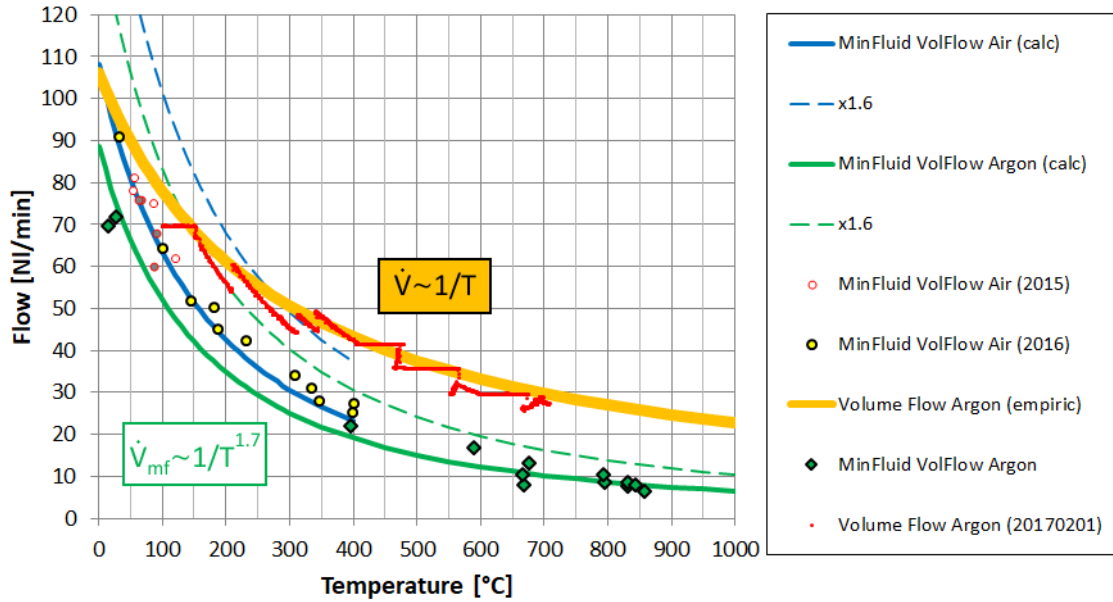


Fig. 138: Norm volume flow vs. temperature. Calculated (lines) and measured (markers) data.

The red dots in Fig. 138 represent the gas flow rate during the heating phase of the test on Feb. 01, 2017. Thanks to the large window for the coupling of solar energy, it was very easy to observe the fluidized bed during solar operation with the help of a camera (Fig. 139). Until 200 °C, the red dots followed the green dashed line in Fig. 138, but then, soon it was apparent that the fluidized bed became increasingly "lazy" (or: less vivid) as the temperature increased, and the multiplication factor had to be adjusted upwards several times during the heat-up of the fluidized bed. The red dots, produced by purely visual observation, are the result of the



Fig. 139: Monitor for observation of the fluidized bed during operation.

manual corrections. The upward leaps show the adjustments of the “multiplication factor”, while the downward leaps are corrections with the MV13 manual valves, reducing the net output of the Recirculation Pump P1.

The orange curve represents quite well the “measured” points for the real gas flow as a function of temperature. It follows the law $\dot{V}_N \sim 1/T$, i.e., it is inversely proportional to the absolute temperature in the bed. Since the gas density follows the same proportionality, the conclusion is that the gas velocity, which corresponds to the actual (not norm!) volume flow, remains practically constant regardless of the temperature. This regularity was included in the control program under the name “*empiric*” and used in all subsequent experiments. From there on, a manual correction never became necessary again. From the orange curve, the gas velocity for proper operation of the Oresol fluidized bed with Ilmenite-150 particles at all temperatures is calculated to be $u_G = 3.3$ cm/s.

In principle, the gas velocity has to be increased when hydrogen is added to the feed gas. However, due to the ongoing problems with the Filter F3, the hydrogen share was always rather low and therefore this has not yet been done.

5.2 Particle Feed

One of the unique features of the Oresol experiment is that the solid reactants can be continuously fed into and discharged from the reactor without the need to interrupt the process, see chapters 3.7 and 3.8. Two load cells (MT01 and MT02) constantly measure the mass of the hopper with the fresh particles (MT01) and the mass of the bucket with the spent material, the tailings (MT02). The instantaneous measured value is compared with the value from exactly one minute ago, and the difference directly gives the mass flow in g/min. While the outflow is passively self-regulated by the overflow from the reactor, the inflow quantity is actively adjusted by the gas supply through FC05 into the standpipe. Initially, it was planned to use preliminary tests to determine a relation for the solids flow as a function of the gas flow. However, the repeatability was so poor that an active control had to be implemented instead. The software code for this is briefly explained in chapter 3.14.2 on page 134.

The non-solar test from May 15, 2015 shows the effect of the difference between active control and static gas flow into the standpipe through FC05 on the particle mass flow. On the left side in Fig. 140, at 11:10, FC05 was set to an argon flow rate of 0.8 l_N/min and then left unchanged. For the first about 30 minutes, the particle flow remained remarkably (and unusually) constant, but then started to drop more and more, possibly because the static pressure from the particles in the hopper diminished. On the right side in Fig. 140, at 12:14, the automatic solids mass flow rate control was set to 190 g/min. In the first approximately 10 minutes, the system overreacted somehow, but then was able to keep the mass flow very constant until complete depletion of the particles in the feed hopper. Towards the end, the automatic system increases slightly the gas flow through FC05 into the standpipe to maintain the solids flow.

Multiples of 110 g/min were often chosen for the particle mass flow rate, as this is the amount necessary to produce 700 g of water per hour assuming 90% ilmenite in the raw material and the ideal case of 100% yield. Just under 7 kg of particles in the hopper are thus sufficient for one hour of operation. Rates of 220 and 330 g/min were easy to achieve, above that it became more difficult. For higher flows, e.g. 1 kg/min if a raw material with only 10% ilmenite content were used, the tube diameters involved would then have to be increased accordingly.

Ideally (without chemical reaction), the mass flow into and out of the reactor is identical. For the load cells, it should be $MT01 + MT02 = \text{const.}$ However, one observation during the experiments was that the outflow often lagged behind the inflow by a not inconsiderable amount. The difference could grow to 2 kg and more. This lag can be clearly seen in Fig. 140, where the red line always is slightly behind (shifted to the right) the black line. A possible reason might have been that even when operating without particle feed, a small amount of material always splashed into the Outpipe and therefore the particle level in the reactor decreased with time. Another possibility is that the voidage of the bed and therefore its total volume increases during fluidization.

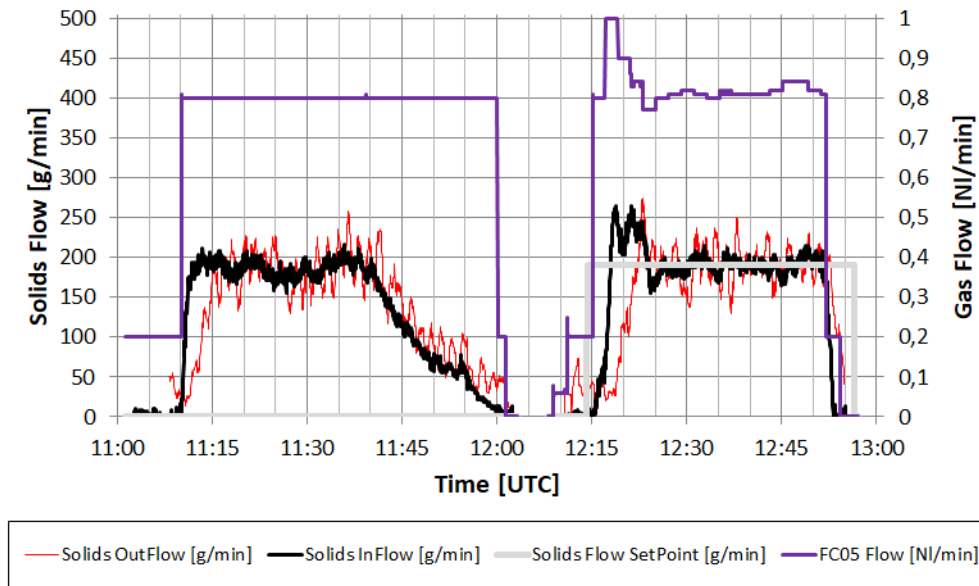


Fig. 140: Particle flow with constant (11:10-12:00) and actively controlled (12:14-12:52) standpipe gas flow rate.

All in all, the system worked quite well, but there were also occasional cases where either the particle flow did not get going properly or it took a very long time until the correct value was reached. In these cases, "manual" help was needed, either by manipulating FC04 and FC05, or by a light stroke with a hammer or a screwdriver against the bottom of the standpipe.

5.3 Temperature and Power

Fluidized Bed Temperature

As already outlined in chapter 3.2.3, the thermocouples TC01-TC15 are used to determine the temperature in the reactor. Due to the arrangement in three levels in crosses of five each (see Fig. 43 on page 76), the *distribution of the temperature in the reactor* can be easily followed in real time during the tests. Thereby, it soon became apparent that the temperature in some regions lagged behind the overall trend (Fig. 141), indicating that these zones were not well fluidized. Since this was generally the case for the bottom level and for the east column, these measuring points were in most cases excluded from the averaging by default to keep the different testing days more comparable. In the case of the test on January 09, 2019, during heat-up, it was observed that the temperature at the middle-south position (TC09) also was lower than usual, and therefore manually deactivated at 10:25 by the operator. In Fig. 141, the upward jump of the calculated average temperature (red line) by 66 °C at this moment can be clearly noticed. The usefulness of this measure becomes clear when one realizes that before

10:25, the local maximum temperature was more than 100 °C above the average temperature. With a target value of 950 °C for the mean, this would have resulted in peaks well above 1000 °C, which would inevitably have led to sintering of the particles at this location. By switching off TC09, the remaining temperature spread was reduced to generally below ± 50 °C.

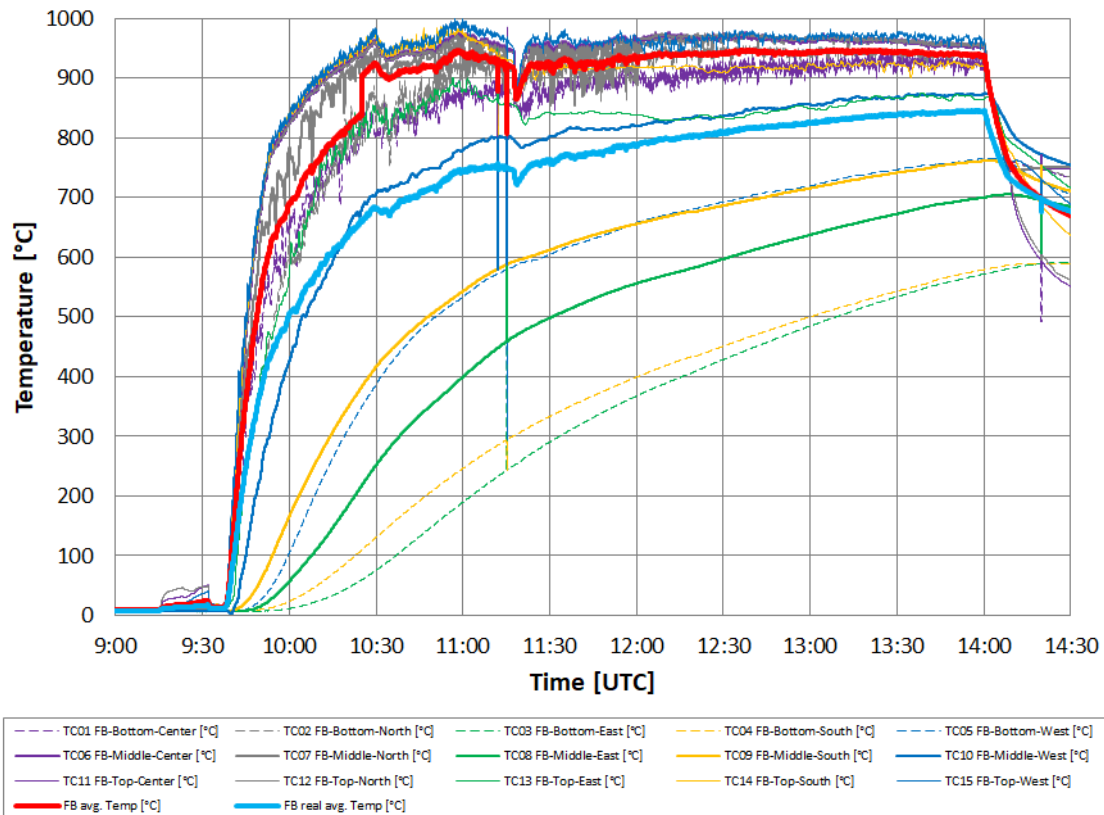


Fig. 141: Reactor temperatures (raw data) on January 9, 2019. Also included the average temperature without (red) and with (light blue) the deactivated thermocouples. The leap in the red line at 10:25 is due to the deactivation of TC09 (thick orange line) at that moment.

Table 8 shows the temperature distribution in the reactor for this day at 13:30, a moment with mostly steady-state operating conditions. It can be seen that especially the center and the north side of the fluidized bed show a very homogeneous temperature distribution over the entire height and should therefore be well fluidized. While the east is, as it happened in most tests, obviously poorly fluidized, the south and west sides show a behavior that improves towards the top. Since the bubbles in a fluidized bed of Geldart Group B increase in size from bottom to top, it is likely that this temperature distribution correctly reflects the quality of fluidization. The cause of this uneven fluidization is probably to be found in a too low pressure drop across the gas distribution nozzles. Slight differences in geometry, possibly aggravated by stuck particles, can then cause significant differences in the local gas volume flows.

[°C]	Center	North	East	South	West
Top	958.6	959.3	(866.0)	922.0	973.8
Middle	962.6	962.5	(672.5)	(741.4)	868.7
Bottom	(921.4)	(943.6)	(533.7)	(542.7)	(746.1)

Table 8: Temperature distribution in the fluidized bed on January 9, 2019 at 13:30.

Parenthesis: Temperatures not used for averaging ("deactivated"). Green: Spread within ± 30 °C from average. Orange: Deactivated during the test (TC09).

The average temperature of the “active” thermocouples at that moment is 943.9 °C, the minimum 868.7 °C and the maximum 973.8 °C. The mean value of all sensors in the bed (“real avg.”) is 838.3 °C. This value is needed for proper calculation of the energy consumed by transient heating of the bed. The average temperature of the top level (TC11-TC15) is 935.9 °C, later used in this chapter to calculate the radiative losses of the fluidized bed.

Energy Balance

According to the First Law of Thermodynamics, the energy balance must always be in equilibrium. For a reactor operated with concentrated solar power, this means that the incident radiant power (*heat source*) is always equal to the thermal power converted within the reactor (*heat sink*). Thereby, the latter can be divided *during stationary operation* (constant temperature and flow rates) into:

- Thermal losses (conduction, convection and radiation)
- Material inflow (solids and gases)
- Reaction enthalpy

During heating and cooling, the thermal mass of the particles in the reactor (gases can be neglected) and of the internals (installations within the fluidized bed such as baffles, supports, thermocouples...) and the adjacent wall and insulation of the fluidized bed must be taken into account as well.

The data required to calculate all these contributions to the heat balance can be obtained from the measured data and the log-file as follows:

Solar Power

The different parameters that influence the solar radiation before being absorbed in the reactor are described in chapter 1.3. Two of them are available in the logged data, the Direct Normal Irradiation (DNI) and the opening of the shutter. Together with the nominal power of the solar furnace (60kW, hence the designation "SF-60"), the instantaneous solar radiation power can in principle be calculated. However, the value obtained in this way is clearly too high, since various losses are not considered in the “nominal power”. These losses are cosine of the heliostat (especially early in the morning and around the summer solstice), shadow of the experiment located in the non-concentrated beam between the heliostat and the concentrator, shadow of the experiment in the concentrated beam before hitting the diagonal mirror, incomplete coverage (intercept) of the incoming concentrated ray by the diagonal mirror, reflectance of the diagonal mirror, and losses in the reactor by reflection on the window, the aperture cone, and the particles. In addition, there might be dust on the heliostat and, to a lesser extent, the concentrator, the diagonal mirror and the window (inside!), which can change over time. All these losses can be summarized in an additional “Efficiency Factor”. A rough, geometric estimation⁸⁴ lets expect a value between 0.5 and 0.6 for this factor. A more precise determination will be made with the power balance later in this chapter.

⁸⁴ The largest contributions are the incomplete intercept of the diagonal mirror for the rays coming from the upper half of the concentrator (about 20% losses), and the shadow of the radiation shield of the reactor for the rays coming from the bottom part of the concentrator (about 10% losses).

Finally, the solar source power can be written as:

$$\left(\frac{\text{Absorbed}}{\text{Solar Radiation}} \right) [kW] = 60kW \times \frac{(DNI) [W/m^2]}{1000 W/m^2} \times \left(\frac{\text{Shutter}}{\text{Opening}} \right) [\text{area \%}] \times \left(\frac{\text{Efficiency}}{\text{Factor}} \right) \quad (36)$$

The “area-%” means that the data from the shutter opening given in angle-% has to be converted into the percentage of the area of the gaps between the blades of the shutter compared to the total area. This, together with the multiplication with the DNI and the nominal power of the Furnace, is already done during the experiments by the control software as explained in chapter 3.14.2 on page 132, and the result is written as "Solar Power [kW] (est.)" into the log-file.

Thermal Radiation

The total power radiated from a body per unit surface area is given by the Stefan-Boltzmann law, see equation (15) in chapter 1.3.1 on page 40. As no direct measurement of the surface temperature of the bed is available, the mean value from the thermocouples located in the top layer (TC11 - TC15) is taken (see Fig. 43 and Table 3 in chapter 3.2.3 on page 76).

The emissivity of the material in the infrared, even if not completely black, has to be close to 1 due to the rough surface of a fluidized bed that causes an important amount of self-irradiation (“micro-cavity-effect”). Measurements on the Moon (Bandfield, Hayne, Williams, Greenhagen, & Paige, 2015), derived with the LRO (Lunar Reconnaissance Orbiter) Deviner Radiometer, suggest a value of 0.95 for Mare regolith. As that value is widely used (Zhang et al., 2019), and because this work does not pretend to make high precision measurements, that value is also used here.

The determination of the radiating surface area is not as trivial as it should appear at first. It could be used the hole in the aperture cone or that of the radiation shield on top of the window. As both are in a complex thermal and geometric environment, the best choice appears to be the surface of the fluidized bed itself (ø260 mm).

Conduction, Convection, and Cooling Water

Thanks to the excellent thermal insulation of the Oresol reactor with a thickness of 100 mm and a thermal conductivity of only 0.049 W/(m·K) (see chapter 3.5.8), the losses due to heat conduction are low. This was confirmed by the thermocouples TC53 - TC56 located on the outside of the reactor wall, which gave values between about 30 °C (unprotected west side) and 60 °C (south side, covered by the radiation shield). This results in a heat flux of less than 0.25 kW when operating at high temperature⁸⁵. Since the inner reactor wall and the gas distributor are supported on the thermal insulation, there are also hardly any thermal bridges that could significantly increase this value.

Since the window is in a horizontal position in a shallow recess, it is unlikely that it forms significant free convection at this point. However, during the tests, a fan was located at a certain distance from the window, which had the purpose of keeping possible outgassing from the ceramic radiation shield away from the diagonal mirror. But since there is practically no data available about the possible forced convection caused by the fan, a similar heat flux as for the conductive losses is supposed in the power balance.

⁸⁵ Rough estimation: With insulation inner radius 135 mm, outer radius 235 mm, height 460 mm (whole reactor!), the heat flow becomes: $0.049W/(m \cdot K) \times 2\pi \times 0.46m \times (950^\circ C - 30^\circ C) / \ln(235/135) = 235 W$.

The temperature rise in the cooling water of the window flange during operation at 950 °C is approximately 1.2 K. With a mass flow of about 200 g/s, this corresponds to a dissipated power of at least 1 kW. However, this value must not be inserted so simply into the heat balance, since a certainly not insignificant part of it comes from the thermal radiation of the surface of the fluidized bed and is thus already taken into account. Therefore, only half (0.5 kW) is taken into account here as a rough estimate.

Since the heat fluxes for conduction, convection, and cooling water depend more or less linearly on temperature, they can be combined into one parameter "linear heat losses". As they combine to roughly 1 kW when operating close to 1000 °C, the associated coefficient can be assumed as approximately 1 W/K that has to be multiplied by the difference of the Fluidized Bed average temperature and the ambient temperature (TC67).

Solids Inflow

When particles flow into the reactor, additional heat is needed to rise their temperature to the one in the fluidized bed. The calculation is straightforward with the product of the mass flow rate, the heat capacity, and the temperature increase. The mass flow rate is measured with the load cell MT01 as explained in the previous chapter and saved in the log-file as "Solids InFlow [g/min]". For the start temperature of the feed, the value of TC35 ("InPipeBottom") is taken, while the end temperature is the average temperature of the fluidized bed.

Shomate (Shomate, Naylor, & Boericke, 1946) measured the *specific heat capacity of ilmenite* up to the melting point at 1640 K and gave an empiric equation for the results. Anovitz (Anovitz et al., 1985) repeated that measurement with improved precision, but only for temperatures up to 1000 K. Therefore, in this work, for $T > 1000$ K, the expression from (Shomate et al., 1946) is used, but with an offset of 25.4 J/kgK to seamlessly combine the two equations. Some resulting values are (0 °C; 625 J/kgK), (400 °C; 838 J/kgK), (800 °C; 911 J/kgK), and (950 °C; 932 J/kgK).

Gas Inflow

The power needed to heat the feed gas is calculated in a very similar way as for the solids. It's also the product of the mass flow rate, the specific heat capacity, and the temperature difference. Argon and hydrogen have to be considered separately. The total argon feed is FC01 + FC02 + $\frac{1}{2}$ FC03 + FC04 + FT07 + FT08. As the fluidization gas of the main bed is the most important component, the temperature measured in the supply pipe, TC37, is the best value for the lower temperature. The upper temperature is a little bit tricky, because not all gas flows pass through the fluidized bed and heat up to its temperature. The window protection gas (FC02+FT08), the north-leg of the Outpipe ($\frac{1}{2}$ FC03), and the Inpipe (FC04) fluidization gases enter the reactor above the bed surface and leave it without close contact to the bulk of the particles. Therefore, these gases do not heat up as much as the fluidization gas of the main bed (FC01+FT07). The solution is to use the value from the thermocouple (TC40) in the gas exit pipe as the higher gas temperature. The confluence of all gas flows at this point should give a good average of the upper temperature for the argon. For the hydrogen, the temperature of the fluidized bed is the adequate upper value to take.

As the measured values of the flow sensors are the norm-volume flows, they have to be converted into mass flow rates. This is easily done with a division by the norm-density of the corresponding gas (see Appendix A.1). The specific heat capacity at constant pressure of the gases is calculated by the coefficients given in (Rohsenow et al., 1998). Since argon is a

monoatomic gas, the specific heat capacity is constant over the entire temperature range of interest here. The value is 0.52034 kJ/kgK.

During many of the Oresol tests, the hydrogen inflow was chosen to 2.0 l_N/min, corresponding to a mass flow of 3.0·10⁻⁶ kg/s. With the heat capacity between 14.2 and 15.5 kJ/kgK, the power needed to heat up the gas from 20 °C to 950 °C is a mere 0.04 kW. Even at twice the flow rate, the value is still so low that the hydrogen inflow can be safely ignored when setting up the energy balance.

Reaction Enthalpy

Shomate (Shomate et al., 1946) made very detailed measurements of the thermodynamics of the ilmenite reaction with hydrogen (eq. (1)). For the reaction enthalpy they got 47.0 kJ/mol at 1200 K. As this is the measurement closest to the operation conditions in Oresol, and the variation in the interesting range (800 - 1000 °C) is less than 1.5%, that value can be used.

Supposing a hydrogen conversion of 100% (more about this in chapter 5.5.1), the change of the extent of reaction (unit: mol/s) can be taken from the norm-volume flow rate of the hydrogen measured by the flow controller FC06, divided by the molar volume of an ideal gas at ambient conditions, 22.414 dm³/mol. For the common case of a hydrogen inflow of 2.0 l_N/min, the molar flow is 1.5·10⁻³ mol/s. Together with the reaction enthalpy, the power required for the reaction is 0.07 kW, also a value low enough to be neglected.

Fluidized Bed Heating

During heating of the fluidized bed, the power required for the *change* of the temperature is calculated by multiplication of the mass of the bulk of the solids in the fluidized bed, the specific heat capacity of the particles, and the change of the temperature per time unit. It is assumed that the solid mass does not change with time, which is mostly fulfilled for the Oresol reactor. The mass of the particles is 22 kg. The determination of the specific heat capacity of ilmenite has already been described above, and for the temperature change, the corresponding measured data difference over a certain interval is used. With 5 minutes, this interval was chosen relatively wide, but this was necessary to avoid too noisy data. In contrast to the other contributions to the thermal equilibrium, it should be noted that the mean fluidized bed temperature calculated only with the "activated" thermocouples (see page 126) cannot be used here. Instead, the mean value from *all* 15 measurement points must be taken, as this is the way to correctly account for the total mass of all particles.

One difficulty is the thermal inertia of internals and the walls of the reactor. The latter, in particular, cannot be neglected. However, since the effort of an exact modeling would far outweigh the benefit for this work, it was not included in the direct calculation. Instead, it will be derived from the residuals of the energy balance as "Total Heating Power".

It should be remembered that during heating, the thermal mass of the reactor has the effect of a *heat sink*, while during cooling, it acts as a *heat source*. At perfectly steady state operation, its power becomes zero.

Energy Balance

The energy balance will be shown for the test on January 09, 2019. From all tests, this is the day that gave the cleanest data for this purpose. Like already mentioned above, the power source (solar ray) and the power sink (thermal) have to be in equilibrium:

$$\begin{pmatrix} \text{Solar} \\ \text{Power} \end{pmatrix} = \begin{pmatrix} \text{Thermal} \\ \text{Power} \end{pmatrix} \quad (37)$$

On the right side of this equation, the Thermal Power is calculated from the parameters introduced above:

$$\begin{pmatrix} \text{Thermal} \\ \text{Power} \end{pmatrix} = \begin{pmatrix} \text{Thermal} \\ \text{Radiation} \end{pmatrix} + \begin{pmatrix} \text{Linear} \\ \text{Heat} \\ \text{Losses} \end{pmatrix} + \begin{pmatrix} \text{Solids} \\ \text{InFlow} \\ \text{Power} \end{pmatrix} + \begin{pmatrix} \text{Argon} \\ \text{InFlow} \\ \text{Power} \end{pmatrix} + \begin{pmatrix} \text{Fl. Bed} \\ \text{Heating} \\ \text{Power} \end{pmatrix} \quad (38)$$

Unknown parameters in eq. (37) and (38) are the Efficiency Factor for the Solar Power and the uncertainties of the Fluidized Bed Heating Power due to wall and internals heating. During steady state operation, the latter one becomes zero and the Efficiency Factor can be determined. For the test on January 09, 2019, this was close to being the case between 13:15 and 13:45 (Fig. 142, light green area). There, the Thermal Power (blue line) has to coincide with the Solar Power (yellow line), and the residual of the power balance (gray line) should disappear. This is best fulfilled for a value of 0.57 for the Efficiency Factor, in good agreement with the estimation made above. With this value, the transient heating can be determined as the residual from the heat balance. Fig. 143 shows the resulting power graphs.

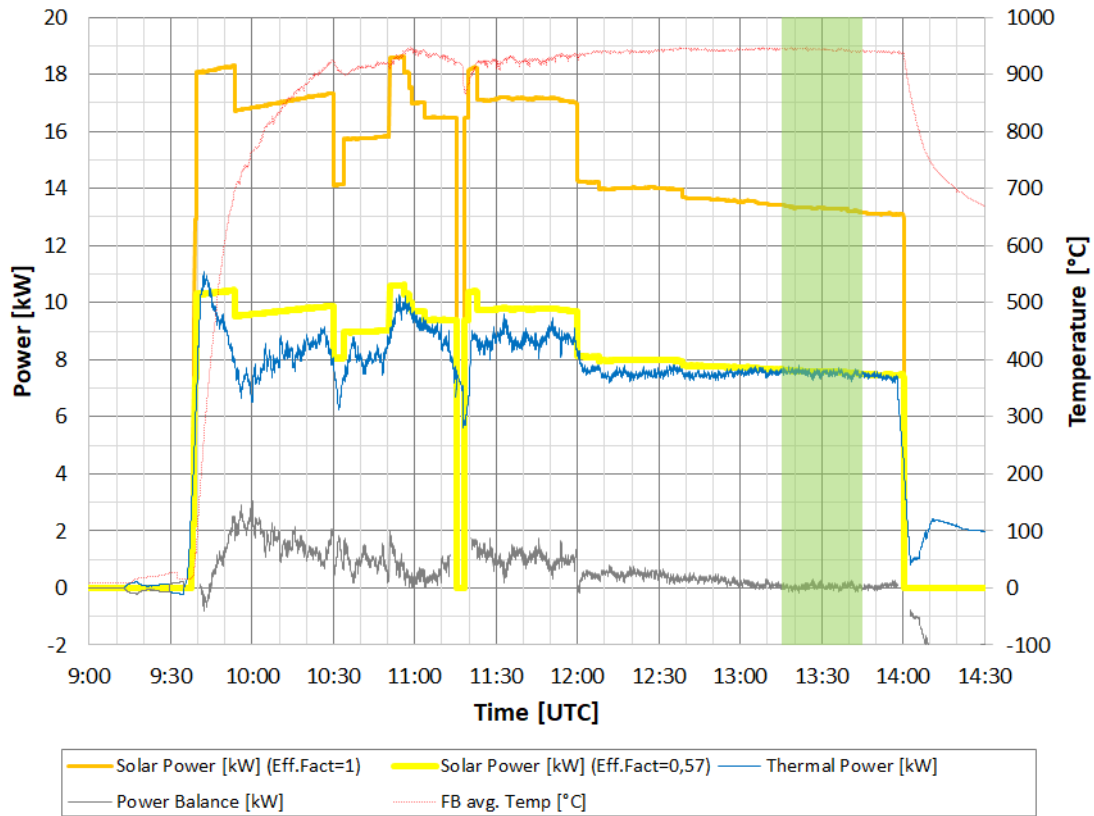


Fig. 142: Thermal balance for the test on January 09, 2019. Orange: Uncorrected solar power. Yellow: Corrected solar power with the factor 0.57. Blue: Thermal power according to eq. (38), including transient heating of the particles in the fluidized bed but not of the walls and internals. Gray: Remaining difference between solar and thermal power. Red: Fluidized bed temperature. Green field: Interval with steady state operation.

As expected, at the very beginning of solar operation at 09:40, the slightly more than 10 kW of solar power (yellow line) go entirely into the heating (gray line) of the particles in the fluidized

bed and the adjacent wall and insulation, resulting in a steep rise of the temperature (thin red line) of over 40 K/min. With increasing temperature, the heating power for the argon (green), the linear heat losses (blue), and in particular the thermal radiation (orange) become appreciable. After barely half an hour of operation, the temperature in the bed surpasses 800 °C, and soon thereafter, the thermal radiation overtakes the heating power of the fluidized bed (crossing of the orange and the gray line) and becomes the dominant heat sink for the rest of the test. At 10:50, the particle feed started, adding an additional power demand of about 1.3 kW. This was foreseen and therefore immediately compensated by additional solar power (step in the yellow curve). As that additional power was slightly too high, the temperature began to rise again. After some manual adjustments and a data glitch at 11:15, finally at around 11:25, the thermal situation became stable until the end of the particle feed at 12:00. To compensate for the now missing power sink, the shutter was closed again somewhat and the solar power reduced from 9.6 kW to 8.1 kW. This time, the thermal equilibrium was hit quite well, and the following two hours of operation required only very minor adjustments. The addition of hydrogen during this period practically did not affect the thermal behavior. As an example, at 13:30 ± 5 min, the power balance was as follows:

- Solar Power: 7.59 kW (100%)
- Thermal Radiation: 6.09 kW (80.2%)
- Linear Heat Losses: 0.92 kW (12.2%)
- Solids Inflow: 0 (off)
- Argon Inflow: 0.41 kW (5.4%)
- Transient Heating: 0.17 kW (2.2%)

At 14:00, the shutter was closed and the solar operation terminated. Instantly, the heat stored in the bed turned into the only heat source, sustaining the thermal radiation and, for 10 minutes, the heating of the still inflowing argon.

With these considerations it becomes clear that the thermal radiation through the quartz window is by far the largest contributor to the energy consumption of the reactor, at least while operated with no or low particle feed. This is not really a surprise, because the design was adapted to the dimension of the focal spot of the Solar Furnace. As the Furnace is somewhat oversized for this experiment, the radiative area was left unnecessarily large. A better design would (from the concentrator side) minimize the size of the focal spot, and (from the reactor side) it should use an aperture with a good insulation towards the inside of the reactor. If, for example, the radiating area could be downsized from 260 mm to 150 mm, the thermal radiation would be reduced by a factor of 3.

Furthermore, future reactors need to run with continuous solids inflow and a feed that very probably has far less than 100% ilmenite content. In this case, the power needed for the heat-up of the particles will become the dominant heat consumer.

Heat recovery might or might not make sense. For the gases, the power savings are low, but reduction of the cooling requirements for the off-gas might be helpful. The tailings (solid output) do not necessarily need to be cooled, so it is a matter of trade-off whether a solid-solid heat exchanger has advantages over a higher solar power input. Moreover, the hot tailings could also be stored in insulated containers to serve as a heat source during the long lunar nights. Cooling might become necessary if the high temperature of the spent particles would pose unsolvable problems for the design of the gas lock. A variant would also be thinkable in which the hot off-gas (and other parts of the system) is cooled with the aid of the fresh

regolith. In a certain sense, the cold particles could serve as a cold reservoir, thus eliminating the need for elaborate cooling panels.

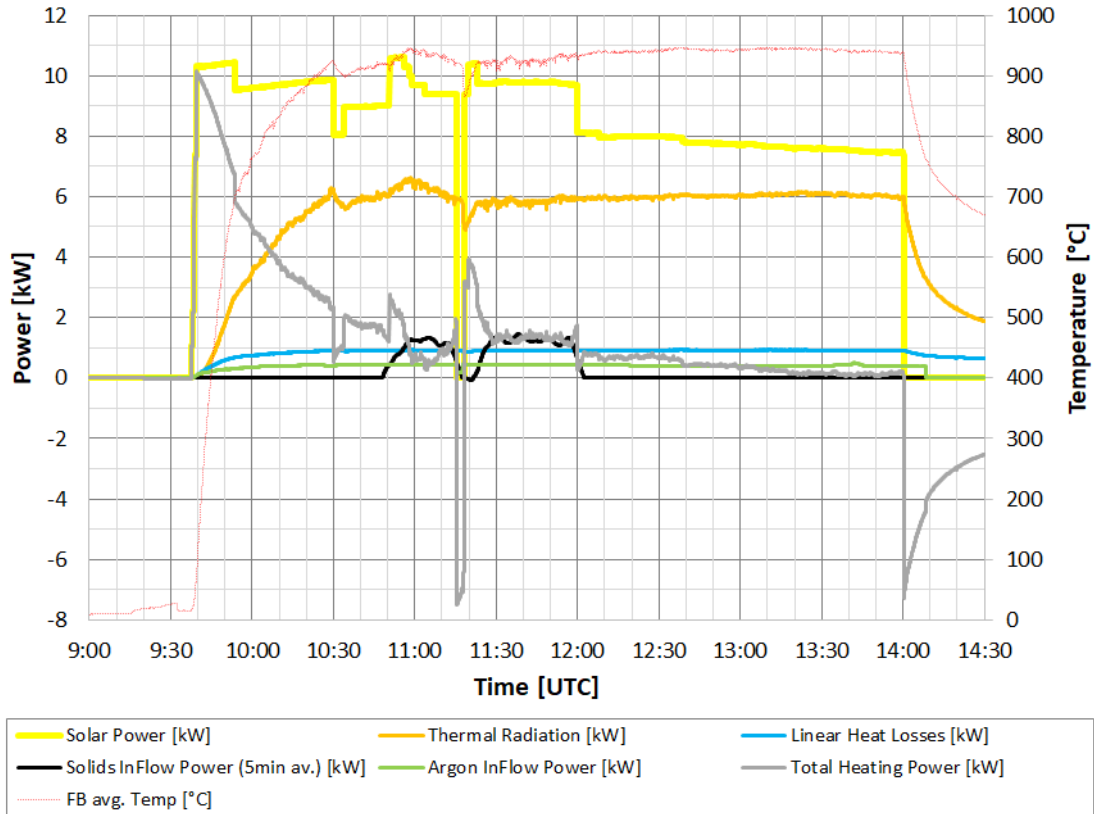


Fig. 143: Energy flow distribution for the test on January 09, 2019. Yellow: Real solar power. Orange: Thermal radiation. Blue: Heat losses through conduction, convection, and cooling water. Black: Heating Power for the solids inflow (smoothed). Green: Heating power for the gas inflow. Gray: Power consumed (+) / released (-) by transient heating / cooling of the reactor. Red: Fluidized bed temperature.

5.4 Pressure

As the Oresol reactor is a terrestrial demonstrator, the easiest design was for operation close to ambient pressure. In particular, this avoids additional complications (cost!) with the quartz window. The maximum overpressure allowed for the window is 100 mbar (see chapter 3.5.1). However, the actual possible maximum pressure in the reactor is smaller, because the length of the branches of the Outpipe syphon is only enough for a maximum pressure difference of 40 mbar. If this value is exceeded, the particles in the Outpipe are completely blown out, which means that it loses its sealing function and operation must be halted. This event is called a “solids blow-out” and happened a few times during the Oresol tests.

At the low end, the requirement is that at no point in the system the pressure must drop below ambient. This prevents ambient air and thus oxygen from mistakenly entering the system. In practice, the lowest pressure is at the intake of the Recirculation Pump P1. With the help of the large gas bag that is located there, it is easy to see if this requirement is met (see also page 113 in chapter 3.10). The nearest pressure sensor is PDT08 in the preceding gas manifold.

Fig. 144 shows the course of the measured values of six pressure sensors during the test on January 09, 2019. The position of the sensors in the closed loop can be seen in Fig. 145 (left). Fig. 145 (right) shows the pressure course over the loop for three different times on that day. In each case, these are mean values from the measurements of ± 1 minute around the specified time.

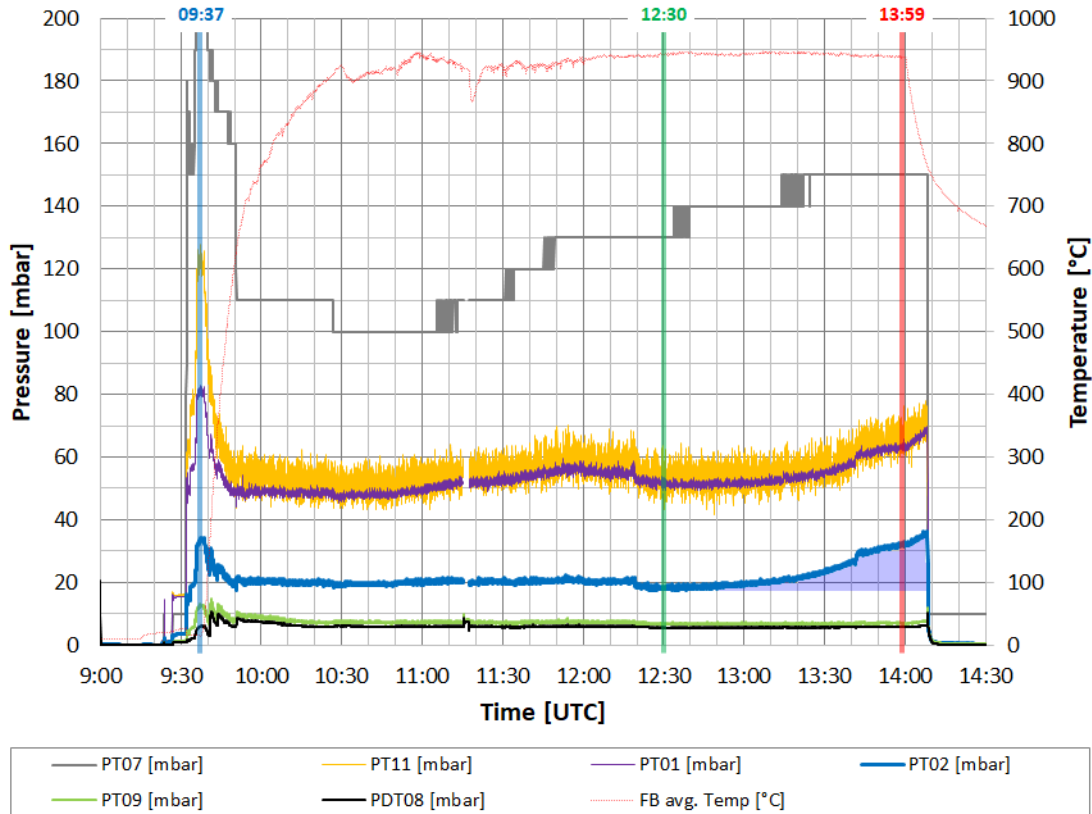


Fig. 144: Pressure distribution for the test on January 09, 2019. For the location of the sensors see Fig. 145 left. The blue line (PT02) represents the reactor pressure. The blue shaded area below marks the deviation from the nominal behavior.

09:37 (blue line in Fig. 145 right) is exactly the moment when the solar operation was started. The reactor is still cold, so the gas flows are very high, with a significant external contribution from FC01 and FC02. The valve MV12 is opened to the maximum to keep the pressure drop across the GValve low. This works well, the measured value of PDT08 is 5.8 mbar. The pressure in the reactor (PT02) is with 33 mbar quite high, but not critical. Overall, the behavior of the plant meets the requirements for this operating condition.

As the reactor temperature increases, the gas flows and thus the pressure losses decrease rapidly. To avoid too low pressure in the gas bag, valve MV12 is first closed halfway and then completely. Then the gas flow from the Recirculation Pump P1 is reduced by the valve group MV13. This process is completed shortly before 10:30, from which moment the conditions remain mostly constant. Only at 12:20 there is a small correction when the flow controllers FC01 and FC02 are completely switched off. 12:30 is therefore a representative time for operation under nominal conditions (green line in Fig. 145 right). The pressure of PDT08 is pleasantly low at 5.6 mbar, but still far enough from zero to become a problem (the automatic warning was usually set at 3 mbar). The pressure ahead of the Cooler C2 and the Water Separators WS1 and WS2 (PT09) is with 6.8 mbar only slightly higher, what confirms that these

In the further course of the experiment, however, the situation changes. In particular, the pressure in the reactor (PT02) increases continuously. The deviation from the nominal behavior is marked as the blue shaded area in Fig. 144. In Fig. 145 right, the situation is shown for the time 13:59 (red line), one minute before the end of operation with solar radiation. Since the pressure behind the Filter F3 (PT09) does not follow this trend, it is obvious that an increasing clogging of this filter must be the reason. While for PT09 and PDT08 the values for 12:30 (green curve) and 13:59 (red curve) are practically identical, for PT11, PT01 and PT02 there is an almost constant offset of 12-14 mbar disfavoring the values at 13:59. In fact, the pressure in the reactor has returned to the level when the system was started up. Since the trend continued and the reactor pressure was steadily approaching the maximum permitted pressure, the test was terminated at this point.

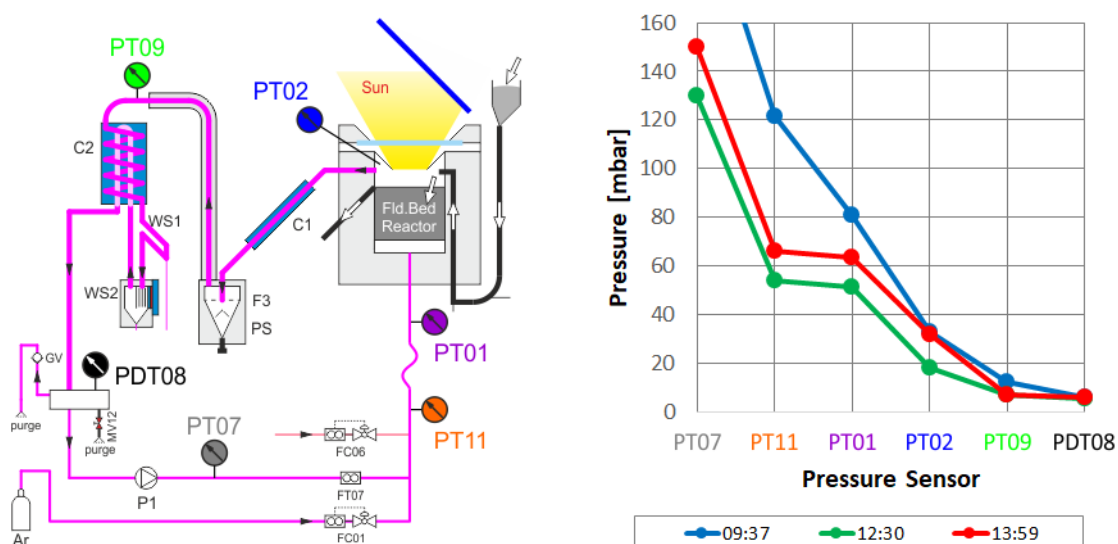


Fig. 145: Left: Oresol gas loop with the locations of the pressure sensors. Right: Pressure course over the loop for three different times on January 09, 2019.

182

5.5 Product Water

The most important goal of the experiments was to demonstrate that actually water can be generated from the reaction and separated from the off-gas stream. This was a qualitative, not a quantitative, goal. Due to the ongoing problems with the filter, no definitive statements about yield or reaction kinetics can yet be derived from the experiments. However, some preliminary and quite interesting conclusions are possible.

5.5.1 Water Quantity

The first surprise of the tests was that even at well below 800 °C and operation with pure argon, small amounts of water came out from the plant. First, a leak in the cooling water was suspected, but it soon turned out that in reality it was water of crystallization or other traces of moisture contained in the particles. This was a good sign, as it demonstrated that the Oresol downstream section was able to extract water fractions < 0.2% (by mass) in the particles.

However, this also posed a certain problem, because how could be made a distinction between water from hydrated minerals and water from the reaction? Only the latter one is of interest, because on the Moon, if at all, only tiniest traces of water can be found in the top layer of the soil (Benna, Hurley, Stubbs, Mahaffy, & Elphic, 2019). In principle, there are two options. One is to refrain from the supply of particles during the operation with hydrogen. Then the water of crystallization can be expelled almost completely before the hydrogen is supplied. This was the normal way how the Oresol experiments were done, and the reason why only few tests were made with hydrogen and particles inflow combined. The other possibility is to assume a constant value for the fraction of water of crystallization in the particle feed. This value was determined to be 0.84% in the autumn-2018 campaign on two test days specially designed for this purpose. However, comparison with other experiments showed that it is not completely constant. Values between 0.65% and 0.96% were observed. This is probably related to the variable humidity in the storage room. The ilmenite data sheet from the supplier even specifies only 0.24%. Therefore, results from this type of tests must always be taken with a certain degree of caution.

The experiments in spring 2017 (chapter 4.1.4) provided quite variable results for the water yield from hydrogen, but always below 50% except on the final day. The main reason for the low values was probably the small leak in the hydrogen feed line due to not properly tightened fittings. In autumn 2018, with values between 60% and 70%, things became somewhat better but not yet great. One possible reason was that the Particles Separator did not reach a temperature above 100 °C everywhere and therefore offered condensation surfaces at unwanted locations. This was solved by converting the Cooler C1 into an air cooler.

Finally, the four days of testing in January 2019 and another four in September 2019 provided more useful results. Table 9 lists some global values from these tests. With two exceptions, all tests followed the pattern:

1. Solar heat up
2. Particle feed
3. Wait for crystal water production cease
4. Hydrogen feed
5. Wait for reaction water production cease
6. Shutdown

A detailed description of an example test day of this kind (Jan 11, 2019) can be found in chapter 4.2. Exceptions from this scheme were the 10th and the 14th of January, 2019. On the 10th, the steps 2-5 were done twice. On the 14th, step 4 “hydrogen feed” was combined with a second particle feed. Since in these cases the physical separation of the product water types was not always possible, the fraction of the water of crystallization calculated with the first particle feed (step 2) was used for the values in Table 9.

Test/Date	Max. Temp.	Particles Supply	Particles H ₂ O	(Norm-) H ₂ -Supply	H ₂ O-Production Particles+Reaction	Yield
2019/Jan/09	947 °C	6.2 kg	0.65%	168 dm ³	40 + 127 cm ³	94%
2019/Jan/10	958 °C	9.9 kg	0.90%	190 dm ³	90 + 141 cm ³	92%
2019/Jan/11	956 °C	14.6 kg	0.96%	246 dm ³	140 + 172 cm ³	87%
2019/Jan/14	953 °C	12.2 kg	0.84%	95 dm ³	103 + 68 cm ³	89%
2019/Sep/24	900 °C	1.8 kg	0.72%	115 dm ³	13 + 93 cm ³	101%
2019/Sep/25	949 °C	2.6 kg	0.73%	106 dm ³	19 + 76 cm ³	89%
2019/Sep/27	873 °C	3.9 kg	0.54%	125 dm ³	21 + 74 cm ³	73%
2019/Sep/30	911 °C	3.8 kg	0.55%	125 dm ³	21 + 71 cm ³	71%

Table 9: Reactants feed and water production data from the tests in January and September 2019. The values are global for the whole days. A discrimination is made between water production from the particles (water of crystallization) and from the chemical reaction.

An interesting observation was that a certain amount of time passed always between the beginning of the supply of hydrogen (or particles) and the appearance of the "first drop" of water, in extreme cases up to 25 minutes. For the tests in January 2019, the delay was between 10 and 14 minutes. In September, it was only 4 to 5 minutes, except the first day with 14 minutes. Likewise, water production continued for a similar time after the hydrogen supply had stopped. This occurred often asymptotically, so it was not easy (and required certain patience) to determine the "end of water production" and thus the correct amount.

With the stoichiometric coefficients $\nu_{H_2} = \nu_{H_2O} = 1$ of the chemical reaction given in eq. (1), the yield of water from hydrogen according to eq. (27) can be written as

$$Y_{H_2O,H_2} = \frac{\dot{n}_{H_2O}}{\dot{n}_{H_2}} \frac{\nu_{H_2}}{\nu_{H_2O}} = \frac{\dot{m}_{H_2O} / M_{H_2O}}{\dot{V}_{N,H_2} / V_m} \quad (39)$$

with the molar volume $V_m = 22.414 \text{ dm}^3/\text{mol}$ of hydrogen at ambient conditions supposing ideal gas behavior, and the molar mass $M_{H_2O} = 18.015 \text{ g/mol}$ of the product water. The mass flow rate of the product water and the norm-volume flow rate of the hydrogen feed can be obtained from the data log files of the tests. While the hydrogen feed flow rate is directly adjusted and measured by the flow controller FC06, the water production rate is derived from the operation time of the Pump P3, which in turn is controlled by the level sensors in the water separator. Therefore, the temporal resolution of this measurement is in the order of not shorter than about one minute.

Table 10 shows some measured and calculated key data from one instant of time from each of the four testing days in January 2019, Table 11 does the same for the experiments in September of that year. The values are averaged over 121 measurements each, made in two-second steps over a total interval of two minutes. These points in time were carefully chosen with the goal to represent stationary conditions. Therefore, they are preceded by a longer

phase (> 15 min) of steady state operation, in particular with no large variation in the hydrogen feed rate (flow controller FC06), a rather constant product water outflow through the Pump P3, and no sign of hydrogen accumulation in the loop (FT07, FT08)⁸⁶. (For the detailed location of the sensors see Fig. 41 on page 72.)

	Description	Source	Value (mean from ± 1 min)				Unit
	Experiment / Date		09-Jan 2019	10-Jan 2019	11-Jan 2019	14-Jan 2019	UTC
	Time		13:00	11:30	12:30	11:33	
	Reactor temperature	TC01...TC15	944	950	947	937	°C
(A)	Ar flow into reactor	FC01+FT07	24.5	24.2	19.2	22.9	l _N /min
(B)	H ₂ flow into reactor	FC06	2.0	2.0	3.0	2.9	l _N /min
(C)	Total gas flow into reactor	(A)+(B)	26.5	26.2	22.2	25.8	l _N /min
(D)	H ₂ fraction (C_{H_2})	(B)/(C)	7.5%	7.6%	13.5%	11.3%	
(E)	External Ar feed = vent through GV	FC01+FC02+ ½FC03+FC04	2.0	2.1	5.6	2.4	l _N /min
(F)	Recirculated flow (P1)	FT07+FT08	31.8	32.6	25.8	31.9	l _N /min
(G)	Total reactor Ar outflow	(E)+(F)	33.8	34.7	31.5	34.3	l _N /min
(H)	Vent (GV) fraction	(E)/(G)	6%	6%	18%	7%	
(I)	H ₂ O flow from water sep.	P3	90	72	114	86	g/h
(J)	H ₂ O yield from H ₂ (Y_{H_2O,H_2})	eq. (39)	93%	75%	79%	61%	
(K)	H ₂ O yield from H ₂ (whole day)	Table 9	94%	92%	87%	89%	
(L)	H ₂ O yield from feed gas	(D)x(J) = $C_{H_2} \times Y_{H_2O,H_2}$	7.0%	5.7%	10.6%	6.9%	
(M)	Theoretical yield	(Shomate, 1946)	8.1%	8.3%	8.2%	7.9%	

Table 10: Measured and calculated data from four instants of time with stationary conditions during the testing campaign in January 2019. Row (K) refers to the whole day.

⁸⁶ As FT07 and FT08 are fed by the Recirculation Pump P1, there is no reason why that flow should change (P1 is a membrane pump working with volumetric displacement and therefore the volume flow rate is independent of the gas composition). If this happens nevertheless, the easiest explanation is that the composition of the gas started to change and therefore the calibration of the sensors is no longer valid. With other words, this indicates that the H₂-conversion is no longer complete and hydrogen starts to accumulate in the loop.

	Description	Source	Value (mean from ± 1 min)				Unit
	Experiment / Date		24-Sep 2019	25-Sep 2019	27-Sep 2019	30-Sep 2019	UTC
	Time		12:30	11:14	11:10	10:55	
	Reactor temperature	TC01...TC15	905	942	863	900	°C
(A)	Ar flow into reactor	FC01+FT07	26.7	24.8	29.0	30.9	l _N /min
(B)	H ₂ flow into reactor	FC06	1.8	2.1	1.7	1.9	l _N /min
(C)	Total gas flow into reactor	(A)+(B)	28.6	26.9	30.7	32.8	l _N /min
(D)	H ₂ fraction (C_{H_2})	(B)/(C)	6.4%	7.8%	5.4%	5.7%	
(E)	External Ar feed = vent through GV	FC01+FC02+ ½FC03+FC04	2.2	2.0	1.9	1.7	l _N /min
(F)	Recirculated flow (P1)	FT07+FT08	38.5	36.5	41.6	44.0	l _N /min
(G)	Total reactor Ar outflow	(E)+(F)	40.8	38.5	43.6	45.8	l _N /min
(H)	Vent (GV) fraction	(E)/(G)	5%	5%	4%	4%	
(I)	H ₂ O flow from water sep.	P3	30	72	51	84	g/h
(J)	H ₂ O yield from H ₂ (Y_{H_2O,H_2})	eq. (39)	34%	71%	64%	93%	
(K)	H ₂ O yield from H ₂ (whole day)	Table 9	101%	89%	73%	71%	
(L)	H ₂ O yield from feed gas	(D)x(J) = $C_{H_2} \times Y_{H_2O,H_2}$	2.2%	5.5%	3.4%	5.3%	
(M)	Theoretical yield	(Shomate, 1946)	7.1%	8.0%	6.0%	6.9%	

Table 11: Measured and calculated data from four instants of time with stationary conditions during the testing campaign in autumn 2019. Row (K) refers to the whole day.

The qualitative impression during the first three experiments in January was that at hydrogen flow rates ≤ 2 l_N/min (corresponding to a H₂-fraction $< 8\%$), mostly all the hydrogen must have reacted, because it did apparently not accumulate in the loop. Whole-day yields between 87% and 94% (Table 10, row (K)) suggest this. This changed however when the flow rate was increased.

Shomate (Shomate et al., 1946) investigated the thermodynamic properties of ilmenite, including the hydrogen reduction. This included the equilibrium constant and therefore the composition of the gas phase in thermodynamic equilibrium as a function of the temperature. In the temperature range of interest here, the equilibrium gas has an H₂O content of 7% at 900 °C, 8% at 940 °C and 9% at 975 °C. Row (M) in Table 10 and Table 11 shows the values for the temperatures of the respective test.

This is interesting for two reasons. First, if the hydrogen content in the feed gas is smaller than the value for the equilibrium of the water (row (D) < row (M)), then nearly all of the hydrogen apparently reacts. However, when the hydrogen content is greater, the hydrogen begins to accumulate in the system. This happened during the test on January 11, explained in chapter 4.2.7, event (27) and clearly visible in Fig. 135 on page 161. This event was after the instant of time put in Table 10 for this day, where the momentary yield (row (L)) appears to be greater than the equilibrium composition allows. This must be a temporal phenomenon because the yield for the whole day is below 100% (row (K)). On the next day (Jan 14), despite a similarly high hydrogen flow, things look “correct”.

The other interesting observation is that the equilibrium apparently depends only on the water content, but not on the hydrogen content of the gas mix. The hydrogen can seemingly be completely replaced by argon with little (if any) change in the equilibrium state. In equation (29) (page 58) can be set not Y_{PG} alone, but $C_G \cdot Y_{PG} \approx 0.07 \dots 0.09$. This suggests that the rate-limiting step in the reaction is product water diffusion and not reaction velocity or hydrogen diffusion.

The water content of the equilibrium gas can be roughly approximated for the temperatures in question by the linear expression $9.5\% + 5\%/200^\circ\text{C} \times (T - 1000^\circ\text{C})$. An automatic mode for the hydrogen feed flow controller FC06 following this rule was implemented into the Oresol.vi and used from January 14 on and during all tests in September 2019.

The goal of the tests in September 2019 was to demonstrate this relation for different temperatures between 850°C and 950°C . As can be seen in Table 11, the values in row (D) are always slightly smaller than those in row (M). The tests showed all in all a somewhat worse performance than those from January. A main difference was that the quantity of fresh particles fed into the reactor every day was considerably lower than in January. The reason was that, in purely arithmetical terms, there was still an ilmenite excess of a factor of 4 or more, but apparently this reduction nevertheless affected performance.

The first day of the tests, September 24, was particularly weird. During one hour of operation with H_2 feed, the performance was extremely poor (Table 11, rows (J) and (L)), and only about 32 g of water were produced, while up to 90 g would have been expected. In the following half hour however (now without hydrogen), the water out flow rate increased(!) by about 50% and the extracted amount by 23 g to 55 g. And after that, for no apparent reason, a “deluge” started and another 33 g, practically all of the still missing amount of water, was released within only three minutes, a 20x higher flow than during the hour with hydrogen feed. Possibly the time was even shorter, but the Pump P3 was on its limit and could simply not deliver the amount of water faster to the outside. The result was an exceptionally high 100% yield measured over the whole day (Table 11, row (K)). Such a “flood-event” occurred only once during the whole operation history of Oresol, and the reason remains completely unclear. But, together with the “delay” of the water extraction at the beginning of the hydrogen feed, it makes obvious that there are a lot of non-stationary effects going on in the tests and that all results concerning yield or efficiency, especially when measured at a certain instant of time, have to be taken with a grain of salt. Totally independent of this, the deluge-event was very useful, because it was a unique opportunity to take a video of the water extraction under full load conditions with concentrated solar power.

The other three days in September 2019 gave mixed results. To show the expected dependence of the equilibrium composition on temperature, the tests were generally not long

enough. As a reminder, operation with hydrogen rarely lasted longer than one and a half hours because of the omnipresent filter problem.

To summarize the chapter, the hydrogen reduction of ilmenite appears to be largely complete when the hydrogen fraction in the feed gas remains below the amount of water to be expected in thermodynamic equilibrium. This means that the reaction is largely controlled by the water and not by the hydrogen. However, the yield seems to decrease when the solid feedstock is partially consumed. All in all, the data does not yet give a clear picture, so that further experiments are necessary.

5.5.2 Water Separation

As the production of water from ilmenite is the primary goal of this work, the extraction of the water from the gas stream is of paramount importance. In order to obtain the largest possible amount of water, the gas flow in the Water Separator is actively cooled down below the ambient temperature (see chapter 3.9.4). Fig. 146 shows the temperature curves for the test on Jan. 11, 2019. The wet gas enters the Water Separator at near ambient temperature (green line). This temperature is determined by the cooling water temperature, which has risen by about 8 degrees during the day. The Peltier element (thermoelectric cooler, TEC) located in the Water Separator has on its cold side a temperature of only a few degrees Celsius (gray line) above the freezing point of water. To avoid the formation of ice, the TEC is switched off when the temperature falls below 2.9 °C and switched on again when the temperature rises by one degree. This is clearly visible between 10:00 and 10:30, after which water production begins and the TEC no longer reaches this low temperature. Only at 13:20, when the gas flow is interrupted for a short time for filter cleaning (see chapter 4.2.8), the temperature drops once again to this value. The gas cools down considerably due to the contact with the heat

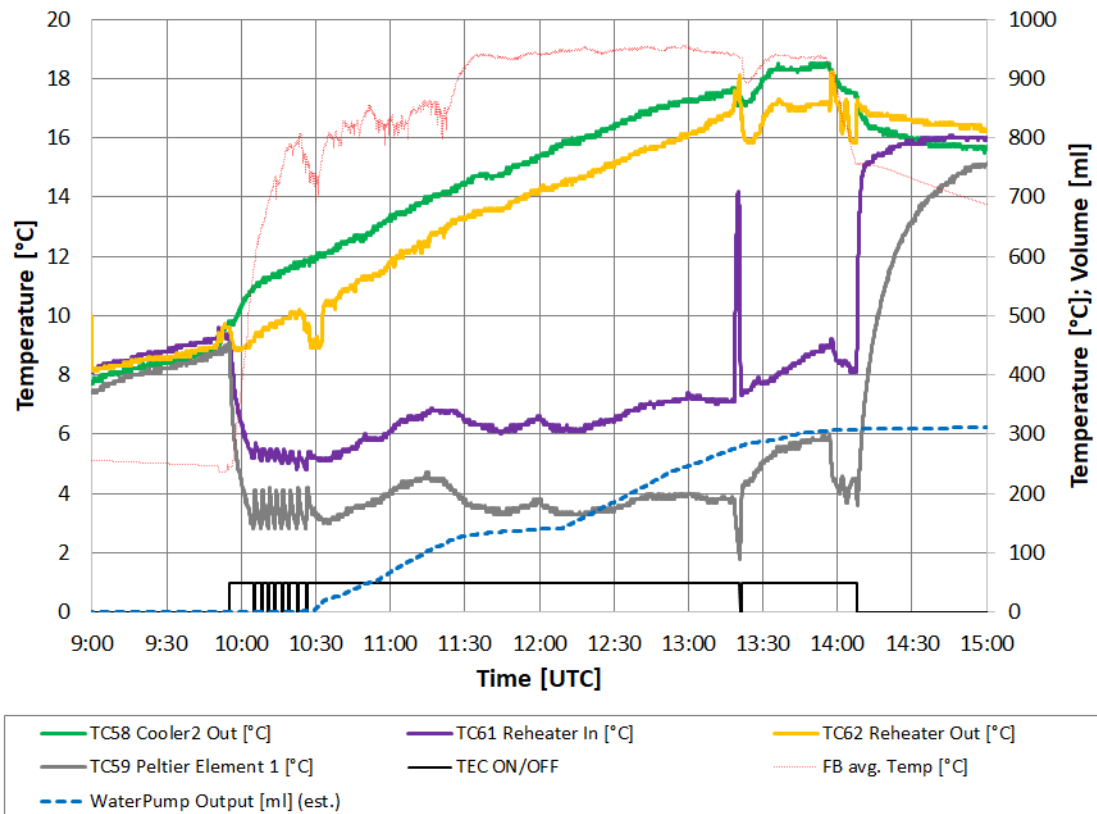


Fig. 146: Temperatures of the water separation system on Jan 11, 2019.

exchanger fins on the Peltier element and leaves the water separator with a temperature (purple line) up to 10 °C lower than at the inlet. It is then warmed up again in the "re-heater" (integrated in the Cooler-2) to almost the ambient temperature (orange curve).

The humidity sensor RHT is located at this point (outlet of the re-heater). Its measurement data are shown in Fig. 147 (orange line). During water production, the values range between 50 and 70%. This is low enough to prevent condensation in the downstream system components, but only if pressure there isn't increased significantly by the Recirculation Pump P1. For this reason, the gas flow is regulated by means of short-circuit valves (MV13) instead of valves connected in series (MV21, MV22).

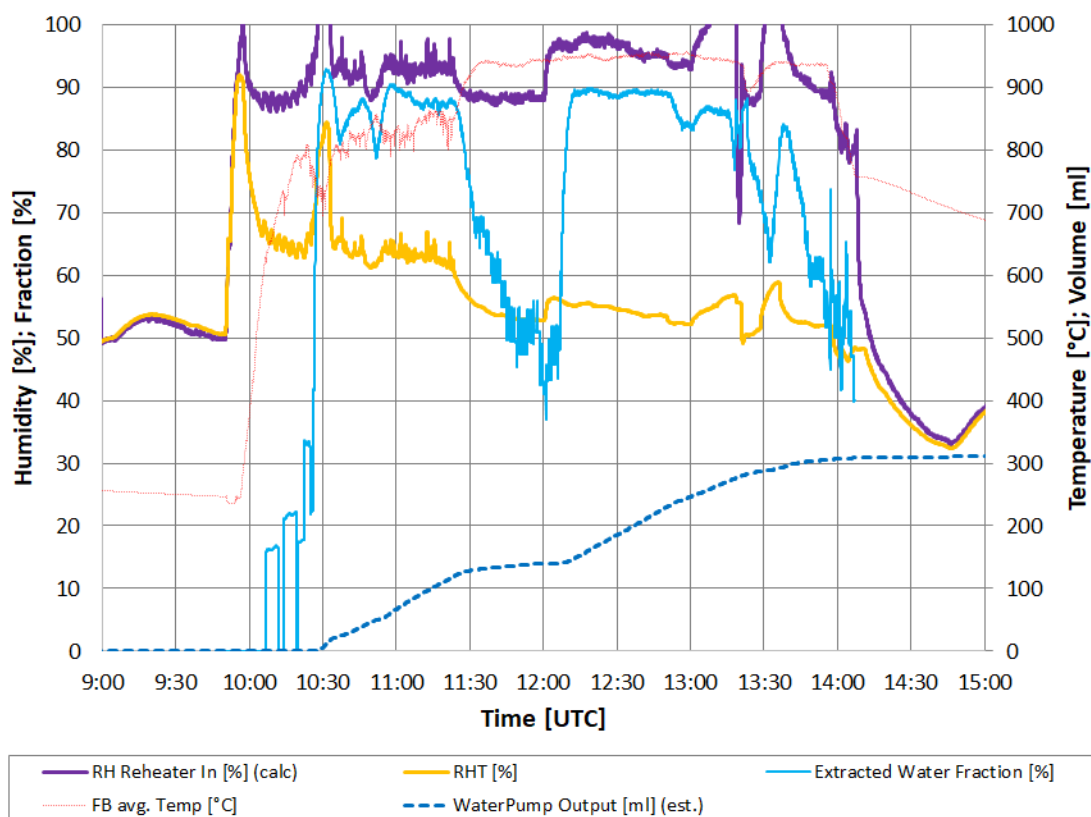


Fig. 147: Humidity measurements of the water separation system on Jan 11, 2019.

Using equations for calculating the saturation vapor pressure (Buck, 1981), the mass flow of the water vapor remaining in the gas stream can be calculated at the location of the humidity sensor RHT. Its value of 0.25 to 0.3 g/min is quite constant over the course of the test day. Then, for the outlet of the water separator, the relative humidity (purple line in Fig. 147) can be calculated from the temperature there. As expected, it is close to 100%, which confirms the correct function of the water separator. With the help of the measured quantity of separated water, it is also possible to determine the degree of separation. It is 90% during the phases with water production (light blue line in Fig. 147). However, this does not mean that the remaining 10% are lost. They remain in the loop and can be separated during the next lap.

The diagrams in Fig. 146 and Fig. 147 provide a good illustration of how the water separator works. The water-laden, wet gas from the reactor enters the water separator at ambient temperature. There it is chilled down by up to 10 °C, and the condensed water is removed by gravity. The remaining cold gas is saturated with water vapor (100% RH). In the reheater, it is

warmed up back to ambient temperature, with its relative moisture content dropping to about 50%, i.e. the gas becomes dry.

5.5.3 Water Chemistry

At the end of every test day, samples of the product water (Fig. 148 left) and the particles were taken. The usual procedure was to take one water sample ("a") from the Imhoff cone and another one ("b") from the valve MV27 at the bottom of the Water Separator. When both Imhoff cones were used to separate the source of the water, samples were taken from each, the water of crystallization from the particles ("a1"), and the water from the hydrogen reaction ("a2"). For all samples, the electrical conductivity was measured immediately after the test (Fig. 148 right). During the test on November 02, 2018, a sample was taken for every 20 ml of water produced, resulting in four extractions ("019a1", "019a2", "019a3", "019a4").



Fig. 148: Left: Product water samples from the Oresol tests. Right: Conductivity measurement.

The measured conductivity of the samples varied widely, with extreme values of $135 \mu\text{S}/\text{cm}$ at the low end and $7000 \mu\text{S}/\text{cm}$ as the highest one. The average value for the "a"-samples was around $3000 \mu\text{S}/\text{cm}$, with no pronounced distinction between water from hydration and water from the reaction. The samples with high conductivity had a slightly yellowish tone. It's hard to find any meaningful pattern in the data. The clearest one seems to be that the conductivity dropped notably over the course of a testing day. Furthermore, samples from tests with more fresh particles feed appear to be slightly more contaminated.

A total of 17 of the samples were further analyzed in the chemistry laboratory of the PSA. They were checked for pH, organic and inorganic carbon, anions, and cations including $\text{Fe}^{2+/3+}$. Table 12 shows the results for the four samples from Nov 02, 2018 (019a1-a4), and two from Jan 11, 2019 (025a1+a2). The product water from the two Imhoff cones from the latter day was then blended (sample 025a3) and distilled (025a5). Measured, but not included in the table are the anions bromide (Br^-), nitrite (NO_2^-), nitrate (NO_3^-), and phosphate (PO_4^{3-}) as well as the cations sodium (Na^+), potassium (K^+), magnesium (Mg^{2+}), and Calcium (Ca^{2+}). Their contribution to the overall contamination was in most cases less than 1%.

The samples 019 from Nov. 02, 2018 show the general trend to less contamination with the progressing of the test. The conductivity is decreasing from 4000 to $1000 \mu\text{S}/\text{cm}$. The acidity (pH) remains constant at 3.5 to 3.6. The carbon content is low. Among the anions, chloride (Cl^-) dominates with a molar share of 75%, and the remainder is evenly distributed between fluorides (F^-) and sulfates (SO_4^{2-}). The practically only cation present is ammonium (NH_4^+); iron accounts for just 1%.

As the sample 025a1 from Jan. 11, 2019 is taken from water produced before sample 025a2, the trend of the decreasing conductivity is also visible here. The pH is approximately the same,

but with about 2.5 notably more acidic than in the samples 019. Carbon is quite high in the first sample, but then back to “normal” values. The anions are somewhat less dominated by chlorides, followed by fluorides and then sulfates. The cations again are mostly ammonium, but this time with a more notable iron share of up to 20%. The distillation applied to the blended product water appears to be efficient. It removed virtually all cations and 95-99% of the anions. Acidity (pH) went up and conductivity went down, but still not far enough to be usable in the electrolyzer.

Date	2018-Nov-02				2019-Jan-11			
Comment	from reaction				from ilmenite	from reaction	blended	distilled
Sample	019a1	019a2	019a3	019a4	025a1	025a2	025a3	025a5
Volume [cm ³]	20	20	20	14	140	172	≈230	≈195
Conduct. [μS/cm]	3970	2090	1510	1090	5880	2690	2580	166
pH	3.55	3.55	3.53	3.6	2.28	2.56	2.56	3.44
C [mg/dm ³] [mmol/dm ³]	13.3 1.1	24.9 2.1	20.0 1.7	no data	124 10.3	20 1.6	24 2.0	18 1.5
F ⁻ [mg/dm ³] [mmol/dm ³]	49.4 2.6	43.4 2.3	30.8 1.6	12.0 0.6	137 7.2	158 8.3	123 6.5	5.5 0.3
Cl ⁻ [mg/dm ³] [mmol/dm ³]	858 24.2	369 10.4	255 7.2	87 2.5	1074 30.3	400 11.3	246 6.9	0.6 0.02
SO ₄ ⁻ [mg/dm ³] [mmol/dm ³]	259 2.7	213 2.2	160 1.7	67 0.7	955 9.9	337 3.5	299 3.1	7.3 0.08
NH ₄ ⁺ [mg/dm ³] [mmol/dm ³]	493 27.3	247 13.7	167 9.3	39 2.1	662 36.7	185 10.3	133 7.4	0.0 0.0
Fe ^{2+/3+} [mg/dm ³] [mmol/dm ³]	14.3 0.26	2.7 0.05	6.9 0.12	5.5 0.10	158 2.8	139 2.5	84 1.5	0.0 0.0

Table 12: Product water samples analysis results.

The *origin of the impurities* is most likely the solid feedstock. During the test on Jan. 11, 2019, a total of 14.6 kg of solids were supplied, this allows, based e.g. on the analysis of the sample 023a3, a rough estimation of the amount of the impurities.

- Carbon (C): 5.5 mg or 0.4 ppm⁸⁷. In the box with the ilmenite, small, dry plant remains are found sporadically. When from this material the mass of only one ant has entered the reactor, then the carbon content is already explained.
- Anions: Fluoride (F⁻): 28 mg or 1.9 ppm. Chloride (Cl⁻): 57 mg or 3.9 ppm. Sulfur (S): 23 mg or 1.6 ppm. Only sulfur is mentioned in the data sheet with “<0.01%”, this is 100 ppm. The impurities occurring here are considerably smaller, so that an origin from the ilmenite is likely.
- Iron (Fe²⁺ and Fe³⁺): Since iron is a major constituent of the particles, its presence is to be expected.

⁸⁷ Parts Per Million or mg/kg, referring to the mass of the impurity in the solid feedstock.

- Nitrogen (N): This is the hardest one to explain, because nitrogen is not a common constituent of minerals. But it is the main component of Earth's atmosphere, suggesting that an unintentional intrusion into the system is possible. To account for the amount of ammonium measured, about 25 cm³ of air would be needed, the volume of a small schnapps glass. This does not sound like very much, and could easily have entered e.g. when cleaning the filter before starting operation. However, each time the gas is cycled, a certain amount is removed from the system through the GV valve and at the beginning also through the valve MV12, so that the quantity of false air in the stream should drop to zero relatively quickly. But there is another possibility that might play a role. The particles in the *standpipe* slide down against an argon flow, but since this pipe is only poorly fluidized, it would be quite thinkable that small amounts of air remain trapped in the porosity of the packed particles finding this way their path into the reactor.

It should be noted that these calculations are only very rough estimates based on certain assumptions. These are in particular that sample 025a3 is representative, and that all impurities have made their way somehow into the product water. But even if the estimates are wrong by one order of magnitude, nothing fundamental changes in the statements.

Distillation demonstrated to be an efficient but not sufficient means to condition the product water for the electrolyzer. A two-stage cleaning system is likely to be necessary. On the Moon, a major advantage of distillation as the first stage over other processes such as reverse osmosis or ion exchange is that, in principle, the entire volume of water can be purified (evaporated), and wastewater does not necessarily have to remain. This is mandatory because all of the hydrogen must be recovered. Furthermore, no additional chemicals (consumables) are necessary. The impurities are then present in solid form on the bottom surface and can be removed from the system. The thermal energy required for the distillation can be taken directly from the off-gas, or, if this is not sufficient, from the reactor or the tailings. The second step could be, for example, electrodeionization, as it also does not require additional consumables and can operate in continuous mode (Alvarado & Chen, 2014). The resulting wastewater from this step can be returned to the first stage and is therefore not lost.

5.6 Miscellaneous

In this chapter, a few less important but nonetheless interesting results are presented.

Window Gas Effectiveness

The large quartz window is a unique feature of reactors powered by concentrated solar energy. It allows solar radiation to be coupled directly into the interior of a reactor without the need for (lossy) heat exchanger walls. To accomplish this task, the window must remain as transparent as possible for the entire operating time. Due to the presence of particles, there is generally a risk that it can become dirty. Cleaning from the outside is possible without major problems, but in case of contamination from the inside, the window must be dismantled.

The most important factor for contamination is gravity. Upwardly oriented surfaces foul considerably more than downwardly oriented surfaces, which benefits the reactor. The sticking of particles to the window occurs mainly through electrostatic and adhesion forces. Larger particles do not adhere to the window, especially if the window is not electrically charged. This can be achieved, for example, by stroking the window with a carbon fiber brush. Very fine particles, on the other hand, can in principle also stick to the bottom of the window.

To avoid this, the aperture cone is permanently flowed through by a gas stream from top to bottom.

There is no clear criterion that can be used to determine the amount of this gas flow. So the flow rate in Oresol was set quite arbitrarily at one quarter of the gas flow through the fluidized bed, but not less than 10 l_N/min. With these settings, there were never any problems with contamination. Since this is a subordinate issue, no further investigations have yet been made to find out how far the gas flow could actually be reduced.

Nevertheless, the window did not remain completely clean all the time. From the outside, it occasionally happened that a fly was attracted by the bright light. From the inside, the larger particles splashed against the window from time to time, but never stuck there. However, they do remain on an area of the aperture cone that is not tilted, resulting in a clearly visible black ring (Fig. 149). Since the window gas is injected just above this ring, and at a 45° upward angle, a certain amount of extremely fine dust was deposited in this area on the inside of the window (Fig. 149 red arrows). This did not pose any problem for operation, but should nevertheless be avoided in future reactors by making appropriate design adjustments.

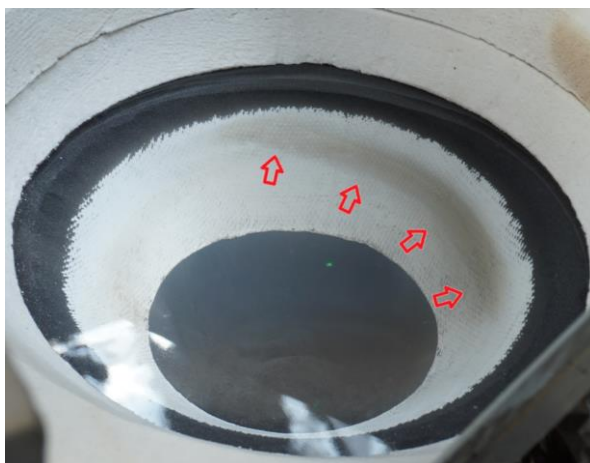


Fig. 149: Dirt on the inside of the reactor window.

Window Crack

On February 09, 2017, the first and only window damage of all Oresol tests happened (Fig. 150 left). The reactor flange inside temperatures measured at the time of the incident (12:31) were:

- TC27 Reactor-Flange-Inside North: 67.6 °C
- TC29 Reactor-Flange-Inside South: 65.3 °C
- TC28 Reactor-Flange-Inside East: 114.7 °C
- TC30 Reactor-Flange-Inside West: 225.7 °C

The reason for the elevated temperature on the east side is the proximity of the gas outlet (for the location see Fig. 44 on page 77). On the west side however, the reason is not immediately obvious. It turned out that due to the gap in the thermal insulation on the west side of the reactor, which is necessary for the feedthrough of the thermocouples (Fig. 150 right), hot gas reached the window flange from the bottom. The resulting asymmetric heat load was sufficient to bend the flange far enough that the window broke. The problem was solved by

adding an additional layer of insulating material to the inside of the flange (see Fig. 58 bottom right on page 94).

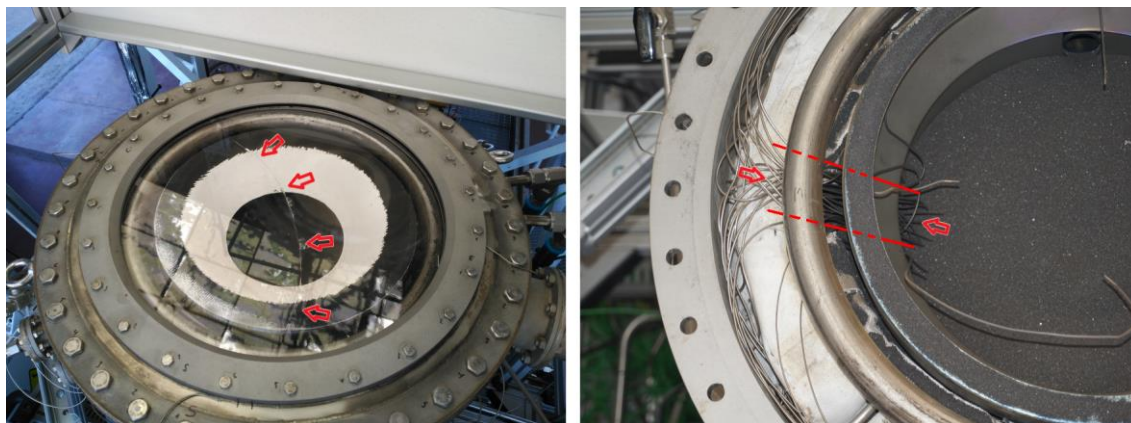


Fig. 150: Left: Broken window. Right: Feedthrough for thermocouples.

Argon Consumption

The recirculation of the gas stream with the Pump P1 turned out to be a very efficient way to reduce strongly the argon consumption. For example, on Jan 09, 2019, the total operation time was 286 minutes (4.8 h). The total argon flow through the system during this time was 11.5 m³. As 77% or 8.8 m³ of this flow were recycled by P1 through FT07 and FT08, only 2.7 m³ had to be supplied from the bottle (Fig. 151). This stretches the lifetime of the argon supply by at least a factor of four. As the PSA Solar Furnace has normally a stock of four bottles with a capacity of 10.6 m³ at a maximum pressure of 200 bar each, the recirculation makes the difference between resupply every week or once a month.



Fig. 151: Argon pressure in the bottle before (left) and after (right) the test from Jan09, 2019. The difference of 50 bar indicates that ¼ of the capacity of the bottle (10.6 m³) was consumed.

Particles Analysis

This work was practically exclusively dedicated to reactor technology and water production. The raw material, however, the ilmenite, was used "as is", and only little attention was paid to its state. One day, though, I wanted to know more precisely how much weight loss the particles actually had. To find out, one sample container was filled completely with unused particles (Fig. 152), and a second one was filled with particles from the bucket under the Outpipe. It should be expected that the latter would have up to 10% less mass. In fact, however, there was no difference in weight at all. The question now arises, of course, why?

One reason could be that only a small portion of the particles had reacted that day. Another would be that the reduced ilmenite has a somewhat reduced volume, but this seems rather unlikely. Finally, it is also possible that the reduced ilmenite was re-oxidized very rapidly when leaving the reactor. Since the material comes into contact with the ambient air at a high temperature, this is quite plausible. This implies for future experiments that the tailings should cool down under inert gas. This should be relatively easy to do technically simply by putting a lid on the bucket that is flushed with the argon from the Outpipe.



Fig. 152: Particle weighing.

6 Summary and Conclusions

In the Oresol project, a solar-powered fluidized bed reactor was designed, built, and successfully tested in the Solar Furnace SF-60 of the Plataforma Solar de Almería in southeast Spain. Its aim is the demonstration of the reduction of the mineral ilmenite with hydrogen in a solar powered, full-scale test plant. This chemical reaction could be used to extract oxygen from lunar regolith in a future settlement on the Moon. Since oxygen makes up most of the mass of rocket fuel, and fuel in turn represents the dominant portion of the mass to be brought up into space, future lunar travel could become significantly cheaper if it were possible to build an oxygen refueling station on the Moon.

Reactor

The heart of the Oresol experiment is the solar-heated, isothermal and continuously operated gas-solid reactor. It contains a cylindrical vessel inside, filled with 22 kg of particles. At the top of the reactor is a large quartz window through which the concentrated solar radiation enters into the interior. Inside, the solar radiation hits directly the surface of the particle bed where it is absorbed (Fig. 153 top left). The gas, a mixture of argon and hydrogen, flows through the particle bed from the bottom to the top. By suitable selection of the gas velocity, the particles are fluidized, making them behave like a bubbling liquid. This allows the continuous feed and discharge of solids (Fig. 153 bottom left), and ensures excellent mixing of the particles both with the gas and with themselves, what causes a homogeneous temperature distribution throughout the reactor (Fig. 153 top right). Moreover, the gas makes a chemical reaction with the particles. The hydrogen (H_2) in the feed gas removes an oxygen atom from the ilmenite ($FeTiO_3$) and reacts with it to form water (H_2O) (Fig. 153 bottom right). This water leaves the reactor together with excess hydrogen, inert argon, and possible by-products of the reaction.

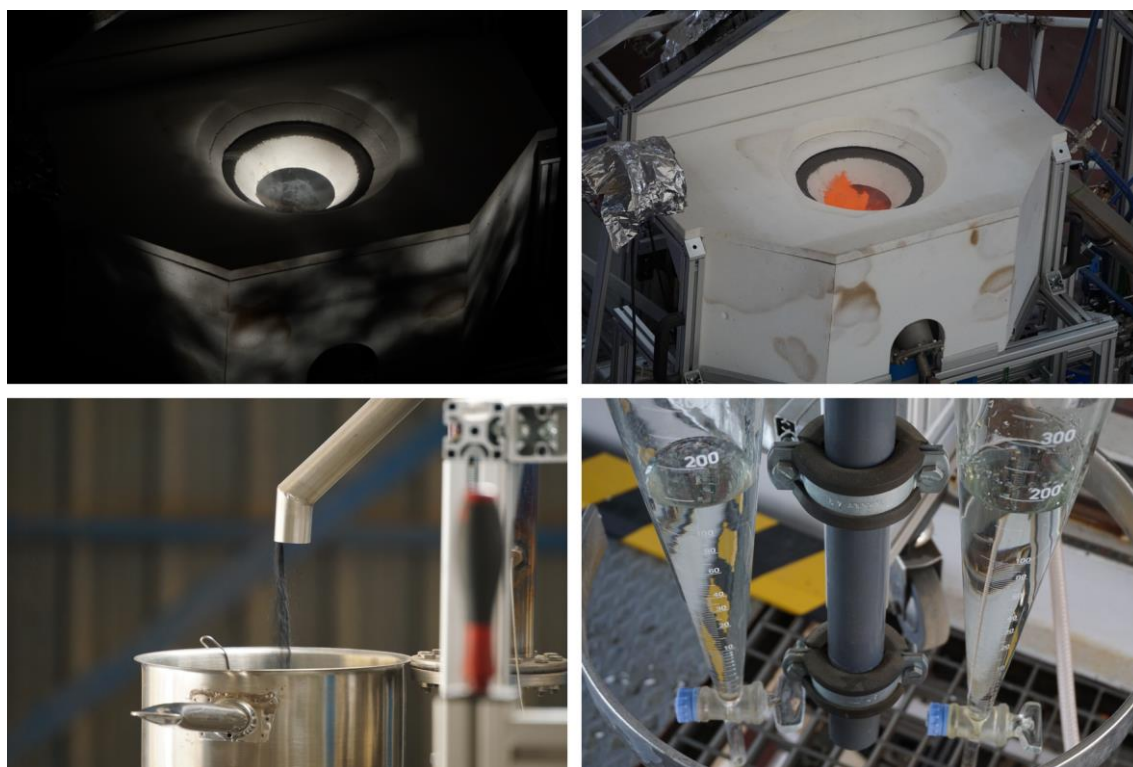


Fig. 153: The Oresol plant. Top left: Reactor during solar operation. Top right: Reactor after solar operation, still hot. Bottom left: Continuous particles flow. Bottom right: Product water.

Periphery

In addition to the reactor itself, the Oresol plant includes a large part of the auxiliary equipment necessary for its operation. It might be considered as a small but rather complete chemical factory. This includes the systems for the particle supply and removal, the gas supply, and the off-gas treatment and recirculation. The solids supply and removal takes place in continuous mode via siphon-like designs, which create a sealing effect for the gas in the reactor and allow for mass flow control without the need for any moving parts in the dusty or hot area. The solids mass flow rate is regulated by the partial fluidization of the standpipe. As the off-gas from the reactor is "hot, wet and dirty", it needs a multi-stage treatment doing cooling, drying and cleaning. The first step is a *Cooler* that cools the gas down to about 300 °C. Next, the *Particle Separator* separates the larger stray particles from the gas stream, and a subsequent *Filter* removes the fines. The operation of these components at over 100 °C ensures that the product water remains in the gas phase. The second *Cooler* then cools the gas down to ambient temperature, whereby a large part of the product water condenses. In the *Water Separator* below, the gas is further cooled down with the aid of a thermoelectric cooler. This way, the maximum amount of water is extracted from the gas. While that water is then transported out of the system by a small peristaltic *Pump*, the gas is warmed back up to ambient temperature. This way, unwanted condensation of residual moisture at unsuitable places is prevented. Finally, a *Recirculation Pump* returns the gas to the reactor.

Feedstock

Since real lunar material with the required properties is presently (end of 2021) not yet available in the needed quantities and for an affordable price, terrestrial ilmenite with a grain size of 150 µm was used in the experiments. For safety reasons, the feed gas was mainly argon, with only small amounts of hydrogen (usually <8%).

Goals

The testing campaigns of the Oresol plant had three primary and two additional goals. They were, in order of importance:

1. **Chemistry:** Demonstration of water production from the ilmenite-hydrogen reaction.
2. **Temperature:** Operation of the reactor at a minimum of 800 °C, heated exclusively with concentrated solar energy.
3. **Gas Flow:** Identification of the gas flow demand of the main fluidized bed in the reactor as a function of the temperature.
4. **Solids Flow:** Demonstration of continuous particle feed and discharge.
5. **Kinetics:** Gaining basic information about the maximum possible rate of the reaction.

Test Campaigns

The experiments were carried out in several test campaigns. First was the installation which was accompanied by non-solar pre-tests. Then the fluid dynamics and the general behavior of the plant was tested with air at up to 400 °C. In the subsequent series of tests, the feed gas was switched to argon and the reactor temperature was increased to 800 °C. Finally, up to 8% of hydrogen was added to the argon, and a peak temperature of almost 1000 °C was reached. In further tests, the amount of hydrogen was increased with the aim of achieving a higher product water yield. The fluidized bed accumulated a total of 200 operation hours, 150 of them with solar power.

Results

It turned out that the fluidization works best when the *gas velocity* in the reactor is kept constant, regardless of the temperature. The determined value for the combination Argon / Ilmenite-150 is 3.3 cm/s. Since the specific volume of the gas increases with temperature, the amount (mass) of the supplied gas must be inversely proportional to the absolute temperature.

Controlling the continuous *particle mass flow* turned out to be not entirely easy, but feasible. A subroutine for the control program was developed, which regulates the gas flow required for the control of the solids flow. Mass flows of 110 g/min and 220 g/min were used regularly. Higher values were possible but difficult to maintain. This would require an increase of the pipe diameters and the size of the solids feed hopper.

Many tests were carried out at a *temperature* of around 950 °C without problems. The maximum mean temperature reached in the reactor was 977 °C, with local peaks above 1000 °C. The limitation was the tendency of the particles to start sintering at local temperatures above 1000°C.

A *power balance* for the reactor has been established. The energy source is the concentrated solar beam. The energy sinks are made up of thermal radiation, conduction and convection losses, and heating of the feed particles and gas. During transient operation phases, heating of the entire reactor inventory has to be taken into account too. The contribution of the reaction enthalpy is negligible. The required solar power during steady state operation was about 8 kW, well below the maximum power the PSA Solar Furnace can provide. During phases with particle supply (110 g/min), 10 kW were needed. With about 6 kW, most of the power went into thermal radiation losses, the rest was evenly distributed among the other sinks. For reactors on the Moon, a considerably higher power requirement for the particle stream can be expected, since the ilmenite content is likely to be significantly lower than in the Oresol experiments and therefore a higher solids throughput, e.g. by a factor of 5, will be necessary.

The system produced water. This happened initially even without the addition of hydrogen. It turned out that the Water Separator was quite efficient in driving out the *water of crystallization* contained in the particles. In order to distinguish this from the water of the reaction, in most of the experiments, operation with particle supply was separated from operation with hydrogen supply. The water usually came out of the reactor with a delay of several minutes. The content of water of crystallization in the solids ranged from 0.5% to 1%.

In particular, during the January 2019 tests, over 100 cm³ of water were produced each day by the *chemical reaction*. This corresponded to a *yield* of over 90% with a hydrogen content of 8% in the feed gas. A major problem during the experiments was that the particle Filter in the downstream section clogged relatively quickly, so that the maximum allowed pressure in the reactor was always reached quite soon. For this reason, until now, it has not been possible to operate the reactor with hydrogen for longer than one and a half hours without interruption. To solve the problem, a 20x larger filter was designed and built, but not yet tested.

The product water presented significant *impurities* and was very acidic. The electrical conductivity was in some cases several 1000 µS/cm and the pH value was in the range of 3. The chemical analysis detected mainly sulfate, chloride and ammonium. Although other interfering substances are to be expected on the Moon, it is likely that water purification will be necessary before the product water can be fed into the electrolyzer.

Impact

To this date, the Oresol plant is the only large scale reactor demonstrating an end-to-end process to obtain water or oxygen from a regolith simulant using concentrated solar radiation as heat source. The hydrogen reduction of ilmenite has been one of three processes evaluated by the European Space Agency (ESA) during the past three years as potential prototypes for future commercial payloads to the Moon. Even though other processes may provide higher yields, they have yet to be proven at scale, e.g. with full-scale demonstrators as this one. Consequently, the research presented here has been a successful terrestrial proof-of-concept and starting point for the production of oxygen/water outside our planet.

Moreover, the characterization of the fluidized bed and the experience with the reactor operation in the solar furnace can also be transferred to other sectors, such as hydrogen production. This is a field with big interest for the renewable energy community, where process engineering approaches are needed in order to meet current plans for a low-carbon or carbon neutral society in the future.

Further Insights

An important lesson learned from the work is that it is not enough to focus only on the reaction or the reactor. Instead, the entire system must always be considered, in particular the preparation of the raw material and the post-processing of the product. This has to be kept in mind especially when comparing processes for lunar oxygen production, but in principle it applies to any process technology on the Moon. In particular, it is important that hardly any substances are consumed or lost that cannot be easily obtained on the Moon itself. For the ilmenite process this means that the involved hydrogen must be recovered almost completely, the product water must be purified without loss, and possible accumulations of by-products in the loop (H_2S can be expected) must be eliminated without any loss of hydrogen. The more different chemical elements are involved, the more difficult it becomes to fulfill this condition properly. Since in the ilmenite process only H, O and Fe are part of the primary reactions, this is an important argument in favor of this process.

All in all, the Oresol project can be considered very successful. Perhaps the most important result of the work is the deep insight obtained into the design and operation of a low-expansion fluidized bed with concentrated solar radiation for gas-solid reactions. With the experience gained, it should be possible to design early prototypes for in-situ experiments on the Moon with high confidence of success.

7 Outlook

7.1 Further Tests on Earth

As usual with prototype testing, there remains always a long wish list at the end. This concerns both hardware improvements and questions about the test results. The most important open items are listed in this chapter.

New Filter F3

The experiments especially of the test phase with $H_2 > 8\%$ were strongly hampered by the fast clogging of the Filter F3. For this reason, a new Particle Separator with a considerably larger filter area than the original device was designed and built. One condition was that the device had to have the same connection dimensions and piping positions as the original Particle Separator. Another limitation was that the available installation volume is tightly constrained. Nevertheless, it was possible to increase the filter surface area by a factor of 20. This was achieved by connecting ten rectangular (instead of one round) filter cloths in parallel. The new design is shown in Fig. 154.



Fig. 154: New off-gas filter with 20x increased filter area.

Left: CAD drawing. Middle: General view. Right: Filter cassette (without filter cloths).

Just like the old model, the separation of the coarse particles is done by the combination of cross-sectional expansion and inertia (see chapter 3.9.2). The filter material is also the same (except that it no longer has to be cut into the circular shape), as is the thermal insulation. Since the mass and thus the heat capacity has increased considerably, an additional electrical heating element is included in case the heating time becomes too long. The Cooler C1, which has so far only been provisionally converted into an air cooler, will get a proper interface to the fan and a chimney for discharging the hot cooling air.

Further Hardware and Software Modifications

An extension of the length of the two branches of the Outpipe siphon would allow operation at somewhat higher reactor pressure.

To avoid reoxidation of the spent particles, the solids collection bucket requires a lid with two small openings. One will be connected to the Outpipe. This connection must be flexible in order not to interfere with the measurements of the strain gauge MT02. The other one allows the argon coming out from the Outpipe to be released into the atmosphere.

A similar device is needed for the inlet hopper. It should be purged with argon to prevent entrainment of air with the particle column in the standpipe.

During the tests, the behavior of the gas distributor was not completely satisfactory. In order to be able to better influence the gas distribution, the possibility of a zone-by-zone control would be desirable. This could be done, for example, by dividing the gas distributor into 5 equal areas. If the gas distributor is designed with horizontal pipes with small bores directed downwards by 45° (so-called spargers), then emptying the reactor would also be easier to realize than before. It is not yet clear when this modification can be implemented, since at present (end of 2021) the necessary high-temperature steels are virtually unobtainable in Europe.

Finally, it would be nice to have a distillation stage for the product water, which is operated with the heat of the off-gas from the reactor.

On the software side, it would be desirable to have an automatic control of the Solar Furnace shutter with the temperature in the reactor as an input variable.

Experiments and Analysis

A flux density measurement in or near the focal plane would improve the calculation of the energy balance (see chapter 5.3). The usual method, the photographic measurement of the brightness distribution on a white, diffusely reflecting plate, is very difficult to realize for the Oresol reactor, because the focal plane is inside the reactor.

Furthermore, a better, preferably continuous, analysis of the off-gas would be desirable. This could be done, for example, with a gas chromatograph. In addition, a better knowledge of the composition of the feed gas would also be welcome. So far, the hydrogen sensor H2CT failed to provide usable results. Continuous measurement of nitrogen and oxygen at this point would also be useful. Furthermore, a continuous recording of the conductivity of the product water would also be interesting.

For the experiments themselves, the most important goal is of course to increase the water production. Besides extending the operating time, it is also possible to increase the hydrogen supply. On the one hand, operation can be made with a higher hydrogen content (and with less argon, or completely without), and on the other hand, it should be tested how far the gas velocity in the reactor can be increased without too much particle entrainment or negative impact on the window.

Beyond the Oresol facility, research about fluidization and off-gas filtering will be done with the small 3D printed fluidized bed built during the Alchemist project (see Fig. 11 on page 30). Different lunar simulants will be tested at ambient temperature with air, argon, and hydrogen.

Finally, it is also planned to design an off-axis concentrator as described in chapter 1.3.7.

7.2 Oxygen Production on the Moon

This chapter goes beyond the objectives of this work. It identifies a few more issues that need to be addressed if an oxygen production facility will eventually be established on the Moon. The list is certainly not exhaustive.

Some of the environmental conditions on the Moon differ significantly from those on Earth, which has a direct impact on the design of a process plant. The most important differences are

the complete lack of an atmosphere (hard vacuum), the chemical and mineralogical composition of the regolith in comparison to the simulants, the lower gravity (1/6 g), and the 29x longer day-night cycle. Therefore, it is not possible to test a lunar factory to 100% on Earth. However, some of these conditions can indeed be pretested, at least approximately.

Vacuum

An important component of the solar thermal reactor is the window. It must withstand the operating pressure. Should it be selected to one bar on the Moon, as it is on Earth, then a thicker window is necessary. Such windows already exist. For example, the central (round) window of the Cupola on the International Space Station has a diameter of 80 cm and is also made of fused silica⁸⁸. With a cooled frame and a design similar to the Oresol reactor, it should be possible to transmit between 100 and 200 kW of concentrated solar power. With a modified design putting the window closer to the focal plane, it could be even more.

To avoid problems with the tightness of the countless pipes and tubes, there is the possibility of installing the entire system inside a pressure vessel filled with a hydrogen "atmosphere". This would also simplify the pressure and thermal control of many parts of the system. A trade-off must be made to determine if the advantages outweigh the disadvantage of the higher system mass.

Regolith

Beneficiation of the feedstock is desirable if it can significantly reduce the size of the reactor. On Earth, the methods used for this usually consume a lot of water. On the Moon, however, only "dry" techniques can be used ((Rasera et al., 2020), see also page 68). How well which technology works will ultimately have to be tested on the Moon itself.

On the Moon, some sulfur is present in the regolith in the form of Troilite (FeS) ("Lunar Sourcebook - A User's Guide to the Moon," 1991). Therefore, methods should be explored that either remove the sulfur before it is fed into the reactor, or that remove the probably formed H₂S from the off-gas and recover the hydrogen bound in it. For this purpose, it can be taken advantage of the high temperature of the gas when leaving the reactor. For tests on Earth, an appropriate simulant should be developed. Since Troilite is extremely scarce on earth, it might be substituted by Pyrrhotite⁸⁹.

Low Gravity

As already stated in chapter 1.4.4 on page 59, the reactor geometry on the Moon is likely to resemble a pan rather than a pot. Since this is quite unfavorable for a fluidized bed, appropriate measures have to be taken. The simplest is to build the reactor higher and to accept the increased volume and therefore a residence time of many hours for the solids. Another possibility is to divide the fluidized bed into several, individually fluidized zones. This could even be done with internal walls to achieve a kind of series connection of the zones, which would have a very favorable effect on the residence time distribution of the particles in the reactor.

Of particular interest, of course, is the fluidization behavior of the particles under lunar gravity conditions, preferably with particles having a shape similar to the real lunar regolith. The goal

⁸⁸ <https://directory.eoportal.org/web/eoportal/satellite-missions/i/iss-cupola>

⁸⁹ Pyrrhotite (Fe_(1-x)S with x = 0...0.2) is a nonstoichiometric variant of Troilite (FeS).

should be to determine the Geldart AC-boundary (see chapter 1.4.3) as well as the gas velocity for minimum fluidization. This has already been partially tested on parabolic flights (Shao et al., 2006). However, further research on this is needed. Ideally, hydrogen would be used at 950 °C, but this is obviously very difficult to realize in an airplane for safety reasons.

Day-Night Cycle

The long day-night cycle on the Moon is a great advantage for a solar-powered oxygen production system. This allows it to run for 14 days without interruption, minimizing losses due to start-up and shut-down. An interesting option is not to simply dispose of the spent particles (tailings) after processing, but to store them in well-insulated containers so that they can then be used as a convenient heat source during the lunar night. In this case, it might even be advantageous to refrain from the beneficiation of the regolith (ilmenite enrichment) in order to have a larger amount of solid material available for this purpose.

...Research on the Moon

Despite the greatest efforts, it will not be possible to determine all relevant operating parameters of a lunar oxygen factory with final certainty by preliminary tests on Earth. This applies in particular to the replication of the mechanical and chemical properties of the regolith. For example, already in 1946 Shomate et al. found that FeO instead of FeTiO₃ at 1200 K (927 °C) gives 5x more water in the off-gas (38.7% vs. 7.6%). “The marked difference in theoretically possible hydrogen utilization is the direct result of the free energy of binding of FeO and TiO₂ in FeTiO₃” (Shomate et al., 1946). If pure FeO were available on the Moon, e.g. from pyroclastic deposits, and if this theoretical prediction would actually hold, this could reduce notably the required hydrogen flow rate and therefore the diameter of a reactor⁹⁰.

Lunar ISRU only makes sense beyond research purposes if large amounts of O₂ are produced. This seems to be only necessary in the case of permanent human presence on the Moon. Due to the complexity and the large number of variables in the processes, it will therefore ultimately come down to becoming part of a Lunar ISRU Research line on a future, permanently crewed lunar base. With all environmental conditions and unlimited amounts of raw material available, the various concepts can be tested thoroughly on a small scale, comparable to the Oresol system. The most suitable one could then be implemented in a large-scale facility producing the oxygen needed to refuel the rockets for the return flights. If one day facilities for the propellantless launch of payloads, such as mass drivers, were to be built on the Moon, then it would also become possible to export the oxygen to other locations in the Earth-Moon system, like the Lagrange Points or even Low Earth Orbit.

⁹⁰ Footnote 18 on page 25 repeated: Since the Spanish word "feo" means "ugly" in English, the motto for the site selection should be (pun intended!): “*FeO is beautiful!*”

Appendix

A.1 Chemical Elements and Substance Properties

Chemical Elements

Atomic Number	Symbol	Name	Atomic Mass [u]
1	H	Hydrogen	1.0080
6	C	Carbon	12.011
8	O	Oxygen	15.999
12	Mg	Magnesium	24.305
13	Al	Aluminium	26.982
14	Si	Silicon	28.085
16	S	Sulfur	32.06
17	Cl	Chlorine	35.45
20	Ca	Calcium	40.078
22	Ti	Titanium	47.867
26	Fe	Iron	55.845

Table 13: List of chemical elements that appear in this work. $1 \text{ u} = 1.660539 \cdot 10^{-27} \text{ kg}$.

Substances

Formula	Name	State of Matter	Mole Mass [g/mol]	Density [kg/m ³]		Heat Capacity [J/kgK]	
				0 °C	950 °C	0 °C	950 °C
H ₂	Hydrogen	gas	2.016	0.0899	0.0201	14170	15410
Ar	Argon	gas	39.948	1.782	0.398	520	520
Air	Air	gas	28.9644	1.292	0.289	1005	1187
H ₂ O	Water	liquid/gas	18.015	999.8	0.180	4204	2431
FeTiO ₃	Ilmenite	solid	151.744	4450	4450	625	932

Table 14: List of the most important substances that appear in this work. The heat capacity is at constant pressure. Data from (Rohsenow et al., 1998).

A.2 Units and Conversions

Since this work is largely about engineering, the units usually utilized in this discipline are mostly used instead of the strictly scientific (SI) units. This is especially valid for sensors where the units provided by the suppliers are used without conversion.

Length (technical dimensions) in mm: $1 \text{ mm} = 10^{-3} \text{ m}$

Length (grain size) in μm : $1 \mu\text{m} = 10^{-6} \text{ m}$

Wavelength (electromagnetic radiation) in nm: $1 \text{ nm} = 10^{-9} \text{ m}$

Temperature in $^{\circ}\text{C}$: $0^{\circ}\text{C} = 273.15 \text{ K}$

Pressure in mbar or bar: $1 \text{ bar} = 1000 \text{ mbar} = 10^5 \text{ Pa}$

Gas flow in l_n/min or NI/min : standard (normal) liters per minute. $1 \text{ l}_n/\text{min} = 1/60000 \text{ m}^3/\text{s}$. The normal conditions are 0.00°C and 1013.25 mbar ⁹¹.

Unit used by manufacturers of flow sensors and controllers. Index n normally should be used in the symbols and not in the units. But since the text often does not require formula symbols (and omitting them simplifies legibility), and the distinction between standard and non-standard volume flows is essential, the notation of the manufacturer⁹² is adopted here.

Since every gas has a given density under standard conditions, the standard volume flow is actually a mass flow. The conversion⁹¹ is for:

- Air: $1 \text{ l}_n/\text{min} = 1.293 \text{ g}/\text{min} = 2.155 \cdot 10^{-5} \text{ kg}/\text{s}$
- Argon: $1 \text{ l}_n/\text{min} = 1.784 \text{ g}/\text{min} = 2.973 \cdot 10^{-5} \text{ kg}/\text{s}$
- Hydrogen: $1 \text{ l}_n/\text{min} = 0.0899 \text{ g}/\text{min} = 1.498 \cdot 10^{-6} \text{ kg}/\text{s}$

Water volume (flow) in ml (ml/min): milliliters (per minute).

$1 \text{ ml} = 1 \text{ cm}^3 = 10^{-6} \text{ m}^3$. $1 \text{ ml}/\text{min} = 1/60000000 \text{ m}^3/\text{s}$. The mass of 1 ml of water is 0.001 kg.

Amount of matter in mol: The conversion is based on the molecular mass. Note that the atomic mass unit makes the conversion $\text{mol} \leftrightarrow \text{g}$ or $\text{kmol} \leftrightarrow \text{kg}$. For conversion of the correct SI-units mol and kg, a factor of 10^{-3} has to be applied.

- Hydrogen (H_2): $1 \text{ mol} \leftrightarrow 2.016 \text{ g}$
- Water (H_2O): $1 \text{ mol} \leftrightarrow 18.015 \text{ g}$
- Ilmenite (FeTiO_3): $1 \text{ mol} \leftrightarrow 151.744 \text{ g}$

With the molar volume $22.414 \text{ dm}^3/\text{mol}$ of ideal gases at standard conditions, gas flows can be converted by:

- $1 \text{ l}_n/\text{min} = 0.0446 \text{ mol}/\text{min} = 2.68 \text{ mol}/\text{h}$
- $1 \text{ mol}/\text{min} = 22.4 \text{ l}_n/\text{min}$

Example: The Oresol reactor frequently was running with a hydrogen feed flow rate of $2 \text{ l}_n/\text{min}$. This is $120 \text{ l}_n/\text{h}$ or $5.35 \text{ mol}/\text{h}$. With 100% yield, the maximum possible water production rate would be $96 \text{ g}/\text{h}$.

⁹¹ <http://www.fluidat.com/>

⁹² <https://www.bronkhorst.com/int/products/gas-flow/>

Fluid flows:

- Norm Volume Flow = Mass Flow / Norm Density
- Molar Flow = Mass Flow / Molar Mass
- Volume Flow = Norm Volume Flow $\times T/T_0$ (ideal gas only)
- Gas Velocity = Volume Flow / Cross Section (empty reactor or pipe only)

A.3 Brief Historical Review

The very first draft of the Oresol process is shown in Fig. 155. It's already rather close to the one finally realized and presented in chapter 3.2.1, although some important components are still missing, like e.g. a gas vent with pressure control. One of the most important differences is that the solids outlet syphon still was internal, a concept that didn't work well later and eventually was replaced by a syphon on the outside. Also, all kind of gas cleaning steps were still missing. A gas bottle with a mix of 5% hydrogen and 95% argon even was purchased, but finally never used, because instead, the mix was eventually made with the help of a 6th flow controller for pure hydrogen. An interesting detail for future designs is the pump for the water feed of the electrolyzer. If the electrolyzer were to operate at high pressure, power-consuming compressors for hydrogen and oxygen storage could be avoided.

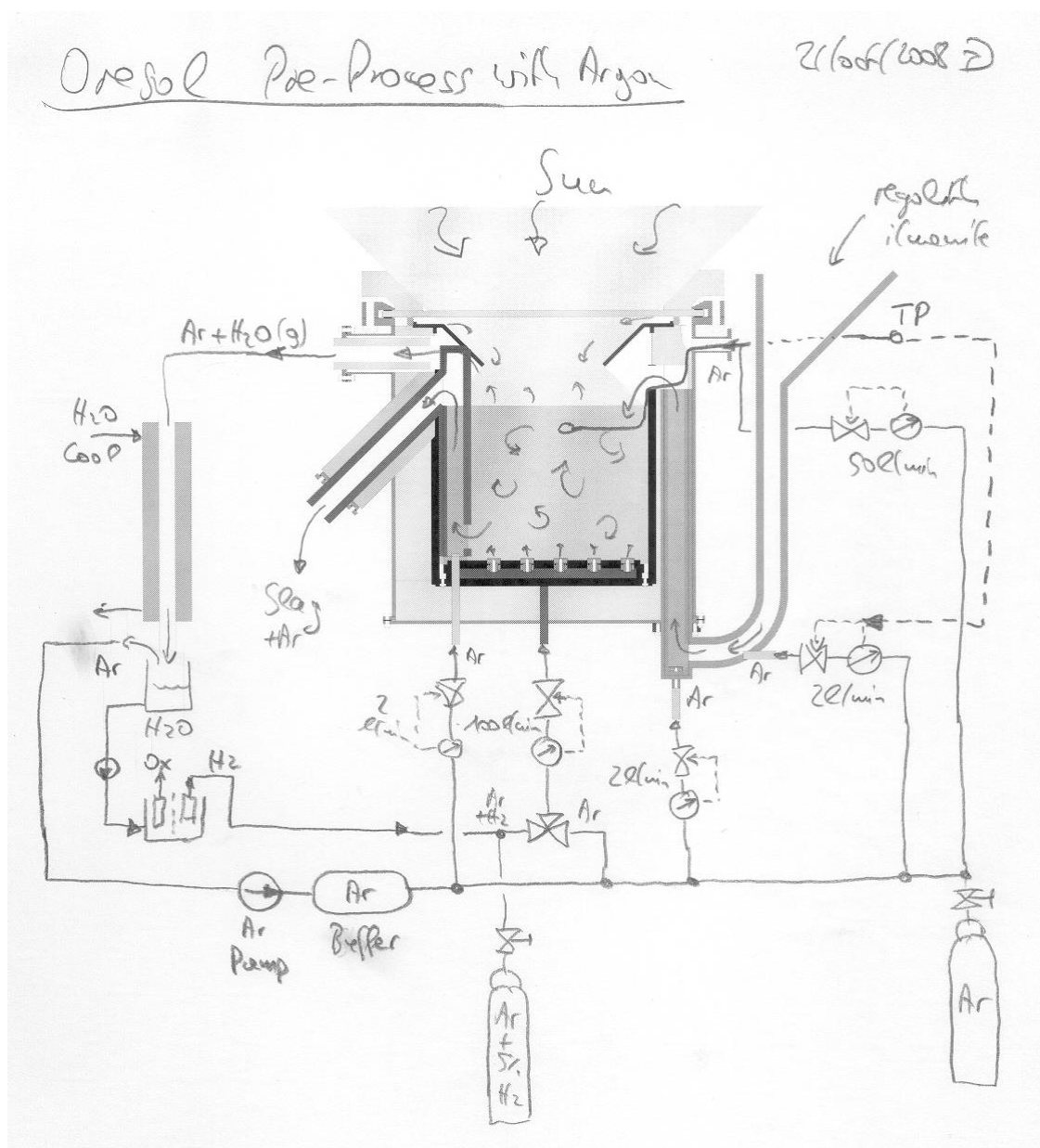


Fig. 155: Early sketch of the Oresol process. “TP” is Spanish “TermoPar” = “ThermoCouple”. The solids outlet syphon is the pipe with the shape of the number “1” at the reactor’s left side, with one leg submerged in the fluidized bed and the other one marked with the word “Slag”.

A.4 Technical Drawings

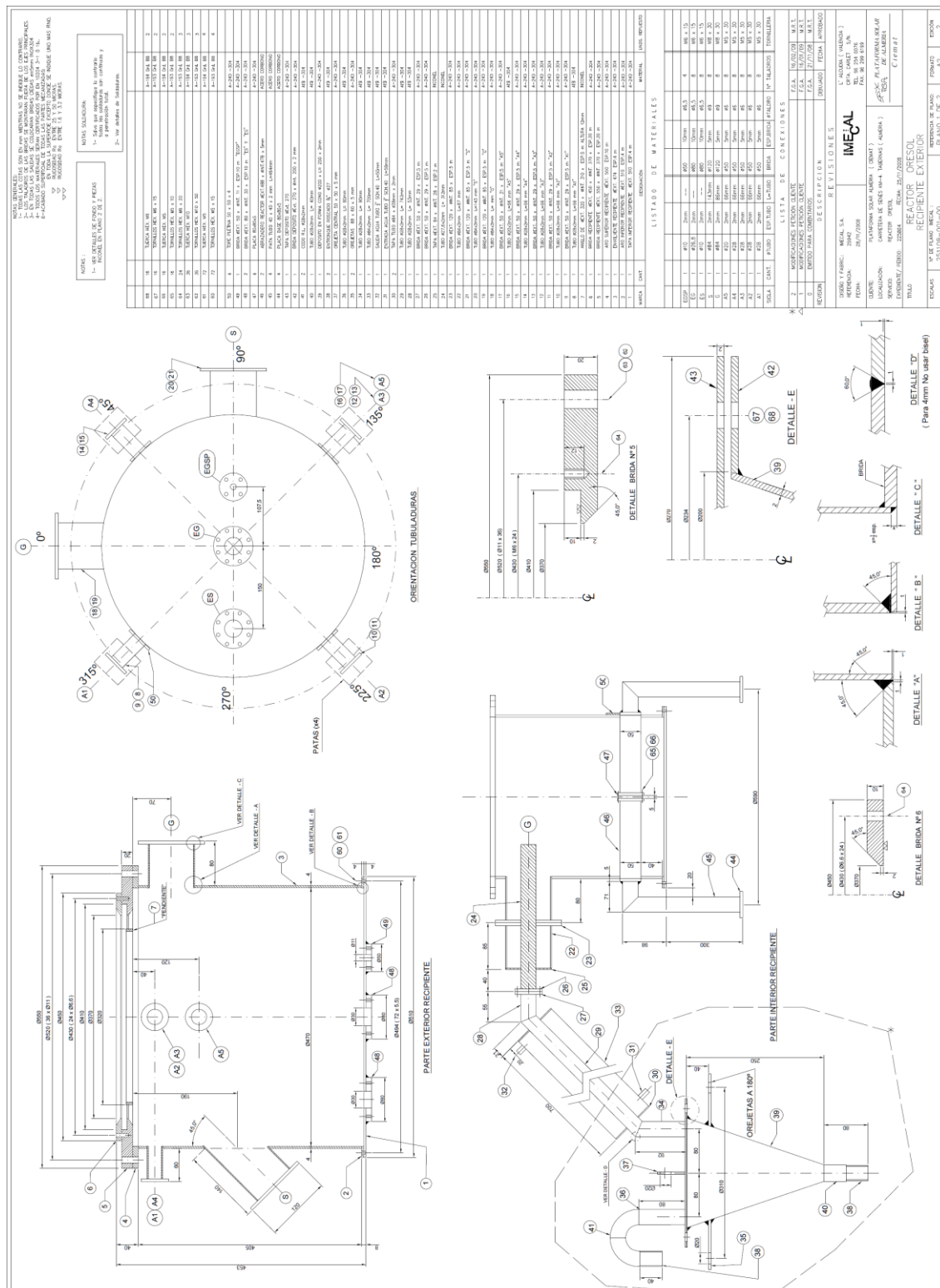


Fig. 156: Oresol reactor, original technical drawing (1/2).

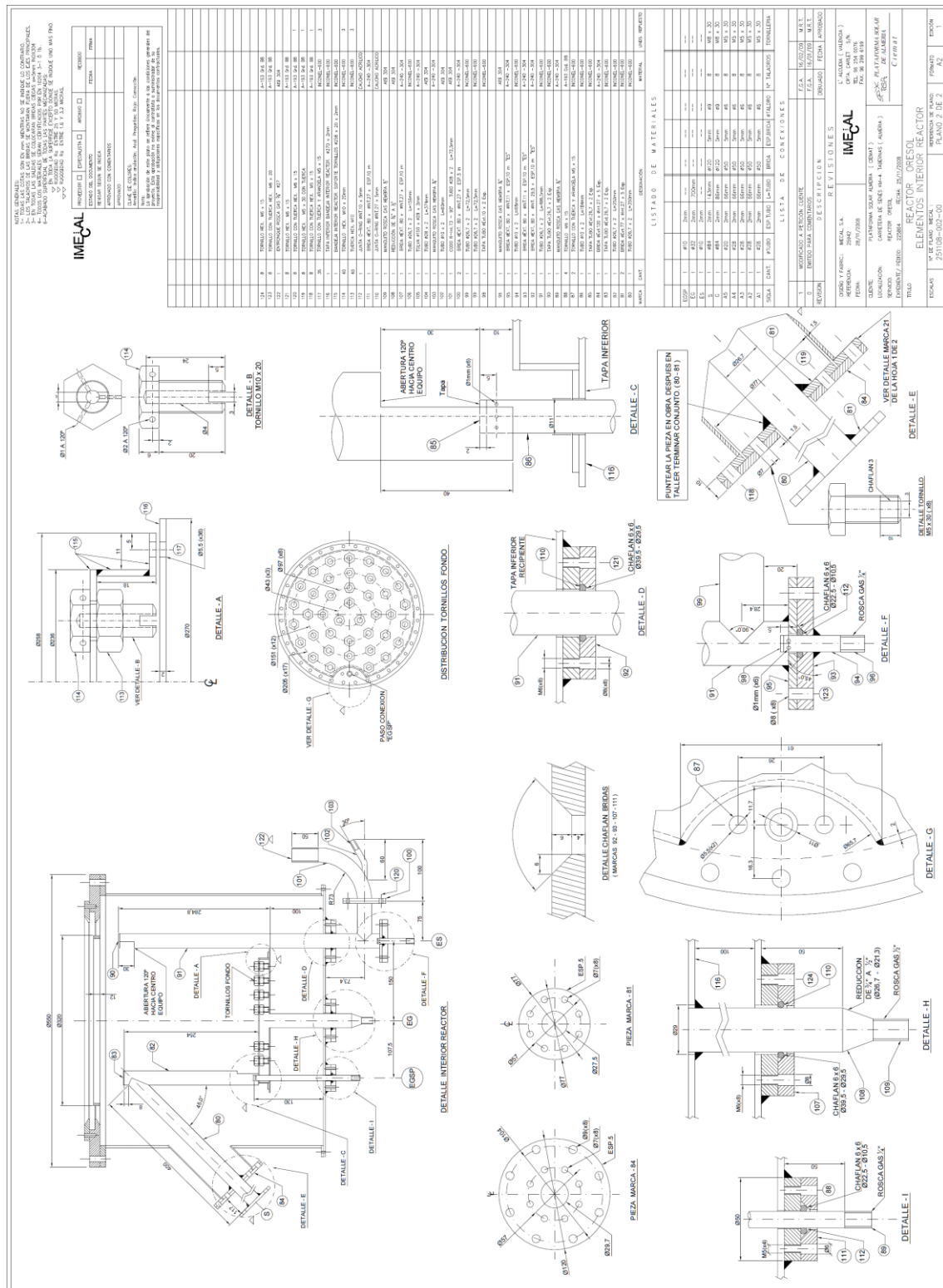


Fig. 157: Oresol reactor, original technical drawing (2/2).

A.5 Instrumentation

Table 15 and Table 16 provide information about the sensors used. The first group are external sensors of the solar furnace, which are retrieved via an OPC server. The column "ADAM" indicates the module and channel number in the AD converter. "Conn. Row/Col" contains the connection position on the back of the electronics box (see Fig. 92 on page 119). The "Min./Max. Values" are the preset values for Warning and Emergency respectively. However, these values can be changed during operation. The last 8 thermocouples were intended for the air-cooled diagonal mirror (see chapter 3.4) and were therefore not used.

Name	Description	Sensor Type	Signal	Wires	IO	ADAM Type	Ch.	Conn. Row/Col	Range from to	unit	Min. Values alarm	Max. Values emerg.	Sensor Manuf.	Model	Status	Remarks
DN1	Direct Normal Solar Irradiation	pyrheliometer			in	OPC			0 12007	W/m2					implemented	
Tamb1	Ambient Temperature				in	OPC			7 7	°C					implemented	from CESA-17
vWind	Wind Speed				in	OPC			0 7	km/h					implemented	
dWind	Wind Direction				in	OPC			0 360						implemented	
pAmb1	Ambient Pressure				in	OPC			7 7	mbar(a)					implemented	from CESA-17
Sh(Pa)	Shutter Angular Position				in	OPC			0 100	%					implemented	From Home-SetPoint
m(CW)	CoolingWater Flow				in	OPC			0 7	l/min					est. from HP-Pump	
p(CWIn)	CoolingWater Pressure In				in	OPC			0 7	bar					implemented	no data (24Jun2016)
p(CWOut)	CoolingWater Pressure Out				in	OPC			0 7	bar					implemented	no data (24Jun2016)
HP-PumpON	WaterPump On/Off				in	OPC			F T						not yet implemented	
HP-PumpON	WaterPump SetPoint				in	OPC			0 100	%					not yet implemented	manual input
p(A)	Argon Bottle Pressure				in	OPC			0 200	bar					not yet implemented	Sensor not yet connected. Value calculated from flows.
SolarOp	Shutter enabled		0/1		out	OPC			0 100	%					not yet	For emergency close.
FC1-SP	Flow Controller Main Bed Fluid. Gas	flow controller	4-20mA	5	in	4017+	01 00	1/1	0 80	Nl/min Ar			Bronkhorst			before oct2017: 100 Nl/min
FC01-V	FC Main Bed Fluid. Gas Valve Pos.	flow cont. valve	0-20mA		in	4017+	01 01	1/1	0 100	%						
FC02	Flow Controller Window Protection Gas	flow controller	4-20mA	5	in	4017+	01 02	1/2	0 50	Nl/min Ar			Bronkhorst			
FC02-V	FC Window Protection Gas Valve Pos.	flow cont. valve	0-20mA		in	4017+	01 03	1/2	0 100	%						
FC03	Flow Controller OutPipe Gas	flow controller	4-20mA	5	in	4017+	01 04	1/3	0 5	Nl/min Ar			Bronkhorst			before aug2014: 2 Nl/min
FC03-V	FC OutPipe Gas Valve Pos.	flow cont. valve	0-20mA		in	4017+	01 05	1/3	0 100	%						
FC04	Flow Controller InPipe Gas	flow controller	4-20mA	5	in	4017+	01 06	2/1	0 2	Nl/min Ar			Bronkhorst			
FC04-V	FC InPipe Gas Valve Pos.	flow cont. valve	0-20mA		in	4017+	01 07	2/1	0 100	%						
FC01-SP	FC Main Bed Fluid. Gas SetPoint	flow controller	4-20mA		out	4024	02 00	1/1	0 80	Nl/min Ar						with galvanic separator
FC02-SP	FC Window Protection Gas SetPoint	flow controller	4-20mA		out	4024	02 01	1/2	0 50	Nl/min Ar						with galvanic separator
FC03-SP	FC OutPipe Gas SetPoint	flow controller	4-20mA		out	4024	02 02	1/3	0 5	Nl/min Ar						with galvanic separator
FC04-SP	FC InPipe Gas SetPoint	flow controller	4-20mA		out	4024	02 03	2/1	0 2	Nl/min Ar						with galvanic separator
FC05	Flow Controller StandPipe Gas	flow controller	4-20mA	5	in	4017+	03 00	2/2	0 2	Nl/min Ar			Bronkhorst			
FC05-V	FC StandPipe Gas Valve Pos.	flow cont. valve	0-20mA		in	4017+	03 01	2/2	0 100	%						
FC06	Flow Controller Hydrogen	flow controller	4-20mA	5	in	4017+	03 02	2/3	0 16	Nl/min H2			Bronkhorst			before oct2017: 2 Nl/min
FC06-V	FC Hydrogen Valve Pos.	flow cont. valve	0-20mA		in	4017+	03 03	2/3	0 100	%						
FT07	Flow Transmitter Main Bed Fluid. Gas	flow transmitter	4-20mA	4	in	4017+	03 04	3/1	0 60	Nl/min Ar			M&W			
FT08	Flow Transmitter Window Protection Gas	flow transmitter	4-20mA	4	in	4017+	03 05	3/2	0 60	Nl/min Ar			M&W			
MT01	Particles Feed Hopper Mass	strain gauge	4-20mA	4	in	4017+	03 06	3/3	0 10	kg			Boische			before jan2018: 10kg
MT02	Particles Outlet Bucket Mass	strain gauge	4-20mA	4	in	4017+	03 07	4/1	0 80	kg			Boische			
FC05-SP	FC StandPipe Gas SetPoint	flow controller	4-20mA		out	4024	04 00	2/2	0 2	Nl/min Ar						with galvanic separator
FC06-SP	FC Hydrogen SetPoint	flow controller	4-20mA		out	4024	04 01	2/3	0 16	Nl/min H2						with galvanic separator
vacant	vac. S13		4-20mA	7	out	4024	04 02	4/4	0 100	%						with galvanic separator?
vacant	vacant		4-20mA		out	4024	04 03									with galvanic separator?
PT01	Pressure Main Bed Fluid. Gas	rel. pressure tr.	4-20mA	2	in	4017+	05 00	4/2	0 160	mbar			140 160	Bürkert		
PT02a	Pressure Reactor (Sensor a)	rel. pressure tr.	4-20mA	2	in	4017+	05 01	4/3	0 100	mbar			30 40	Bürkert		
PT12	Pressure Window Protection Gas	rel. pressure tr.	4-20mA	2	in	4017+	05 02	5/1	0 160	mbar			140 160	Bürkert		ADAM Channel swapped with PT02b.
PT03	Pressure OutPipe Gas	rel. pressure tr.	4-20mA	2	in	4017+	05 03	5/2	0 160	mbar			140 160	Bürkert		
PT04	Pressure InPipe Gas	rel. pressure tr.	4-20mA	2	in	4017+	05 04	5/3	0 250	mbar			220 250	Bürkert		
PT05	FC Supply Pressure	rel. pressure tr.	4-20mA	2	in	4017+	05 05	6/1	0 10	bar	2.0			Bürkert		
PT06	External Gas Supply Pressure	rel. pressure tr.	4-20mA	2	in	4017+	05 06	6/2	0 10	bar	5.0			Bürkert		
PT07	Recirculation Pump Discharge Pressure	rel. pressure tr.	4-20mA	2	in	4017+	05 07	6/3	0 10	bar			7.5 7.8	Bürkert		
PD08	OutCollector Pressure	dif. pressure tr.	4-20mA	4	in	4017+	06 00	7/1	-100 100	mbar			80	Testo		
PT09	Cooler2 Inlet Pressure	abs. pressure tr.	4-20mA	2	in	4017+	06 01	7/2	0 100	mbar				Bürkert		since oct2017 connected
PAT10	Ambient Pressure	abs. pressure tr.	4-20mA	2	in	4017+	06 02	7/3	0 1000	mbar(a)				Bürkert		Former "Recirculation Pump Inlet Pressure"
PT11	Pressure/Flow Main Bed Fluid. Gas	rel. pressure tr.	4-20mA	2	in	4017+	06 03	8/1	0 250	mbar			220 250	Bürkert		Value-estimated-via-piamb)
PT02b	Pressure Reactor (Sensor b)	rel. pressure tr.	4-20mA	2	in	4017+	06 04	8/2	0 100	mbar			30 40	Bürkert		Swapped with PT12 for increased redundancy/safety.
PATE7	Electrolyzer Hydrogen Pressure	abs. pressure tr.	4-20mA	2	in	4017+	06 05	8/3	0 1000	mbar(a)				Bürkert		Dif to PAT10 treated as PDTE1 (rel. pressure)
PT02	External Hydrogen Supply Pressure	rel. pressure tr.	4-20mA	2	in	4017+	06 06	8/4	0 10	bar				Bürkert		since oct2017 Shares ADAM-Port with PATE1
RHT	Reheater Out Humidity	rel. humidity tr.	4-20mA	2	in	4017+	06 06	9/1	0 100	%			80	Testo		Former Cooling Water Supply Pressure
H2CT	Main Bed Supply Hydrogen Concentration	H2 conc. gauge	4-20mA	4	in	4017+	06 07	9/2	0 50	%			10	BlueSens		
P1	Recirculation Pump ON/OFF	3p-400V	0/1		out	4055	07 D00	400V right							ok	
P2	Hydrogen Pump ON/OFF	24V+	0/1	2	out	4055	07 D01	400V left							ok	
P3	Water Extraction Pump ON/OFF	24V+	0/1	2	out	4055	07 D02	/ 1							ok	
Ely	Electrolyzer Power Supply ON/OFF	230V	0/1		out	4055	07 D03	230V right							ok	
CoolF1	Cooling Fans 1 ON/OFF	24V+	0/1	2	out	4055	07 D04	2							ok	since 13nov2017
CoolF2	Cooling Fans 2 ON/OFF	24V+	0/1	2	out	4055	07 D05	/ 3							ok	since 13nov2017
Peltier	Peltier Cooler Power Supply ON/OFF	open/close	0/1	2	out	4055	07 D06	/ 4							ok	Minor protection from vapours (moved from F2).
Alarm?	Alarm Light	24V+	0/1	2	out	4055	07 D07	5							ok	Switches Power Supply 38V/10A. (Might be replaced by main-voltage for other?).
EB	Emergency Button	"mushroom"	0/1	2	in	4055	07 D08	/ 6					false		ok	Other cable with easier-access connector?
ElyPB	Electrolyzer ON pushbutton	pushbutton	0/1	2	in	4055	07 D09	/ 7							ok	
LW4	Water Separator Water Level High	level switch	0/1		in	4055	07 D02	/ 8							ok	Power/Data 3 Level Sensors combined in 1 socket w/ 5 pins.
LW4	Water Separator Water Level Mid	level switch	0/1	5	in	4055	07 D03	/ 8							ok	1-power, 2-ground, 3-Lv1, 4-Lv2, 5-Lv3.
LW4	Water Separator Water Level Low	level switch	0/1		in	4055	07 D04	-							ok	With DC-DC Converter 24V=>12V.
vacant	vacant		0/1		in	4055	07 D05	-							-	
vacant	vacant		0/1		in	4055	07 D06	-							-	
vacant	vacant		0/1		in	4055	07 D07	-							-	

Table 15: Oresol sensors (without thermocouples)

Name	Description	Sensor	Type	Signal	Wires	IO	ADAM	Conn.	from	Range	Min. Values	Max. Values	Sensor	Remarks
							Type	Row/Col	to	unit	alarm	emerg	Model	
TC01	FB-Bottom-Center	TC Type K	mV	in	4018+	08	00	1/1	0	1100 °C			CAAFIT	K 1.5/1400 installed Inside Reactor
TC02	FB-Bottom-North	TC Type K	mV	in	4018+	08	01	1/2	0	1100 °C			CAAFIT	K 1.5/1400 installed Inside Reactor
TC03	FB-Bottom-East	TC Type K	mV	in	4018+	08	02	1/3	0	1100 °C			CAAFIT	K 1.5/1400 installed Inside Reactor
TC04	FB-Bottom-South	TC Type K	mV	in	4018+	08	03	1/4	0	1100 °C			CAAFIT	K 1.5/1400 installed Inside Reactor
TC05	FB-Bottom-West	TC Type K	mV	in	4018+	08	04	2/1	0	1100 °C			CAAFIT	K 1.5/1400 installed Inside Reactor
TC06	FB-Middle-Center	TC Type K	mV	in	4018+	08	05	2/2	0	1100 °C			CAAFIT	K 1.5/1400 installed Inside Reactor
TC07	FB-Middle-North	TC Type K	mV	in	4018+	08	06	2/3	0	1100 °C			CAAFIT	K 1.5/1400 installed Inside Reactor
TC08	FB-Middle-East	TC Type K	mV	in	4018+	08	07	2/4	0	1100 °C			CAAFIT	K 1.5/1400 installed Inside Reactor
TC09	FB-Middle-South	TC Type K	mV	in	4018+	09	00	3/1	0	1100 °C			CAAFIT	K 1.5/1400 installed Inside Reactor
TC10	FB-Middle-West	TC Type K	mV	in	4018+	09	01	3/2	0	1100 °C			CAAFIT	K 1.5/1400 installed Inside Reactor
TC11	FB-Top-Center	TC Type K	mV	in	4018+	09	02	3/3	0	1100 °C			CAAFIT	K 1.5/1400 installed Inside Reactor
TC12	FB-Top-North	TC Type K	mV	in	4018+	09	03	3/4	0	1100 °C			CAAFIT	K 1.5/1400 installed Inside Reactor
TC13	FB-Top-East	TC Type K	mV	in	4018+	09	04	4/1	0	1100 °C			CAAFIT	K 1.5/1400 installed Inside Reactor
TC14	FB-Top-South	TC Type K	mV	in	4018+	09	05	4/2	0	1100 °C			CAAFIT	K 1.5/1400 installed Inside Reactor
TC15	FB-Top-West	TC Type K	mV	in	4018+	09	06	4/3	0	1100 °C			CAAFIT	K 1.5/1400 installed Inside Reactor
TC16	Reactor-InnerCone-North	TC Type K	mV	in	4018+	09	07	4/4	0	1100 °C			CAAFIT	K 1.5/1400 installed Inside Reactor
TC17	Reactor-InnerCone-East	TC Type K	mV	in	4018+	10	00	5/1	0	1100 °C			CAAFIT	K 1.5/1400 installed Inside Reactor
TC18	Reactor-InnerCone-South	TC Type K	mV	in	4018+	10	01	5/2	0	1100 °C			CAAFIT	K 1.5/1400 installed Inside Reactor
TC19	Reactor-InnerCone-West	TC Type K	mV	in	4018+	10	02	5/3	0	1100 °C			CAAFIT	K 1.5/1400 installed Inside Reactor
TC20	FB-Ground-West	TC Type K	mV	in	4018+	10	03	5/4	0	1100 °C			CAAFIT	K 1.0xx installed Inside Reactor. Wrong Fitting (1.0 instead of 1.5mm)
TC21	Reactor-OuterCone-North	TC Type K	mV	in	4018+	10	04	6/1	0	1100 °C			CAAFIT	K 1.5/1400 installed Inside Reactor
TC22	Reactor-OuterCone-East	TC Type K	mV	in	4018+	10	05	6/2	0	1100 °C			CAAFIT	K 1.5/1400 installed Inside Reactor
TC23	Reactor-OuterCone-South	TC Type K	mV	in	4018+	10	06	6/3	0	1100 °C			CAAFIT	K 1.5/1400 installed Inside Reactor
TC24	FB-Surface-North	TC Type K	mV	in	4018+	10	07	6/4	0	1100 °C			CAAFIT	K 1.0xx installed Inside Reactor. Wrong Fitting (1.0 instead of 1.5mm)
TC25	FB-Surface-South	TC Type K	mV	in	4018+	11	00	7/1	0	1100 °C			CAAFIT	K 1.0xx installed Inside Reactor. Wrong Fitting (1.0 instead of 1.5mm)
TC26	Reactor-OuterCone-West	TC Type K	mV	in	4018+	11	01	7/2	0	1100 °C			CAAFIT	K 1.5/1400 installed Inside Reactor
TC27	Reactor-Flange-Inside North	TC Type K	mV	in	4018+	11	02	7/3	0	1100 °C			CAAFIT	K 1.5/1400 installed Inside Reactor
TC28	Reactor-Flange-Inside East	TC Type K	mV	in	4018+	11	03	7/4	0	1100 °C			CAAFIT	K 1.5/1400 installed Inside Reactor
TC29	Reactor-Flange-Inside South	TC Type K	mV	in	4018+	11	04	8/1	0	1100 °C			CAAFIT	K 1.5/1400 installed Inside Reactor
TC30	Reactor-Flange-Inside West	TC Type K	mV	in	4018+	11	05	8/2	0	1100 °C			CAAFIT	K 1.5/1400 installed Inside Reactor
TC31	Gas Distributor-1	TC Type K	mV	in	4018+	11	06	8/3	0	1100 °C			SEDEM	K 1.5/600 installed
TC32	Gas Distributor-2	TC Type K	mV	in	4018+	11	07	8/4	0	1100 °C			SEDEM	K 1.5/600 installed
TC33	InPipe-Top	TC Type K	mV	in	4018+	12	00	9/1	0	1100 °C			SEDEM	K 1.5/600 installed
TC34	InPipe-Middle	TC Type K	mV	in	4018+	12	01	9/2	0	1100 °C			SEDEM	K 1.5/600 installed
TC35	InPipe-Bottom	TC Type K	mV	in	4018+	12	02	9/3	0	1100 °C			SEDEM	K 1.5/200 installed
TC36	FC Supply (8PT05)	TC Type K	mV	in	4018+	12	03	9/4	0	1100 °C			SEDEM	K 1.5/200 installed
TC37	Main Bed Fluid, Gas Supply (8PT01)	TC Type K	mV	in	4018+	12	04	10/1	0	1100 °C			CAAFIT	K 1.5/200 installed replaced (2016-oct-31)
TC38	OutPipe1-North	TC Type K	mV	in	4018+	12	05	10/2	0	1100 °C			SEDEM	K 1.5/200 installed
TC39	OutPipe2-South	TC Type K	mV	in	4018+	12	06	10/3	0	1100 °C			SEDEM	K 1.5/200 installed
TC40	GasOutPipe	TC Type K	mV	in	4018+	12	07	10/4	0	1100 °C			SEDEM	K 1.5/600 installed
TC41	Cooler1 In	TC Type K	mV	in	4018+	13	00	11/1	0	1100 °C			SEDEM	K 1.5/200 installed
TC42	Cooler1 Out	TC Type K	mV	in	4018+	13	01	11/2	0	1100 °C			SEDEM	K 1.5/200 installed
TC43	Particles Separator	TC Type K	mV	in	4018+	13	02	11/3	0	1100 °C			SEDEM	K 1.5/600 installed
TC44	Particles Separator Out	TC Type K	mV	in	4018+	13	03	11/4	0	1100 °C			SEDEM	K 1.5/200 installed
TC45	OutCollector	TC Type K	mV	in	4018+	13	04	12/1	0	1100 °C			SEDEM	K 1.5/200 installed
TC46	Cooler1 Water In	TC Type K	mV	in	4018+	13	05	12/2	0	1100 °C			CAAFIT	K 1.5/200 installed
TC47	Cooler1 Water Out	TC Type K	mV	in	4018+	13	06	12/3	0	1100 °C			CAAFIT	K 1.5/200 installed
TC48	P1-HeadTemp	TC Type K	mV	in	4018+	13	07	12/4	0	1100 °C			CAAFIT	K 1.5/200 installed
TC49	Reactor-Flange-Outside North	TC Type K	mV	in	4018+	14	00	13/1	0	1100 °C			SEDEM	K 1.5/600 installed
TC50	Reactor-Flange-Outside East	TC Type K	mV	in	4018+	14	01	13/2	0	1100 °C			SEDEM	K 1.5/600 installed
TC51	Reactor-Flange-Outside South	TC Type K	mV	in	4018+	14	02	13/3	0	1100 °C			SEDEM	K 1.5/600 installed
TC52	Reactor-Flange-Outside West	TC Type K	mV	in	4018+	14	03	13/4	0	1100 °C			SEDEM	K 1.5/600 installed
TC53	Reactor-Wall-Outside North	TC Type K	mV	in	4018+	14	04	14/1	0	1100 °C			CAAFIT	K 1.5/200 installed
TC54	Reactor-Wall-Outside East	TC Type K	mV	in	4018+	14	05	14/2	0	1100 °C			CAAFIT	K 1.5/200 installed
TC55	Reactor-Wall-Outside South	TC Type K	mV	in	4018+	14	06	14/3	0	1100 °C			CAAFIT	K 1.5/200 installed
TC56	Reactor-Wall-Outside West	TC Type K	mV	in	4018+	14	07	14/4	0	1100 °C			CAAFIT	K 1.5/200 installed
TC57	Cooler2 In	TC Type K	mV	in	4018+	15	00	15/1	0	1100 °C			CAAFIT	K 1.5/200 installed
TC58	Cooler2 Out	TC Type K	mV	in	4018+	15	01	15/2	0	1100 °C			CAAFIT	K 1.5/200 installed
TC59	Peliter Gas 1	TC Type K	mV	in	4018+	15	02	15/3	0	1100 °C			CAAFIT	K 1.5/200 installed
TC60	Water Separator	TC Type K	mV	in	4018+	15	03	15/4	0	1100 °C			SEDEM	K 1.5/600 installed
TC61	Reheater In	TC Type K	mV	in	4018+	15	04	16/1	0	1100 °C			CAAFIT	K 1.5/200 installed
TC62	Reheater Out	TC Type K	mV	in	4018+	15	05	16/2	0	1100 °C			CAAFIT	K 1.5/200 installed
TC63	Peliter Gas 2	TC Type K	mV	in	4018+	15	06	16/3	0	1100 °C			CAAFIT	K 1.5/200 installed
TC64	Below ParticlesOutPot	TC Type K	mV	in	4018+	15	07	16/4	0	1100 °C			CAAFIT	K 1.5/200 installed
TC65	E-Box East	TC Type K	mV	in	4018+	16	00	17/1	0	1100 °C			CAAFIT	K 1.5/200 installed
TC66	E-Box West	TC Type K	mV	in	4018+	16	01	17/2	0	1100 °C			CAAFIT	K 1.5/200 installed
TC67	Ambiens-1	TC Type K	mV	in	4018+	16	02	17/3	0	1100 °C			SEDEM	K 1.5/600 installed
TC68	Ambiens-2	TC Type K	mV	in	4018+	16	03	17/4	0	1100 °C			SEDEM	K 1.5/600 installed
TC69	Ambiens-3	TC Type K	mV	in	4018+	16	04	18/1	0	1100 °C			SEDEM	K 1.5/600 installed
TC70	Ambiens-4	TC Type K	mV	in	4018+	16	05	18/2	0	1100 °C			SEDEM	K 1.5/600 installed
TC71	StandPipe-ReactorSide	TC Type K	mV	in	4018+	16	06	18/3	0	1100 °C			CAAFIT	K 1.5/200 installed
TC72	StandPipe-HeliosSide	TC Type K	mV	in	4018+	16	07	18/4	0	1100 °C			CAAFIT	K 1.5/200 installed
TC73	Cooling Water In	TC Type K	mV	in	4018+	17	00	19/1	0	1100 °C			CAAFIT	K 1.5/200 installed
TC74	Peliter Water Out	TC Type K	mV	in	4018+	17	01	19/2	0	1100 °C			CAAFIT	K 1.5/200 installed
TC75	Cooler2 Water Out	TC Type K	mV	in	4018+	17	02	19/3	0	1100 °C			CAAFIT	K 1.5/200 installed
TC76	WinFlange Water In	TC Type K	mV	in	4018+	17	03	19/4	0	1100 °C			CAAFIT	K 1.5/200 installed
TC77	WinFlange Water Out	TC Type K	mV	in	4018+	17	04	20/1	0	1100 °C			CAAFIT	K 1.5/200 installed
TC78	Peliter Copper Cooler	TC Type K	mV	in	4018+	17	05	20/2	0	1100 °C			CAAFIT	K 1.5/200 installed
TC79	Cooling Water Out	TC Type K	mV	in	4018+	17	06	20/3	0	1100 °C			CAAFIT	K 1.5/200 installed
TC80	Joker	TC Type K	mV	in	4018+	17	07	20/4	0	1100 °C			SEDEM	K 1.5/600 installed
TC81	Mirror-Top	TC Type K	mV	in	4018+	18	00	X1	0	1100 °C			SEDEM	K 1.5/600 installed
TC82	Mirror-Center	TC Type K	mV	in	4018+	18	01	X2	0	1100 °C			SEDEM	K 1.5/600 installed
TC83	Mirror-CylAxis	TC Type K	mV	in	4018+	18	02	X3	0	1100 °C			SEDEM	K 1.5/600 installed
TC84	Mirror-Bottom	TC Type K	mV	in	4018+	18	03	X4	0	1100 °C			SEDEM	K 1.5/600 installed
TC85	Mirror-East	TC Type K	mV	in	4018+	18	04	X5	0	1100 °C			SEDEM	K 1.5/600 installed
TC86	Mirror-West	TC Type K	mV	in	4018+	18	05	X6	0	1100 °C			SEDEM	K 1.5/600 installed
TC87	BehindMirror-1	TC Type K	mV	in	4018+	18	06	X7	0	1100 °C			SEDEM	K 1.5/600 installed
TC88	BehindMirror-2	TC Type K	mV	in	4018+	18	07	X8	0	1100 °C			SEDEM	K 1.5/600 installed

Table 16: Oresol sensors (thermocouples)

A.6 Solar Operation

Table 17 lists all test days with solar operation. It contains times for start and end of fluidized bed ("FB") operation, with sun ("Solar"), and with hydrogen ("H2"), as well as the associated duration. Further columns provide information on the maximum temperature reached on the corresponding day, the amount of water produced (separated into water of crystallization and reaction water), as well as the average hydrogen conversion and the average water production rate. In addition, maximum or total values for the various subphases ("05" etc.)⁹³ and main phases (in red, see chapter 4.1) are displayed.

Date	Gas	Start FB	Start Solar	Start H2	End H2	End Solar	End FB	Time FB	Time Solar	Time H2	MaxTemp	Water Crys	Water H2	Conversion	Rate	Comment
Phase 1								47,9 h	30,8 h	0,0 h	415°C	5 ml				
05-Solar Phase 1a								28,6 h	18,6 h	0,0 h	415°C	0 ml				
13/07/2016	Air	9:45	10:11			12:40	12:40	2:55	2:29	0:00	168	0				First Solar
14/07/2016	Air	8:38	9:56			12:30	12:40	4:02	2:34	0:00	213	0				
19/07/2016	Air	8:41	8:54			12:30	13:30	4:49	3:36	0:00	404	0				Cloudy
20/07/2016	Air	8:41	9:36			10:55	10:56	2:15	1:19	0:00	157	0				
21/07/2016	Air	9:00	9:22			12:00	13:28	4:28	2:38	0:00	407	0				
26/07/2016	Air	8:31	8:58			10:30	11:25	2:54	1:32	0:00	406	0				
27/07/2016	Argon	9:18	9:37			10:26	10:34	1:16	0:49	0:00	373	0				Argon
28/07/2016	Air	8:00	8:22			12:00	13:57	5:57	3:38	0:00	415	0				
07-Solar Phase 1b								19,3 h	12,2 h	0,0 h	413°C	5 ml				
"Air / New Downstream"																
14/12/2016	Air	8:57	9:17			11:31	12:21	3:24	2:14	0:00	408					
20/12/2016	Air	9:15	9:36			11:30	12:11	2:56	1:54	0:00	403					
24/01/2017	Air	8:55	9:18			13:00	14:02	5:07	3:42	0:00	407					
25/01/2017	Air	9:26	9:45			11:44	12:59	3:33	1:59	0:00	410					
30/01/2017	Air	9:23	9:51			12:14	13:41	4:18	2:23	0:00	413	4,5				
Phase 2								26,9 h	15,4 h	0,0 h	814°C	113 ml				
08-Solar Phase 2								26,9 h	15,4 h	0,0 h	814°C	113 ml				
"Argon / 800°C"																
31/01/2017	Argon	9:43	9:54			12:00	14:15	4:32	2:06	0:00	556	18				First hot Argon
01/02/2017	Argon	9:43	10:00			11:23	12:57	3:14	1:23	0:00	708	14				Gas Demand
09/02/2017	Argon	8:55	9:05			12:31	14:42	5:47	3:26	0:00	773	10				Win Crack
10/03/2017	Argon	9:05	9:20			12:55	14:45	5:40	3:35	0:00	729	40				
27/03/2017	Argon	8:36	8:46			10:04	10:54	2:18	1:18	0:00	520	9				Cloudy
29/03/2017	Argon	7:58	8:12			11:50	13:23	5:25	3:38	0:00	814	22				>800°C
Phase 3								59,7 h	44,4 h	8,3 h	977°C	85 ml	250,6 ml	56%	63ml/h	
09-Solar Phase 3								59,7 h	44,4 h	8,3 h	977°C	85 ml	251 ml	56%	63ml/h	
"Argon+H2 / 900°C"																
30/03/2017	Ar+H2	8:20	8:30	10:15	10:31	11:15	13:19	4:59	2:45	0:16	844	0	4,5	25%	17ml/h	First H2
03/04/2017	Ar+H2	8:36	8:52	11:00	11:45	11:59	13:35	4:59	3:07	0:45	837	0	0	0%	0ml/h	
05/04/2017	Ar+H2	8:45	8:57	10:50	11:01	11:30	11:30	2:45	2:33	0:11	852	0	1,3	10%	7ml/h	
07/04/2017	Argon	8:03	8:24			11:45	13:20	5:17	3:21	0:00	852	5,7				
11/04/2017	Ar+H2	8:15	8:25	10:20	10:43	11:30	12:22	4:07	3:05	0:23	872	0	6	15%	16ml/h	
12/04/2017	Argon	8:08	8:14			11:00	12:34	4:26	2:46	0:00	883	1,9				
17/04/2017	Ar+H2	9:06	9:13	11:05	11:30	12:00	13:37	4:31	2:47	0:25	916	0	3,3	10%	8ml/h	
25/04/2017	Ar+H2	8:33	8:40	10:30	11:30	12:15	13:07	4:34	3:35	1:00	924	0	26	27%	26ml/h	
18/05/2017	Ar+H2	8:07	8:25	10:22	12:15	13:00	13:21	5:14	4:35	1:53	956	0	60	33%	32ml/h	
06/06/2017	Ar+H2	8:23	8:34	11:00	11:56	12:30	13:16	4:53	3:56	0:56	942	0	9,5	11%	10ml/h	
07/06/2017	Argon	8:23	8:30			12:35	12:50	4:27	4:05	0:00	933	7,7				P-Flow
15/06/2017	Argon	10:56	11:12			11:35	11:39	0:43	0:23	0:00	387	0				CanalSur
21/06/2017	Argon	10:21	10:27			10:42	11:08	0:47	0:15	0:00	359	0				RTVE
29/06/2017	Ar+H2	9:20	9:26	11:22	12:19	13:10	13:37	4:17	3:44	0:57	931	0	60	40%	63ml/h	Doku
30/06/2017	Ar+H2	8:30	8:38	10:00	11:30	12:05	12:11	3:41	3:27	1:30	977	0	80	56%	53ml/h	a tope!
Phase 4								66,3 h	59,4 h	13,2 h	962°C	581 ml	1069 ml	100%	125ml/h	
10-Solar Phase 4a								28,0 h	25,0 h	2,9 h	962°C	133 ml	248 ml	68%	125ml/h	
"More H2 / 900°C"																
17/10/2018	Argon	8:23	9:12			10:15	10:21	1:58	1:03	0:00	109	0				Shutter not ok
24/10/2018	Argon	9:15	9:23			12:35	12:44	3:29	3:12	0:00	664	61				Crys. Water
25/10/2018	Argon	9:00	9:27			12:20	12:29	3:29	2:53	0:00	934	63,1				
31/10/2018	Ar+H2	10:27	10:35	12:00	12:28	13:30	13:37	3:10	2:55	0:28	950	0	30,6	68%	66ml/h	
02/11/2018	Ar+H2	10:02	10:09	11:16	11:56	12:17	12:17	2:15	2:08	0:40	937	0	74,4	62%	112ml/h	
06/11/2018	Ar+H2	9:38	9:46	11:45	12:25	13:04	13:06	3:28	3:18	0:40	962	0	83,2	65%	125ml/h	
07/11/2018	Argon	9:22	9:30			10:19	10:19	0:57	0:49	0:00	853	0				PT02 high
08/11/2018	Ar+H2	10:22	10:28	11:55	13:03	14:30	14:33	4:11	4:02	1:08	951	0	60,1	59%	53ml/h	
12/11/2018	Argon	8:42	8:54			11:35	11:40	2:58	2:41	0:00	906	9,2				Cloudy
13/11/2018	Argon	9:28	9:34			11:30	11:30	2:02	1:56	0:00	926					Cloudy
11-Solar Phase 4b								17,0 h	15,7 h	5,2 h	958°C	373 ml	507 ml	94%	108ml/h	
"More H2O / 900°C"																
09/01/2019	Ar+H2	9:23	9:37	12:18	13:41	14:00	14:08	4:45	4:23	1:23	947	40	126,6	94%	92ml/h	
10/01/2019	Ar+H2	9:05	9:12	10:45	13:08	13:30	13:34	4:29	4:18	1:28	958	90,5	140,6	92%	96ml/h	
11/01/2019	Ar+H2	9:50	9:55	12:00	13:36	13:55	14:07	4:17	4:00	1:36	956	140	172,1	87%	108ml/h	
14/01/2019	Ar+H2	9:01	9:08	11:11	11:59	12:10	12:30	3:29	3:02	0:48	953	102,9	67,9	89%	85ml/h	
12-Solar Phase 4c								21,4 h	18,7 h	5,0 h	949°C	74 ml	314 ml	100%	74ml/h	
"More H2O / 900°C"																
24/09/2019	Ar+H2	8:09	8:17	11:32	12:48	13:20	13:31	5:22	5:03	1:16	916	13,4	93,3	100%	74ml/h	Deluge
25/09/2019	Ar+H2	8:22	8:28	10:45	11:50	12:30	12:58	4:36	4:02	1:05	949	19	75,9	89%	70ml/h	
27/09/2019	Ar+H2	8:17	8:25	10:34	12:05	12:35	12:54	4:37	4:10	1:31	873	21	73,5	73%	48ml/h	
30/09/2019	Ar+H2	8:16	8:24	10:30	11:37	12:30	12:37	4:21	4:06	1:07	911	20,9	70,8	71%	63ml/h	
02/10/2019	Argon	8:04	8:10			9:30	10:30	2:26	1:20	0:00	906	0				PT02 high
Total								200,8 h	150,0 h	21,4 h	977°C	783 ml	1320 ml	100%	125ml/h	

Table 17: Oresol solar operation data.

⁹³ Internal numbering during the project. 01-04 and 06 are not listed because they were non-solar tests.

References

- Allen, C. C. (2015). Taurus Littrow Pyroclastic Deposit: High-Yield Feedstock For Lunar Oxygen. *Proceedings of the 46th Lunar and Planetary Science Conference*, p. 1140. Hampton: NASA/Langley Research Center.
- Allen, C. C., Morris, R. V., & McKay, D. S. (1996). Oxygen extraction from lunar soils and pyroclastic glass. *Journal of Geophysical Research E: Planets*, 101(E11), 26085–26095. <https://doi.org/10.1029/96JE02726>
- Alvarado, L., & Chen, A. (2014). Electrodeionization: Principles, strategies and applications. *Electrochimica Acta*, 132, 583–597. <https://doi.org/10.1016/j.electacta.2014.03.165>
- Anovitz, L. M., Treiman, A. H., Essene, E. J., Hemingway, B. S., Westrum, E. F., Wall, V. J., ... Bohlen, S. R. (1985). The heat-capacity of ilmenite and phase equilibria in the system Fe-T-O. *Geochimica et Cosmochimica Acta*, 49(10), 2027–2040. [https://doi.org/10.1016/0016-7037\(85\)90061-4](https://doi.org/10.1016/0016-7037(85)90061-4)
- Bandfield, J. L., Hayne, P. O., Williams, J. P., Greenhagen, B. T., & Paige, D. A. (2015). Lunar surface roughness derived from LRO Diviner Radiometer observations. *Icarus*, 248, 357–372. <https://doi.org/10.1016/j.icarus.2014.11.009>
- Bellgardt, D., & Werther, J. (1984). Paper 7.6. *16th Int. Symp. on Heat and Mass Transfer*. Dubrovnik.
- Benna, M., Hurley, D. M., Stubbs, T. J., Mahaffy, P. R., & Elphic, R. C. (2019). NASA Public Access. *Nat Geosci.*, 12(May), 333–338. <https://doi.org/10.1038/s41561-019-0345-3>
- Buck, A. L. (1981). New Equations for Computing Vapor Pressure and Enhancement Factor. *Journal of Applied Meteorology and Climatology*, 20(12), 1527–1532.
- Bürgel, B. H. (1975). *Bürgels Himmelskunde* (E. Krug, Ed.). Gütersloh, Berlin, München, Wien: Bertelsmann-Lexikon-Verlag.
- Carr, B. B. (1963). Recovery of Water or Oxygen by Reduction of Lunar Rock. *AIAA Journal*, 1(4), 921–924. <https://doi.org/10.2514/3.1674>
- Clark, D. L., Keller, B. W., & Kirkland, J. A. (2009). Field test results of the PILOT hydrogen reduction reactor. *AIAA 2009-6475, AIAA Space*. Pasadena, CA.
- Colaprete, A., Schultz, P., Heldmann, J., Wooden, D., Shirley, M., Ennico, K., ... Sollitt, L. (2010). Detection of water in the LCROSS ejecta plume. *Science*, 330(6003), 463–468. <https://doi.org/10.1126/science.1186986>
- Colorado School of Mines. (2021). Planetary Simulant Database. Retrieved from <https://simulantdatab.com/>
- Denk, T., González-Pardo, A., Cañadas, I., & Vidal, A. (2017). Design and test of a concentrated solar powered fluidized bed reactor for ilmenite reduction. *SolarPACES*.
- Duffie, J. A., & Beckman, W. A. (1980). *Solar Engineering of Thermal Processes* (2nd ed.). Madison: Wiley.
- Ebert, M., Amsbeck, L., Rheinländer, J., Schlögl-Knothe, B., Schmitz, S., Sibum, M., ... Buck, R. (2019). Operational experience of a centrifugal particle receiver prototype. *AIP Conference Proceedings*, 2126(July), 2012–2016. <https://doi.org/10.1063/1.5117530>

- Ellingham, H. J. T. (1944). Reducibility of oxides and sulphides in metallurgical processes. *Journal of the Society of Chemical Industry*, 63(5).
<https://doi.org/doi:10.1002/jctb.5000630501>
- Ergun, S. (1952). Fluid flow through packed columns. *Chemical Engineering Progress*, 48, 89–94.
- Fereres, S., Morales, M., Denk, T., Osen, K., McGlen, R. J., Seidel, A., ... Binns, D. (2021). Payload Concept Evaluation for Water/Oxygen production on the Moon based on Thermo- or Electro-Chemical Reduction of Lunar Regolith. *50th International Conference on Environmental Systems*. Lisboa, Portugal.
- Flamant, G., & Olalde, G. (1983). High temperature solar gas heating comparison between packed and fluidized bed receivers-I. *Solar Energy*, 31(5), 463–471.
[https://doi.org/10.1016/0038-092X\(83\)90050-6](https://doi.org/10.1016/0038-092X(83)90050-6)
- Fray, D. J. (2001). Emerging molten salt technologies for metals production. *JOM*, 53(10), 26–31. <https://doi.org/10.1007/s11837-001-0052-5>
- Gaddis, L. R., Staid, M. I., Tyburczy, J. A., Hawke, B. R., & Petro, N. E. (2003). Compositional analyses of lunar pyroclastic deposits. *Icarus*, 161(2), 262–280.
[https://doi.org/10.1016/S0019-1035\(02\)00036-2](https://doi.org/10.1016/S0019-1035(02)00036-2)
- Geldart, D. (1973). Types of Gas Fluidization. *Powder Technology*, 7 (5), 285–292.
- Georgi, W., & Metin, E. (2012). *Einführung in LabVIEW* (5. Auflage). München: Carl Hanser Verlag.
- Gibson, M. A., & Knudsen, C. W. (1985). Lunar Oxygen Production from Ilmenite. *Lunar Bases and Space Activities of the 21st Century*, 543–550.
- González-Pardo, A., & Denk, T. (2016). A novel off-axis solar concentrator providing a vertical beam. *AIP Conference Proceedings 1734*, 020006. <https://doi.org/10.1063/1.4949030>
- Goswami, Y. (2015). *Principles of Solar Engineering* (3rd Ed.). Boca Raton: CRC Press, Taylor & Francis Group.
- Hauri, E. H., Weinreich, T., Saal, A. E., Rutherford, M. C., & Van Orman, J. A. (2011). High Pre-Eruptive Water Contents Preserved in Lunar Melt Inclusions. *Science*, 333(6039), 213–215. <https://doi.org/10.1126/science.1204626>
- Hintze, P. E., Curran, J., & Back, T. (2009). Lunar surface stabilization via sintering or the use of heat cured polymers. *47th AIAA Aerospace Sciences Meeting Including the New Horizons Forum and Aerospace Exposition*, (January 2009). <https://doi.org/10.2514/6.2009-1015>
- Ho, C. K. (2016). A review of high-temperature particle receivers for concentrating solar power. *Applied Thermal Engineering*, 109, 958–969.
<https://doi.org/10.1016/j.applthermaleng.2016.04.103>
- Honniball, C. I., Lucey, P. G., Li, S., Shenoy, S., Orlando, T. M., Hibbitts, C. A., ... Farrell, W. M. (2021). Molecular water detected on the sunlit Moon by SOFIA. *Nature Astronomy*, 5(2), 121–127. <https://doi.org/10.1038/s41550-020-01222-x>
- Just, G. H., Smith, K., Joy, K. H., & Roy, M. J. (2020). Parametric review of existing regolith excavation techniques for lunar In Situ Resource Utilisation (ISRU) and recommendations for future excavation experiments. *Planetary and Space Science*, 180(April 2019), 104746.
<https://doi.org/10.1016/j.pss.2019.104746>

- Koenigsdorff, R. (1994). *Direkteinkopplung konzentrierter Solarstrahlung in eine zirkulierende Wirbelschicht*. VDI-Verlag, Düsseldorf.
- Kunii, D., & Levenspiel, O. (1991). *Fluidization Engineering* (Second Ed.). Boston: Butterworth-Heinemann.
- Lavagna, M., & Lunghi, P. (2018). Demonstrator design for lunar In Situ Utilisation and Oxygen production. *IAC18-A3.2.C1, International Astronautical Congress 2018*. Bremen, Germany.
- Lin, H., Li, S., Xu, R., Liu, Y., Wu, X., Yang, W., ... Wang, C. (2022). In situ detection of water on the Moon by the Chang'E-5 lander. *Science Advances*, 8(1). <https://doi.org/10.1126/sciadv.abl9174>
- Lomax, B. A., Conti, M., Khan, N., Bennett, N. S., Ganin, A. Y., & Symes, M. D. (2020). Proving the viability of an electrochemical process for the simultaneous extraction of oxygen and production of metal alloys from lunar regolith. *Planetary and Space Science*, 180(September 2019), 104748. <https://doi.org/10.1016/j.pss.2019.104748>
- Lunar Sourcebook - A User's Guide to the Moon. (1991). In G. H. Heiken, D. T. Vaniman, & B. M. French (Eds.), *Cambridge University Press*. Cambridge.
- Mamajek, E. E., Prsa, A., Torres, G., Harmanec, P., Asplund, M., Bennett, P. D., ... Stewart, S. G. (2015). *IAU 2015 Resolution B3 on Recommended Nominal Conversion Constants for Selected Solar and Planetary Properties*. 1–6. Retrieved from <http://arxiv.org/abs/1510.07674>
- Mckay, D. S., Morris, R. V., & Jurewicz, A. J. (1991). Experimental reduction of simulated lunar glass by carbon and hydrogen and implications for lunar base oxygen production. *22nd Lunar Planetary Science Conference*, 49–52.
- Messerschmid, E., & Fasoulas, S. (2011). *Raumfahrtssysteme* (4. Auflage). Springer.
- Meurisse, A., Lomax, B., Selmeç, Á., Conti, M., Lindner, R., Makaya, A., ... Carpenter, J. (2021). Lower temperature electrochemical reduction of lunar regolith simulants in molten salts. *Planetary and Space Science*, 211(October 2021), 105408. <https://doi.org/10.1016/j.pss.2021.105408>
- Mueller, R. P., & Townsend, I. (2009). Lunar regolith simulant feed system for a hydrogen reduction reactor system. *47th AIAA Aerospace Sciences Meeting Including the New Horizons Forum and Aerospace Exposition*, (November), 1–8. <https://doi.org/10.2514/6.2009-1658>
- Müller-Erlwein, E. (2007). *Chemische Reaktionstechnik* (2. Auflage). Wiesbaden: Teubner.
- Nakamura, T., Van Pelt, A. D., Smith, B. K., & Clark, L. (2008). Solar thermal power system for oxygen production from lunar regolith. *AIP Conference Proceedings*, 969(January 2008), 178–185.
- NASA. (2007). *MoonROx Challenge Rules and Requirements Document*. Retrieved from <https://web.archive.org/web/20110915170553/http://moonrox.csewi.org/files/MoonROx-Rules.pdf>
- Neal, C. R., & Taylor, L. A. (1992). Petrogenesis of mare basalts: a record of lunar volcanism. *Geochimica et Cosmochimica Acta*, 56, 2177–2211.

- Ouaida, M. B., Badie, J. M., & Flamant, G. (1985). High temperature thermochemical treatment of ilmenite FeTiO₃ in solar chemical reactors. *Solar and Wind Technology*, 2(1), 15–24. [https://doi.org/10.1016/0741-983X\(85\)90023-2](https://doi.org/10.1016/0741-983X(85)90023-2)
- Ovadia, Y. (2021). Helios is powering lunar settlements of the future. Retrieved August 5, 2021, from CTECH website: <https://www.calcalistech.com/ctech/articles/0,7340,L-3907723,00.html>
- Pieters, C., Mccord, T. B., Charette, M. P., & Adams, J. B. (1974). Lunar surface: Identification of the dark mantling material in the Apollo 17 soil samples. *Science*, 183(4130), 1191–1194. <https://doi.org/10.1126/science.183.4130.1191>
- Rasera, J. N., Cilliers, J. J., Lamamy, J. A., & Hadler, K. (2020). The beneficiation of lunar regolith for space resource utilisation: A review. *Planetary and Space Science*, 186(April 2019), 104879. <https://doi.org/10.1016/j.pss.2020.104879>
- Rodriguez, J., Cañadas, I., Monterreal, R., Enrique, R., & Galindo, J. (2019). PSA SF60 solar furnace renewed. *AIP Conference Proceedings*, 2126(July). <https://doi.org/10.1063/1.5117558>
- Rohsenow, W. M., Hartnett, J. P., & Cho, Y. I. (Eds.). (1998). *Handbook of Heat Transfer* (3rd Ed.). McGraw-Hill.
- Romberg, O., Braukhane, A., Gonzalez-Elipe, A., Baumeister, J., & Spennberg, D. (2007). Acquisition of Moon Oxygen Ressources. *Proceedings of the International Astronautical Congress (IAC)*. Hyderabad.
- Sanders, G.B., Simon, T., & Larson, W. E. (2009). NASA in-situ resource utilization program. *AIAA 2009-0412, AIAA Aerospace Science Meeting*. Orlando, FL.
- Sanders, Gerald B., & Larson, W. E. (2013). Progress Made in Lunar In Situ Resource Utilization under NASA's Exploration Technology and Development Program. *Journal of Aerospace Engineering*, 26(1), 5–17. [https://doi.org/10.1061/\(asce\)as.1943-5525.0000208](https://doi.org/10.1061/(asce)as.1943-5525.0000208)
- Sanders, Gerald B., & Larson, W. E. (2015). Final review of analog field campaigns for in Situ Resource Utilization technology and capability maturation. *Advances in Space Research*, 55(10), 2381–2404. <https://doi.org/10.1016/j.asr.2014.12.024>
- Sargeant, H. M. (2020). *Water from Lunar Regolith - Reduction by hydrogen for a small-scale demonstration of in situ resource utilisation for the Moon* (The Open University). <https://doi.org/10.21954/ou.ro.00011fb6>
- Sauerborn, M. (2005). *Pyrolyse von Metalloxiden und Silikaten unter Vakuum mit konzentrierter Solarstrahlung*. Retrieved from <https://hdl.handle.net/20.500.11811/2298>
- Schlüter, L., & Cowley, A. (2020). Review of techniques for In-Situ oxygen extraction on the moon. *Planetary and Space Science*, 181(September 2019), 104753. <https://doi.org/10.1016/j.pss.2019.104753>
- Schuler, J., Smith, D., Mueller, R., Nick, A., Langton, A., Buckles, B., & Leucht, K. (2019). RASSOR Excavator for ISRU Lunar Mining. Retrieved August 6, 2021, from USRA ISRU Workshop website: https://www.hou.usra.edu/meetings/lunarisru2019/presentations/5061_Schuler.pdf
- Schwandt, C., Hamilton, J. A., Fray, D. J., & Crawford, I. A. (2012). The production of oxygen and metal from lunar regolith. *Planetary and Space Science*, 74(1), 49–56. <https://doi.org/10.1016/j.pss.2012.06.011>

- Seidel, A., Häming, M., Monchieri, E., Quadbeck, P., Fereres Rapoport, S., Pal, U., & Spierings, A. (2021). ROXY: Regolith to Oxygen & Metal Conversion Lunar Demonstrator. *Luxembourg Space Resources Week 2021*.
- Shao, R., Williams, R. R., & Overfelt, R. A. (2006). Fluidization Behavior of Fine Powders in Reduced Gravity Conditions. *Journal of Thermophysics and Heat Transfer*, 20(3), 371–375. <https://doi.org/10.2514/1.16278>
- Shomate, C. H., Naylor, B. F., & Boericke, F. S. (1946). *Thermodynamic Properties of Ilmenite and Selective Reduction of Iron in Ilmenite*.
- Sibille, L., Sadoway, D. R., Sirk, A., Tripathy, P., Melendez, O., Standish, E., ... Poizeau, S. (2009). Recent advances in scale-up development of molten regolith electrolysis for oxygen production in support of a lunar base. *47th AIAA Aerospace Sciences Meeting Including the New Horizons Forum and Aerospace Exposition*, (659). <https://doi.org/10.2514/6.2009-659>
- SolarPACES. (2018). How CSP Works: Tower, Trough, Fresnel or Dish. Retrieved from <https://www.solarpaces.org/how-csp-works/>
- Sowers, G. (2020). Thermal Mining of Lunar Ices. *Future In-Space Operations (FISO) Seminar*.
- SpaceX. (2020). *Starship User Guide*. Retrieved from https://www.spacex.com/media/starship_users_guide_v1.pdf
- Spudis, P. D. (2016). *The Value of the Moon*. Washington, DC: Smithsonian Books.
- Taylor, L. A. (2015). Status of Lunar Regolith Simulants - an Update. In *Lunar Exploration Analysis Group*.
- Taylor, L. A., & Carrier, W. D. (1993). Oxygen production on the Moon: an overview and evaluation. In *Resources of Near-Earth Space* (pp. 69–108).
- Tchobanoglous, G., & Schroeder, E. D. (1987). *Water Quality: Characteristics, Modelling, Modification*. Reading, Mass.: Addison-Wesley Publishing.
- University of Cambridge. (2021). The Interactive Ellingham Diagram. Retrieved from https://www.doitpoms.ac.uk/tlplib/ellingham_diagrams/interactive.php
- Urbina, D. A., Madakashira, H. K., Salini, J., Govindaraj, S., Bjoerstad, R., Gancet, J., ... Prodeka, E. (2017). Robotic prototypes for the solar sintering of regolith on the lunar surface developed within the Regolight project. *Proceedings of the International Astronautical Congress, IAC*, 4(November), 2632–2641.
- Wang, D., Gmitter, A. J., & Sadoway, D. R. (2011). Production of Oxygen Gas and Liquid Metal by Electrochemical Decomposition of Molten Iron Oxide. *Journal of The Electrochemical Society*, 158(6), E51–E54. <https://doi.org/10.1149/1.3560477>
- Weir, A. (2017). *Artemis*. New York: Crown Publishing Group.
- Wen, C. Y., & Yu, Y. H. (1966). A Generalized Method for Predicting the Minimum fluidization velocity. *American Institute of Chemical Engineers Journal*, 12, 610–612.
- Werther, J. (2007). Fluidized-Bed Reactors. In *Ullmann's Encyclopedia of Industrial Chemistry* (pp. 319–366). https://doi.org/10.1002/14356007.b04_239.pub2
- Whittington, M. (2015). *Why is it So Hard to Go Back to the Moon?* Houston.

Winter, C.-J., Sizmann, R. L., & Vant-Hull, L. L. (1991). *Solar Power Plants*.

<https://doi.org/10.1007/978-3-642-61245-9>

Zhang, J., Ping, J., Zeng, Z., Yang, Y., Wang, M., & Li, X. (2019). Surface temperature simulation of lunar dayside and its geological applications: A case in sinus iridum. *Sensors (Switzerland)*, 19(24). <https://doi.org/10.3390/s19245545>